Institut für Physik und Astronomie

Unraveling massive star and binary physics in the nearby low-metallicity galaxy, the Small Magellanic Cloud, as a proxy for high-redshift galaxies

Daniel Pauli

Kumulative Dissertation
zur Erlangung des akademischen Grades
“doctor rerum naturalium”
(Dr. rer. nat.)
in der Wissenschaftsdisziplin Astrophysik

eingereicht an der
Mathematisch-Naturwissenschaftlichen Fakultät
der Universität Potsdam

August 15, 2024

Main supervisor:
apl. Prof. Dr. Lidia Oskinova

Supervisors:
Prof. Dr. Stephan Geier
Prof. Dr. Katja Poppenhäger

Reviewers:
apl. Prof. Dr. Lidia Oskinova
Prof. Dr. Stephan Geier
Prof. Dr. Nicole St-Louis

Date of the defense: 14.08.2024

Published online on the
Publication Server of the University of Potsdam:
https://doi.org/10.25932/publishup-65318
https://nbn-resolving.org/urn:nbn:de:kobv:517-opus4-653184

Abstract

Massive stars ($M_{\rm ini} > 8\,M_{\odot}$) are the key feedback agents within galaxies, as they shape their surroundings via their powerful winds, ionizing radiation, and explosive supernovae. Most massive stars are born in binary systems, where interactions with their companions significantly alter their evolution and the feedback they deposit in their host galaxy. Understanding binary evolution, particularly in the low-metallicity environments as proxies for the Early Universe, is crucial for interpreting the rest-frame ultraviolet spectra observed in high-redshift galaxies by telescopes like Hubble and James Webb.

This thesis aims to tackle this challenge by investigating in detail massive binaries within the low-metallicity environment of the Small Magellanic Cloud galaxy. From ultraviolet and multi-epoch optical spectroscopic data, we uncovered post-interaction binaries. To comprehensively characterize these binary systems, their stellar winds, and orbital parameters, we use a multifaceted approach. The Potsdam Wolf-Rayet stellar atmosphere code is employed to obtain the stellar and wind parameters of the stars. Additionally, we perform consistent light and radial velocity fitting with the Physics of Eclipsing Binaries software, allowing for the independent determination of orbital parameters and component masses. Finally, we utilize these results to challenge the standard picture of stellar evolution and improve our understanding of low-metallicity stellar populations by calculating our binary evolution models with the Modules for Experiments in Stellar Astrophysics code.

We discovered the first four O-type post-interaction binaries in the SMC (Chapters 2, 5, and 6). Their primary stars have temperatures similar to other OB stars and reside far from the helium zero-age main sequence, challenging the traditional view of binary evolution. Our stellar evolution models suggest this may be due to enhanced mixing after core-hydrogen burning. Furthermore, we discovered the so-far most massive binary system undergoing mass transfer (Chapter 3), offering a unique opportunity to test mass-transfer efficiency in extreme conditions. Our binary evolution calculations revealed unexpected evolutionary pathways for accreting stars in binaries, potentially providing the missing link to understanding the observed Wolf-Rayet population within the SMC (Chapter 4). The results presented in this thesis unveiled the properties of massive binaries at low-metallicity which challenge the way the spectra of high-redshift galaxies are currently being analyzed as well as our understanding of massive-star feedback within galaxies.

Zusammenfassung

Massereiche Sterne ($M_{\rm ini} > 8\,M_{\odot}$) beeinflussen ihre Umgebung durch ihre starke Winde, ionisierende Strahlung und wenn sie als Supernova explodieren. Sie sind daher die Schlüsselfaktoren für die Rückkopplungsprozesse innerhalb von Galaxien. Die meisten massereichen Sterne entstehen in Doppelsternsystemen, in welchen sie mit ihren Begleitern interagieren können, was weitreichende Konsequenzen für ihre weitere Entwicklung und die Rückkopplung auf ihre Galaxie beeinflusst. Ein tiefgreifendes Verständnis der Entwicklung von Doppelsternen, insbesondere in metallarmen Umgebungen als Näherung für Sterne im frühe Universum, ist entscheidend für die richtige Interpretation der Spektren von Galaxies bei hohen Rotverschiebungen die von Weltraumteleskopen wie Hubble und James Webb beobachtet werden.

Diese Dissertation widmet sich der Herausforderung für ein besseres Verständnis von Doppelsternsystemen, indem sie massereiche Doppelsterne in der metallarmen Umgebung der Galaxie „Kleinen Magellanischen Wolke“ detailliert untersucht. Anhand von zahlreichen ultravioletten und optischen Spektroskopiedaten konnten Doppelsterne, die schon miteinander interagiert haben, entdeckt werden. Um diese Doppelsternsysteme, die Parameter der einzelnen Sterne und ihrer Sternwinde sowie die Bahnparameter zu erhalten und zu charakterisieren, verwenden wir einen mehrteiligen Ansatz. Als erstes, um die Parameter der Sterne und ihrer Winde zu gewinnen, wird der Potsdamer Wolf-Rayet-Sternatmosphärencode eingesetzt. Darüber hinaus führen wir mit der Software „Physics of Eclipsing Binaries“ eine konsistente Licht- und Radialgeschwindigkeitsanpassung durch, die eine unabhängige Bestimmung der Bahnparameter und Komponentenmassen ermöglicht. Abschließend werden diese Ergebnisse verwendet, um die traditionelle Sichtweise der Doppelstern-Entwicklung in Frage zu stellen und unser Verständnis von Sternpopulationen mit geringer Metallizität zu verbessern, indem wir Evolutionsmodelle von Doppelsternen mithilfe des Codes „Modules for Experiments in Stellar Astrophysics“ berechnen.

In dieser Arbeit konnten erstmalig vier massereiche O-Typ-Doppelsterne nach einer Wechselwirkung innerhalb der Kleinen Magellanischen Wolke entdeckt werden (Kapitel 2, 5 und 6). Überraschenderweise sind die Temperaturen der Massegeber vergleichbar mit denen anderer OB-Sterne und daher kühler als zuvor erwartet. Dies stellt die traditionelle Sichtweise der Doppelstern-Entwicklung in Frage. Unsere Sternenentwicklungsmodelle deuten darauf hin, dass die beobachtete Diskrepanz gelöst werden kann wenn man eine stärkere Durchmischung nach dem Wasserstoffbrennen im Kern annimmt. Darüber hinaus haben wir das bisher massereichste Doppelsternsystem entdeckt, welches sich gerade in einem Massenaustausch befindet (Kapitel 3). Dieses System bietet eine einzigartige Gelegenheit, die Effizienz des Massentransfers unter extremen Bedingungen zu testen. Des Weiteren haben unsere Berechnungen zur Doppelsternentwicklung unerwartete Entwicklungspfade für akkretierende Sterne in Doppelsternsystemen enthüllten, die möglicherweise das fehlende Bindeglied zum Verständnis der beobachteten Wolf-Rayet-Population in der Kleinen Magellanschen Wolke darstellen (Kapitel 4). Die in dieser Dissertation präsentierten Ergebnisse enthüllen die einzigartigen Eigenschaften von massereichen Doppelsternen in metallarmen Umgebungen, die sowohl die aktuelle Analyse der Spektren von Galaxien mit hoher Rotverschiebung als auch unser Verständnis der Rückkopplungsprozesse von massereichen Sternen in Galaxien in Frage stellen.

Contents

Chapter 1

Introduction

The late 19th and early 20th centuries mark the birth of stellar astronomy and spectroscopy. In the 1880s Edward Pickering started a systematic program to classify stellar spectra, but it finally was one of his co-workers Annie Jump Cannon who brought spectral classification to the next level by collecting spectra from about several hundred thousand stars and classifying them into distinct groups (namely O, B, A, F, G, K, M; Cannon & Pickering 1918), which was accepted as the new standard in 1922 by the International Astronomical Union. Shortly after that, it was understood that spectral types correlate to a star's surface temperature, with OB-type stars ($T_{\rm eff} \gtrsim 10\,000$ K) being among the hottest known stellar objects (Payne 1924). Today, it is known that early B and O-type stars are over ten times more massive and thousands to millions of times more luminous than our Sun. While our Sun can only fuse hydrogen to helium and later on helium to carbon (and oxygen) in its core, massive stars can fuse heavier elements up to iron inside their cores. At some point, the iron core will become unstable and collapse, leading to an energetic explosion called supernova that marks the death of a massive star (e.g. Smartt 2009). Supernova explosions release copious amounts of mechanical energy into a star's surroundings and enrich the neighboring interstellar medium with heavy elements (e.g. Yorke et al. 1989; Nomoto et al. 2013; Erdim et al. 2021).

Massive OB-type stars are hot and emit most of their radiation in the ultraviolet (UV) part of the spectrum. A portion of this UV radiation is absorbed and scattered by heavy elements, such as iron, within the stellar atmosphere. This process transfers so much energy from the radiation field into the atmosphere's material that it is radially blown away from the star's surface via a so-called stellar wind. Throughout their life, massive stars can lose several solar masses through their winds and in the most extreme cases even more than half of their initial mass. Massive stars deposit large amounts of mechanical energy and heavy elements into their surroundings via their stellar winds (e.g. Cescutti & Chiappini 2010; Rogers & Pittard 2013, and references therein). Additionally, the escaping UV radiation ionizes and shapes the nearby interstellar medium (e.g. Weaver et al. 1977; Tenorio-Tagle & Bodenheimer 1988). All of this makes massive stars the main feedback agents in galaxies as they dictate the chemical evolution and serve as regulators of star formation (e.g. Vink 2006; Rogers & Pittard 2013; Ramachandran et al. 2018b; Crowther 2019, and references therein).

However, the picture is more intricate since massive stars rarely live alone: The majority (more than 50%) of massive stars are born within close binary systems (Garmany et al. 1980; Sana et al. 2012; Moe & Di Stefano 2017). Stars in close binaries can interact and transfer mass between companions, resulting in the removal of the hydrogen-rich envelope of the mass donor. Such events drastically change a star's evolution and, hence, its feedback. Binarity complicates our understanding of massive stars, their winds, ionizing fluxes, and their final fate (e.g. Paczyński 1967; Vanbeveren 1991; Vanbeveren et al. 1998; Belczynski et al. 2002; de Mink et al. 2013a; Laplace et al. 2020). Yet, despite the key role massive binary stars play in galaxies, their properties, evolution, and feedback are poorly understood, especially at low-metallicity. Among the many open questions are: How efficient are binary interactions in removing a star's hydrogen-rich envelope? Do all stars in binaries evolve into helium stars? What are the chemical abundances of binary components? How to distinguish binary stars among general stellar populations?

Individual massive stars and binaries can only be resolved within our immediate cosmic neighborhood, the Local Group. For galaxies beyond our Local Group, it is only possible to obtain spectra that contain the integrated light of their underlying stellar population. Over the last decades, the Hubble Space Telescope (HST) has detected and obtained spectra of distant highly redshifted galaxies (Steidel et al. 1996; Oesch et al. 2016, e.g). The recently launched James Webb Space Telescope (JWST) has started a new era of high-resolution spectroscopy of distant

galaxies, enabling the detailed spectroscopic study of the spectra of galaxies up to redshifts of $z \approx 10 - 13$ (Curtis-Lake et al. 2023). These integrated spectra contain a wealth of information, and if interpreted correctly they reveal important details about the conditions of a distant galaxy's interstellar medium, its metallicity, and its star-formation rate (Kewley et al. 2019). From observations, it is suggested that the peak of star formation in galaxies occurred around redshift $z \approx 2$, in environments with a metallicity of approximately $Z \approx 1/7\,Z_\odot$ (Madau & Dickinson 2014; Tanvir et al. 2021).

To model the underlying stellar population hidden in the integrated spectra of high-redshift galaxies, astronomers rely on spectral synthesis codes. Within these codes, stellar evolution models are combined with spectral libraries to generate a synthetic spectrum for an entire stellar population. In their early stages, these codes only incorporated single-star models. The integration of binary evolution into synthetic stellar populations has demonstrated that these populations appear bluer at older than populations assuming only single-star evolution (Cerviño & Mas-Hesse 1994; Dionne & Robert 2006). However, the metallicities probed by HST and JWST ($Z \approx 0.2 - 0.025\,Z_\odot$; e.g., see Madau & Dickinson 2014; Tanvir et al. 2021; Curtis-Lake et al. 2023) are not covered by current spectral libraries and the evolution of stars in binaries is extrapolated from observations at higher metallicity. It was so far not clear how metallicity affects the evolution and spectral appearance of massive stars in binaries, which account for half of the stellar content inside a galaxy. Therefore, a crucial question remains: How can we analyze the integrated spectra of entire galaxies if the characteristics of individual stars and those in binaries are not well understood?

To properly unveil the underlying stellar population hidden in the integrated spectra of high-redshift galaxies, a deeper understanding of stellar and binary evolution at low metallicity is essential. Empirical studies are needed to serve as benchmarks for theoretical evolution models. Fortunately, within our cosmic neighborhood, we have two actively star-forming dwarf galaxies, the Large Magellanic Cloud (LMC) and the Small Magellanic Cloud (SMC). The LMC has a reduced metallicity of $Z_{\rm LMC} = 1/2\,Z_\odot$ (Rolleston et al. 2002), whereas its smaller counterpart, the SMC, exhibits an even lower metallicity of $Z_{\rm SMC} = 1/7\,Z_\odot$ (Hunter et al. 2007; Trundle et al. 2007). Its proximity and low metallicity make the SMC an excellent laboratory for studying massive stars with properties similar to those in distant young galaxies.

Over the last decades, several surveys have uncovered nearly the complete massive star population within the SMC. Extensive photometric surveys have revealed that there are more than 500 OB-type stars within the SMC that have visual magnitudes below $m_V < 15$ mag (Humphreys & McElroy 1984; Blaha & Humphreys 1989; Massey et al. 1995; Schootemeijer et al. 2021). However, the unveiled population is puzzling: there are fewer massive stars with initial masses above $\gtrsim 40\,M_\odot$ than expected (Schootemeijer et al. 2019). Few detailed spectroscopic surveys that considered and treated all stars as being effectively single (Mokiem et al. 2006; Bouret et al. 2013; Dufton et al. 2019; Ramachandran et al. 2019) have revealed discrepancies between observed and expected stellar and wind parameters. Notably, the mass-loss rates are significantly weaker than expected and cannot be explained by theory (Vink et al. 2001; Krtička & Kubát 2018; Ramachandran et al. 2019; Rickard et al. 2022; Björklund et al. 2023). Separately, dedicated searches have identified 12 Wolf-Rayet (WR) stars (massive stars in a late evolutionary stage; see Section 1.3.3) in the SMC (Azzopardi & Breysacher 1979; Morgan et al. 1991; Massey & Duffy 2001; Massey et al. 2003), with 5 confirmed as binary systems (Foellmi et al. 2003). Qualitative spectroscopic and orbital analyses (Foellmi et al. 2003; Kohler et al. 2014; Niedzielski & Skorzynski 2002; Moffat et al. 1990; St-Louis et al. 2005; Martins et al. 2009; Hainich et al. 2015; Shenar et al. 2016, 2018) have revealed their stellar and wind parameters, but opened more questions than answers. How could these WR stars form when the stellar winds of the stars in the SMC are too weak to remove the hydrogen-rich envelope? What is the role of binarity in explaining their stellar parameters? How do the WR star winds compare to those from OB-type stars?

In 2020, the HST Large program "Ultraviolet Legacy Library of Young Stars as Essential Standards" (ULLYSES) was launched. This initiative aimed at creating a comprehensive spectroscopic UV library of single massive stars at low metallicity and includes the SMC. The ULLYSES project is complemented by the XShootU project, which acquired single-epoch optical data to supplement the UV spectra (Vink et al. 2023). This combined dataset should enable a consistent analysis, yielding stellar and wind parameters of individual stars. In order to achieve the full scientific potential and deliver new important results, the ULLYSES and XShootU programs should be utilized to search for and study binaries in the sample. Such a detailed approach is needed to achieve a comprehensive understanding of young stellar populations, which have at least half of their stars in binary systems.

The goal of this thesis is to uncover the most massive (post) interaction binaries residing within the SMC galaxy, an to analyze, and fully characterize their stellar, wind, and orbital parameters.

- **Binary evolution:** Do we understand mass-transfer in binaries at low metallicity? Do low-metallicity mass-donors really lose most of their hydrogen-rich envelope during a mass-transfer event? How do the accretors evolve after the former donor died?

- **Stellar winds:** What are the mass-loss rates of (post) interaction binaries? Can they explain how a wind transitions from an OB-star wind to a strong WR wind? How does this affect the spectral appearance of a massive star?

- **Integrated spectra of young high-redshift galaxies:** Can current spectral synthesis codes model the spectra of integrated spectra of young galaxies? Do post-interaction binaries provide the majority of the ionizing feedback inside a galaxy?

To achieve these goals we initiated a dedicated HST program to create a dataset of UV spectra of the earliest O-type (i.e., the most massive) stars in the SMC (GO 15837; PI: Oskinova). During the time this thesis was conducted our observations were incorporated in the ULLYSES sample. The UV dataset is supplemented by multi-epoch optical spectra obtained with the European Southern Observatory's (ESO) X-Shooter spectrograph (ID: 109.22V0, PI: Pauli), allowing the identification of binary systems. By consistently modeling the optical and UV spectra with state-of-the-art stellar atmosphere models, along with incorporating light and radial velocity curves, we derive the stellar, wind, and orbital parameters of these binary systems. These data is used to calculate stellar evolution models, enhancing our understanding of massive binary at low metallicity and potentially leading to a revision of our interpretation of the integrated spectra of young high-redshift galaxies.

In the subsequent sections a theoretical overview of the fundamental physical principles used throughout this work is provided. Chapters 2 to 6 contain a collection of papers about detailed observation-based works on the spectral appearance of massive stars in binaries and their implications for our understanding of low-metallicity binary evolution. In Chapter 7, the results are discussed, highlighting their consequences for our understanding on massive binary evolution at low metallicity and their implications for young star populations as in high-redshift galaxies. A summary of the new discoveries made in this work is provided in Chapter 8.

1.1. Stellar atmospheres and winds

1.1.1. Atmopsheres of hot massive stars

Accurate stellar and wind parameters, crucially needed to understand stellar evolution, can solely be derived from detailed spectroscopic analysis. Due to the complexity of stellar atmopsheres, this can only be done by comparing state-of-the-art numerical stellar atmosphere models with multi-wavelength spectroscopic data. To be able to follow the analyses and discussions presented in this thesis, a brief overview of the structure and different line formation regions of a stellar atmosphere of a hot star is provided in the following. For a more in-depth exploration of the physics of stellar atmospheres, refer to the works of Castor et al. (1975); Mihalas (1978); Lamers & Cassinelli (1999) and Kudritzki & Puls (2000).

A stellar atmosphere can be divided into two regions: i) The quasi-hydrostatic domain (i.e. the photosphere), where gravity and the pressure are in balance, and ii) the wind regime where the pressure exceeds gravity. In the case of hot massive stars, the gas at the surface is highly ionized and consists of free electrons, (fully) ionized hydrogen and helium as well as multiply ionized species of heavier elements.

Photons originating from the interior of a star can be described in good approximation by the radiation field of a black body. When traveling through the quasi-hydrostatic layers, photons interact with electrons and ions. Electron interactions primarily involve scattering events such as elastic Thomson scattering, whereas interactions with ions are more complex. Photons with energies corresponding to transition levels can be used to excite an ion. However, this new state is typically short-lived, and a photon is quickly reemitted in a random direction, leading to a decrease in flux traveling towards the observer at wavelengths corresponding to line transitions. The spectrum originating from the photospheric layers is a continuum with distinct absorption features.

During atomic transitions, ions exchange energy and momentum with the radiation field. In regions with constant velocity, like the photosphere, the number of photons that can be utilized for line transitions and an effective exchange of energy and momentum is limited. However, in regions where the radiation pressure dominates over gravity, gas particles can be efficiently accelerated. The line transitions of accelerated ions will get Doppler-shifted, allowing the ion to absorb photons of different energies with respect to the rest-wavelength. Ions can efficiently gain more energy, accelerating the particles and powering radially outgoing winds. The effect of coupling energy and momentum of the radiation field to an atmosphere is often termed as line-driven or radiation-driven wind.

Whether or not a star can drive a wind, depends on its physical properties and conditions at the surface. To transfer a significant amount of energy from a radiation field to the wind, a certain fraction of the energetic (UV) photons needs to be absorbed and scattered in the stellar atmosphere. The transfer of energy happens mostly in optically thick line transitions of iron group elements, but also carbon, nitrogen, and oxygen play a role. This means, that the strength and the velocity field of the stellar wind depend i) on the luminosity and temperature

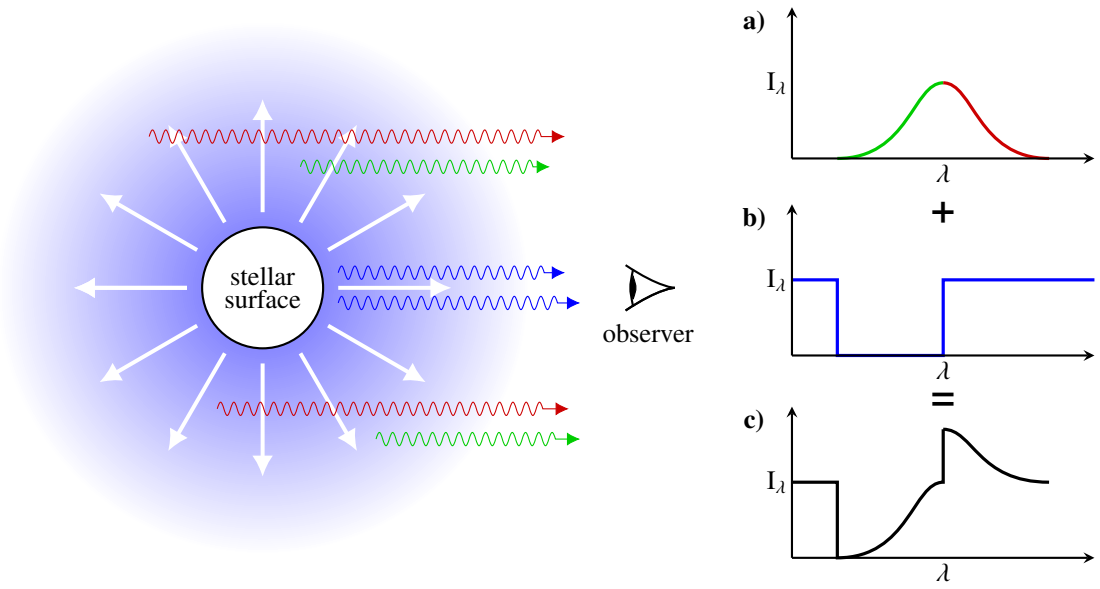

Fig. 1.1.1. Illustration on the physical mechanism creating P Cygni profiles for wind lines. The stellar wind is indicated as blue shaded area and is expanding in the direction of the arrows. The scattered photons from the "side" of the wind (red and green) form an emission profile (panel a). Photons in the line of sight are scatted away (blue) and will not be observable (panel b). The observer sees a combination of both effects which is called a P Cygni profile (panel c).

which quantify how many energetic photons can be used to power the wind, ii) the mass, which defines the gravitational force, working against the acceleration, and iii) the metal content that is responsible for the coupling of the radiation field to the wind itself. The luminosity-to-mass (L/M) ratio is a common parameter to quantify the strength of a stellar wind. As a rule of thumb, the higher the L/M ratio, the stronger the wind. However, the exact relationship between L/M and the strength of a stellar wind remains an area of ongoing research (Section 1.1.2).

When assuming that a stellar wind is spherically symmetric expanding, stationary, and homogeneous, the outflow of a star can be described by the continuity equation, yielding that the mass-loss rate is given by

$$\dot{M} = 4\pi r^2 v(r)\rho(r). \tag{1.1.1}$$

The mass-loss rate of a star depends on the density stratification $\rho(r)$ of the wind and the underlying velocity field $v(r)$. In the photospheric regime the density stratification and, hence, the velocity field are defined by the hydrostatic equation. In the wind domain of an expanding atmosphere the velocity field of the accelerating region can be described by a so-called β-law (Castor et al. 1975) of the form

$$v(r) = v_\infty \left(1 - \frac{R}{r}\right)^\beta, \tag{1.1.2}$$

where v_∞ is the terminal wind velocities of the wind, R is the radius of the star, and β is a free parameter. For OB-type stars, this parameter has a typical value of $\beta \approx 0.8$ (e.g. see Pauldrach et al. 1986; Puls et al. 2008).

Resonance lines that are formed inside the winds of OB-type stars have the characteristic shape P Cygni profiles. These profiles are characterized by prominent blue-shifted absorption features, resulting from the stellar core shielding to the observer, and red-shifted emission features, caused by the scattering of radiation from the expanding wind material. An illustration can be seen in Fig. 1.1.1. By modeling these lines, one can infer the terminal wind velocity from the blue edge of the absorption trough and the mass-loss rate from the strength of the non-saturated lines.

The densities inside a stellar wind can be so low that the statistical distribution functions of the radiation field and the gas are decoupled, meaning that the radiation field cannot be approximated any longer by a black body field. Hence, the conditions in a stellar wind depart from the local thermodynamic equilibrium (LTE) approximation. This means, that the radiative transfer problem and the rate equations have to be solved numerically. In this work, we employ the state-of-the-art Potsdam Wolf-Rayet (PoWR)[1] stellar atmosphere code (Gräfener et al. 2002; Hamann & Gräfener 2004), which has been applied to a large variety of hot stars and binaries (e.g., Hainich et al. 2014, 2015; Oskinova et al. 2011; Reindl et al. 2014; Shenar et al. 2015).

[1] More details on the PoWR code and the physical assumptions within are provided in the manuscripts presented in the later Chapters of this thesis.

1.1.2. Mass-loss rates

Despite the ability to model stellar winds consistent with observations and to obtain the stellar and wind parameters, a comprehensive theoretical framework encompassing the diverse wind-driving mechanisms across different stellar types, such as O-stars or WR stars, remains elusive. In recent decades, extensive spectroscopic surveys of massive OB-type stars and WR stars across various metallicities have provided valuable insights into their stellar and wind properties and serve as valuable anchor points for mass-loss prescriptions. Numerous attempts have been made to utilize this observational data and develop new empirical mass-loss recipes (e.g., Hamann et al. 2006; Mokiem et al. 2007b; Crowther 2007; Hainich et al. 2014; Tramper et al. 2016; Yoon 2017; Shenar et al. 2019, 2020c; Ramachandran et al. 2018b, 2019; Rickard et al. 2022), yet there is no uniform empirical relation describing the winds of hot stars. And even worse, for stars that are postulated by stellar evolution models but not observed yet, no empirical mass-loss relation exists.

The applicability of existing empirical mass-loss recipes in stellar evolution calculation is limited due to their focus on specific groups of stars. Interpolations are often necessary when transitioning between different regimes covered by the recipes, leading to uncertainties and potential inconsistencies in modeled mass-loss rates. Typically, linear interpolations between different regimes are employed in stellar evolution models to avoid abrupt changes in mass-loss rates. More physically motivated approaches, such as using the optical depth at a certain point to determine when to transition between different wind recipes, have also been proposed but are less frequently employed (e.g., Gräfener 2021).

Theoretical models offer the advantage of covering large parameter spaces and eliminating the need for crude interpolations. However, the modeling of stellar winds is complex, and the physical processes behind the launching of the wind are not yet well understood. Consequently, proposed mass-loss rates are highly dependent on the assumed physics defining the wind-driving mechanism as a function of stellar parameters. For example, Vink et al. (2001) proposed a significant increase in the mass-loss rate for massive stars around $T \approx 25\,\mathrm{kK}$, corresponding to the transition where Fe IV recombines to Fe III, which is suggested to be a more efficient wind driver. However, recent hydrodynamic stellar atmosphere models by Björklund et al. (2023) do not predict such a jump at all challenging this idea. Unfortunately, it is not clear from observations if such a jump exists or not. Similar uncertainties arise when transitioning from hot OB-stars to the WR regime, namely when transitioning from normal optically thin to strong optically thick winds.

There are copious attempts to create theoretical predictions for the winds of massive stars at different evolutionary stages (e.g., Castor et al. 1975; Vink et al. 2000, 2001; Vink 2017; Krtička & Kubát 2018; Sander & Vink 2020; Bestenlehner 2020; Björklund et al. 2022). Yet, there is no uniform formalism describing radiation-driven winds for all hot massive stars. While the clear strength of these theoretical models lies in their ability to cover larger parameter spaces and to predict stellar winds for types of stars with limited observational data, such as intermediate-mass helium stars, discrepancies emerge when comparing them across entire stellar populations at various metallicities. These differences can become significant, even spanning orders of magnitude, thereby restricting their applicability to stellar evolution models.

One obstacle hindering a more comprehensive understanding of hot star winds is the lack of observations of stars near or during the crucial transition phase from OB-star winds to the powerful WR winds. Mass donors in binary systems offer a unique opportunity to address this gap. These stars can lose several solar masses during a mass-transfer event and, upon detachment, they are more luminous than before. This leads to a significant increase in their L/M ratio, which suggests a potential boost in their wind strength. While the exact increase in mass-loss rates remains unquantified, these mass-donor stars hold immense potential as the missing puzzle piece for a more comprehensive understanding of how winds evolve in hot stars.

1.2. Orbital analysis of binary systems

For a comprehensive analysis of a binary system, just having information on the stellar and wind parameters is insufficient. To gain a complete understanding of the binary's evolutionary stage, it is essential to know its current orbital configuration. The orbit of a binary system can be completely characterized by the set of following parameters: its orbital separation a (or period P_{orb}), eccentricity e, the argument of the periastron ω, inclination i, time of the periastron passage t_0, and the mass ratio of the stars q.

1.2.1. Radial velocity movements

Within a binary system, as one star moves toward the observer the other one moves away, this results in a blue and redshift of the stellar spectra, respectively. According to the low-velocity approximation ($v \ll c$) of the Doppler

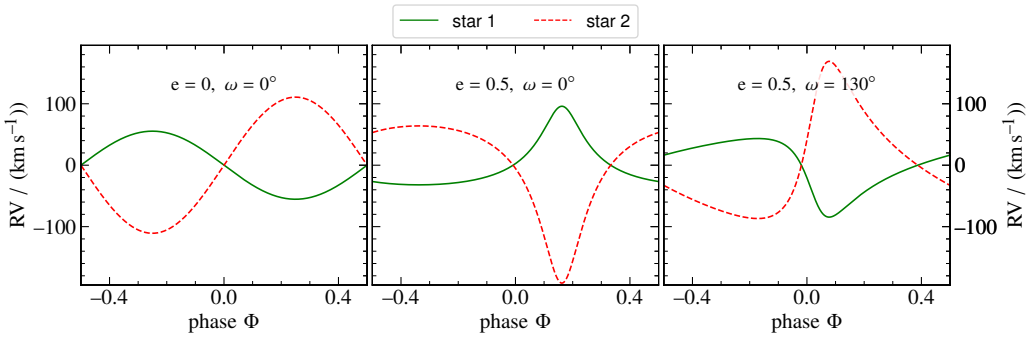

Fig. 1.2.1. Synthetic radial velocity curves, calculated using the PHOEBE code, illustrate how different orbital parameters influence their radial velocity curve. All binary systems shown have a mass ratio of $q = 0.5$, an orbital separation of $a = 100\,\mathrm{d}$ and an inclination of $i = 70°$. *Left:* The binary is assumed to have a circular orbit ($e = 0$). *Middle:* A binary with an eccentric orbit ($e = 0.5$), where the periastron is in the line of sight ($\omega = 0°$). *Right:* A binary with an eccentric orbit ($e = 0.5$), but now with the periastron being shifted out of the line of sight ($\omega = 130°$).

effect, the shift in wavelength $\Delta\lambda$ is directly related to the velocity with which an object moves radially toward or away from the observer v_r as

$$\Delta\lambda = \lambda_0 \frac{v_r}{c}, \tag{1.2.1}$$

with λ_0 being the reference wavelength of a considered line and c being the speed of light. The specific shape of the radial velocity curve is determined by the system's orbital parameters. Examples illustrating how the radial velocity curve changes for different orbital parameters are shown in Figure 1.2.1. By analyzing multi-epochs of spectra, the velocities of the binary components can be measured over time, yielding important information on the radial velocity curve and, hence, the binary's orbital configuration. The peak radial velocities $K_{1,2} = v_{r\,1,2} \sin i$ of both stars depend on the system's inclination angle i and provide valuable information about the total mass of the binary

$$M_{\mathrm{tot}} \sin^3 i = \frac{((K_1 + K_2)\sqrt{1-e^2})^3}{G} \frac{P_{\mathrm{orb}}}{2\pi}, \tag{1.2.2}$$

as well as about the masses of both stars

$$M_{2,1}^3 \sin^3 i = \frac{(K_{1,2}\sqrt{1-e^2})^3}{G} \frac{P_{\mathrm{orb}}}{2\pi} M_{\mathrm{tot}}^2. \tag{1.2.3}$$

1.2.2. Eclipsing binaries

In a binary system where the orbital plane aligns with the observer's line of sight ($i \approx 90°$), it is possible that both stars pass in front of one another, resulting in an eclipse. When obtaining a time series of such a binary system, one can observe that during these passages the total luminosity of the system drops. These eclipses provide valuable information about the orbital period as well as the eccentricity and the inclination of the system. An illustrative example of an synthetic eclipsing binary on a circular orbit is presented on the left side of Figure 1.2.2.

However, if the inclination is too low and the stars no longer obscure each other, there will not be any eclipses. Nevertheless, in cases where one of the stars is distorted, perhaps due to rapid rotation or being close to filling its Roche lobe, its luminosity varies depending on its orientation relative to the observer. As an example lets consider a Roche lobe filling star that has teardrop shape. When observed from the side, this star appears larger and consequently brighter than when observed from its "back" or "front" when its projection is closer to a sphere. As in a binary, its orientation changes over time, this results in a sinusoidal variation in the light curve. An example of such a scenario is depicted on the right side of Figure 1.2.2.

A consistent fit of the light and radial velocity curves yields important constraints on the orbital configuration of the binary system and provides an accurate, independent measurement of the stars' masses. These results of the orbital analysis are fundamental for understanding the evolutionary history of a binary system. Within the work presented in this thesis, the spectral analysis is supplemented by a fit of the radial velocity curve, and when available, also a consistent fit to the light curve. Their fits are done with the Physics of Eclipsing Binaries

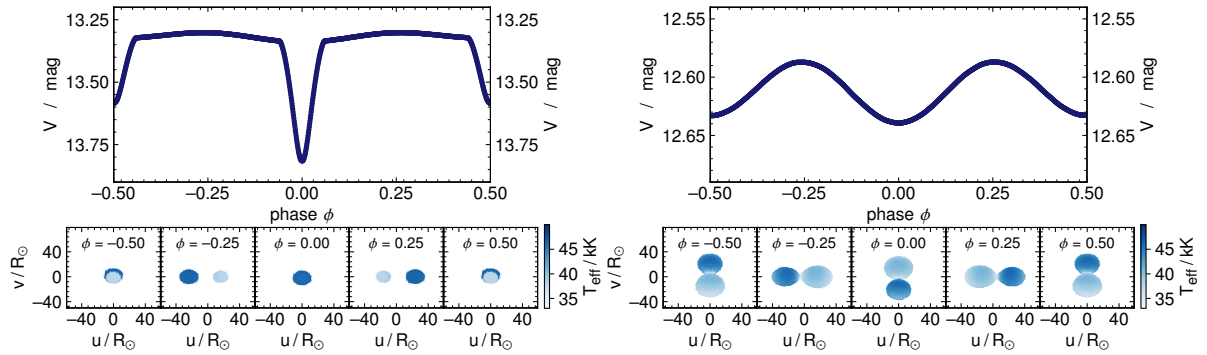

Fig. 1.2.2. Synthetic lightcurves of an ecclipsing binary (left) and a binary showing ellipsoidal variability calculated with the PHOEBE code. In the upper panels the lightcurve as a function of one orbital phase is shown. In the lower plots, the orbital configuration in the plane of sky coordinates (u and v) at several phases is illustrated. *Left:* Shown is a circular binary system ($e = 0$) with a short period of 3 d. The binary has an inclination of $i = 85°$. The first star (blue) has a temperature of $T_1 = 44$ kK and a radius of $R_1 = 9\,R_\odot$. The second star (light blue) has a lower temperature of $T_1 = 30$ kK and a radius of $R_2 = 6\,R_\odot$. *Right:* The orbital parameters are the same as in the left figure, but inclination angle $i = 30°$ is too low and, hence, the stars do not ecclipse. The stars in this example are however deformed and fill their Roche lobes. The first star (blue) has a temperature of $T_1 = 44$ kK and a radius of $R_1 = 13.8\,R_\odot$ and the second star (light blue) has $T_1 = 39$ kK and a radius of $R_2 = 16.5\,R_\odot$.

(PHOEBE; Prša & Zwitter 2005; Prša et al. 2016; Horvat et al. 2018; Jones et al. 2020; Conroy et al. 2020)[2] code, specifically designed for a consistent modeling and fitting of these data.

1.3. Stellar evolution

The spectroscopic analysis yields important insights into the physical parameters of stars of all kinds. These results are employed to calibrate stellar evolution models and advance our theoretical understanding of the physical processes in stars. In the following, an overview of the most important physical parameters and concepts that are needed to follow the discussions within this thesis is presented. For more in-depth explanations on stellar physics, please refer to Pols (2009) and Maeder (2009).

1.3.1. Timescales and observability of different evolutionary stages

By definition, a star is a gaseous body bound by its own gravity, radiating energy produced internally. Depending on the presence of an internal energy source, a star can be in different equilibrium states. These have different durations and determine the likelihood of observing a star at a certain evolutionary phase.

In the absence of an internal energy source, a star is balanced only by gravity and gas pressure. When both forces are in balance throughout the star, it will neither expand nor contract and is in hydrostatic equilibrium. The time required for a star to return to hydrostatic equilibrium following a perturbation is given by the dynamical timescale

$$t_{\rm dyn} = \sqrt{\frac{R^3}{GM}}, \tag{1.3.1}$$

where G is the gravitational constant, R is the radius of a star, and M its mass. Typically, hydrostatic equilibrium in a star is regained on the order of minutes to hours. Changes on the dynamical timescale are highly unlikely to be observed. One of the few observable examples, when a star cannot retain its hydrostatic equilibrium is at the end of its life when it is no longer powered by internal sources, leading to a rapid explosion or collapse.

When a star generates as much energy ($E_{\rm int}$) as it radiates away (L), it achieves a stable condition where its total energy is conserved, the thermal equilibrium. In this state, a star neither contracts nor expands as long as it is not perturbed. The duration of this stable phase is set by the nuclear timescale, defined as

$$t_{\rm nuc} = \frac{E_{\rm nuc}}{L} = Q\,f_{\rm nuc}\,\frac{Mc^2}{L}, \tag{1.3.2}$$

with Q being the rest mass energy, $f_{\rm nuc}$is the fraction of the star's total mass available for fusion, and c is the speed of light. The specific duration a star spends burning a particular element depends on the dominant nuclear fuel and

[2] More details on the PHOEBE software and the physical assumptions within are provided in the manuscripts presented in the later Chapters of this thesis.

the ongoing reaction process. The nuclear timescale of a massive star is typically on the order of a few million years and covers 99% of a star's lifetime. Consequently, most stars are observed while they are actively fusing elements in their cores.

In the case when a star's nuclear energy source is depleted or its structure changes (e.g., removal of mass), it deviates from thermal equilibrium. In response, the star seeks to restore hydrostatic equilibrium by either contracting or expanding. The timescale for this transition, known as the thermal timescale, is determined by the virial theorem ($E_{\rm int} = -0.5\,E_{\rm grav}$) and defined as

$$t_{\rm therm} = \frac{E_{\rm int}}{L} = \frac{GM^2}{2RL}. \tag{1.3.3}$$

This timescale in the case of massive stars is on the order of several tens of thousands years, making it much longer than the dynamical timescale but much shorter than the nuclear timescale $t_{\rm nuc} \gg t_{\rm therm} \gg t_{\rm dyn}$. Consequently, the likelihood of detecting stars during rapid transition phases when they deviate from thermal equilibrium is small, but not impossible.

1.3.2. Hydrogen burning

During core hydrogen burning, four protons (^{1}H) are needed to create a new helium nucleus (^{4}He). In stars there are two major pathways to produce ^{4}He, the so-called p-p chains and the CNO cycle. In the p-p chains, hydrogen nuclei are combined to create heavier elements such as deuterium (^{2}H) or ^{3}He. These heavier elements can then undergo further reactions to create ^{4}He. The CNO cycle uses carbon (C), nitrogen (N), and oxygen (O) as catalysts to convert hydrogen into helium. This cycle becomes the dominant fusion process at core temperatures higher than $T_{\rm core} \gtrsim 1.5{\cdot}10^7$ K as found in the cores of massive stars (Weizsäcker 1937, 1938; Bethe 1939). Therefore, particulat focus is put on the CNO cycle in this section.

The CNO cycle can be split into two major steps: the CN cycle and the CNO bi-cycle. Within the CN cycle, several isotopes of carbon, nitrogen, and oxygen are created. These isotopes have half-lives significantly shorter than a star's lifespan. Consequently, the abundances of C, N, and O in hydrogen-burning regions will change according to the ratio of their decay rates. This means, that the isotope of an element with the longest lifetime will have the highest abundance, while isotopes of elements with shorter lifetimes will have lower abundances. As a result, regions in which the CN equilibrium is reached will exhibit a net increase in nitrogen and a decrease in carbon, while the total number of C, N, and O nuclei remains conserved.

During the last step of the CN cycle, the unstable nucleus ^{16}O* is created. While in 99.9% of the cases from this nucleus ^{12}C and ^{4}He are produced, in the remaining 0.1% a stable state of ^{16}O can be achieved, which is the starting point of the CNO bi-cycle. While the creation of a stable ^{16}O is rare and not of significance for the energy generation of a star, it has a severe impact on the CNO abundances as additional decay channels have to be considered. Regions inside the star, that have reached the CNO equilibrium, such as the stellar core after hydrogen burning is completed, will exhibit strongly increased nitrogen abundances, while carbon and oxygen are depleted. Inside a star, where hydrogen is converted to helium via the CNO cycle first CN equilibrium and then the CNO equilibrium will be established. Efficient mixing within a star can distribute elements produced in the core to the outer layers. Stellar winds or interactions in binary systems can remove the outermost layers, exposing a star's interior and prior hydrogen-burning regions. Measuring a star's CNO abundance from detailed spectroscopic analysis with stellar atmosphere models provides valuable insights into a (binary) star's previous history and current evolutionary status.

1.3.3. Single star evolution

To understand the evolution of stars, astronomers plot their luminosities against their effective temperatures in a so-called Hertzsprung-Russell diagram (HRD). A star's luminosity (L), effective temperature (T), and radius (R) are linked via the Stefan-Boltzmann law

$$L = 4\pi\sigma R^2 T^4, \tag{1.3.4}$$

where σ is the Stefan-Boltzmann constant. Consequently, compact stars and remnants will be located in the lower left part of the HRD, while extended objects are positioned in the upper right.

In the following, an overview over the standard picture of massive star evolution is be provided. For clarity, we will only discuss evolutionary channels of stars with initial masses $M_{\rm ini} = 15\,M_\odot$, $30\,M_\odot$, and $60\,M_\odot$. Note, that if one changes the input physics, such as the mass-loss rates or the mixing efficiencies the discussed boundaries and evolutionary stages for a given mass can change.

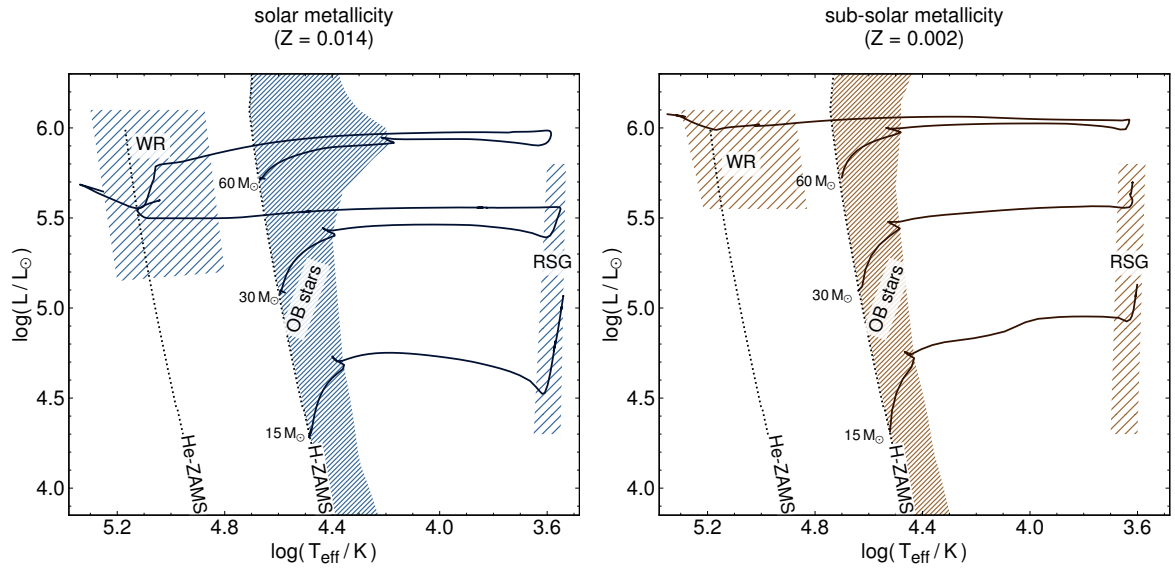

Fig. 1.3.1. Hertzsprung Russell diagrams showing stellar evolutionary tracks for single stars with initial masses of 15 $M_\odot$, 30 $M_\odot$, and 60 $M_\odot$ at solar (left) and SMC (right) metallicity. The tracks are adopted from the BPASS project (Eldridge et al. 2017; Stanway & Eldridge 2018). The hatched regions mark long-lived stellar evolutionary phases associated with core hydrogen burning (OB stars) and core helium burning (RSG or WR) stars. One can see that with metallicity also the regions in the HRD populated by massive stars change.

On the left side of Fig. 1.3.1, an HRD illustrating the stellar evolutionary tracks of massive stars at solar metallicity is shown. Upon formation, when hydrogen fusion in the core initiates, the star is situated at the (hydrogen) zero-age main sequence (H-ZAMS) and has a fixed luminosity depending on its mass. After that, the evolution of massive stars is everything else than straightforward. Massive stars spend approximately 90% of their lives on the main sequence (shaded region next to the H-ZAMS), during which they already lose mass via their stellar winds. The mass-loss rates increase with increasing mass (luminosity), shedding off the outer hydrogen-rich layers and impacting the evolution.

For a single star with an initial mass of 15 $M_\odot$ mass-loss during the main sequence is not relevant, as it removes only negligible fractions of the outer envelope. Once all hydrogen in the core is fused to helium, the star will be without an internal energy source and drops out of thermal equilibrium. Consequently, the star will contract and heat up. When the regions close to the former core are sufficiently hot enough hydrogen burning in shells can be ignited, feeding more helium to the core. During the phase of hydrogen shell burning, the core is still contracting and heating up. To regain thermal equilibrium the star expands so that the energy produced via hydrogen shell burning can be radiated away. This leads to an efficient cooling of the stellar surface and thus to a rightward evolution in the HRD, moving the star quickly to the area populated by red supergiant stars (RSG). As soon as the core reaches a temperature of $T_{\rm core} > 10^8$ K the helium core can be ignited. The star is now an RSG and in a stable configuration, where it will spend the remaining $\approx$ 10% of its life. After core helium burning more advanced burning stages, such as carbon burning will take over until the formation of an iron core. When the iron core becomes unstable, it will collapse, leading to a supernova explosion, leaving behind a neutron star.

In the case of a 30 $M_\odot$ star, more mass will be lost during the main sequence evolution, but still not enough to remove the entire hydrogen-rich envelope. Similarly to the 15 $M_\odot$ star, this star will expand and evolve into an RSG. During this phase, it will once again experience substantial mass loss that removes the remaining hydrogen-rich layers and exposes the hot helium core. Consequently, as the last layers of the hydrogen envelope are removed, the star will wander towards the helium zero-age main sequence (He-ZAMS), where it will be observed as a massive helium star. These helium stars have surface abundances consistent with the CNO equilibrium abundances. In our galaxy most massive helium stars can power strong optically thick winds, leading to strong emission line spectra, which are associated with WR stars. Whether a helium star can develop an strong optically thick wind depends on its mass-to-luminosity ratio as well as the metal content.

More massive stars such as the 60 $M_\odot$ star shown on the left side of Fig. 1.3.1 can power winds so strong that they efficiently remove the hydrogen-rich envelope during the main sequence or the short expansion phase afterward. These stars skip the RSG phase and evolve directly into WR stars.

On the right side of Fig. 1.3.1, an HRD containing stellar evolution tracks of stars at a metallicity similar to the one of the SMC are depicted. By comparison to the Galactic models, one can see that metallicity impacts the

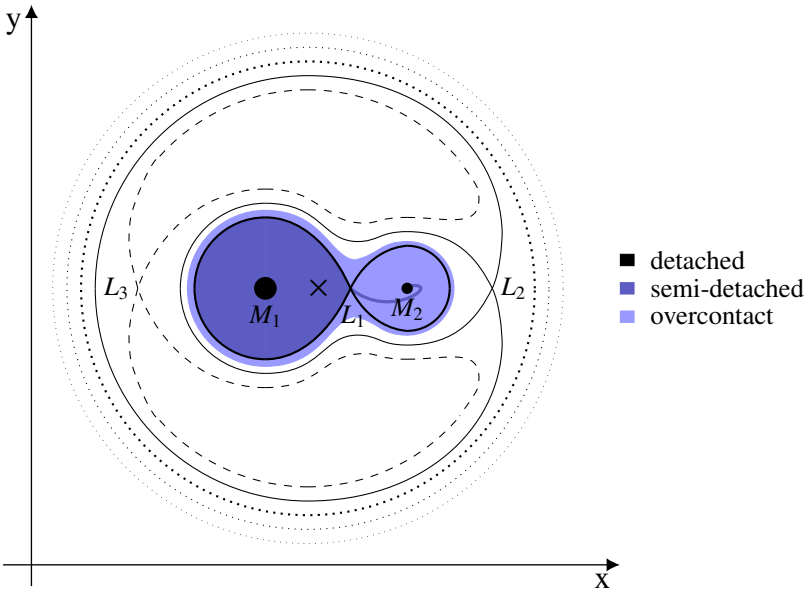

Fig. 1.4.1. Sketch of the cross-section of the equipotential surfaces in a binary system along the equatorial plane. The innermost (thick) curve that crosses through the L_1 point is the Roche lobe. The position of the detached stars is indicated by the black dots. In the case of a semi-detached binary, one star fills its Roche lobe and initiates mass transfer, as illustrated by the dark blue contour. When both stars overfill their Roche lobes, the system is in an overcontact phase, as shown by the light blue shaded areas. The labels M_1 and M_2 mark the center of mass of each binary component while their common center of mass is indicated by an $\times$. The Lagrangian points of higher-level equipotential surfaces are labeled as L_2 and L_3.

evolution of a star in multiple ways. First, a decrease in metallicity means lower abundances of C, N, and O. For a low-metallicity star powered by the CNO cycle this means that higher core temperatures are required to create the same energy as a star at higher metallicity. Consequently, the H-ZAMS is shifted to higher temperatures (leftwards in the HRD) for decreasing metallicity. Additionally, the strength of line-driven winds diminishes with decreasing metallicity (see Section 1.1). This means, that for stars formed in lower metallicity environments, only the initially most massive ones can expel the hydrogen-rich envelope to form WR stars. Before the discovery that the majority of massive stars were formed in binaries, this challenged our understanding of the formation of low metallicity WR stars.

1.4. Binary physics

Close binary systems, where two stars are sufficiently close to interact, have profound consequences for their stars' evolutionary pathways. In the following a short overview of the fundamental principles of binary interactions and their consequences on stellar evolution is provided. For a more detailed description please refer to Tauris & van den Heuvel (2006, 2023) and Marchant & Bodensteiner (2023).

1.4.1. Roche lobe overflow

The proximity of stars in binary systems affects their effective gravitational potential, which encompasses the individual gravitational potentials of both stars as well as the centrifugal potential introduced by their orbital motion (Kopal 1955). The effective potential can be expressed as

$$\Phi = -\frac{GM_1}{r_1} - \frac{GM_2}{r_2} - \frac{\omega r_3^2}{2}, \tag{1.4.1}$$

where M_1 and M_2 are the masses of both stars, r_1 and r_2 their distances to the center of mass, ω is the orbital angular velocity, and r_3 is the distance to the rotation axis of the system.

Under the assumption of a circular orbit, the effective gravitational potential of a binary system can be used to identify equipotential surfaces in a co-moving frame, as depicted in Fig. 1.4.1. The innermost potential corresponds to the Roche lobe and is characterized as a teardrop-shaped region around each star. When both stars are well within their Roche lobes they can evolve independently and the system is in a detached state. As a star evolves and

expands in size, it will start to fill its Roche lobe and gets deformed. All material that would expand beyond the Roche lobe will experience a stronger gravitational pull from the companion star and will initiate mass transfer from the overflowing star across the first Lagrangian point (L_1) towards its companion, also termed "Roche lobe overflow" (RLOF). During the phase of stable mass transfer via RLOF, the system is called semi-detached. In very close binary systems, the transfer of mass is very efficient and the accreting companion star quickly grows in mass and size. When both stars (over)fill their Roche lobes and come into direct contact, the system is classified as an (over)contact binary.

Stellar evolution models are one-dimensional and assume spherical symmetry. However, stars filling their Roche lobes deviate from a perfect sphere. To account for mass transfer via RLOF in binary evolution models, an approximation for the radius ($R_{\rm RL}$) of a star when filling its Roche lobe is required. Under the assumption that the volume of the Roche lobe should be conserved when considering spherical models Eggleton (1983) was able to express this radius as

$$R_{\rm RL} = \frac{0.49q^{2/3}}{0.6q^{2/3} + \log(1 + q^{1/3})} \cdot a, \tag{1.4.2}$$

where q is the mass ratio of the stars and a their orbital separation. This means, that the onset of mass-transfer is primarily set by the orbital separation (or orbital period) and that the mass ratio only has a secondary impact.

As discussed in Section 1.3.3, massive stars expand during their evolution. Depending on the initial orbital period stars will fill their Roche lobes during different evolutionary phases, providing three distinct scenarios (Kippenhahn & Weigert 1967):

- **Case A:** In systems with short orbital periods that are typically on the order of days, massive stars may fill their Roche lobes while still being core hydrogen burning. As a reaction to the removal of mass, the donor star will drop out of thermal equilibrium. Initially, copious amounts of mass will be removed on the thermal timescale (fast Case A), until the star can regain the equilibrium state. Then the star will only expand and transfer mass slowly on the nuclear timescale as it continues core hydrogen burning (slow Case A).

- **Case B:** In wider binary systems, with periods typically ranging from tens of days to years, massive stars will fill their Roche lobes when they are in the quick expansion phase from the main sequence to the RSG stage. As these stars are not in thermal equilibrium when mass transfer is initiated, they will undergo a rapid removal of the envelope until the helium core becomes exposed and the expansion of the star stops. Note, that donor stars of Case A systems also expand after depleting hydrogen leading to a similar mass-transfer phase, the so-called Case AB.

- **Case C:** Systems with the widest orbits (typically a few years) might allow the donor star to expand to the RSG phase and RLOF will only be initiated during burning stages later than helium shell burning which leads to an additional expansion and, hence, a filling of the Roche lobe.

Mass transfer can occur on different timescales, impacting how frequently one can observe stars in this phase. Stars transferring mass on the nuclear timescale, such as during the slow Case A phase, spend a significant portion of their entire lifespan in this state, making them the most commonly observed mass-transferring binary types. In contrast, the thermal timescale is much shorter than the nuclear timescale (see Section 1.3.1), which makes it highly unlikely to directly observe binary systems during the fast Case A, Case B, and Case C mass-transfer phase. It's important to note that this discussion applies to the standard picture of stellar evolution. Recent theoretical predictions from (Klencki et al. 2022) suggest, that if one uses more efficient mixing during the later evolutionary phases that shorten the Hertzsprung gap (the region in the HRD where stars transition from core hydrogen burning to core helium burning), it might be possible that there are systems that undergo also slow Case B mass-transfer. This makes it particularly interesting to search for post-interaction binaries with wide periods, to see if they quickly evolve towards the He-ZAMS or stay among OB-star populations. A topic that will be addressed within this thesis.

The transfer of mass via RLOF is not always stable. If too much mass is transferred within a short time or the infalling material can neither be accreted nor ejected from the system, the material will quickly lead to an overfilling of the Roche lobe and might be lost via the L_2 or even the L_3 point leading to the formation of a common envelope in which both stars spiral in. If the released orbital energy from the inspiral is not enough to eject the common envelope both stars will merge.

1.4.2. Tidal interactions

Binary interactions encompass more than just the exchange of mass. In close binary systems, where the stars are so close, that they can feel each other's gravitational pull, tides will be created (Zahn 1975, 1977; Hut 1981; Hurley

et al. 2002). Over time, these tides will synchronize the rotation of the stars with the orbit. The synchronization timescale can be expressed as

$$\tau_{\text{tides}} = \frac{q^2}{3} \frac{I}{MR^2} \frac{T}{k} \frac{a^6}{R^6}, \tag{1.4.3}$$

with q being the mass ratio of the two stars, $I/(MR^2)$ the inverse gyrotation radius, and T/k the inverse viscous dissipation time. From this equation, it is evident that the orbital separation a and the radius of a star R dominate the time it takes for a star to synchronize its rotation with the orbit. However, also the stars mass ratio plays an important role. Consequently, tidal synchronization during stellar evolution is only relevant for the closest binary systems, typically those with periods below $P \lesssim 10\,\text{d}$.

1.4.3. Efficiency of mass transfer

Due to the rapid nature of mass transfer events, gaining insights into the physical mechanisms of RLOF is a challenge. Only systems undergoing slow Case A mass transfer are observable for extended periods and provide a small sample. Consequently, quantitatively measuring the amount of mass exchanged between stars or the total mass loss from the system is difficult. Our current understanding of mass transfer efficiencies is primarily derived from the work of de Mink et al. (2007). They compared stellar evolution models incorporating different mass transfer efficiencies with observations of semi-detached binary systems in the SMC and concluded that mass transfer efficiency decreases with increasing orbital period.

During mass transfer, material does not flow directly from one star to another. Instead, an accretion disk forms around the companion star, leading to the transfer of both mass and angular momentum. Packet (1981) demonstrated that stars need to accrete only a small fraction of their initial mass to achieve critical rotation, where centrifugal force balances gravitational force. Once a mass-accreting star reaches critical rotation, it can no longer accrete mass efficiently. Efficient mass transfer in close binary systems requires effective braking mechanisms, such as spin-down due to tidal forces (e.g., Petrovic et al. 2005). As a rule of thumb, one can say that with an increasing orbial period, the efficiency of mass-transfer decreases.

1.4.4. Binary evolution

At the beginning, stars formed in binary systems evolve more or less similar to stars formed in isolation. Only after an interaction with the companion star, the evolution of the stars will be significantly influenced. During a mass-transfer phase, the donor star loses large fractions of its hydrogen-rich envelope, exposing the hot helium core. Subsequently, after a mass-transfer event, the donor star contracts and evolves towards the He-ZAMS, as depicted in Fig. 1.4.2. The impact of mass transfer on the companion star depends on its ability to efficiently accrete material. In binaries with short orbital periods undergoing Case A mass transfer (left side of Fig. 1.4.2), the accretor is spun-down due to the tidal interactions, can accrete quasi conservatively and gets rejuvinated, which influences its future evolution (left side of Fig. 1.4.2). Conversely, in binaries with wider orbits (right side of Fig. 1.4.2), the accretor may not efficiently spin down, hindering effective material accretion and leading to the formation of a star rotating (right side of Fig. 1.4.2) so fast that the centrifugal force equals the gravitational force. Such stars are expected to form an decretion disc and are classified as Oe/Be stars.

One can separate post-interaction binaries containing two stars into three major groups: i) Those systems that have recently undergone interaction, with donor stars transitioning towards the He-ZAMS. According to the standard stellar evolution model, these donor stars have decreased surface hydrogen abundances and are expected to display surface C, N, and O abundances indicative of CN or even CNO equilibrium. Depending on the previous mass transfer scenario (Case A or Case B), these companions may appear as massive OB stars with modest rotations or rapidly rotating stars with rotation rates exceeding 350 km/s. ii) Those systems where the donor star has evolved into a helium star that is massive and luminous enough to develop an optically thick wind. Such systems typically consist of a Wolf-Rayet (WR) star, which exhibits strong emission lines in the optical spectrum, and an OB(e) companion which might not be visible in the spectrum. iii) Those systems where the donor star is an intermediate-mass helium star incapable of developing an strong optically thick wind. In these systems typically the Oe/Be companion dominates the optical spectrum as the helium star is bright in the UV, meaning that the helium star can be outshined in the optical and might only be detecable in high quality spectra or in the UV part of the spectrum.

Yet, observations of post-interaction binary systems in the contraction phase towards the He-ZAMS especially at low metallicity are scarce. This crucial phase plays a fundamental role in determining the future evolution and final fate of massive stars. Therefore, identifying and characterizing post-interaction binary systems offers a valuable opportunity to obtain constraints on the removal of mass from the donor during RLOF and its consequences

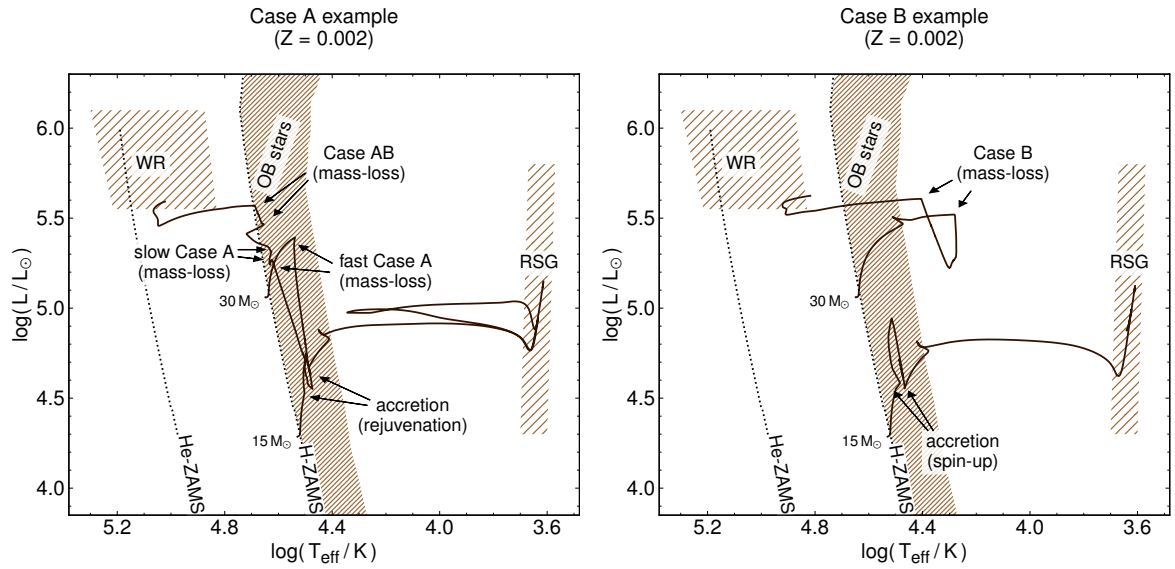

Fig. 1.4.2. Hertzsprung Russell diagrams showing binary evolutionary tracks for primary and secondary stars with initial masses of $M_1 = 30\,M_\odot$ and $M_2 = 15\,M_\odot$ at SMC metallicity. The tracks are calculated with MESA and similar input physics as described in Appendix 4.6.1. Within the models, it is assumed, that as the primary explodes as a supernova, the system gets disrupted. The hatched regions mark long-lived stellar evolutionary phases associated with core hydrogen burning (OB stars) and core helium burning (RSG or WR) stars. *Left:* Example of a binary with initial period $P_{\rm ini} = 4\,$d is shown. The system goes through Case A and Case AB mass-transfer, efficiently removing the donor star's hydrogen-rich envelope and positioning it in the region populated by the WR stars. The secondary accretes several solar masses and gets rejuvenated. *Right:* Example of a Case B binary with an initial period of $P_{\rm ini} = 40\,$d is shown. The primary sill loses a large fraction of its hydrogen-rich envelope and wanders towards the WR stars, while the secondary quickly spins up, preventing an efficient accretion.

for the subsequent evolutionary pathways of partially stripped stars. Only by doing this, one can fully understand the underlying stellar population of distant galaxies and their integrated spectra. In this thesis the Modules for Experiments in Stellar Astrophysics (MESA; Paxton et al. 2011, 2013, 2015, 2018, 2019)[3] code is employed to put our new discoveries of post-interaction binaries into an evolutionary context and to discuss how and if they fit into the standard picture of stellar evolution.

[3] More details on the MESA code and the physical assumptions within are provided in the manuscripts presented in the later Chapters of this thesis.

1.5. Overview of the manuscripts

In the following five scientific papers dedicated to comprehending the interactions among binary stars at low metallicity are presented. These papers have either been published or submitted for publication in peer-reviewed journals. Here, a brief overview of the scientific content and my contributions to the works are provided. The subsequent chapters include reprints of the manuscripts.

1.5.1. Manuscript I

Status: Published in *Astronomy & Astrophysics*, 2022, Volume: 659, ID: A9, 23 pp., DOI: 10.1051/0004-6361/202141738

Title: The earliest O-type eclipsing binary in the Small Magellanic Cloud, AzV 476: A comprehensive analysis reveals surprisingly low stellar masses

Authors: D. Pauli, L. M. Oskinova, W.-R. Hamann, V. Ramachandran, H. Todt, A. A. C. Sander, T. Shenar, M. Rickard, J. Maíz Apellániz, R. Prinja

Objective: This study aimed at fully characterizing and understanding the nature of the eclipsing binary system, AzV 476, in the SMC. To achieve this a consistent analysis of the light- and radial velocity curves is performed to determine the orbital parameters. This is complemented by a multi-epoch spectral analysis in the UV and optical yielding stellar and wind parameters. These results are compared with binary evolution tracks to understand the system's history and current state. Using such an approach provides new insights into binary evolution and the spectral appearance of massive stars in binaries at low metallicity.

Contribution: As the lead author, I conducted all of the presented research, including the extraction of the radial velocities from the multi-epoch spectra, the analysis of the light and radial velocity curves, the spectral analysis of the multi-wavelength spectra, as well as the calculation of the binary evolution models. Additionally, I wrote the entire manuscript.

1.5.2. Manuscript II

Status: Published in *Astronomy & Astrophysics*, 2023, Volume: 674, ID: A56, 19 pp., DOI: 10.1051/0004-6361/202346055

Title: A low-metallicity massive contact binary undergoing slow Case A mass transfer: A detailed spectroscopic and orbital analysis of SSN 7 in NGC 346 in the SMC

Authors: M. J. Rickard & D. Pauli

Objective: This work aimed to bridge the observational gap of interacting short-period massive binary systems, which are thought to be the progenitors of gravitational waves. To achieve this a comprehensive spectroscopic and orbital analysis of NGC 346 SSN 7, a promising candidate of an interacting binary in a low-metallicity environment is performed. This in-depth analysis of its orbital, stellar, and wind parameters provides valuable data to refine our theoretical understanding of binary physics, especially mass-transfer, and the formation of gravitational wave sources.

Contribution: Both authors have contributed equally to the paper. I was responsible for an equal share of the overall research and manuscript preparation. I performed the orbital analysis, the stellar evolution modeling, and interpreting the results of both. Additionally, I assisted with the spectroscopic analysis and made significant contributions to writing the manuscript, in particular I wrote the sections on orbital analysis and stellar evolution, as well as a significant part of the discussion.

1.5.3. Manuscript III

Status: Published in *Astronomy & Astrophysics*, 2023, Volume: 673, ID: A40, 19 pp., DOI: 10.1051/0004-6361/202345881

Title: Spectroscopic and evolutionary analyses of the binary system AzV 14 outline paths toward the WR stage at low metallicity

Authors: D. Pauli, L. M. Oskinova, W.-R. Hamann, D. M. Bowman, H. Todt, T. Shenar, A. A. C. Sander, C. Erba, V. M. A. Gómez-González, C. Kehrig, J. Klencki, R. Kuiper, A. Mehner, S. E. de Mink, M. S. Oey, V. Ramachandran, A. Schootemeijer, S. Reyero Serantes, A. Wofford

Objective: This paper aimed to address the poorly understood origin of WR stars in low-metallicity environments like the SMC. The central object of the analysis is the massive binary system AzV 14. By performing a consistent light-curve and spectroscopic analysis, we aim to unlock the different evolutionary paths that lead from O-type stars to the WR stage. Particularly, we investigate how conservative mass transfer happening in short-period binaries like AzV 14 can explain the observed bimodal temperature distribution of WR stars in low-metallicity environments.

Contribution: As the first author of this paper I conducted almost all of the research, namely the spectroscopic analysis, the modeling of the light curve, and the calculations of the stellar evolution models. The manuscript was fully written by myself.

1.5.4. Manuscript IV

Status: Published in *Astronomy & Astrophysics*, 2023, Volume: 674, ID: L12, 11 pp., DOI: 10.1051/0004-6361/202346818

Title: A partially stripped massive star in a Be binary at low metallicity: A missing link towards Be X-ray binaries and double neutron star mergers

Authors: V. Ramachandran, J. Klencki, A. A. C. Sander, D. Pauli, T. Shenar, L. M. Oskinova, W.-R. Hamann

Objective: Numerous intermediate-mass helium stars are predicted to be accompanied by rapidly rotating main sequence B-type stars. With this work, we present one of the first studies that have discovered and fully consistently analyzed the UV and optical data of such a bizar object. This provides valuable insights into the stellar and wind properties of these objects, which have been so far only theorized. Such an analysis is an important anchor point for binary evolution models and has implications for our understanding of the production of neutron star merger rates.

Contribution: Within this work, I calculated and tested different evolutionary channels and input physics, that could help to explain the observed properties of the system. I assisted with the text writing about stellar evolution and the discussion about its implications for our understanding of binary evolution at low metallicity.

1.5.5. Manuscript V

Status: Accepted by *Astronomy & Astrophysics*, 2024

Title: X-Shooting ULLYSES: Massive Stars at low metallicity VIII. Stellar and wind parameters of newly revealed stripped stars in Be binaries

Authors: V. Ramachandran, A.A.C. Sander, D. Pauli, J. Klencki, F. Backs, F. Tramper, M. Bernini-Peron, P. Crowther, W.-R. Hamann, R. Ignace, R. Kuiper, S. Oey, L. M. Oskinova, T. Shenar, H. Todt, J.S. Vink, L. Wang, A. Wofford, and the XShootU collaboration

Objective: Inspired by the discovery of a partially stripped helium star, which is accompanied by a rapidly rotating B-type star, we conducted a targeted search for similar systems within the ULLYSES and XShootU datasets. Three potential post-interaction binary candidates were identified, and a comprehensive analysis of their UV and optical data, including multi-epoch observations from other programs, was performed to further characterize these low-metallicity systems. By incorporating radial velocity measurements and light curve fits,

we were able to derive their orbital parameters. These findings present crucial benchmarks for challenging and refining binary evolution models, particularly regarding the contribution of helium stars to stellar populations in low-metallicity environments.

Contribution: Parts of the spectroscopic analysis was done using the multi-epoch spectra from my ESO observing program (ID: 109.22V0, PI: Pauli). I measured the radial velocities of one of the targets (2dFS 2553) and conducted the subsequent orbital analysis. Furthermore, I calculated of stellar evolution models based on the SMC targets, highlight shortcomings in our current understanding, suggesting the need for potential revisions. I wrote the sections on the orbital analysis about 2dFS 2553 as well as large fractions of the evolutionary modelling and their discussion.

Chapter 2

Manuscript I: The earliest O-type eclipsing binary in the Small Magellanic Cloud, AzV 476: A comprehensive analysis reveals surprisingly low stellar masses

D. Pauli, L. M. Oskinova, W.-R. Hamann, V. Ramachandran, H. Todt, A. A. C. Sander, T. Shenar, M. Rickard, J. Maíz Apellániz, R. Prinja

Astronomy & Astrophysics, 2022, Volume: 659, ID: A9, 23 pp.

Abstract

Massive stars at low metallicity are among the main feedback agents in the early Universe and in present-day star forming galaxies. When in binaries, these stars are potential progenitors of gravitational-wave events. Knowledge of stellar masses is a prerequisite to understanding evolution and feedback of low-metallicity massive stars. Using abundant spectroscopic and photometric measurements of an outstandingly bright eclipsing binary, we compare its dynamic, spectroscopic, and evolutionary mass estimates and develop a binary evolution scenario. We comprehensively studied the eclipsing binary system, AzV 476, in the Small Magellanic Cloud (SMC). The light curve and radial velocities were analyzed to obtain the orbital parameters. The photometric and spectroscopic data in the UV and optical were analyzed using the Potsdam Wolf-Rayet (PoWR) model atmospheres. The obtained results are interpreted using detailed binary-evolution tracks including mass transfer. AzV 476 consists of an O4 IV-III((f))p primary and an O9.5: Vn secondary. Both components have similar current masses (20 $M_\odot$ and 18 $M_\odot$) obtained consistently from both the orbital and spectroscopic analysis. The effective temperatures are 42 kK and 32 kK, respectively. The wind mass-loss rate of $\log(\dot{M}/(\,M_\odot\,\mathrm{yr}^{-1})) = -6.2$ of the primary is a factor of ten higher than a recent empirical prescription for single O stars in the SMC. Only close-binary evolution with mass transfer can reproduce the current stellar and orbital parameters, including orbital separation, eccentricity, and the rapid rotation of the secondary. The binary evolutionary model reveals that the primary has lost about half of its initial mass and is already core helium burning. Our comprehensive analysis of AzV 476 yields a consistent set of parameters and suggests previous case B mass transfer. The derived stellar masses agree within their uncertainties. The moderate masses of AzV 476 underline the scarcity of bright massive stars in the SMC. The core helium burning nature of the primary indicates that stripped stars might be hidden among OB-type populations.

2.1. Introduction

The most important parameter defining the evolution of a star is its mass. An often reported problem in stellar astrophysics is the "mass discrepancy" problem, which refers to the inconsistent masses derived from spectroscopy, evolutionary tracks, and, for binaries, from orbital motions (Herrero et al. 1992; Weidner & Vink 2010; Markova & Puls 2015). The analysis of O-type stars located in the Galaxy and the Large Magellanic Cloud (LMC) performed by Weidner & Vink (2010) reveal good agreement between the aforementioned mass estimates, but the study of Markova et al. (2018) suggests a mass discrepancy. Mahy et al. (2020) investigate a sample of O-type binaries in the LMC and find good agreement between spectroscopic and dynamic mass estimates while the evolutionary masses are at odds. These latter authors suggest previous binary interactions as a possible solution for this discrepancy.

However, the mass discrepancy problem has not yet been studied at metallicities lower than $\lesssim 1/2\,Z_\odot$. Sufficiently low metallicity is offered by the nearby Small Magellanic Cloud (SMC) galaxy ($Z_{\rm SMC} \approx 1/7\,Z_\odot$;Hunter et al. (2007); Trundle et al. (2007)). Precise stellar masses in the SMC allow us to tackle questions about stellar evolution and feedback at low metallicity.

Stars with spectral types around O2-4 are expected to be very massive with $M_* \gtrsim 50\,M_\odot$ (Martins & Palacios 2021). However, the true masses of the early-type O stars are only poorly known, and therefore spectral types and masses might be falsely mapped. So far, only a couple of the SMC eclipsing binaries with early spectral types have been studied. Morrell et al. (2003) investigated the O6V+O4/5III(f) system Hodge 53-47 (alias MOA J010321.3-720538) and found dynamic masses of $\approx 26\,M_\odot$ and $\approx 16\,M_\odot$ for the primary and secondary, respectively. The eclipsing binary, OGLE SMC-SC10 108086, studied by Abdul-Masih et al. (2021) contains even less massive stars with $\approx 17\,M_\odot$ and $\approx 14\,M_\odot$. Only one eclipsing multiple stellar system in the SMC, HD 5980, appears to contain stars with masses $\gtrsim 30\,M_\odot$. Koenigsberger et al. (2014) and Hillier et al. (2019) studied this system in detail and found an inner eclipsing binary consisting of an LBV and a Wolf-Rayet (WR) star, and a third O-type supergiant star with a potential fourth companion. The orbital masses of the LBV and the WR star are $\approx 61\,M_\odot$ and $\approx 66\,M_\odot$, respectively. Koenigsberger et al. (2014) suggest that there was little or no mass transfer, and that the WR star has formed via quasi-chemically homogeneous evolution. These examples highlight the complexity of massive star evolution and the need for advanced studies on the mass discrepancy problem in the high-mass regime.

For single stars, mass estimates rely on spectroscopic diagnostics or comparison with evolutionary tracks. Currently, standard stellar evolutionary models predict that the most massive stars, either single or in binary systems, start their lives on the main sequence (MS) as early-type O stars. Single stars expand and evolve away from the MS. During this phase, stars undergo strong mass loss where they might lose their entire hydrogen-rich envelope, revealing the helium core and becoming WR stars. In the case of close binaries, evolutionary models predict that the expanding star is likely to interact with its companion. In the majority of cases, the expanding star will transfer its envelope to the companion, and become a binary-stripped helium star, possibly also with a WR-type spectrum (Dionne & Robert 2006; Shenar et al. 2020b; Götberg et al. 2020).

The SMC hosts a handful of WR stars that have relatively high masses ranging from $10\,M_\odot$ to $60\,M_\odot$ (Shenar et al. 2016). These stars are so massive that their hydrogen-burning progenitors must have been early O-type (or WNL/Of) stars. However, in their recent study of the SMC OB-type population, Ramachandran et al. (2019) reveal a strong deficiency of massive stars ($> 30\,M_\odot$) close to the MS in the upper part of the empiric Hertzsprung–Russell diagram (HRD) (see Holgado et al. 2020; Ramachandran et al. 2018b, for studies of Galactic and the LMC O star populations). O-type stars are hot and luminous and are therefore easily detectable. Hence, a paucity of the earliest O-type stars in the SMC cannot be explained either by selection effects or stellar evolution scenarios (Schootemeijer et al. 2021). Thus, the deficiency of most massive O stars strongly questions the formation process of the WR stars in the SMC, as well as our basic understanding of stellar evolution in low-metallicity environments. In this context it is crucial to quantify the budget of massive stars ($\gtrsim 30\,M_\odot$) in the SMC.

Poorly constrained processes that affect the lives of massive stars include radiatively driven winds, stellar envelope inflation, core overshooting, and rotationally induced internal mixing. In particular their dependence on mass and metallicity are not yet fully understood. These effects can drastically alter the evolution of a star. Studies of objects in low-metallicity environments are needed to constrain these metallicity-dependent effects and thus allow the establishment of reliable stellar evolutionary tracks.

To address these outstanding questions, we selected one of the earliest subtype O stars in the SMC that is an eclipsing binary, allowing us to estimate its mass by various methods. The subject of this paper, AzV 476, is located in the cluster NGC 456 in the SMC Wing. The cluster contains an active star-forming region and hosts young stellar objects (Muraoka et al. 2017). AzV 476 is embedded in a H II region. The system was identified as an eclipsing binary by the Optical Gravitational Lensing Experiment (OGLE), which monitors stellar variability in the SMC and LMC (Pawlak et al. 2016). The primary star was classified by Massey et al. (2005) as an O2-3 V

star based on its optical spectral appearance and is therefore one of the earliest type stars in the entire SMC. Here we present the first consistent analysis of AzV 476, based on photometric and spectroscopic data, and in particular accounting for its binary nature. Newly obtained high-resolution UV and optical data give us the opportunity to perform such an analysis, yielding estimates on masses and stellar and wind parameters.

This paper is structured as follows. In Sect. 2.2 we describe the observations and the known stellar and orbital parameters used in the analysis below. The results of the orbital and spectral analysis as well as those from evolutionary modeling are presented in Sects. 2.3, 2.4, and 2.5, respectively. Their implications, similarities, and disagreements on the stellar masses and other stellar parameters are discussed in Sect. 2.6, and conclusions are given in Sect. 2.7.

2.2. Observations

2.2.1. Spectroscopy

Over the last decade, a handful of AzV 476 spectra covering the UV, optical (VIS), and infrared (IR) have been obtained, yielding multi-epoch data well suited for measuring radial velocities (RVs) and spectroscopic analysis. We used a spectroscopic dataset consisting of 12 spectra and Table 2.2.1 gives a brief overview of these, their covered wavelength ranges, their observed date, and their associated orbital phase. In the remainder of this paper, we refer to the individual observed spectra by their ID in Table 2.2.1.

The wavelength regime 950 Å – 1150 Å is covered by an archival FUSE (Oegerle et al. 2000) observations[1]. The FUSE spectrum (ID 1) was taken with a total exposure time of 21 567 s and a resolving power of $R \approx 20\,000$. Incidentally, the FUSE observation was taken close to the primary eclipse. This FUSE spectrum has a known but unsolved calibration issue. Therefore, we only used the LiF1A, LiF2A, and SiC2A channels, which appear to be the least affected by this problem. The spectrum is rectified by division through the combined continuum flux of our models.

AzV 476 is part of the ULLYSES program[2]. It was observed with the HST/COS (Hirschauer et al. 2021) using the G130M (1178 Å – 1472 Å) and G160M (1383 Å – 1777 Å) medium-resolution gratings (ID 2), $R \approx 19\,000$. The two spectra were taken sequentially with exposure times of 330 s and 1100 s, respectively. In addition, the star was re-observed in the UV with the HST/STIS spectrograph (Branton et al. 2021) using the E140M echelle graiting (ID 3) as part of the HST program 15837 (PI Oskinova). The spectrograph covers a wavelength regime of 1140 Å – 1735 Å. The exposure time was 2707 s and the final resolving power is $R \approx 45\,800$.

There is another spectrum in the ULLYSES program (ID 4) taken with the HST/STIS spectrograph using the E230M echelle gratings covering a wavelength range 1574 Å – 2673 Å. The exposure time was 2820 s and the resolving power is $R = 30\,000$.

For the optical and near-IR range, we use the publicly available spectra taken with the X-SHOOTER spectrograph (Vernet et al. 2011) mounted on the ESO Very Large Telescope (VLT). The spectrum (ID 5) was taken as part of the ESO 106.211Z program, which is part of the XSHOOTU program (their Paper I; Vink and the XShootU Collaboration, in prep.). The X-SHOOTER spectrograph consists of three different spectroscopic arms, which are optimized for the wavelength ranges in the UBV (3000 Å – 5550 Å), VIS (5300 Å – 10 000 Å), and near-IR (10 000 Å – 25 000 Å). The resolving powers are $R \approx 6\,600$, $R \approx 11\,000$, and $R \approx 8\,000$, respectively. The spectra were obtained with exposure times of 750 s, 820 s, and 300 s for the UBV, VIS, and NIR arm, respectively.

The remaining seven spectra (ID 6 – 12) used for our analysis are taken with the UVES spectrograph (Dekker et al. 2000) mounted on the ESO VLT. Each spectrum was taken with the DIC1 setup covering the wavelength ranges of 3000 Å – 4000 Å and 5000 Å – 11 000 Å. The exposure times are about 2895 s for both spectrographs and have a resolving power of $R \approx 65\,000$ and $R \approx 75\,000$, respectively. The UVES spectra were rectified by hand.

2.2.2. Photometry

The UBI photometry is adopted from the catalog of the SMC stellar population (Bonanos et al. 2010). For the VR photometry, we use the magnitudes from the fourth United States Naval Observatory (USNO) CCD Astrograph Catalog (UCAC4) (Zacharias et al. 2013). For completeness, we compare the values of the V- and I-band magnitudes to those listed in the IVth OGLE Collection of Variable Stars (Pawlak et al. 2016) (V_{OGLE} and I_{OGLE}). Unfortunately, the OGLE magnitudes are published without error margins. Nonetheless, we find that they are in

[1] the shorter wavelengths in the FUSE range are largely contaminated by interstellar features that yield no information about the stellar parameters

[2] https://ullyses.stsci.edu/

Table 2.2.1. List of all spectra of AzV 476 used in this work and their associated orbital phase. RVs and the wavelengths ranges and lines used for their measurements are also listed. The listed RVs are already corrected for the barycentric motion and the velocity of the NGC 456 complex with $v_{\rm SMC} = 152\,{\rm km\,s^{-1}}$.

spectral ID	Instrument	Wavelength [Å]	MJD[(a)] [d]	Phase ϕ [(b)]	RV_1 [$\rm km\,s^{-1}$]	RV_2 [$\rm km\,s^{-1}$]
1	FUSE	950 Å – 1150 Å	52478.3849	0.0192	—	—
2	HST/COS	1178 Å – 1777 Å	56185.2387	−0.2305	194 ± 5 [(c)]	—
3	HST/STIS	1140 Å – 1735 Å	59022.5673	−0.3124	91 ± 5 [(c)]	−86 ± 12 [(c)]
4	HST/STIS	1574 Å – 2673 Å	57321.6698	0.0968	−55 ± 5 [(d)]	64 ± 45 [(d)]
5	X-SHOOTER	3000 Å – 10 000 Å	59163.2501	−0.2928	112 ± 14	−110 ± 10
6	UVES	3000 Å – 11 000 Å	57703.2868	−0.1610	223 ± 9	−171 ± 15
7	UVES	3000 Å – 11 000 Å	57748.0479	−0.3823	60 ± 16	−42 ± 17
8	UVES	3000 Å – 11 000 Å	57749.0558	−0.2747	126 ± 8	−104 ± 29
9	UVES	3000 Å – 11 000 Å	57749.0923	−0.2708	141 ± 16	−95 ± 37
10	UVES	3000 Å – 11 000 Å	57750.1132	−0.1618	201 ± 13	−184 ± 34
11	UVES	3000 Å – 11 000 Å	57750.1492	−0.1580	207 ± 9	−186 ± 43
12	UVES	3000 Å – 11 000 Å	57751.0782	−0.0588	148 ± 12	−71 ± 37

[(a)] Mid-exposure in HJD - 2400000.5 [(b)] Calculated with Eq. (2.3.2). [(c)] Obtained from a fit over the range 1360 Å – 1405 Å. [(d)] Obtained from a fit over the range 2100 Å – 2230 Å.

Table 2.2.2. UBVRIJHK photometry of AzV 476.

Band	Apparent magnitude [mag]
U	12.49 ± 0.04
B	13.54 ± 0.07
V	13.48 ± 0.01
V_{OGLE}	13.49
R	13.72 ± 0.06
I	13.54 ± 0.20
I_{OGLE}	13.56
J	13.70 ± 0.03
H	13.72 ± 0.04
K	13.86 ± 0.06
G	13.51 ± 0.06
G_{BP}	13.46 ± 0.01
G_{RP}	13.57 ± 0.01

agreement with the V- and I-band magnitude from Zacharias et al. (2013) and Bonanos et al. (2010). JHK photometry is from the 2MASS catalog (Cutri et al. 2003). Additionally, we use the recent EDR3 Gaia photometry (Gaia Collaboration et al. 2016, 2021). A total list of the used magnitudes is shown in Table 2.2.2. Massey et al. (2005) estimated the extinction towards AzV 476 to be $E_{\rm B-V} = 0.28$ mag based on averaging the color excesses in $B - V$ and $U - B$ based on the spectral type. From our spectral energy distribution (SED) fit we find better agreement when using a lower extinction of $E_{\rm B-V} = 0.26$ mag (see Sect. 2.4.1). The slight difference can be due to the use of different reddening laws.

For the light curve modeling, we use the OGLE I-band photometry from the IVth OGLE Collection of Variable Stars (Pawlak et al. 2016). The photometric data are taken over the period from May 2010 to January 2014. We do not use the OGLE V-band photometry because it contains too few data points and therefore cannot be used to resolve the eclipses.

AzV 476 was observed by the TESS space telescope in 2018 (sector 2) and 2020 (sectors 27 and 28). However, the relatively low spatial resolution of TESS ($21''\,{\rm px^{-1}}$) precludes accurate point source photometry in the crowded region around our target. Therefore, the TESS data are not used for light-curve modeling. However, we use the TESS data to improve the ephemeris (see Sect. 2.3.1.1).

2.2.3. Distance and location

Our target, AzV 476 is part of the NGC 456 cluster which is located in the SMC Wing. The distance to the SMC Wing was estimated by Cignoni et al. (2009) $d \approx 55$ kpc corresponding to a distance modulus of DM = 18.7 mag. This is in agreement with Nidever et al. (2013) who use red clump stars to study the structure of the SMC, including the SMC Wing, and find that it follows a bimodal distribution with a near component at a distance of $d \approx 55$ kpc and a far component at $d \approx 67$ kpc. Tatton et al. (2021) confirm this distance, but they speculate that young structures, such as the NGC 456 cluster, do not trace substructures that are associated with the intermediate-age populations and might be located in front of them (see Sect. 2.6.1). In this work we adopt a distance of $d = 55$ kpc.

The observed spectra of AzV 476 are corrected for barycentric motion, which was calculated with the tool described in Wright & Eastman (2014). Additionally, we shifted the spectra by the RV of the NGC 456 complex in the SMC $v_{\mathrm{SMC}} = 152\,\mathrm{km\,s^{-1}}$ determined by fitting Gaussians to several interstellar medium (ISM) lines that we associate with the environment of AzV 476. The RV is not uniform throughout the different regions in the SMC and our finding is in agreement with the results of De Propris et al. (2010).

2.3. Analysis of the binary orbit

2.3.1. Method: Eclipse light-curve and RV curve modeling

2.3.1.1. Light curve

Our target, AzV 476, is listed in the IVth OGLE Collection of Variable Stars (Pawlak et al. 2016) with an orbital period of $P_{\mathrm{OGLE}} = 9.366\,319\,8$ d and an epoch of the primary eclipse of $T_{0,\,\mathrm{OGLE}} = 2457002.7608$ in Heliocentric Julian Date (HJD). Unfortunately, the orbital period and the epoch of the primary eclipse are given without error margins. The observations that constitute the OGLE I-band light curve were taken with a cadence of ≈ 2 d, and therefore the individual eclipses are not well resolved. In contrast, the TESS light curve has a much finer time coverage of ≈ 5 h, allowing better constraint of the orbital period and the epoch of the primary eclipse.

The date at which an eclipse occurs can be expressed as

$$T(n) = P \cdot n + T_0, \tag{2.3.1}$$

where T is the time of the primary eclipse at orbital cycle n. We fitted Gaussians to the primary eclipses in the TESS light curve; the corresponding orbital cycles and dates of all eclipses are listed in Table 2.3.1. Using this procedure, we obtain $P = 9.366\,65 \pm 0.000\,25$ d and $T_0 = 2457002.7968 \pm 0.0052$.

Figure 2.3.1 shows a part of the phased light curve centered on the primary eclipse for the two different ephemerides, those published in the OGLE catalog and those we obtain in this work. As can be seen, our newly obtained ephemeris adequately describes the OGLE as well as the TESS light curves, i.e., the data set that covers > 10 yr of observations.

In order to convert a date t at which a spectrum was taken to a phase Φ, the following formula is used

$$\phi(t) = \begin{cases} \dfrac{t - T_0}{P} & \mod 1 \qquad \text{if } \phi < 0.5 \\ \dfrac{t - T_0}{P} & \mod 1 - 1 \quad \text{otherwise.} \end{cases} \tag{2.3.2}$$

With the improved ephemerides and their small error margins, the uncertainties on the phases are negligible and are therefore not taken into account here. The OGLE I-band light curve is shown in the upper panel of Fig. 2.3.2. The conjunctions are at phases $\phi = 0.0$ and $\phi = -0.34$, implying that the orbit is eccentric.

2.3.1.2. RVs

To measure the RVs, we use a Markov chain Monte Carlo (MCMC) method combined with a least-square fitting method. In the MCMC method, the individual synthetic spectra of the primary and secondary (see Sect. 2.4.1) are shifted by different RVs. The combined synthetic spectrum is then compared to the observation. Using a least-square likelihood function we estimate the quality of the used RVs. The MCMC method quickly explores a large parameter space of different RVs until it converges toward the true solution. In the vicinity of the true solution, the MCMC method calculates the probabilities of different combinations of the RVs. This yields the final probability distribution around the true solution. A more detailed explanation is given in Appendix A.1.

Table 2.3.1. Dates of the primary eclipses in the TESS light curve.

orbital cycle n	MJD$^{(a)}$ [d]
145	58360.4633 ± 0.0027
146	58369.8256 ± 0.0030
147	58379.1905 ± 0.0029
218	59044.2165 ± 0.0016
219	59053.5942 ± 0.0016
220	59062.9590 ± 0.0014
221	59072.8303 ± 0.0014
222	59081.6913 ± 0.0015

$^{(a)}$ MJD = HJD − 2400000.5. The TESS data are given in TBJD = BJD − 2457000.0 and that we converted the BJD to HJD to be comparable to the OGLE data.

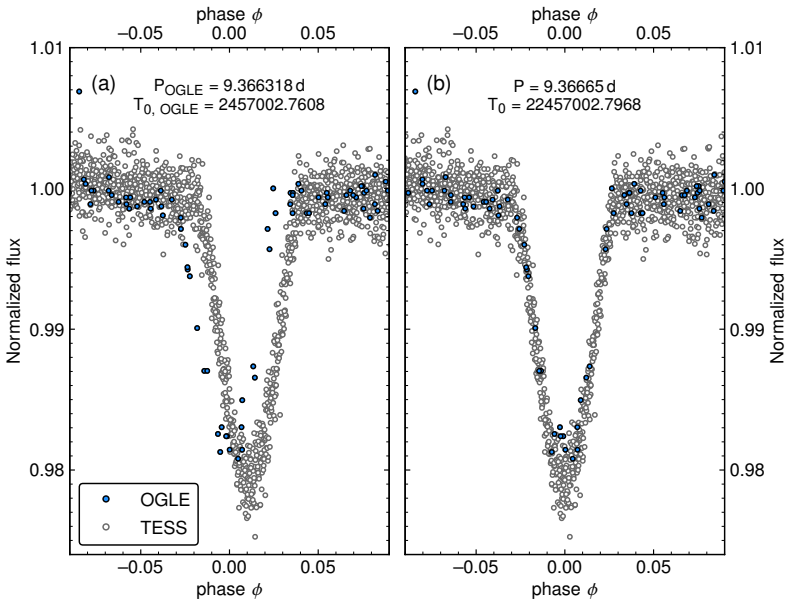

Fig. 2.3.1. Phased OGLE I-band and TESS light curves around the primary eclipse. *Left panel:* Light curve phased according to the ephemeris from the OGLE catalog. *Right panel:* Light curve phased according to the ephemeris we derive in this work by fitting the primary's eclipses of the TESS light curve.

Because the final probability distribution obtained with the MCMC method is not necessarily a Gaussian, we quote the error as the 68% confidence interval. The PHOEBE code cannot handle asymmetric errors, and therefore we only use the larger margin of the probability distribution as it is the safer choice. The uncertainties are included in the eclipsing binary modeling as described in Sect. 2.3.1.3.

The primary dominates the emission and absorption lines. In order to avoid uncertainties due to the intrinsic variability of lines formed in the stellar wind, the RVs listed in Table 2.2.1 are the averaged values of the RVs obtained from selected individual lines. A more detailed list of the RVs obtained from the individual lines in the different optical spectra is given in Tables A.1.1 and A.1.2.

All the absorption lines that are associated with the secondary show a contribution from the primary. Furthermore, the depths of these absorption lines are at the level of the noise, which introduces additional uncertainties; these are reflected in the larger error margins. Two selected optical spectra obtained at different phases are depicted in Fig. 2.3.3 to demonstrate how the spectral lines associated with the different binary components shift.

2.3.1.3. Modeling with PHOEBE

The Physics of Eclipsing Binaries (PHOEBE) v.2.3 modeling software (Prša & Zwitter 2005; Prša et al. 2016; Horvat et al. 2018; Jones et al. 2020; Conroy et al. 2020) is employed to derive dynamic masses as well as to

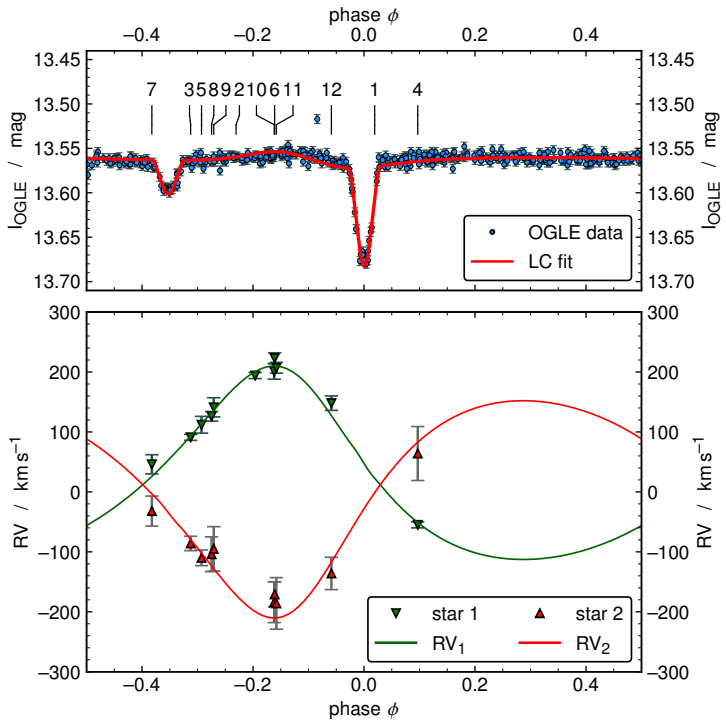

Fig. 2.3.2. *Upper panel:* Phased OGLE I-band light curve of AzV 476 (blue dots) and the best fit obtained with the PHOEBE code (red line). Above the light curve, the spectral IDs of all used spectra (see Table 2.2.1) are indicated. *Lower panel:* Observed (triangles) and fitted (solid lines) RV curves for the primary (green) and secondary (red). The fits of the light-curve fit and the RVs are consistently obtained by the PHOEBE code.

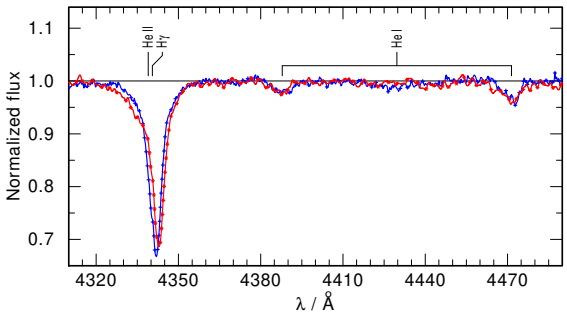

Fig. 2.3.3. X-SHOOTER spectrum (ID 5 in Table 2.2.1) displayed in blue and one of the UVES spectra (ID 10 in Table 2.2.1) in red. The spectra are convolved with a Gaussian with an FWHM = 0.4 Å to reduce the noise and to make the RV shifts visible. The region containing Hγ, He I λ4387, and He I λ4471 lines is shown. In the spectrum shown by the red line, the primary's spectrum is redshifted (see Hγ), while the secondary's spectrum (broadened He I lines) is blueshifted. We note that the primary also partially contributes to the He I lines.

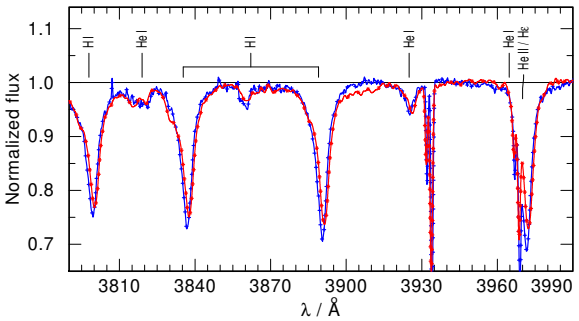

Fig. 2.3.4. Same as Fig. 2.3.3, but now for the region around the He I λ3819 and Hϵ lines. Most of the lines, including He I λ3926, are redshifted and associated with the primary, while the He I λ3819 line which is associated with the secondary is blueshifted.

obtain measures of the stellar parameters independently from the spectroscopic model. The simultaneous fitting of the RV and light curve is done with the `emcee` sampler (Foreman-Mackey et al. 2013).

To reduce the parameter space, we fix the orbital period and the epoch of the primary eclipse to the values we derive from the TESS light curve; see Sect. 2.3.1.1. As we are using only one passband, the temperatures of the components cannot be obtained reliably. Therefore, the temperatures of the primary and secondary are fixed to the results from the spectral analysis (see Sect. 2.4.1), $T_{\rm eff,\,1} = 42\,$kK and $T_{\rm eff,\,2} = 32\,$kK, respectively.

The PHOEBE code assumes synchronous stellar rotation. The actual fast rotation of the secondary with $v \sin i = 425\,{\rm km\,s^{-1}}$ is therefore not consistently taken into account for modeling the secondary eclipse. Gravita-

tional darkening is modeled by a power law with a coefficient of $\beta_{\rm grav} = 1$, as recommended for radiative envelopes in the PHOEBE documentation[3]. Given the period of ~ 10 d, this renders gravitational darkening unimportant.

The atmospheres of both components are approximated by a blackbody. We compared the blackbody flux to the SED of our atmospheric model and find that it is a valid approximation for the I-band flux. We calculated the emergent flux distribution using our spectral models (see Sect. 2.4.1) and fitted different types of limb-darkening laws (e.g., Diaz-Cordoves & Gimenez 1992). We find that the limb-darkening law that best describes the primary and secondary is a quadratic approximation in the form of

$$I(\mu) = I(1)\,[1 - a_i\,(1-\mu) - b_i\,(1-\mu)^2], \tag{2.3.3}$$

where $\mu = \cos\theta$ is the cosine of the directional angle θ, and a_i and b_i are the limb-darkening coefficients of each stellar component i. For the primary, the best fit is achieved with coefficients $a_1 = 0.2032$ and $b_1 = 0.0275$, while for the secondary $a_2 = 0.1668$ and $b_2 = 0.0802$ are required.

In a binary where both stellar components have large radii, on the order of $\gtrsim 20\%$ of their separation, and rather similar temperatures, the so-called "reflection effect" becomes important (Wilson 1990). This effect accounts for the irradiation of the surface by the other component (Prša 2011; Prša et al. 2016). As AzV 476 is a close binary with two hot O-stars, the reflection effect is modeled with two reflections. The effect of ellipsoidal variability due to tidal interaction, which induces periodic variations in the light curve, is important in close binary systems with orbital periods on the order of a few days (Mazeh 2008). However, as none of the binary components are close to filling their Roche lobe (see Table 2.3.3) and the mass ratio is not extreme ($q_{\rm orb} = 0.89$) this effect is expected to be negligible (Gomel et al. 2021).

2.3.2. Resulting binary parameters

The best fitting model light curve and RV fit obtained with the PHOEBE code are shown in Fig. 2.3.2. The corresponding orbital parameters are listed in Table 2.3.2 and the stellar parameters of both components in Table 2.3.3. The orbital solution yields similar masses for both components, while the light curve fit reveals different $T_{\rm eff}$ and L. This indicates that there was a prior mass-transfer phase that has stripped away most of the primary's envelope, such that now has similar mass to its companion. From the light-curve fit, the fundamental stellar parameters –stellar radius and the surface gravity— are determined, giving us the opportunity to cross-check the spectral analysis. Furthermore, the PHOEBE code calculates the light ratio of the binary components in the observed band outside conjunctions, which is compared to the light ratio obtained from the spectroscopic analysis in Sect. 2.4.

Table 2.3.2. Orbital parameters obtained from the RV and light curves by the PHOEBE code

Parameter	Value
P (d)	9.36665 (fixed)
HJD_0	7002.7968 (fixed)
e	$0.240^{+0.002}_{-0.002}$
ω_0 (°)	19^{+2}_{-1}
$q_{\rm orb}$	$0.89^{+0.06}_{-0.06}$
γ	12^{+3}_{-3}
i (°)	$77.9^{+0.3}_{-0.3}$
a ($R_\odot$)	63^{+2}_{-2}

Table 2.3.3. Stellar parameters obtained from the RV and light curves by the PHOEBE code

Parameter	Primary	Secondary
$T_{\rm eff}$ [kK]	42 (input)	32 (input)
K [km s^{-1}]	161^{+13}_{-13}	181^{+14}_{-14}
$M_{\rm orb}$ [$M_\odot$]	$20.2^{+2.0}_{-2.0}$	$18.0^{+1.8}_{-1.8}$
R [$R_\odot$]	$10.7^{+0.4}_{-0.4}$	$7.0^{+0.4}_{-0.4}$
$R_{\rm RL}$ [$R_\odot$]	$24.5^{+0.9}_{-0.9}$	$23.3^{+0.8}_{-0.8}$
$\log g$ [cm s^{-2}]	$3.69^{+0.06}_{-0.06}$	$4.00^{+0.07}_{-0.07}$
$\log L$ [$L_\odot$]	$5.51^{+0.13}_{-0.13}$	$4.67^{+0.22}_{-0.22}$
$M_{\rm bol}$ [mag]	$-8.94^{+0.32}_{-0.32}$	$-6.83^{+0.56}_{-0.56}$
f_2/f_1 (OGLE I-band)	$0.31^{+0.05}_{-0.05}$	

[3] www.phoebe-project.org

2.4. Spectral analysis

2.4.1. Method: Spectral modeling with PoWR

Synthetic spectra for both stellar components were calculated with the Potsdam Wolf-Rayet (PoWR) model atmosphere code (Gräfener et al. 2002; Hamann & Gräfener 2004). In the following, we briefly describe the code. For further details, we refer to Gräfener et al. (2002), Hamann & Gräfener (2003), Todt et al. (2015b), and Sander et al. (2015).

The PoWR code models stellar atmospheres and winds permitting departures from local thermodynamic equilibrium (non-LTE). The code has been widely applied to hot stars at various metallicities (e.g., Hainich et al. 2014, 2015; Oskinova et al. 2011; Reindl et al. 2014; Shenar et al. 2015). The models are assumed to be spherically symmetric, stationary, and in radiative equilibrium. Equations of statistical equilibrium are solved in turn with the radiative transfer in the co-moving frame. Consistency is achieved iteratively using the "accelerated lambda operator" technique. This yields the population numbers within the photosphere and wind.

The emergent spectrum in the observer's frame is calculated with the formal integral in which the Doppler velocity is split into the depth-dependent thermal velocity and a "microturbulence velocity" $\zeta(r)$. The microturbulence grows from its photospheric value $\zeta_{\rm ph} = 10\,{\rm km\,s^{-1}}$ linearly with the wind velocity up to $0.1 v_\infty$.

By comparison of the synthetic spectrum with the observations, it is possible to determine the main stellar parameters. In addition to the chemical composition, the main stellar parameters that specify the model atmosphere are the luminosity L, stellar temperature T_*, surface gravity g_*, wind mass-loss rate $\dot{M}$, and the wind terminal wind velocity v_∞. The stellar temperature is defined as the effective temperature referring to the stellar radius R_* by the Stefan-Boltzmann equation $L = 4\pi\sigma R_*^2 T_*^4$. The stellar radius is defined at the Rosseland mean optical depth of $\tau = 20$. The differences between T_* and the effective temperature $T_{\rm eff}$ (referring to the radius where the optical depth $\tau = 2/3$) are negligibly small, as the winds of OB-type stars are optically thin.

In the subsonic regions of the stellar atmosphere, the velocity law is calculated such that the density, related by the equation of continuity, approaches the hydrostatic stratification. The hydrostatic equation consistently accounts for the radiation pressure (Sander et al. 2015). In the supersonic regions, it is assumed that the wind velocity field can be described by a so-called double β-law as was first introduced by Hillier & Miller (1999):

$$v(r) = v_\infty \left[(1-f)\left(1 - \frac{r_0}{r}\right)^{\beta_1} + f\left(1 - \frac{r_1}{r}\right)^{\beta_2} \right]. \tag{2.4.1}$$

In this work, we assume $\beta_1 = 0.8$, a typical value for O-stars, $\beta_2 = 4$, and a contribution of $f = 0.4$ of the second β-term. r_0 and r_1 are close to the stellar radius R_* and are determined such that the quasi-hydrostatic part and the wind are smoothly connected. This choice of the wind velocity law leads to better agreement between the Hα absorption line and the C IV P Cygni line profile than the classical β-law (Castor et al. 1975).

Inhomogeneities within the wind are accounted for as optically thin clumps ("microclumping") which are specified by the "clumping factor" D, which describes by how much the density within the clumps is enhanced compared to a homogeneous wind with the same mass-loss rate (Hamann & Koesterke 1998b). In our analysis, we use a depth-dependent clumping which starts at the sonic point and increases outward until a clumping factor of $D = 20$ is reached at a radius of $R_{\rm D} = 7\,R_*$ for the primary and at a radius $R_{\rm D} = 10\,R_*$ for the secondary. The smaller radius at which the clumping factor is reached in the primary's wind profile is needed to model the observed O V λ1371 line properly.

The PoWR model atmospheres used here account for detailed model atoms of H, He, C, N, O, Mg, Si, P, and S. The iron group elements Sc, Ti, V, Cr, Mn, Fe, Co, and Ni are combined to one generic element "G" with solar abundance ratios, and treated in a superlevel approach (Gräfener et al. 2002). The abundances of Si, Mg, and Fe are based on Hunter et al. (2007, their table 17) and Trundle et al. (2007, their table 9). For the remaining elements, we divide the solar abundances of Asplund et al. (2005, their table 1) by seven to match the previously mentioned metallicity of the SMC. This yields the following mass fractions: $X_{\rm H} = 0.73$, $X_{\rm Si} = 1.3 \times 10^{-4}$, $X_{\rm Mg} = 9.9 \times 10^{-5}$, $X_{\rm P} = 8.32 \times 10^{-7}$, $X_{\rm S} = 4.42 \times 10^{-5}$, and $X_{\rm G} = 3.52 \times 10^{-4}$. The CNO individual abundances of both stellar components are not fixed but derived from the analysis. The complement mass fraction to unity is $X_{\rm He}$.

We determined the color excess $E_{\rm B-V}$ and the luminosity L of the binary components by fitting the composite SED to photometry (top panel in Fig. 2.4.5). Reddening is modeled as a combined effect of the Galactic foreground, for which we adopt the reddening law of Seaton (1979) with $E_{\rm B-V} = 0.03$ mag, and the reddening law of Bouchet et al. (1985) for the SMC.

We use the `iacob-broad` tool (Simón-Díaz & Herrero 2014) in combination with the high S/N X-SHOOTER spectrum (S/N $\sim$ 100) to determine the rotation rates of the primary and the secondary. The helium lines are potentially pressure broadened and thus are not optimally suited for rotation broadening measurements. There-

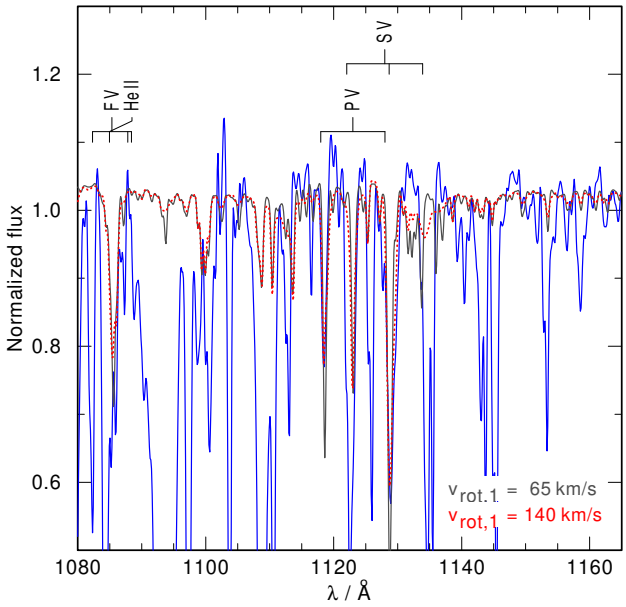

Fig. 2.4.1. Part of the observed FUSE spectrum (ID 1 in Table 2.2.1) covering the wavelength range of the LiF2 channel – the same as used by Penny & Gies (2009) to determine the projected rotational velocity. The observed spectrum, corrected for the velocity of the SMC, is shown as a solid blue line. The red dotted line is our best-fitting model with the primary's projected rotational velocity $v_1 \sin i = 140\,\mathrm{km\,s^{-1}}$. The gray solid line is another model where the primary's projected rotational velocity is reduced to $v_1 \sin i = 140\,\mathrm{km\,s^{-1}}$. The line identification marks correspond to the wavelengths in the rest frame.

fore, for the primary, we use the few metal lines that are visible in the optical spectrum, namely the N IV λ3478 and the O IV λ3403 absorption lines and the N IV λ4058 emission line. We determine a projected rotation rate of $v_1 \sin i = 140\,\mathrm{km\,s^{-1}}$ for the primary. The secondary only contributes to the He I lines. Fitting the He I λ4387 and He I λ4471 absorption lines —in which the contribution of the primary is smallest— yields a rotation rate of $v_2 \sin i = 425\,\mathrm{km\,s^{-1}}$ for the secondary.

Previously, Penny & Gies (2009) determined the projected rotational velocity of the primary to $v_1 \sin i = 65\,\mathrm{km\,s^{-1}}$ using a cross-correlation of the FUSE spectrum in the far-UV with a template spectrum. We calculate tailored spectral models with the respective projected rotational velocities and find that also the FUSE spectrum is better reproduced when using $v_1 \sin i = 140\,\mathrm{km\,s^{-1}}$ (see Fig. 2.4.1). We assume that the template spectrum used in Penny & Gies (2009) might not have been perfectly calibrated for our target and that the binary nature leads to additional uncertainties.

2.4.2. Resulting spectroscopic parameters

2.4.2.1. Temperature and surface gravity of the primary

AzV 476 was previously classified as O2-3 V plus a somewhat later O-type companion. This implies that nitrogen lines are expected in absorption and emission in the primary spectrum, while He I absorption lines should be present in the secondary spectrum.

Indeed, we find that the N IV λ4057 (hereafter N IV) emission line, the N IV absorption lines at $\lambda\lambda$ 3463 Å, 3478 Å, 3483 Å, and 3485 Å, and the He II λ6528 absorption can be entirely assigned to the primary. We observe only marginal N III $\lambda\lambda$4634, 4640 (hereafter N III) emission and N V $\lambda\lambda$4603, 4619 (hereafter N V) absorption; see Fig. A.2.1. Thus, the optical spectrum shows nitrogen only as N IV, while N III as well as N V are virtually absent. This restricts the temperature of the primary to a narrow range (Rivero González et al. 2012). We also find that the O IV multiplets around 3400 Å are purely associated with the primary. Because these lines are highly contaminated by ISM absorption lines of Ti II λ3385 and Co I λ3414, they are only used as a crosscheck of the oxygen abundance applied in our spectral model. A more detailed description of this line complex is given in Appendix A.2.2.

The secondary does not contribute noticeably to these weak metal lines. However, the secondary strongly dominates the He I absorption lines at $\lambda\lambda$ 3819 Å, 4387 Å, and 4471 Å, indicating a lower effective temperature. The primary star also contributes to these lines, giving additional constraints on the temperature of the primary.

The surface gravity $g_{*,1}$ of the primary is determined by fitting the wings of the Balmer lines using those UVES spectra with the least wavy patterns and highest RV shifts as well as the X-SHOOTER spectrum, which

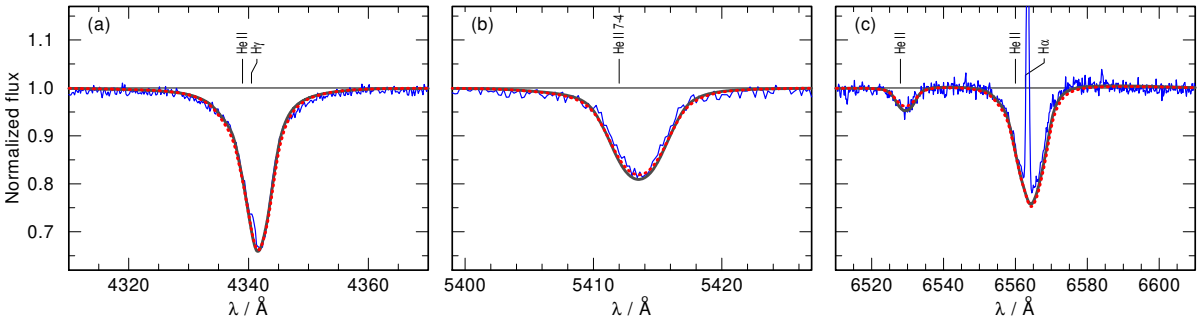

Fig. 2.4.2. Selected regions of the X-SHOOTER spectrum (ID 5 in Table 2.2.1) compared to different synthetic spectra. The observed spectrum, corrected for the velocity of the SMC and the barycentric motion, is shown as a solid blue line. The red dotted line is our best-fitting model which consists of the primary with $T_{\rm eff,1} = 42\,{\rm kK}$ and $\log g_{*,1} = 3.7$ and the secondary with $T_{\rm eff,2} = 32\,{\rm kK}$ and $\log g_{*,1} = 4.0$. The gray solid line is again a combined synthetic spectrum of the primary and secondary, but this time the surface gravity of the primary has been reduced to $\log g_{*,1} = 3.6$ (and the temperature and mass-loss rate are slightly adjusted so that the spectrum matches the observations) while the parameters of the secondary are kept fixed. The line identification marks correspond to the wavelengths in the rest frame. Panel (a) shows the Hγ line, in which the red wing is dominated by the primary and the blue wing by the secondary. Panel (b) shows the He II λ5412 absorption line, which is dominated by the primary and is sensitive to surface gravity. Panel (c) shows the region of He II λ6528 and Hα. While the Hα wings are only barely affected by the change in $\log g_{*,1}$, the He II λ6528 line is more sensitive to it.

has a higher S/N. Because both stars contribute to the Balmer lines, the He II λ5412 absorption line that is mostly originating from the primary and also sensitive to changes in surface gravity is used. Unfortunately, this line is only contained in the X-SHOOTER spectrum. Surface gravity affects the density structure and therefore the ionization balance of, for example, nitrogen and helium. As the temperature is adjusted such that the nitrogen lines are reproduced, changes in the surface gravity will not only affect the wings of the He II lines but also change the depth of the He II absorption lines. This gives the opportunity to use the He II λ6528 absorption line in the UVES spectra as second criterion for the surface gravity estimate in the primary.

We tested different temperature values in the range $T_{\rm eff,1} = 39\,{\rm kK} - 50\,{\rm kK}$ and surface gravities in the range $\log(g_{*,1}/({\rm cm\,s^{-2}})) = 3.5 - 4.1$ and found that a temperature of $T_{\rm eff,1} = 42 \pm 3\,{\rm kK}$ and a surface gravity of $\log(g_{*,1}/({\rm cm\,s^{-2}})) = 3.7 \pm 0.2$ are most suitable for reproducing the primary's spectrum. The given error margins take into account that the measurements of temperature and surface gravity are not independent.

Different regions of the X-SHOOTER spectrum that are used to determine the surface gravity are shown in Fig. 2.4.2. The accuracy in surface gravity highly depends on the calibration of the spectrum. One can see that Hγ and He II λ5412 line fits show preference to a surface gravity for the primary of $\log(g_{*,1}/({\rm cm\,s^{-2}})) = 3.7$, while H$\alpha$ and He II λ6528 indicate that $\log(g_{*,1}/({\rm cm\,s^{-2}})) = 3.6$ might be more suitable. However, from fitting the UVES data with the highest RV shifts we find that a surface gravity for the primary of $\log(g_{*,1}/({\rm cm\,s^{-2}})) = 3.7$ yields the best fit.

2.4.2.2. Temperature and surface gravity of the secondary

It is more difficult to determine the temperature of the secondary, as only a few He I lines are associated with the secondary and all these line have a contribution from the primary. However, from the spectra with the highest RV shifts (e.g., UVES spectrum with ID 10), we find that the secondary does not contribute to the He II λ4200 line, and therefore we have an additional constraint that can be used as an upper limit on the temperature of the secondary. In addition to the limited number of lines that are associated with the secondary, the ionization balance that changes depending on the surface gravity introduces another uncertainty in our temperature estimation.

Therefore, we first adjust $g_{*,2}$ of the secondary such that the wings of the Balmer lines are well reproduced while keeping the surface gravity and temperature of the primary fixed. As in the case of the primary, in order to distinguish the contributions of the binary components to the Balmer wings, we employ the UVES spectra in the phase with the largest RV shifts. This gives additional information and a surface gravity of $\log(g_{*,2}/({\rm cm\,s^{-2}})) = 4.0$ can be determined. Finally, the temperature of the secondary is adjusted such that the He I absorption lines at $\lambda\lambda$ 3819 Å, 4387 Å, and 4471 Å match the observation. Following this procedure, the spectrum of the secondary is best reproduced with a temperature of $T_{\rm eff,2} = 32\,{\rm kK}$. This method is accurate to $\Delta T_{\rm eff,2} = \pm 4\,{\rm kK}$ in temperature and $\Delta \log(g_{*,2}) = \pm 0.2$ for the surface gravity. The obtained values of the surface gravity of the primary and the secondary are in agreement with those obtained from the orbital analysis (see Sect. 2.3).

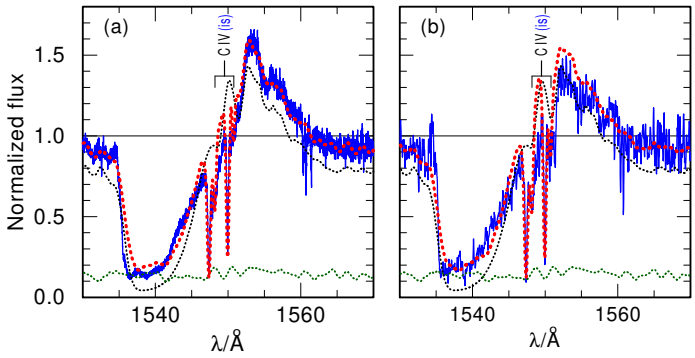

Fig. 2.4.3. Observed (blue) and synthetic (red) C IV resonance doublet of our final model. The individual primary and secondary spectra are shown as dotted black and green lines, respectively. The sharp interstellar absorptions arise in the Galactic foreground and in the SMC, and are also modeled with their respective RV shifts. (a) COS observation (ID 2 in Table 2.2.1) (b) STIS observation (ID 3 in Table 2.2.1).

2.4.2.3. Luminosity

To estimate the light ratio, the luminosities of both stars are adjusted such that the shapes of the optical He II lines match the observations. This is an iterative process done simultaneously with the temperature and surface gravity estimate. The total luminosity of the system is calibrated such that the calculated visual magnitude of the synthetic flux matches the observed one. This results in luminosities of $\log(L_1/L_\odot) = 5.65$ for the primary and $\log(L_2/L_\odot) = 4.75$ for the secondary. This estimate is sensitive to synthetic spectra, light ratio, and distance modulus. Therefore, we estimate that our measurements of the luminosity of each stellar component are accurate to $\Delta \log(L/L_\odot) = \pm 0.2$.

Taking these uncertainties into account, the model flux ratio in the OGLE I-band yields $f_2/f_1 = 0.26 \pm 0.1$ which is in agreement with the flux ratio derived using PHOEBE $f_2/f_1 = 0.31 \pm 0.05$ (see Sect. 2.3).

2.4.2.4. Mass-loss rates

After determining the temperatures, surface gravities, and luminosities of both binary components, we proceed to measuring the properties of their stellar winds. The Hα line in the optical as well as the C IV resonance line in the UV are used as the main diagnostic tools for measuring the mass-loss rate of the primary. In addition, we also pay attention to the appearance of the optical He I λ4686 and the UV He II λ1640 line; see Fig C.4.4. When calibrating the mass-loss rate of the primary, the best fit is archived with a mass-loss rate of $\log(\dot{M}_1/(\,M_\odot\,\mathrm{yr}^{-1})) = -6.1 \pm 0.2$ and a terminal wind velocity of $v_{\infty,1} = 2500\,\mathrm{km\,s^{-1}}$.

We have two spectra covering the C IV resonance line at different phases, the COS and the STIS spectrum (ID 2 and 3 in Table 2.2.1), depicted in Fig. 2.4.3. The C IV P Cygni line profile in both spectra does not show any direct indications for the contribution from the secondary such as a double emission peak or a step in the absorption trough. The C IV resonance line in the STIS spectrum shows slightly weaker emission, which is most likely due to the sensitivity of the different instruments or weak wind variability. We use the bottom part of the P Cygni profile of C IV resonance line to confirm the continuum contribution of the secondary in the UV and therefore the used light ratio (L_2/L_1).

Apparently the secondary does not contribute to the wind lines. Its mass-loss rate can therefore only be limited to $\log(\dot{M}_2/(\,M_\odot\,\mathrm{yr}^{-1})) \leq -8.8 \pm 0.5$. For higher mass-loss rates, we find that the secondary would noticeably contribute to the C IV resonance line in the UV. Due to the lack of indications of the secondary's wind we adopt the terminal velocity of the primary, $v_{\infty,2} = 2500\,\mathrm{km\,s^{-1}}$.

2.4.2.5. CNO surface abundances

As already explained in Sect. 2.4.1, the abundances of hydrogen and the iron group elements are fixed, while the CNO abundances of each stellar component are adjusted during spectral modeling. The nitrogen abundance is adjusted to find good agreement with the optical N IV absorption lines at wavelengths 3463 Å, 3478 Å, and 3483 Å, and the N IV λ4057 and N IV $\lambda\lambda$7103 − 7129 emission lines, as well as the UV N V $\lambda\lambda$1238, 1242 resonance doublet. The best agreement is achieved with a nitrogen mass fraction of $X_\mathrm{N} = (45^{+5}_{-10}) \times 10^{-5}$. The nitrogen lines seen in the optical are displayed in Fig. 2.4.4.

A carbon abundance of $X_\mathrm{C} = (2^{+2}_{-1}) \times 10^{-5}$ reproduces the optical C IV $\lambda\lambda$5801, 5812 lines best while maintaining the fit of the C IV resonance doublet, at least for mass-loss rates that do not conflict with other wind features.

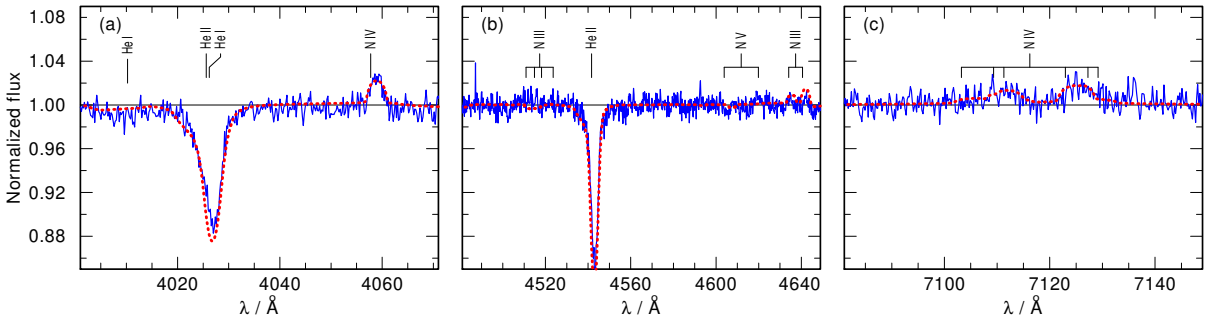

Fig. 2.4.4. Observed X-SHOOTER spectrum (ID 5 in Table 2.2.1) and synthetic spectra of selected regions that show nitrogen emission lines. The observed spectrum is shown as a solid blue line, while the dotted red line is our best-fitting model. The observed spectrum is corrected for the velocity of the SMC and the barycentric motion. The line identification marks correspond to the wavelengths in the rest frame. Panel (a) shows the area around the N IV λ4057. Panel (b) shows the region of N III $\lambda\lambda$4511 – 4523, N V $\lambda\lambda$4604, 4620, and N III $\lambda\lambda$4634, 4641. The N III and N V lines are not observable in the spectrum. Panel (c) shows the region of the N IV $\lambda\lambda$7103 – 7129 complex.

For lower abundances, the latter is no longer saturated. The oxygen abundance of the primary is calibrated with the oxygen absorption lines in the UV and the optical O IV multiplets around 3400 Å, resulting in $X_{\rm O} = (80^{+10}_{-20}) \times 10^{-5}$.

There are no strong CNO lines in the secondary spectrum, and therefore we adopt initial CNO abundances scaled to the metallicity of the SMC ($Z_{\rm SMC} = 1/7\,Z_\odot$). Alternatively, one could assume that the surface abundances in the secondary are close to those in the primary as the accreted material is polluting the surface of the secondary. We explored both assumptions but could not find diagnostic lines that would allow us to pin down the composition of the atmosphere and wind of the secondary. We are only able to fix upper limits for the CNO abundances such that these elements would not produce features that are inconsistent with the observations: $X_{\rm N} \lesssim 50 \times 10^{-5}$, $X_{\rm C} \lesssim 21 \times 10^{-5}$ and $X_{\rm O} \lesssim 110 \times 10^{-5}$.

2.4.2.6. Required X-ray flux

Similar to other O-type stars, AzV 476 shows a notoriously strong P Cygni profile in the O VI $\lambda\lambda$1032, 1038 resonance doublet. However, wind models do not predict a sufficient population of this high ion without the inclusion of additional physical processes. This phenomenon, termed "super-ionization", was described by Cassinelli & Olson (1979) and interpreted as evidence for the presence of an X-ray field in stellar atmospheres.

In order to model the O VI doublet in the observed spectrum of AzV 476, we add a hot plasma component. The X-ray-emitting plasma has an adopted temperature of $T_{\rm X} = 3$ MK and is distributed throughout the wind outside a radius of $R_{\rm X} = 1.1\,R_*$. Its constant filling factor is a free parameter; the best reproduction of the observation is achieved for a model with an emergent X-ray luminosity of $\log\, L_{\rm X} = 31.4\,{\rm erg\,s^{-1}}$.

Current X-ray telescopes are not sensitive enough to detect individual O stars in the SMC. Our final model predicts an X-ray flux at earth of 1.4×10^{-17} erg s^{-1} cm^{-2} Å^{-1} integrated over the X-ray band ($\approx 6 - 60$ Å). The region on the sky where AzV 476 is located was observed by both *XMM-Newton* and *Chandra* X-ray observatories. However, despite the detection of AzV 476 in the UV by the *XMM-Newton* optical monitor, the star is not detected in X-rays. Hence, we set the upper limit on its X-ray flux at the median flux of detected sources in the XMMSSC - XMM-Newton Serendipitous Source Catalog (4XMM-DR10 Version); this is 5×10^{-15} erg s^{-1} cm^{-2} Å^{-1} , which is far from being sufficiently sensitive for our predicted source.

The O VI resonance doublet is not the only feature that is sensitive to X-rays. Other ions which might be populated by Auger ionization are N V and N IV. We find that the N V $\lambda\lambda$1242, 1238 resonance doublet in our model is not significantly affected by the applied X-ray field, while the N IV $\lambda\lambda$1718, 1721 doublet is very sensitive. However, in the region around the N IV $\lambda\lambda$1718, 1721 doublet, the observations are very noisy and can be explained by the model with X-rays as well as without.

The composed model spectrum as well as the individual spectra are shown in Figs. 2.4.2 – 2.4.6. A summary of the stellar parameters including the abundances is given in Table 2.4.1.

2.4.2.7. Spectroscopic stellar masses

The spectroscopic masses derived from our analysis are $M_{\rm spec,\,1} = 29^{+17}_{-11}\,M_\odot$ for the primary and $M_{\rm spec,\,2} = 22^{+13}_{-8}\,M_\odot$ for the secondary. The spectroscopic masses, although a factor of 1.5 higher than the orbital masses, agree with these latter within their respective uncertainties. The large error margins on the spectroscopic masses

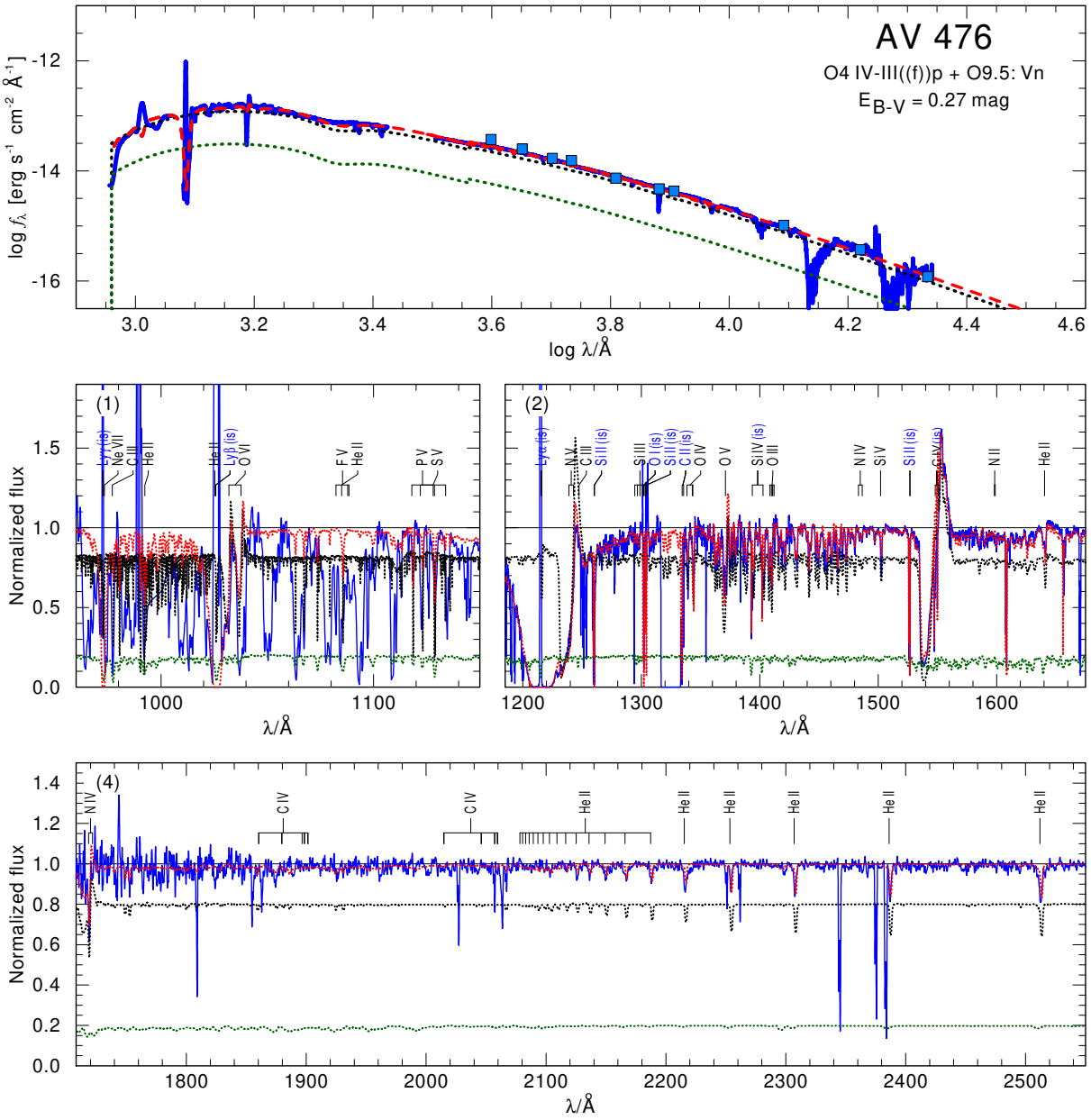

Fig. 2.4.5. Spectral fit for AzV 476. *Top panel:* SED. Flux-calibrated observations (blue lines) are the FUSE (1), COS (2), STIS (4), and X-SHOOTER (5) spectra as listed in Table 2.2.1. The light blue squares are the photometric UBVRIJHK data as listed in Table 2.2.2. The model SED composed of both stellar components is shown as a dashed red line, while the individual SEDs of the primary and the secondary are shown as dotted black and green lines, respectively. *Lower panels:* Normalized FUSE (1), COS (2), and STIS (4) spectra. The number in the upper left corner corresponds to the ID given to a specific spectrum as listed in Table 2.2.1. The line styles are the same as in the top panel. The synthetic spectra are calculated with the model parameters compiled in Table 2.4.1 ("Spectroscopy" columns).

arise mainly from the large uncertainties on surface gravity and luminosity (e.g., Fig. 2.4.2). The spectroscopic mass ratio is $q_{\rm spec} = 0.7$ which is smaller than the one obtained from the orbital analysis.

It appears that the spectroscopically derived masses and luminosities are shifted systematically to higher values compared to the results of the orbital analysis. We discuss this in more detail in Sect. 2.6.1.

Nevertheless, a mass ratio close to unity, while the two stars in a close binary have different spectral types, strongly suggests mass transfer in the past. From our binary evolutionary models (Sect. 2.5), we expect that mass transfer removed most of the hydrogen-rich envelope from the primary. We calculated model spectra with strongly depleted surface hydrogen ($X_{\rm H} = 0.2$ and 0.5). However, these models yield poorer spectral fits as the helium lines become too deep. Still, moderate hydrogen depletion and helium enrichment cannot fully be excluded.

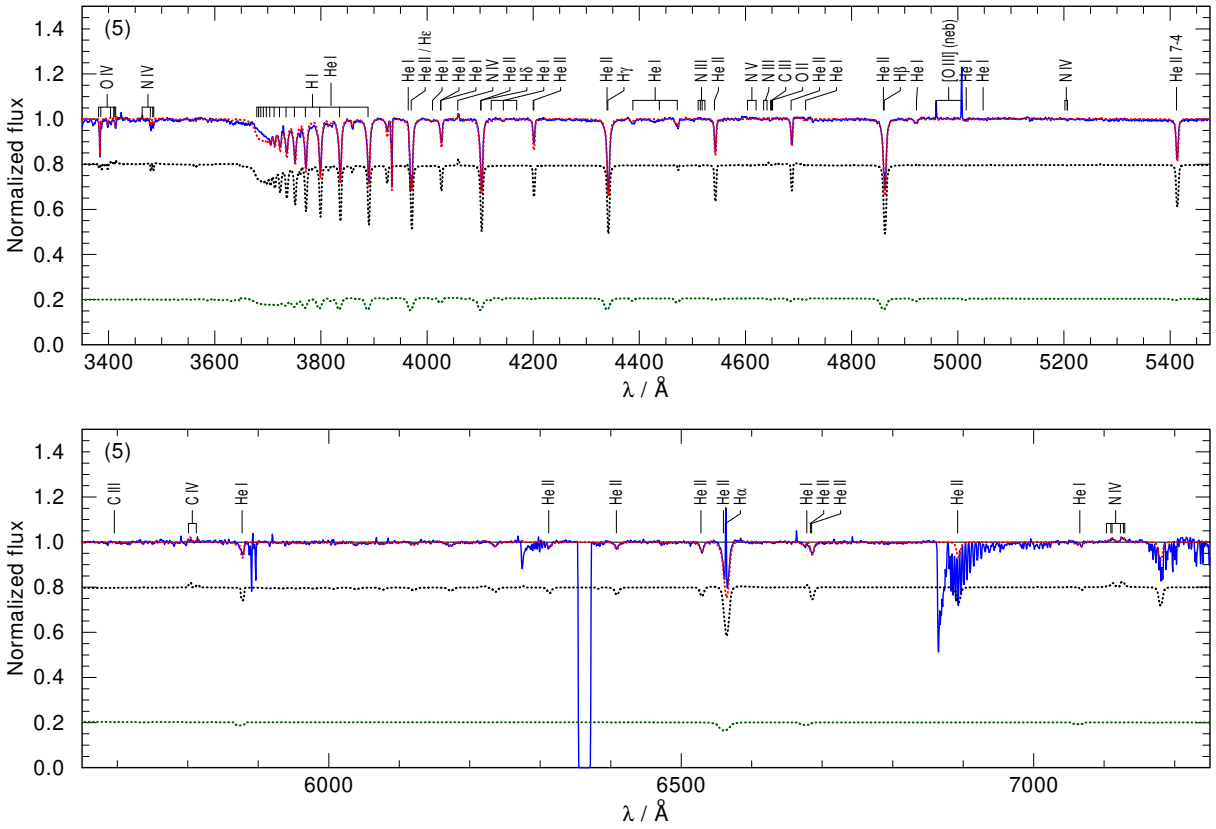

Fig. 2.4.6. Same as Fig. 2.4.5, but now the normalized optical X-SHOOTER spectra (ID 5 in Table 2.2.1) are shown.

2.4.3. Revisiting the spectral classification

2.4.3.1. Spectral classification aided by stellar atmosphere modeling

AzV 476 was previously classified on the basis of the appearance of its optical spectrum. However, during our spectroscopic analysis, we found that most of the classification lines are blended by the companion. Hence, including the additional information from our spectroscopic models and the available UV data allows us to reconsider the spectral classification.

We used the Marxist Ghost Buster (MGB) spectral classification code (Maíz Apellániz et al. 2012; Maíz Apellániz 2019). MGB compares observed spectra with the criteria of Walborn et al. (2000, 2002, 2014) and Sota et al. (2011, 2014) while allowing the presence of two components by iteratively adjusting the spectral types, light ratio, RVs, and rotational indices. This approach poses two problems. First, the low metallicity of the SMC leads to weaker nitrogen lines compared to stars with similar type in the MW and LMC. Second, only the X-SHOOTER spectrum is covering the whole wavelength range of 3900 Å – 5100 Å which is needed for a spectral classification. In addition we consider those UVES spectra with the highest RV shifts in order to better separate the individual binary components.

Therefore, we are forced to use the X-SHOOTER spectrum first and then consider the UVES spectra with the highest RV shifts that cover the range from 3300 to 4500Å.

The MGB code provides the spectral type O4 IV((f)) for the primary. The main reason for the slightly later subtype assigned to the primary is its contribution to the He I λ4471 line. The suffix "((f))" is assigned because of the barely detectable N III $\lambda\lambda$4634, 4641 lines (see Fig. A.2.1). Regarding the secondary, the absence of the He II λ4200 line suggests the latest O subtype, O9.5: Vn. The suffix "n" refers to the high rotational broadening of the lines of the secondary.

The MGB classification code only considers the optical range of the spectrum. If one inspects the UV spectrum, which mostly originates from the primary, and compares it to the N V and C IV UV wind-profile templates with those presented in Walborn et al. (2000), one might prefer a luminosity class "III" for the primary. The difference in the optical spectral appearance is explainable by the high L/M ratio which leads to very strong mass loss and thus to exceptionally strong wind lines in the UV. In light of these circumstances and the unusual chemical composition, we add the suffix "p" for this peculiar object. In the end, we therefore classify the system as O4 IV-III((f))p + O9.5: Vn.

Table 2.4.1. Summary of the stellar parameters of both stellar components obtained from the different methods.

	Spectroscopic analysis		Orbital analysis[a]		Single star evolution[b]		Binary evolution[c]	
	star 1	star 2	star 1	star 2	star 1	star 2	star 1	star 2
$T_{\rm eff}$ [kK]	42^{+3}_{-3}	32^{+4}_{-4}	42 (fix)	32 (fix)	$40.1^{+1.7}_{-1.5}$	$32.5^{+1.8}_{-1.8}$	42.0	31.6
$\log\, g$ [cm s^{-2}]	$3.7^{+0.2}_{-0.1}$	$4.0^{+0.2}_{-0.2}$	$3.69^{+0.06}_{-0.06}$	$4.00^{+0.07}_{-0.07}$	$3.80^{+0.09}_{-0.08}$	$4.03^{+0.10}_{-0.11}$	3.56	4.01
$\log\, L$ [$L_\odot$]	$5.65^{+0.2}_{-0.2}$	$4.75^{+0.2}_{-0.2}$	$5.51^{+0.13}_{-0.13}$	$4.67^{+0.22}_{-0.22}$	$5.60^{+0.18}_{-0.13}$	$4.67^{+0.11}_{-0.14}$	5.55	4.66
R [$R_\odot$]	$12.6^{+1.0}_{-1.0}$	$7.8^{+2.0}_{-2.0}$	$10.7^{+0.4}_{-0.4}$	$7.0^{+0.4}_{-0.4}$	$12.94^{+2.2}_{-1.7}$	$6.57^{+0.8}_{-0.9}$	11.3	7.2
M [$M_\odot$]	29^{+17}_{-11}	22^{+13}_{-8}	$20.2^{+2.0}_{-2.0}$	$18.0^{+1.8}_{-1.8}$	$39.2^{+8.8}_{-5.8}$	$17.4^{+1.4}_{-1.6}$	17.8	18.2
$M_{\rm ini}$ [$M_\odot$]	—	—	—	—	$40.2^{+9.1}_{-6.4}$	$17.4^{+1.4}_{-1.6}$	33.0	17.5
$\log \dot{M}$ [$M_\odot$ yr^{-1}]	$-6.1^{+0.2}_{-0.2}$	$-8.8^{+0.5}_{-0.5}$	—	—	$-6.1^{+0.3}_{-0.3}$	$-7.9^{+0.3}_{-0.3}$	$-6.4^{(f)}$	$-6.46^{(f)}$
v_∞ [km s^{-1}]	2500^{+200}_{-200}	2500	—	—	—	—	—	—
$v \sin i$ [km s^{-1}]	$140^{(d)}$	$425^{(d)}$	—	—	150^{+26}_{-28}	410^{+60}_{-40}	96	575
$X_{\rm H}$ (by mass)	0.73	0.73	—	—	$0.74^{+0.0}_{-0.1}$	$0.74^{+0.0}_{-0.1}$	0.47	0.74
$X_{\rm C}/10^{-5}$ (by mass)	2^{+2}_{-1}	$21^{(e)}$	—	—	27^{+2}_{-5}	7^{+5}_{-3}	3	20
$X_{\rm N}/10^{-5}$ (by mass)	45^{+5}_{-10}	$3^{(e)}$	—	—	6^{+14}_{-6}	61^{+40}_{-30}	91	7
$X_{\rm O}/10^{-5}$ (by mass)	80^{+10}_{-20}	$110^{(e)}$	—	—	91^{+4}_{-14}	70^{+7}_{-37}	35	110
$\log\, Q_{\rm H}$ [s^{-1}]	49.43	47.88	—	—	—	—	$49.34^{(g)}$	$47.72^{(g)}$
$\log\, Q_{\rm He\,I}$ [s^{-1}]	48.72	45.83	—	—	—	—	$48.62^{(g)}$	$45.76^{(g)}$
$\log\, Q_{\rm He\,II}$ [s^{-1}]	40.80	41.38	—	—	—	—	$43.63^{(g)}$	$35.75^{(g)}$
age [Myr]	—	—	—	—	$2.8^{+0.5}_{-0.4}$	$5.9^{+1.5}_{-1.5}$	6.0	6.0

[a] Results from the PHOEBE code, see Sect. 2.3.1.3. [b] Results from the BONNSAI tool, see Sect. 2.5.1. [c] Models calculated with MESA, see Sect. 2.5.2. No uncertainties are given, as we did no in-depth analysis. [d] Obtained with the `iacob` broad tool. [e] Initial CNO abundances scaled to SMC metallicity; for more details see Sect. 2.4.2. [f] According to the mass-loss recipe implemented in our evolutionary models. [g] Values taken from the spectroscopic model that is calculated with the parameters of the binary evolutionary models.

Following the work of Weidner & Vink (2010), an isolated star with spectral type O4 III is expected to have a stellar mass of about $M_{\rm exp,\,1} = 49^{+7}_{-6}\,M_\odot$, which is more than twice as high as that which we derive using two different methods (Sects. 2.3 and 2.4.1). For the O9.5: V secondary, the mass expected from the spectral type would be $M_{\rm exp,\,2} = 16^{+7}_{-3}\,M_\odot$, which agrees within uncertainties with the findings of the orbital and spectroscopic analysis.

2.5. Stellar evolution modeling

From orbital and spectroscopic analysis, we find that the mass ratio is close to unity, although the two binary components have distinctly different luminosities, effective temperatures, and rotation rates: the secondary is a fast rotator while the rotation of the primary is only moderate. These facts strongly indicate that the system has already undergone mass transfer.

2.5.1. Single-star models

As a first approach we investigate whether the stellar parameters of the individual components can be reproduced by single-star evolutionary models. For this purpose, we employ the Bayesian statistic tool "The BONN Stellar Astrophysics Interface" (BONNSAI[4]), (Schneider et al. 2014) in combination with the BONN-SMC tracks (Brott et al. 2011). To find a suitable model, we request the tool to match the current luminosity, effective temperature, rotation rate, and orbital mass of the two stars. Indeed, we find that the fast-rotating secondary can be partially explained by a single-star track. With respect to the primary, the BONNSAI tool cannot find any track that would explain its current low mass. Only when ignoring the mass constraint are we able to find a suitable track that reproduces the remaining stellar parameters. In that case, the predicted ages of the primary and secondary differ

[4] www.astro.uni-bonn.de/stars/bonnsai

by a factor of two. This finding confirms our suggestion that the system has already undergone mass transfer. The best-fitting stellar parameters obtained with the BONNSAI tool —applicable only for single stars— are listed in Table 2.4.1.

2.5.2. Binary evolutionary models

The binary models are calculated with MESA v. 10398. To mimic the BONN-SMC tracks we adjusted MESA in a similar way to that described by Marchant (2016). We follow most of the physical assumptions from the BONN-SMC models (e.g., overshooting, thermohaline mixing, etc.) and adopt them from Marchant (2016) with two exceptions. In our models, we use a more efficient semi-convection with $\alpha_{\rm sc} = 10$ and calculate the mass transfer according to the "Kolb" scheme (Kolb & Ritter 1990), as it allows us to include the eccentricity enhancement mechanism meaning that the evolution of the eccentricity can be modeled properly.

We want to emphasize that our goal is to check whether binary evolutionary models can explain the stellar parameters of AzV 476 and especially its masses. Therefore, we only explore a narrow parameter space and compute a small set of models with initial primary masses in the range of $M_{\rm ini,\,1} = (25-38)\,M_\odot$ and secondary masses $M_{\rm ini,\,2} = (10-25)\,M_\odot$, orbital periods in the range of $P_{\rm ini} = 8\,{\rm d} - 25\,{\rm d}$ and initial eccentricities $e_{\rm ini} = 0.0-0.4$. The initial parameters are adjusted such that at some later stage the model binary has properties similar to AzV 476. We assume that the stellar components initially rotate with $v_{\rm rot} = 0.1\,v_{\rm crit} \approx 65\,{\rm km\,s^{-1}}$. These values are chosen arbitrarily but as we are dealing with a close binary, the tidal forces nevertheless lead to a tidal synchronization. Further important assumptions are as follows:

Our models include the effect of inflation, which appears inside a stellar envelope when the local Eddington limit is reached and exceeded, leading to a convective region and a density inversion (Sanyal et al. 2015).

The stellar wind prescription is inspired by the work of Brott et al. (2011). The winds of hot H-rich stars are described according to the Vink et al. (2001) recipe. For stars with effective temperatures below the bi-stability jump, where mass-loss rates abruptly increase (see Vink et al. 2001), we use the maximum $\dot{M}$ from either Vink et al. (2001) or Nieuwenhuijzen & de Jager (1990). WR mass-loss rates are according to Shenar et al. (2019) but are assumed to scale with metallicity as $\dot{M} \propto Z^{1.2}$ as recommended by Hainich et al. (2017). In the transition phase from a hot H-rich star ($X_{\rm H} \geq 0.7$) to the WR stage ($X_{\rm H} \leq 0.4$), the mass-loss rate is interpolated between the prescriptions of Vink et al. (2001) and Shenar et al. (2019).

Rotational mixing is modeled as a diffusive process including the effects of dynamical and secular shear instabilities, the Goldreich-Schubert-Fricke instability, and Eddington-Sweet circulations (Heger et al. 2000). In addition to the angular momentum transport by rotation, the transport via magnetic fields from the Tayler-Spruit dynamo (Spruit 2002) is also included.

Convection is described according to the Ledoux criterion and the mixing length theory (Böhm-Vitense 1958) with a mixing length parameter of $\alpha_{\rm mlt} = l/H_{\rm P} = 1.5$. For hydrogen burning cores, a steep overshooting is used such that the convective core is extended by $0.335 H_{\rm P}$ (Brott et al. 2011) where $H_{\rm P}$ is the pressure scale height at the boundary of the convective core. Thermohaline mixing is included with an efficiency parameter of $\alpha_{\rm th} = 1$ (Kippenhahn et al. 1980), as well as semiconvection with an efficiency parameter of $\alpha_{\rm sc} = 10$ (Langer et al. 1983).

Mass transfer in a binary is modeled using the "Kolb" scheme (Kolb & Ritter 1990). This allows us to use the Soker eccentricity enhancement (Soker 2000), which assumes phase-dependent mass loss and calculates the change in eccentricity due to the mass that is lost from the system, and the mass that is accreted by the companion. Tidal circularisation is taken into account throughout the entire evolution of the system.

The remaining mass collapses into a compact object —represented by a point mass— when helium is depleted in the stellar core. This simplification avoids numerical problems in the latest burning stages and the unknowns that come with a supernova explosion and a possible kick.

As the luminosities obtained from the spectroscopic and orbital analysis differ to some extent, we put additional focus on reproducing the orbital masses, which are our most reliable estimate. The best agreement with the empirically derived parameters is found for a system with initial masses $M_{\rm ini,\,1} = 33\,M_\odot$ and $M_{\rm ini,\,2} = 17.5\,M_\odot$, initial orbital period $P_{\rm ini} = 12.4\,{\rm d}$, and initial eccentricity $e_{\rm ini} = 0.14$. The model closest to the current stellar parameters gives similar masses for the primary and secondary: $M_{\rm evol,\,1} = 17.8\,M_\odot$ and $M_{\rm evol,\,2} = 18.2\,M_\odot$,. The remaining stellar parameters of our favorite models are listed in Table 2.4.1.

The Hertzsprung-Russell diagram (HRD) displaying the best fitting stellar evolutionary tracks for both binary components is illustrated in Fig. 2.5.1. The binary evolution model is able to reproduce almost all empirically derived stellar parameters including the current orbital period ($P_{\rm model} = 9.3\,{\rm d}$) and the eccentricity of the system ($e_{\rm model} = 0.25$). However, the evolutionary models over-predict the rotation rate of the secondary and the surface abundances of the primary; see Table 2.4.1. We calculated PoWR atmosphere models with the best fitting parameters obtained with our MESA models. The synthetic spectra are shown in Fig. A.2.4.

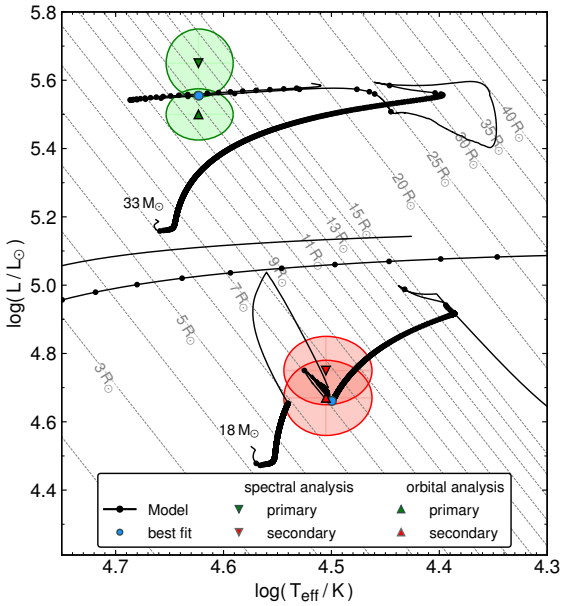

Fig. 2.5.1. HRD showing the positions of each binary component according to the spectroscopic and orbital analysis, and the best fitting binary evolutionary tracks. The results of the spectroscopic analysis are shown as triangles and the orbital analysis as upside-down triangles. The positions of the primary and secondary are marked in green and red, respectively. The shaded areas indicate the respective error-ellipses. Evolutionary tracks (solid lines) of both binary components are according to the best fitting binary model calculated with MESA (see Sect. 2.5.2). The tracks are labeled by their initial masses. The black dots on the tracks correspond to equidistant time-steps of 0.1 Myr to emphasize the most probable observable phases. The light blue dots mark the best-fitting model.

A more fine-tuned model would likely solve some of these problems. For example, we did not include the initial rotation as a free parameter. This might solve the faster rotation of the primary; however, the secondary would still be expected to be rotating too fast as it spins up to criticality during mass transfer. According to our favorite evolutionary model, the primary in AzV 476 is currently evolving towards the helium zero age MS (ZAMS) and will possibly spend the rest of its life as a hot helium or WR-type star.

2.6. Discussion

2.6.1. Comparison of the orbital, spectroscopic, and evolutionary mass estimates

The orbital masses and the masses predicted by the binary evolutionary models agree well within their error margins and deviate only by 10%. On the other hand, the spectroscopic mass and luminosity of both components appear to be higher by a factor of 1.5 compared to the orbital solutions. The question therefore arises as to whether the discrepancy between the orbital and spectroscopic solutions is significant.

2.6.1.1. Orbital versus spectroscopic mass

The simplest way to resolve this discrepancy is to assume that the distance to the system is lower than the canonical SMC distance of ($d = 55$ kpc). As the luminosity depends on the assumed distance as $L \propto d^{-2}$, the radius ($R \propto \sqrt{L} \propto d^{-1}$) and the spectroscopic mass also depend on distance ($M_{\rm spec} \propto R^2 \propto L \propto d^{-2}$). The SMC galaxy is extended, and the distances to its various structural parts are not well established. Tatton et al. (2021) suggest that young structures, such as the NGC 456 cluster, are not well represented by the intermediate age stellar populations, which are usually used for distance estimates. Instead, young clusters might be located in front of these latter. This is in agreement with the argumentation by Hammer et al. (2015), who showed that the interactions between the LMC and SMC could lead to multiple tidal and ram-pressure stripped structures, which spatially separate young star-forming regions from older stellar populations.

In order to bring the spectroscopic and orbital parameters of AzV 476 into accordance, the system needs to be shifted to a distance of 49 kpc. The resulting spectroscopic masses are then $M_{\mathrm{shift,\,1}} \approx 23\,M_{\odot}$ and $M_{\mathrm{shift,\,2}} \approx 18\,M_{\odot}$. However, $d = 49$ kpc would imply that our target is located at the same distance as the LMC.

The LMC has higher metallcity ($Z_{\mathrm{LMC}} = 1/2\,Z_{\odot}$) than the SMC ($Z_{\mathrm{SMC}} = 1/7\,Z_{\odot}$), and therefore we speculate that stars formed in the interaction regions may have higher metallicity than the SMC. To test this, we increased the metallicity content of our spectroscopic models to the LMC metallicity while keeping the remaining stellar parameters unchanged. We find that the lines in the iron forest, especially in the far-UV, are too deep compared to the observations. Therefore, it cannot be confirmed that our target has LMC metallicity, but at the same time this does not provide additional constraints on its distance.

Another option we need to consider is the possibility of a third light contribution. AzV 476 is located in a very crowded region. Therefore, it is possible that the observed light is contaminated by a nearby object and hence the true luminosity (and mass) is lower. We inspected the HST acquisition image of our target and find no other nearby UV-bright stars. Alternatively our target could be a multiple system rather than a binary. If there were a third component, it would need to be of similar luminosity to the secondary in order to have an impact on our analysis. However, we do not see any indications of a third component in our spectra.

A third option is that the surface gravities determined from the spectral analysis are overestimated. The accuracy of the spectroscopic mass strongly depends on surface gravity, $\log g$, which is mainly determined from fitting the pressure-broadened line wings. Such estimates suffer from limited S/N ratio in the spectra. In cases where the Balmer lines include contributions from both components, further uncertainties are induced. As explained in Sect. 2.4.2 and shown in Fig. 2.4.2, the He II lines help to improve the estimates, but still do not allow us to pin point $\log g$ for each component separately. This leaves room for various combinations of $\log g$ able to reproduce the Balmer lines and is reflected in the large uncertainties of the spectroscopic masses.

2.6.1.2. Orbital versus evolutionary mass

The evolutionary modeling yields a slightly lower mass for the primary than the spectroscopic and orbital analyses. As can be seen in Table 2.4.1, the evolutionary mass is $2\,M_{\odot}$ lower than the orbital one.

For a given initial mass, the main parameter defining how much mass is lost during mass transfer by the primary is the initial binary orbital period. As a rule of thumb, the longer the initial orbital period, the less mass is removed from the donor star (Marchant 2016). However, several effects (e.g., eccentricity) influence the response of the orbit to mass transfer. For instance, an eccentric orbit leads to phase-dependent mass transfer, which potentially increases the eccentricity and widens the orbit. Thus, the donor can expand more, and less mass is removed via Roche-lobe overflow (Soker 2000; Vos et al. 2015).

The amount of mass lost during mass transfer is also reduced when the radial expansion of the star is minimized such that the star can stay underneath the Roche lobe. The radial expansion is affected by the mixing processes. For instance, a star with more efficient semi-convective mixing is expected to be more compact (e.g., Klencki et al. 2020; Gilkis et al. 2021). We computed a binary evolutionary model with a less efficient semi-convection of $\alpha_{\mathrm{sc}} = 1$ and find that the post-mass-transfer (after detachment) mass of the primary is lowered by $1\,M_{\odot}$. This is only one example and there are a handful of other processes that impact the mixing efficiency, energy transport, and the expansion of the envelope.

One more process that affects the radial expansion is the mass-loss rate which is described by the adopted mass-loss recipe (see Sect. 2.5). Over- or underestimating the mass-loss rate influences stellar evolution before, during, and after mass transfer. Interestingly, we find approximate agreement between the empirically derived mass-loss rate of the primary and the prediction of the wind recipe (see Sect. 2.6.2.1).

The evolutionary mass of a star after mass transfer is sensitive to various assumptions. Therefore, a difference of $2\,M_{\odot}$ between evolutionary and orbital mass appears to be within the range of the evolutionary model uncertainties. While a more fine-tuned binary evolutionary model is beyond the scope of this paper, our modeling confirms that the orbital masses of AzV 476 are well explained by a post-mass-transfer binary evolutionary model. Therefore, this unique system is a useful benchmark for improving the understanding of mass transfer and mixing processes in close massive binaries. We conclude that the orbital, spectroscopic, and evolutionary mass estimates agree within their uncertainties.

2.6.2. The empirical mass-loss rate

Stellar evolution depends on the mass-loss rate. Stellar evolution models rely on recipes that are only valid for a given evolutionary phase. In transition-phases one typically interpolates between corresponding mass-loss recipes

(e.g., Sect. 2.5). In the following, we compare the mass-loss rates we empirically derive from spectroscopy with other estimates as well as with the various recipes.

In this work, the mass-loss rates are primarily derived from resonance lines in the UV and the Hα line while taking into account the morphology of the He II λ1640 and He II λ4686 lines. The winds of all hot stars are clumpy (e.g., Hamann et al. 2008) which enhances the emission lines fed by recombination cascades (e.g., Hamann & Koesterke 1998a) such as the Hα line. Resonance lines in the UV are mostly formed by line scattering, a process that scales linearly with density and is thus independent from microclumping. Considering both Hα and the resonance lines allows us to constrain the clumping factor D and the mass-loss rate $\dot{M}$ consistently.

2.6.2.1. The primary

The spectroscopically derived mass-loss rate of the primary is $\log(\dot{M}/(\,M_\odot\,\mathrm{yr}^{-1})) = -6.1 \pm 0.2$. Massa et al. (2017) derive a mass-loss rate of $\log(\dot{M}/(\,M_\odot\,\mathrm{yr}^{-1})) = -5.54^{+0.12}_{-0.10}$ from the IR excess. However, the clumping effects were not included in their analysis. As the IR excess originates from free-free emission, it scales with $\sqrt{D}$. Correcting the mass-loss rate with a clumping factor of $D = 20$, as assumed in our spectroscopic models, yields $\log(\dot{M}/(\,M_\odot\,\mathrm{yr}^{-1})) = -6.19^{+0.12}_{-0.10}$, which is in agreement with the optical and UV analyses.

In the massive star evolutionary models, the terminal wind velocity is prescribed as $v_\infty/v_\mathrm{esc} = 2.6$ and the mass-loss rates of OB stars are prescribed according to the Vink et al. (2001) recipe. Using the stellar parameters obtained with spectroscopic analysis (see Table 2.4.1) and the prescribed $v_\infty = 1911\,\mathrm{km\,s^{-1}}$, the "Vink's recipe" yields $\log(\dot{M}/(\,M_\odot\,\mathrm{yr}^{-1})) = -6.1$. Alternatively, applying the actual wind velocity measured from the UV spectra, $v_\infty = 2500\,\mathrm{km\,s^{-1}}$, the theoretical prediction changes to $\log(\dot{M}/(\,M_\odot\,\mathrm{yr}^{-1})) = -6.2$, which is in agreement with our empirical result within the uncertainties.

However, the primary's current mass-loss rate adopted in our favored binary evolutionary model ($\log(\dot{M}/(\,M_\odot\,\mathrm{yr}^{-1})) = -6.4$) is lower. This is mainly caused by the interpolation between the mass-loss rate prescriptions for OB stars by Vink et al. (2001) and for WR stars by Shenar et al. (2019) which is employed when the surface hydrogen mass-fraction of the primary's evolutionary model already dropped below $X_\mathrm{H} < 0.7$. Additionally, the stellar parameters (e.g., mass and luminosity) that enter the different mass-loss recipes employed by the evolutionary code are slightly different than those obtained from our spectral analysis.

Based on dynamically consistent Monte Carlo wind models, Vink & Sander (2021) suggest an updated scaling of metallicity for their mass-loss rates. This scaling yields higher mass-loss rates of $\log(\dot{M}/(\,M_\odot\,\mathrm{yr}^{-1})) = -5.7$, or, using the measured $v_\infty = 2500\,\mathrm{km\,s^{-1}}$, $\log(\dot{M}/(\,M_\odot\,\mathrm{yr}^{-1})) = -5.9$. Correcting in a simple way the former theoretical mass-loss rate for clumping results in $\log(\dot{M}/(\,M_\odot\,\mathrm{yr}^{-1})) = -6.4$, which is somewhat lower than our empirical measurement.

The spectroscopic measurements of mass-loss rates of O-dwarfs in the SMC deliver useful empiric prescriptions (e.g., Bouret et al. 2003; Ramachandran et al. 2019). According to Ramachandran et al. (2019, see their figure 15), the mass-loss rate of the primary star in AzV 476 would be only $\log(\dot{M}/(\,M_\odot\,\mathrm{yr}^{-1})) = -7.4$, which is much lower than obtained from our analysis. We explain this discrepancy by the advanced evolutionary status: the primary has already a substantially reduced mass due to its close-binary evolution, leading to a high L/M ratio. This precludes the comparison with the recipes which use the mass–luminosity relations for single stars.

2.6.2.2. The secondary

There are no indications of wind lines of the secondary in the observed spectra. Therefore, we can only set an upper limit on the mass-loss rate $\log(\dot{M}/(\,M_\odot\,\mathrm{yr}^{-1})) \leq -8.8 \pm 0.5$. The Vink et al. (2001) recipe predicts a higher value of $\log(\dot{M}/(\,M_\odot\,\mathrm{yr}^{-1})) = -8.2$. Correcting for clumping with $D = 20$ yields $\log(\dot{M}/(\,M_\odot\,\mathrm{yr}^{-1})) = -8.8$ which is in agreement with the empirical result.

According to Vink & Sander (2021), the predicted mass-loss rate of the secondary is $\log(\dot{M}/(\,M_\odot\,\mathrm{yr}^{-1})) = -7.8$; correcting it for clumping yields $\log(\dot{M}/(\,M_\odot\,\mathrm{yr}^{-1})) = -8.4$, which is higher than the empirical upper limit. The empirical relation of Ramachandran et al. (2019, their figure 15,) suggests $\log(\dot{M}/(\,M_\odot\,\mathrm{yr}^{-1})) = -8.6 \pm 0.2$, which is somewhat higher than our result but consistent with its error margins.

As can be seen in Table 2.4.1, the mass-loss rate used in the binary evolution calculation is higher than predicted by the recipes as well as empirically measured. This is because in the MESA models, the mass-loss rate of a star rotating close to critical is enhanced compared to slowly rotating stars (Paxton et al. 2013). The synthetic spectrum calculated with the parameters obtained by the binary evolutionary models displayed in Fig. A.2.4 shows strong P Cygni profiles in the spectrum of the secondary (e.g., Si IV $\lambda\lambda$1393.8, 1402.8) that are not observed. We conclude that the mass loss of the secondary is not rotationally enhanced above the observed limit.

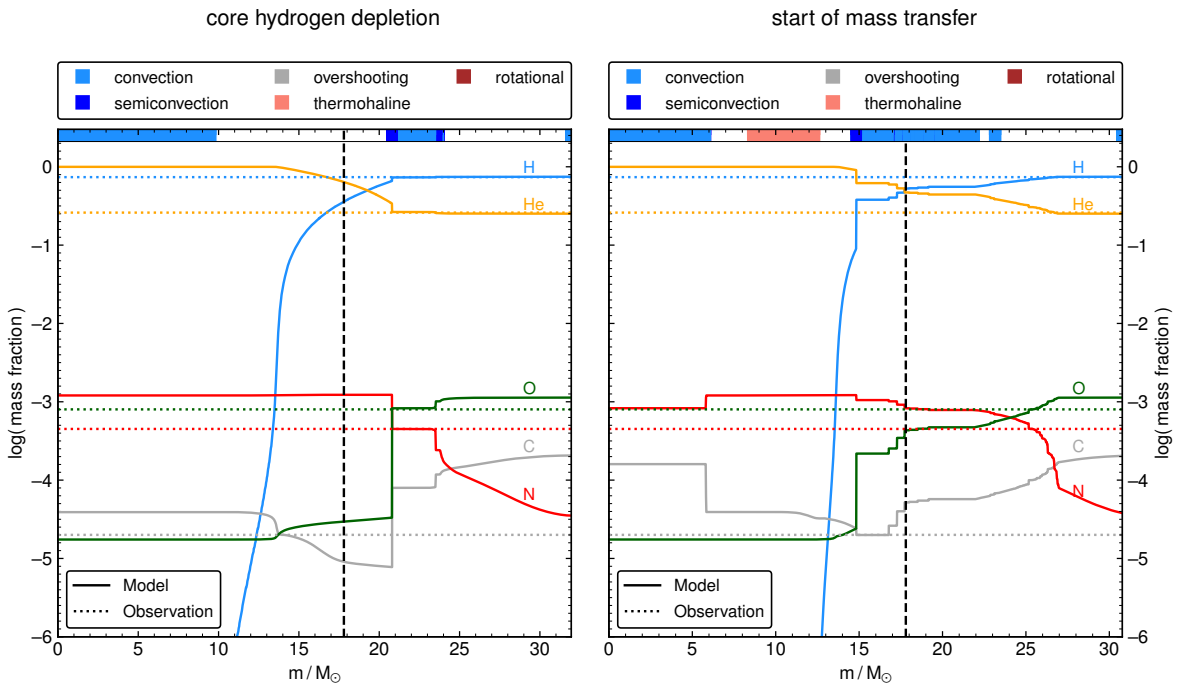

Fig. 2.6.1. Abundance profiles of the primary at different evolutionary stages as predicted by the evolutionary models. The legend at the top of each plot explains the colors indicating the dominating mixing processes. The H, He, C, N, and O abundances of the model are shown as solid lines while the observed surface CNO abundances are shown as dotted lines of the same respective color. The vertical black dotted line indicates the mass of the primary after mass transfer. *Left panel:* Primary has depleted hydrogen in the core and is at the terminal age MS. *Right panel:* Primary fills its Roche lobe and starts transferring mass.

2.6.3. Comparison of the stellar parameters as predicted by MESA evolutionary tracks versus derived spectroscopically

In this work, AzV 476 is studied using two different approaches. (1) The empiric approach is to model the observed light curves and spectra using the PHOEBE code and the stellar atmosphere model PoWR in order to derive orbital, stellar, and wind parameters. (2) The evolutionary modeling approach is to use the MESA code to compute tracks reproducing the current stellar parameters of AzV 476 components (Fig. 2.5.1) simultaneously with its orbital parameters. Below we compare the outcomes of these two approaches.

In binary evolutionary models, during the mass-transfer phase, most of the hydrogen-rich envelope is stripped off such that products of the CNO burning process are exposed at the surface. The predicted surface abundances in our favorite model correspond to an intermediate stage between the initial CNO abundances and the CNO equilibrium at metallicity $Z_{\rm SMC} = 1/7\,Z_{\odot}$. This means that most of the initial C, N, and O become N, and the CO abundances are depleted.

Indeed, the abundances derived spectroscopically are intermediate between the initial CNO abundances and the CNO equilibrium. The C and O abundances are reduced while the N abundance increased drastically. However, we find a factor of two difference between the predicted and observed N and O abundances (see Table 2.2.1). We note that the *surface* CNO abundances predicted by the MESA models are subject to various assumptions; for example, on mixing efficiencies or the mass removal by Roche-lobe overflow. Because of the scarcity of suitable photospheric absorption lines, the CNO abundances of the primary are partially derived from emission lines. Those lines are sensitive to many effects, such as the mass-loss rate, temperature, clumping, and turbulence, introducing additional uncertainties in the abundance measurement.

Furthermore, we find disagreement between the observed and predicted H mass-fraction. In evolutionary models, a significant amount of the H-rich envelope (i.e., with $X_{\rm H} > 0.7$) is removed during the mass-transfer phase, revealing the products of the established chemical gradient between the core and the envelope, leading to the depletion of surface hydrogen. However, from the spectroscopic analysis, we do not find such strong H depletion. As in the case of the CNO measurements, this indicates some deficiencies in the evolutionary models that are likely related to the mass-transfer phase and/or to the mixing.

For a better understanding, we are showing in Fig. 2.6.1 abundance profiles at two different stages. The left panel in Fig. 2.6.1 shows the abundances at core hydrogen depletion. At this stage, the star is hydrogen shell burning, which leads to the formation of an intermediate convection zone (ICZ, Langer (1987)), which ranges from the mass coordinates 21 $M_\odot$ – 24 $M_\odot$. One can see that the H, He, O, and N abundances in this region are the same as the abundances that we observe; only the predicted C abundance is higher. However, the spectroscopically derived C abundance is the least accurate one, as the observed spectra have no photospheric C absorption lines and the C IV resonance line in the UV highly depends on the mass-loss rate. At this evolutionary stage, the envelope is not well mixed, which can be seen in the step-like structure between the different mixing regions.

The right panel in Fig. 2.6.1 shows the abundances at the onset of mass transfer. Mass transfer happens on the dynamical timescale, while the mixing and burning processes take place on longer timescales. Therefore, this plot can be used to decipher the surface composition of the final model if a specific amount of mass is removed from the star. Compared to the left panel, the stellar model has had more time to mix the CNO elements through the envelope. The ICZ is now largely extended and the CNO abundance ratios have changed; for instance N is now the most abundant element in this region. We would like to emphasize that this highly depends on the assumed mixing efficiencies, as a less efficient semi-convection (e.g., $\alpha_{\rm sc} = 1$) would lead to less mixing and might preserve the step-like structure seen the left panel. Semi-convection does not only affect the mixing efficiency but also impacts the change of the stellar radius (Klencki et al. 2020), and therefore a star with more effective semi-convective mixing spends more time hydrogen shell burning before it fills the Roche lobe and initiates mass transfer. This additionally impacts the final chemical composition.

By now it should be evident that accurate prediction of the surface CNO abundances in binary evolutionary models is a nontrivial task and is beyond the scope of this paper. However, this underlines the importance of AzV 476, which can be used to get a better understanding of the different mixing efficiencies, as it reveals the abundances formed by burning stages that would normally be hidden from the observer, making them difficult to calibrate.

In order to understand how the predicted stellar parameters of the binary evolution models — including the surface abundances — compare to the observed spectrum, synthetic spectra of the primary and secondary are calculated using these parameters (see Table 2.4.1). The resulting spectrum is shown in Fig. A.2.4. When comparing the synthetic spectrum to the observed one, it is evident that the N emission lines are too strong and the helium absorption lines are too deep.

The abundances are not the only difference between the evolutionary model predictions and the observations. Evolutionary model predicts much higher rotation rates than observed. In the evolutionary model, the secondary has spun up to critical rotation, which is not observed, and also the rotation rate of the primary is somewhat slower than observed. Vanbeveren et al. (2018) and Shara et al. (2020) studied the rotation rates of O stars in WR+O star binaries at different metallicities and compared them to predictions from evolutionary models. This comparison revealed that the observed rotation rates of the O stars are lower than the predictions from the evolutionary models. These latter authors suggest that there is a process during the fast case A mass transfer that removes the angular momentum of the star; their favored explanation is an angular momentum loss induced by a magnetic field that only develops during the mass-transfer phase.

The disagreements on the chemical abundances and the rotation rates between evolutionary models and the empiric analysis suggest some unconsidered physics during the mass-transfer phase. A more fine-tuned model would likely solve some of these problems. For example, we did not include the initial rotation as a free parameter. This might solve the faster rotation of the primary; however, the secondary would still be expected to be rotating too fast as it spins up to criticality during mass transfer.

2.6.4. AzV 476 and its future evolution in the context of the most massive star population in the SMC

The binary components of AzV 476 are among the most luminous O stars in the entire SMC. Nevertheless, our analysis reveals that the mass of the O4 IV-III((f))p primary star is only $M_{\rm orb,\,1} \approx 20 M_\odot$. We estimate its initial mass to be $M_{\rm ini,\,1} \approx 33\,M_\odot$ which is significantly lower than the most massive O stars in the Galaxy and the LMC (e.g., Ramírez-Agudelo et al. 2017; Gruner et al. 2019). This system therefore further exacerbates the problem with the deficiency of very massive O stars in the SMC (Ramachandran et al. 2019; Schootemeijer et al. 2021).

In the future, the primary in AzV 476 will evolve bluewards on the HRD, but it will never be able to lose its entire H-rich envelope. As its luminosity is on the edge of the least luminous observed WR star of the SMC (Shenar et al. 2016, 2020b), it is unclear as to whether or not it will be able to develop an optically thick wind and become a WR star. Our evolutionary model predicts that the primary will have a final mass of $M_{\rm final,\,1} = 16\,M_\odot$ at

core helium exhaustion. The primary will probably collapse and form a BH (Heger et al. 2003). To our knowledge, no BH has yet been identified in the SMC.

After the primary collapse and the formation of a compact object, the system will consist of a MS star with a compact object. The MESA model predicts that the secondary will have $T_{\rm eff} = 28$ kK and $\log(L/L_\odot) = 4.85$, at the halfway point of its remaining MS lifetime. We calculated a spectroscopic model of the secondary in this evolutionary stage and find that the secondary would be classified as a B0 V star. Its critical rotation makes the system a likely progenitor of a high-mass X-ray binary (HMXB) with a Be donor star. After the stellar model evolves beyond the MS, it undergoes a mass-transfer phase, offering an additional opportunity to show up as a HMXB. After large fractions of the secondary's envelope are stripped off, it will remain as a helium star with some hydrogen left on the surface with a luminosity around $\log(L/L_\odot) \approx 4.9$. Using the recent estimates from Sander & Vink (2020) for massive hydrogen-free stars, the L/M-ratio will be significantly too low to yield a sufficiently strong stellar wind for it to become optically thick at this metallicity (even when accounting for additional hydrogen and larger radii). Thus, our secondary star will most likely never appear as a WR star. With a final mass of $M_{\rm final,\,2} = 7\,M_\odot$ at core helium depletion, the secondary is expected to explode as a supernova leaving a NS. With a final orbital period of about $\approx$ 100 d, this system is not expected to merge within a Hubble time. The impact of a supernova kick is neglected in our binary models; nevertheless, in principle, it could change the final orbital period of the system drastically.

2.7. Summary and conclusions

In this work we study the earliest known O-type eclipsing binary in the SMC, AzV 476. We derived the masses of its companions using a spectroscopic analysis and by modeling its light- and RV curves. We compare the results with binary evolutionary models.

We conducted a quantitative analysis of the multi-phase spectra in the optical and UV obtained by the ESO VLT and the *HST* and supplemented by the *FUSE* spectroscopy in the far-UV. To this end we used the non-LTE stellar atmosphere model code PoWR. The spectra of both components were disentangled, allowing us to determine their masses, stellar, and wind parameters. Independently, we used the PHOEBE code to derive the stellar and the orbital parameters from the light curve in the I-band as well as RV curves. We employed the MESA code to compute detailed binary evolutionary models that are able to reproduce the observed stellar parameters in significant detail (see Table 2.4.1 and Fig. 2.5.1).

Our conclusions can be summarized as follows:

(1) The eclipsing binary AzV 476 harbors one of the most luminous O stars in the SMC. It consists of an O4 IV-III((f))p type primary and an O9.5: Vn type secondary. Single stars with similar spectral types typically have masses of $M_{\rm exp,\,1} = 49 M_\odot$ and $M_{\rm exp,\,2} = 16 M_\odot$.

(2) By analyzing the light curve and the RV curve consistently, we derive orbital masses of $M_{\rm orb,\,1} = 20 M_\odot$ and $M_{\rm orb,\,2} = 18 M_\odot$ for the binary components. We find that the primary has less than half of the mass that is expected from its spectral type. The modest mass of one of the most luminous stars in the SMC highlights the conspicuous deficiency of very massive O-type stars in this metal-poor galaxy.

(3) The spectroscopic masses agree within the uncertainties with the more reliable orbital masses, and they confirm a mass ratio of close to unity. The observed spectra reveal that the surface N abundance of the primary is enhanced while C and O abundances are reduced. These two aspects suggest a prior mass-transfer phase.

(4) The spectroscopic analysis uncovers that the mass-loss rate of the primary with $\log(\dot{M}/(\,M_\odot\,{\rm yr}^{-1})) = -6.1$ is ten times stronger compared to recent empirical prescriptions for single O stars in the SMC. Likely, this is due to its high L/M ratio. Our empirical mass-loss rate is a factor of two higher compared to the one used in the evolutionary models. While for our primary the result as such is in line with standard theoretical predictions, this underlines that the present treatment of wind mass loss in stellar evolution models needs to be improved to properly account for the products of binary evolution.

(5) The current moderate mass of the primary can only be explained by binary evolutionary models. According to our favorite binary model, the initial mass of the primary was $M_{\rm ini,\,1} = 33\,M_\odot$, while the secondary formed with $M_{\rm ini,\,2} = 18\,M_\odot$. The system is ~ 6 Myr old.

(6) The binary evolutionary model confirms that this binary has undergone case B mass transfer and is now in a detached phase. The binary evolutionary model reveals that the primary must be core helium burning and that the observed CNO abundances correspond to those of the hydrogen shell burning layers.

(7) According to our binary evolution model, the primary will become a helium star (or maybe a WR star) with a portion of the hydrogen remaining in the envelope ($X_{\rm H} < 50\%$) and finally collapse to a BH or NS. If the binary system stays bound after core-collapse, it might show up as a HMXB with a rapidly rotating Be-type donor. After core hydrogen depletion, the secondary is expected to expand and transfer mass onto the compact object, stripping off most of its hydrogen-rich envelope. The secondary will spend most of its late evolutionary phases in the blue part of the HRD as a helium star with a small fraction of hydrogen left in the envelope. However, due to its low L/M ratio, it will never be able to display a WR-like spectrum. Finally, the secondary will collapse, and there is a small chance it will form a binary of compact objects that could potentially merge within a Hubble time.

The three different methods that we used to derive the stellar masses of the binary components show that the different mass estimates agree within their respective uncertainties (e.g., Table 2.4.1 and Fig. 2.5.1). Nonetheless, the different methods yield somewhat different results. We point out several difficulties that come along with the different methods applied, for instance when measuring surface gravity (see Fig. 2.4.2). Finally, we conclude that the earliest type eclipsing binary in the SMC, AzV 476, provides a unique laboratory for studying massive binaries at low metallicity.

Acknowledgments: We dedicate this publication to the late Dr. Rodolfo H. Barba, whose passing is a tragic loss to the astrophysics community. As the original referee of this paper, he provided an outstandingly detailed and substantial report, which was extremely helpful and led to significant improvements of this work. Dr. Barba also provided us with the extracted TESS light curve of AzV 476 which resulted in the update in the orbital period. The authors thank Dr. Alex Fullerton for useful discussion and advise related to the FUSE spectroscopy and Soetkin Janssens for very helpful advises regarding the PHOEBE code. We gratefully thank the staff of the FUSE, HST, ESO telescopes for making the useful spectroscopic data publicly available. The results presented in this paper are based on observations obtained with the NASA/ESA Hubble Space Telescope, retrieved from the Mikulski Archive for Space Telescopes (MAST) at the Space Telescope Science Institute (STScI). STScI is operated by the Association of Universities for Research in Astronomy, Inc. under NASA contract NAS 5-26555. Furthermore, its conclusions are based on observations collected at the European Southern Observatory (ESO) under the program 098.A-0049. The authors thank Andrea Mehner for preparing the OBs of the XSHOOTU project and the people on the management committee of XSHOOTU. This work has made use of data from the European Space Agency (ESA) mission *Gaia* (https://www.cosmos.esa.int/gaia), processed by the *Gaia* Data Processing and Analysis Consortium (DPAC, https://www.cosmos.esa.int/web/gaia/dpac/consortium). Funding for the DPAC has been provided by national institutions, in particular the institutions participating in the *Gaia* Multilateral Agreement. DP acknowledges financial support by the Deutsches Zentrum für Luft und Raumfahrt (DLR) grant FKZ 50 OR 2005. AACS is Öpik Research Fellow at Armagh Observatory & Planetarium. AACS and VR acknowledge support by the Deutsche Forschungsgemeinschaft (DFG - German Research Foundation) in the form of an Emmy Noether Research Group (grant number SA4064/1-1, PI Sander). JMA acknowledges support from the Spanish Government Ministerio de Ciencia through grant PGC2018-095 049-B-C22.

Chapter 3

Manuscript II: A low-metallicity massive contact binary undergoing slow Case A mass transfer: A detailed spectroscopic and orbital analysis of SSN 7 in NGC 346 in the SMC

M. J. Rickard & **D. Pauli**

Astronomy & Astrophysics, 2023, Volume: 674, ID: A56, 19 pp.

Abstract

Most massive stars are believed to be born in close binary systems where they can exchange mass, which impacts the evolution of both binary components. Their evolution is of great interest in the search for the progenitors of gravitational waves. However, there are unknowns in the physics of mass transfer as observational examples are rare, especially at low metallicity. Nearby low-metallicity environments are particularly interesting hunting grounds for interacting systems as they act as the closest proxy for the early universe where we can resolve individual stars. Using multi-epoch spectroscopic data, we complete a consistent spectral and orbital analysis of the early-type massive binary SSN 7 hosting a ON3 If*+O5.5 V((f)) star. Using these detailed results, we constrain an evolutionary scenario that can help us to understand binary evolution in low metallicity. We were able to derive reliable radial velocities of the two components from the multi-epoch data, which were used to constrain the orbital parameters. The spectroscopic data covers the UV, optical, and near-IR, allowing a consistent analysis with the stellar atmosphere code, PoWR. Given the stellar and orbital parameters, we interpreted the results using binary evolutionary models. The two stars in the system have comparable luminosities of $\log(L_1/L_\odot) = 5.75$ and $\log(L_2/L_\odot) = 5.78$ for the primary and secondary, respectively, but have different temperatures ($T_1 = 43.6$ kK and $T_2 = 38.7$ kK). The primary ($32 M_\odot$) is less massive than the secondary ($55\,M_\odot$), suggesting mass exchange. The mass estimates are confirmed by the orbital analysis. The revisited orbital period is 3 d. Our evolutionary models also predict mass exchange. Currently, the system is a contact binary undergoing a slow Case A phase, making it the most massive Algol-like system yet discovered. Following the initial mass function, massive stars are rare, and to find them in an Algol-like configuration is even more unlikely. To date, no comparable system to SSN 7 has been found, making it a unique object to study the efficiency of mass transfer in massive star binaries. This example increases our understanding of massive star binary evolution and the formation of gravitational wave progenitors.

3.1. Introduction

Massive stars ($M \gtrsim 8 M_\odot$) have a pivotal role in the evolution of Galaxies. They influence their environments throughout their entire evolution via multiple feedback mechanisms. Core hydrogen-burning massive stars are hot, leading to ionisation feedback (Hollenbach & Tielens 1999; Matzner 2002) and forming spectacular H II regions. Their high ultraviolet (UV) luminosity drives powerful stellar winds, depositing mechanical feedback and heavy elements into the interstellar medium (Rogers & Pittard 2013). When a massive star evolves, it expands and becomes a red supergiant (RSG) and cools down. These stars still have strong winds, powered by radiation pressure on dust grains. Most massive stars are believed to end their lives with a supernova explosion that rapidly deposits substantial amounts of energy in the surrounding medium (Rogers & Pittard 2013). During these events, neutron stars (NSs, Baym et al. 2018; Vidaña 2018) or black holes (BHs, Orosz et al. 2011; Miller-Jones et al. 2021) are formed. All these feedback mechanisms make massive stars, which are the drivers of the chemical evolution of the interstellar medium (Burbidge et al. 1957; Pignatari et al. 2010; Thielemann et al. 2011; Kasen et al. 2017; Kajino et al. 2019) and the arbitrators of stellar formation; massive stars can initiate or abort star formation (Mac Low et al. 2005).

Massive stars preferentially form in multiple systems (Sana et al. 2012, 2013, 2014; Moe & Di Stefano 2017). The evolution of stars in binary systems differs from single star evolution as the two components can interact and exchange mass, for instance when one star in the binary (i.e. the more massive one) expands and fills its Roche lobe (Pols 1994; Vanbeveren et al. 1998; Nelson & Eggleton 2001; Smith 2014). This mass can then, depending on other factors such as rotation, accrete onto the companion star. Due to the fate of massive stars as either NSs or BHs, close massive star binaries are the progenitors of gravitational wave observations (Abbott et al. 2016, 2019). However, the final mass of a star dictates its fate (Heger et al. 2003), and in a binary system the final mass depends on the previous evolution and interaction (Shenar et al. 2020b; Massey et al. 2021; Pauli et al. 2022a).

The duration of mass transfer strongly depends on the evolutionary stage of the star (Paczyński 1967; Vanbeveren & Conti 1980; Wellstein & Langer 1999). If the expanding star is still core H-burning, it first drops out of nuclear equilibrium, making the first phase of mass transfer rapid as it takes place on the thermal timescale (fast Case A). As soon as the star regains nuclear equilibrium, it continues to expand on the nuclear timescale, overflowing its Roche lobe and transferring mass to the companion star (slow Case A). If the mass donor during the slow Case A mass transfer is less massive than the mass gainer, the systems are called Algol-like system (named for β Per, Paczyński 1971; Batten 1989; Li et al. 2022). Alternatively, stars that have finished core H-burning expand on the thermal timescale, filling their Roche lobe quickly, and lose a large fraction of their envelope (Case B). As most of the mass transfer events are on short timescales, it is practically impossible to catch a system during the fast Case A or Case B mass transfer phase. As slow Case A mass transfer occurs on the nuclear timescale, it is possible to find observational counterparts.

Metallicity (Z) has many effects on stellar evolution. For instance, stars are more compact and hotter, and line-driven winds get weaker for lower metallicity stars (Mokiem et al. 2007a). Low-Z environments are of particular interest when looking to understand the origin of gravitational waves as the observed mergers take place in high-redshift galaxies. However, it is only possible to study low-Z stars in nearby irregular dwarf galaxies, such as the Small Magellanic Cloud (SMC, $Z_{\rm SMC} = 1/7\, Z_\odot$) as these stars can be resolved. To date, there are few detailed studies on massive stars in pre- and post-interaction binaries in the SMC (de Mink et al. 2007; Pauli et al. 2022b).

In this paper we remedy this by studying in detail one of the most massive binaries in the low-Z SMC galaxy, namely SSN 7 (Sabbi et al. 2007, also known as MPG 435; Massey et al. 1989, or NMC 26; Niemela et al. 1986). Our target is located within the core of the young cluster NGC 346 (Dufton et al. 2019), which contains a large population of O stars (Niemela et al. 1986; Massey et al. 1989; Rickard et al. 2022). The cluster is nearby ($d = 61$ kpc, Hilditch et al. 2005) and has been studied several times with different instruments. Previous studies have categorised SSN 7 as a spectroscopic binary with two moving components (SB2 Dufton et al. 2019), but it has never been analysed consistently with a stellar atmosphere code.

The archival data, including spectra that cover the full range of the electromagnetic spectrum as well as photometric observations, are detailed in Section 3.2. In Section 3.3 we explain how the spectroscopic data is used to obtain radial velocity (RV) shifts, used to conduct an orbital analysis. Furthermore, this data is used in Section 3.4 to make a consistent spectroscopic analysis, yielding stellar and wind parameters. The empirically derived stellar and orbital parameters are put into an evolutionary context in Section 3.5 and its implications are discussed in Section 3.6.

3.2. Observations

NGC 346 SSN 7 has been observed numerous times across almost the entirety of the electromagnetic spectrum, ranging from the far-ultraviolet (FUV) to the infrared (IR). In this work we complement UV observations from the

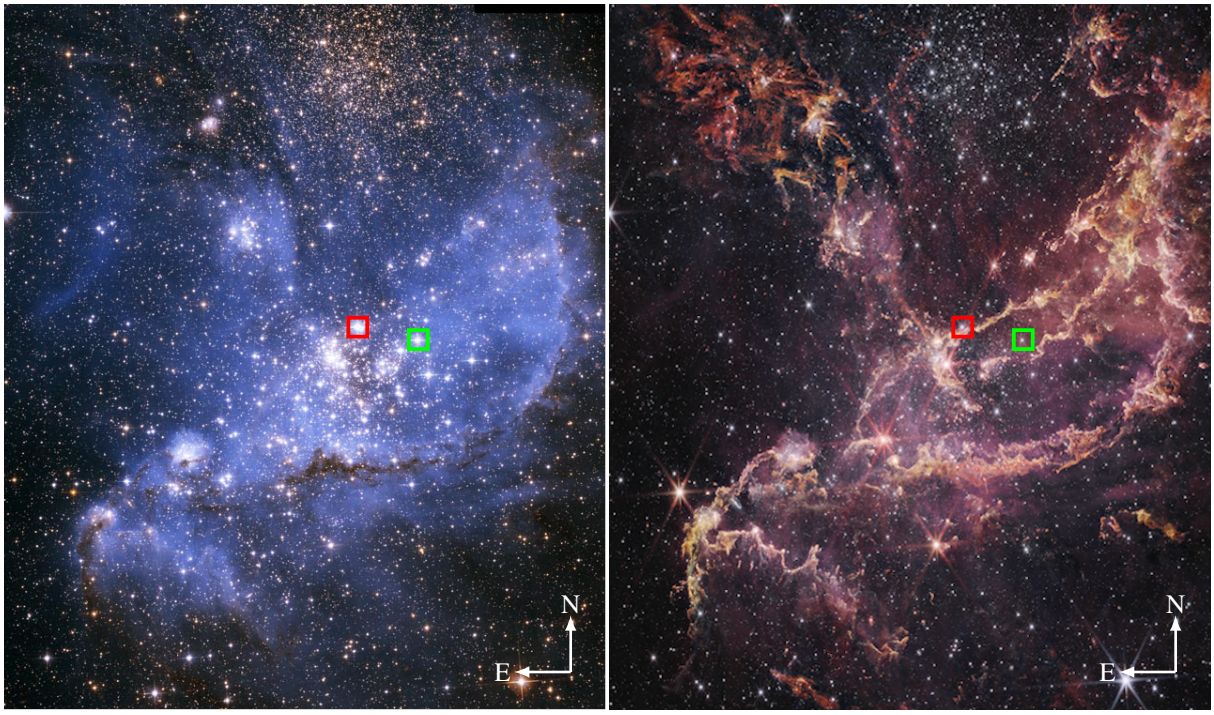

Fig. 3.1.1. Optical (left) and infrared (right) image of NGC346 in the SMC. Each image shows an area on the sky of approximately 3.5′ × 3.5′ (≈ 62 pc × 62 pc at d=61 kpc). The positions of the main ionising sources of NGC 346 (see Sect. 3.6.4), namely SSN 7 (ON3 If*+O5.5 V((f))) and SSN 9 (O2 III(f*)), are highlighted by red and green squares, respectively. The false-colour optical image was taken with the HST ACS. Credit: A. Nota (ESA/STScI). The false-colour infrared image was taken with the James Webb Space Telescopes (JWST) Near Infrared Camera (NIRCam). Credits: NASA, ESA, CSA, O. Jones (UK ATC), G. De Marchi (ESTEC), and M. Meixner (USRA). Image processing: A. Pagan (STScI), N. Habel (USRA), L. Lenkic (USRA), and L. Chu (NASA/Ames).

Hubble Space Telescopes (HST) UV Space Telescopes Imaging Spectrograph (STIS) and multi-epoch datacube observations obtained by the Multi Unit Spectroscopic Explorer (MUSE), which is mounted on the Very Large Telescope (VLT), with archival spectra from X-Shooter, GIRAFFE, the UV-visual Echelle Spectrograph (UVES), and far-ultraviolet (FUV) spectra from the Far Ultraviolet Spectroscopic Explorer (FUSE). A summary of all spectra employed in this work is given in Table 3.1.1, where each spectrum is assigned an ID number.

The UV (including the FUV) spectra are rectified by division through the synthetic model continuum, while the optical and near-IR spectra are rectified by hand. The photometric data used for the fitting of the spectral energy distribution (SED) is given in Table 3.2.1.

The core of NGC 346, including our target and other bright O stars (namely MPG 396 (O7V), MPG 417 (O7.5V), MPG 470 (O8.5III), and MPC 476 (O6V)), was observed with the *Chandra* X-ray telescope (Weisskopf et al. 2000). The core region has a combined X-ray flux, already corrected for reddening, of $F_{\mathrm{X,obs}} = 1.5 \times 10^{34}$ erg s^{-1} cm^{-2} in the 0.3 keV – 10.0 keV (Nazé et al. 2002). We use this as an upper constraint on the X-ray flux that we can include in our atmospheric models. However, we are cautious in our use of this value, as close O-type binaries in the Milky Way suggest that the majority of the X-rays might originate from colliding wind zones of close binaries (Rauw & Nazé 2016).

3.3. Orbital analysis

NGC 346 SSN 7 is a known SB2 binary; both components show contributions in the He I and He II lines. The ephemeris of this system was obtained by Niemela & Gamen (2004) who obtained RVs by fitting helium lines, yielding an orbital period of 24.2 d and an eccentricity of 0.42. The high eccentricity is surprising for an O-star system with an orbital period below 50 d, as theory predicts that the orbit in such systems is quickly circularised. Unfortunately, we do not have access to their data. Still, we have 17 optical spectra, of which 11 (the MUSE spectra) cover half of the reported period, allowing us to make further restrictions to the estimate of the orbital period and the eccentricity, and to constrain a mass ratio.

Table 3.1.1. List of spectroscopic observations of NGC 346 SSN 7.

ID	Instrument	Wavelength [Å]	Res. power [λ / $\delta\lambda$]	Exp. time [s]	MJD[(a)] [d]	Program ID	PI
1	FUSE	920-1180	~ 20,000	4464	52146.44	P203	K. Sembach
2	FUSE	920-1180	~ 20 000	6386	51828.57	P117	J. B. Hutchings
3	HST FOS G130H	1140-1605	~ 1150	2803	48948.09	GO4110	F.-P. Kudritzki
4	HST FOS G130H	1140-1605	~ 1150	2803	49287.81	GO4110	F.-P. Kudritzki
5	HST STIS G140L	1160-1705	~ 1000	225	58482.89	GO15112	L. Oskinova
6	HST FOS G190H	1560-2340	~ 1150	1215	48948.15	GO4110	F.-P. Kudritzki
7	HST FOS G190H	1560-2340	~ 1150	1215	49287.85	GO4110	F.-P. Kudritzki
8	HST STIS G230LB	1640-3100	~ 700	41	59363.76	GO16230	D. L. Massa
9	X-Shooter	2989-5560	6655	440	59216.11	1106.D-0775(A)	J. S. Vink
10	HST STIS G430L	3000-5550	~ 500	118	59363.76	GO16230	D. L. Massa
11	UVES	3281-4562	40 970	180	52249.01	68.D-0328(A)	D. Minniti
12	GIRAFFE	3960-4570	6300	1725	53277.28	074.D-0011(A)	C. J. Evans
13	GIRAFFE	3960-4570	6300	1725	53277.26	074.D-0011(A)	C. J. Evans
14	GIRAFFE	3960-4570	6300	22	53277.26	074.D-0011(A)	C. J. Evans
15	GIRAFFE	3960-4570	6300	50	53277.26	074.D-0011(A)	C. J. Evans
16	GIRAFFE	3960-4570	6300	1725	53276.24	074.D-0011(A)	C. J. Evans
17	GIRAFFE	4450-5080	7500	1725	53292.06	074.D-0011(A)	C. J. Evans
18	GIRAFFE	4450-5080	7500	1725	53280.2	074.D-0011(A)	C. J. Evans
19	UVES	4584-6687	42 310	180	52249.01	68.D-0328(A)	D. Minniti
20	MUSE	4620-9265	2989	315	57611.33	098.D-0211(A)	W.-R. Hamann
21	MUSE	4620-9265	2989	315	57613.25	098.D-0211(A)	W.-R. Hamann
22	MUSE	4620-9265	2989	315	57613.29	098.D-0211(A)	W.-R. Hamann
23	MUSE	4620-9265	2989	315	57617.23	098.D-0211(A)	W.-R. Hamann
24	MUSE	4620-9265	2989	315	57618.1	098.D-0211(A)	W.-R. Hamann
25	MUSE	4620-9265	2989	315	57620.15	098.D-0211(A)	W.-R. Hamann
26	MUSE	4620-9265	2989	315	57620.19	098.D-0211(A)	W.-R. Hamann
27	MUSE	4620-9265	2989	315	57620.23	098.D-0211(A)	W.-R. Hamann
28	MUSE	4620-9265	2989	315	57621.21	098.D-0211(A)	W.-R. Hamann
29	MUSE	4620-9265	2989	315	57621.25	098.D-0211(A)	W.-R. Hamann
30	MUSE	4620-9265	2989	315	57622.15	098.D-0211(A)	W.-R. Hamann
31	X-Shooter	5337-10200	11 333	510	59216.11	1106.D-0775(A)	J. S. Vink
32	X-Shooter	9940-24780	8031	300	59216.11	1106.D-0775(A)	J. S. Vink
33	X-Shooter	9940-24790	8031	300	59216.11	1106.D-0775(A)	J. S. Vink

Notes. [(a)] Mid-exposure time in HJD − 2400000.5. For brevity, the spectra referred to in this paper use the ID numbers listed here.

Table 3.2.1. Photometry of SSN 7, sorted by central wavelength.

Filter	Magnitude	Reference
HST F255W	11.98	Rickard et al. (2022)
B	12.56	Nascimbeni et al. (2016)
G_{BP}	12.39	Gaia Collaboration et al. (2023)
V	12.56	Nascimbeni et al. (2016)
HST F555W	12.61	Sabbi et al. (2007)
G_{RP}	12.69	Gaia Collaboration et al. (2023)
J	12.96	Bonanos et al. (2010)
H	13.00	Bonanos et al. (2010)
K	13.07	Bonanos et al. (2010)

3.3.1. Line associations to individual binary components

To prepare for the extraction of the RVs of each component, we identified which lines originate from which star. The most prominent line, which is detected in almost all of the used optical spectra of SSN 7, is the He II λ 4686 line. In Fig. 3.3.1 we illustrate how the morphology of the line changes within the individual observations. For clarity, only a handful of observations are shown. The emission feature of He II λ 4686 line shifts opposite to the

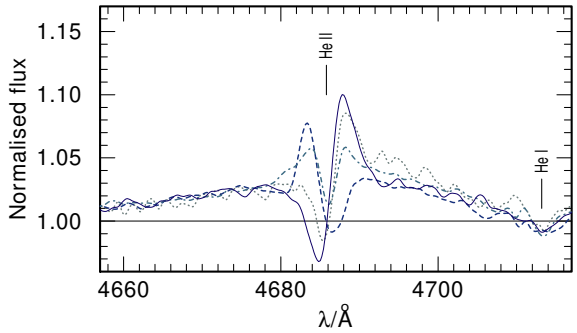

Fig. 3.3.1. Multi-epoch spectral observations of SSN 7. The X-Shooter spectrum (ID 09) is shown as a solid line, the GIRAFFE spectrum (ID 17) as a dashed line, the GIRAFFE spectrum (ID 18) as a dot-dashed line, and the UVES spectrum (ID 19) as a dotted line. The shifting emission and absorption features are associated with the primary and secondary, respectively.

absorption feature across multiple epochs. All lines that shift with the emission feature of the He II λ 4686 line are associated with the spectroscopic primary, and all lines that shift with the He II λ 4686 absorption line are associated with the spectroscopic secondary.

A full table of the considered lines is presented in Table B.1.3, including which line can be assigned to the primary, secondary, or to both. Spectral lines that only show a contribution of either the primary or the secondary are scarce.

3.3.2. Radial velocities

Measuring RVs in a binary, where both stars contribute to most of the diagnostic lines, is a non-trivial task. We employed a Markov chain Monte Carlo (MCMC) method combined with a least-squares fitting method to derive the RVs of each component. In each MCMC step, the individual synthetic spectra, which were obtained from the spectroscopic analysis (see Sect. 3.4), are shifted by a different RV value until the combined synthetic spectrum matches the observations. Thus, we can obtain RVs from complex absorption profiles. For a more detailed explanation we refer to Pauli et al. (2022a, Section 3.1.2 and Appendix B.1).

The MCMC method returns a final probability distribution around the true solution. The errors quoted are the larger error margin of the 68% confidence interval of the final distribution: commonly used codes for inferring binary parameters from observables are not able to include asymmetric uncertainties. To minimise uncertainties introduced by the intrinsic variability of the lines, we fitted several lines that show distinguishable contributions of the primary and secondary components and calculated their mean RV.

The mean RVs obtained for each spectrum, and binary component are listed in Table 3.3.1. The fitted RVs of all lines used in this process are listed in Tables B.1.1 and B.1.2. The change in sign of the RV of the primary (from $\sim 100\,\mathrm{km\,s^{-1}}$ to $\sim -80\,\mathrm{km\,s^{-1}}$) within $\sim 2\,\mathrm{d}$ calls in to question the reported period of 24.2 d and limits the orbital period to a few days.

3.3.3. Radial velocity curve modelling

When fitting RVs obtained from spectroscopic data with observations separated by several years, it is possible to find multiple orbital solutions consistent with the observations. To obtain a constraint on alternative ephemeris, a Monte Carlo sampler suitable for two-body systems with sparse and/or noisy radial velocity measurements, namely *The Joker* (Price-Whelan et al. 2017), is applied to the measured RVs. As *The Joker* is only able to model the RV curve of one component at a time, its output is used in a second step as input parameters for the Physics of Eclipsing Binaries (PHEOBE) code (Prša & Zwitter 2005; Prša et al. 2016; Horvat et al. 2018; Jones et al. 2020; Conroy et al. 2020), which can model the orbits of both binary components simultaneously.

3.3.3.1. Obtaining ephemerides with *The Joker*

The Joker uses a rejection sampling analysis on a densely sampled prior probability density function (pdf) and produces a sample of multimodal pdfs which contain the most important information about the ephemerides. The default pdfs of *The Joker* code (Price-Whelan et al. 2017, their section 2) are used here as the priors. As outlined in Section 3.3.2, the RVs obtained from the MUSE spectra suggest that the orbital period should be of the order of a few days (see Table 3.3.1). Hence, a log-uniform prior for the orbital period in the range of $0.1\,\mathrm{d} - 40\,\mathrm{d}$ is

Table 3.3.1. Mean RVs of the primary and secondary, sorted by MJD. The listed RVs are corrected for the velocity of NGC 346 complex and for the barycentric motion.

ID[(a)]	MJD	RV_{prim} [km s^{-1}]	RV_{sec} [km s^{-1}]
11	52249.01198	11 ± 10	10 ± 21
15	53277.25739	56 ± 7	−34 ± 7
14	53277.25939	51 ± 7	−32 ± 9
13	53277.26022	42 ± 6	−39 ± 7
12	53277.28112	48 ± 6	−39 ± 7
18	53280.19821	18 ± 15	−12 ± 29
17	53292.06195	−57 ± 15	41 ± 27
20	57611.32930	98 ± 14	−57 ± 19
21	57613.24630	−78 ± 15	67 ± 23
22	57613.28829	−77 ± 14	73 ± 21
23	57617.23463	55 ± 13	−22 ± 19
24	57618.10327	72 ± 13	−34 ± 22
25	57620.14865	36 ± 13	−34 ± 22
26	57620.19042	39 ± 13	−34 ± 22
27	57620.23262	43 ± 11	−32 ± 22
28	57621.20640	64 ± 13	−24 ± 22
29	57621.24834	49 ± 11	−30 ± 20
30	57622.14718	−85 ± 13	72 ± 21
31	59216.11133	92 ± 15	−55 ± 19

Notes. [(a)] Spectral ID taken from Table 3.1.1.

Table 3.3.2. Ephemerides obtained using the primary's RVs and *The Joker*.

parameter	value	unit
P	$3.07438^{+0.00002}_{-0.00002}$	[d]
e	$0.00^{+0.09}_{-0.00}$	
ω	$-122.6^{+244.1}_{-38.4}$	[°]
M_0	$-0.80^{+1.05}_{-0.81}$	[d]
K	$81.25^{+6.15}_{-6.05}$	[km s^{-1}]
v_0	$13.40^{+3.26}_{-3.27}$	[km s^{-1}]

adopted for the fitting procedure. The upper limit was chosen as roughly two times the orbital period obtained by Niemela & Gamen (2004) to enable their solution to be considered, while the lower limit was set to a reasonably small value. For the eccentricity we used the Beta distribution from Kipping (2013) with $a = 0.867$ and $b = 3.03$. For the argument of the pericentre and the orbital phase a uniform prior without any restrictions is used. The RVs of the primary, which are more reliable since they have lower error margins, are employed as input data.

From the 1×10^7 samples created, 340 pass the rejection step, equivalent to an acceptance rate of 0.0034%. Afterwards, a standard MCMC method is used to sample around the most likely solution found from the rejection step in order to fully explore the posterior pdf. We find that the ephemerides are described best with a circular orbit ($e = 0$) and an orbital period of $P_{\rm Joker} = 3.074\,38 \pm 0.000\,02$ d. The complete set of emphemerides obtained with *The Joker* are listed in Table 3.3.2.

3.3.3.2. Obtaining orbital parameters with PHOEBE

The ephermerides obtained in Section 3.3.3.1 were determined by only using the RVs of the primary. This was done to get a first constraint on the orbital parameters; however, valuable information such as the mass ratio (q), the projected orbital separation ($a \sin i$), and the projected Keplerian masses ($M \sin i$) can only be obtained when fitting the RVs of the two components simultaneously. Therefore, the PHOEBE light and RV curve modelling software (version 2.3) was employed to model the observed RVs, with the built-in option of the MCMC sampler `emcee` (Foreman-Mackey et al. 2013).

The initial probability distributions of the period P, the argument and phase of the pericentre ω and M_0, and the barycentre velocity v_0 are assumed to be of Gaussian shape. The Gaussians are centred at the best-fitting value as obtained by *The Joker* (see Table 3.3.2) and have a standard deviation similar to their respective largest error margin. The ephemerides obtained with *The Joker* favour a circular orbit, and hence the eccentricity is fixed at $e = 0$. To constrain the current mass ratio we employed the method of Wilson (1941) yielding $q_{\rm wilson} = 1.34 \pm 0.07$. Because of a lack of information about other parameters, we used a uniform distribution in

Table 3.3.3. Ephemerides obtained using the RVs of both binary components and the PHOEBE code.

parameter	value	unit
P	$3.07359^{+0.02481}_{-0.00001}$	[d]
ω_0	242^{+9}_{-30}	[°]
M_0	$1.5^{+7.8}_{-1.4}$	[d]
v_0	$9.1^{+0.2}_{-0.5}$	[km s^{-1}]
$q_{\rm orb}$	$1.47^{+0.13}_{-0.09}$	
$a \sin i$	$11.0^{+0.7}_{-0.3}$	[$R_\odot$]
$i_{\rm orb}$ [(a)]	16^{+1}_{-1}	[°]
a [(b)]	$39.9^{+1.2}_{-2.5}$	[$R_\odot$]

Notes. [(a)] Calibrated such that the orbital and spectroscopic masses agree within their uncertainties. [(b)] Calculated using $i_{\rm orb}$.

Table 3.3.4. Orbital parameters of the individual binary components obtained using the PHOEBE code.

parameter	primary	secondary	unit
K	$107.9^{+3.9}_{-3.9}$	$73.3^{+2.7}_{-2.7}$	[km s^{-1}]
$M_{\rm orb} \sin i^3$	$0.77^{+0.15}_{-0.07}$	$1.13^{+0.21}_{-0.10}$	[$M_\odot$]
$M_{\rm orb}$ [(a)]	$36.5^{+7.04}_{-3.5}$	$53.8^{+10.1}_{-4.9}$	[$M_\odot$]
$R_{\rm RL}$ [(a)]	$13.8^{+0.8}_{-0.4}$	$16.5^{+0.9}_{-0.4}$	[$R_\odot$]

Notes. [(a)] Calculated using $i_{\rm orb}$ (see Table 3.3.3).

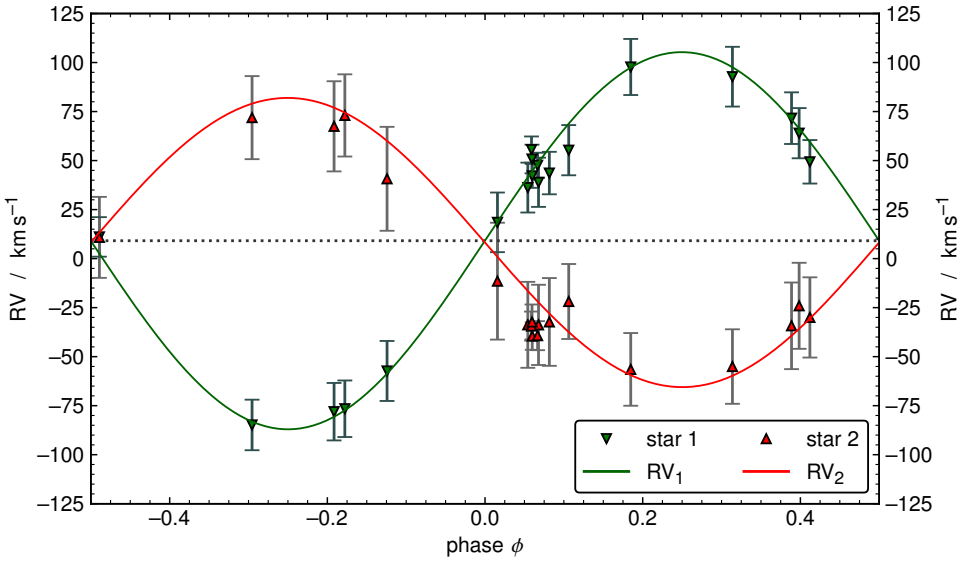

Fig. 3.3.2. Observed (triangles) and synthetic (solid lines) RV curves of the primary (green) and secondary (red) component, as obtained by the PHOEBE code. The dashed black line indicates the barycentric velocity offset v_0.

the range of $q_{\rm orb,i} = 0.33 - 3.0$, where a starting value $q_{\rm orb,i} = q_{\rm wilson}$ is assumed. The initial projected orbital separation is approximated to be of the order of $a \sin i_{\rm i} = 10\,{\rm R}_\odot$ and that it is uniformly distributed over the range of $a \sin i_{\rm i} = 0.1\,{\rm R}_\odot - 100\,{\rm R}_\odot$.

The best fit of the RV curve obtained with the PHOEBE code is shown in Fig. 3.3.2. The final orbital parameters are listed in Tables 3.3.3 and 3.3.4. The RV fit yields masses without information about the inclination. By using the results from the spectroscopic analysis (see Sect. 3.4) we estimate the inclination to be $i_{\rm orb} = 16 \pm 1\,^\circ$.

To date, there is no observed light curve of NGC 346 SSN 7 reported in the literature. Since the PHOEBE code is capable of modelling a light curve, it can be used to make a prediction on the shape of a possible light curve (see Appendix B.2 for more details). From the predicted synthetic light curve, we conclude that a detector with a precision below < 18 mmag in the V band is needed to see any kind of variability. This precision is hardly achievable for stars in the SMC with current ground-based telescopes. Hence, it is not surprising that no light curve has been detected so far.

3.4. Spectral analysis

3.4.1. Stellar atmosphere modelling

Expanding stellar atmospheres of hot stars ($T > 15\,\mathrm{kK}$) are in non-local thermal equilibrium (non-LTE) and can only be calculated using state of the art stellar atmosphere codes such as the Potsdam Wolf-Rayet (PoWR, Gräfener et al. 2002; Oskinova et al. 2011; Hainich et al. 2014, 2015; Shenar et al. 2015; Hamann & Gräfener 2004; Sander et al. 2015) code. Within PoWR, the radiative transfer equations and the rate equations are solved iteratively in the co-moving frame. The code is able to produce a synthetic spectrum that accounts for mass-loss, line blanketing, and wind clumping.

For our stellar atmosphere models, we used tailored surface abundances that are representative of the chemical composition of the SMC. For the modelling of SSN 7 within NGC 346, the initial H abundance is adopted from Asplund et al. (2005), while the initial abundances of C, N, O, Mg, and Si are based on the works of Hunter et al. (2007) and Trundle et al. (2007). The abundances of P and S are taken from Scott et al. (2015b) and are scaled down to the metallicity of the SMC ($Z_{\mathrm{SMC}} = 1/7\,Z_{\odot}$). The iron group elements (Fe, Sc, Ti, V, Cr, Mn, Co, and Ni) are either taken from Trundle et al. (2007) or, when not available, taken from solar values (Scott et al. 2015b) and multiplied by a factor 1/7 to account for the lower metallicity of the SMC (Table 3.4.1). The numerous complex iron lines are handled with a 'superlevel' approach (Gräfener et al. 2002).

Microturbulence within a stellar atmosphere leads to a Doppler-broadening of spectral lines. The PoWR models used assume a depth-dependent microturbulence starting in the photosphere at $\xi_{\mathrm{ph}} = 10\,\mathrm{km\,s^{-1}}$ and increases outwards linearly with the wind velocity $\xi(r) = 0.1 \cdot v(r)$.

Our PoWR models account for wind inhomogeneities and introduced optically thin clumps (microclumping) within the stellar atmosphere. The density contrast of the clumps within the wind is described by the clumping factor D. For NGC 346 SSN 7, a depth-dependent clumping factor is used, starting at the sonic radius and reaching $D = 10$ at ten times the stellar radius.

For the velocity stratification within the wind, a double β-law (Hillier & Miller 1999) of the form

$$v(r) = v_{\infty}\left[f\left(1 - \frac{r_0}{r}\right)^{\beta_1} + (1-f)\left(1 - \frac{r_1}{r}\right)^{\beta_2}\right] \tag{3.4.1}$$

is adopted. The inner part of the velocity stratification is described by an exponent $\beta_1 = 0.8$, which is typical for O stars (Pauldrach et al. 1986). The outer part is described with an exponent $\beta_2 = 4$ and only contributes with a fraction of $f = 0.4$. The parameters r_0 and r_1 are set within the code, such that the wind is smoothly connected.

The effective temperatures quoted in this work are related via the Stefan-Boltzmann law to the radius at which the Rosseland mean continuum optical depth is $\tau = 2/3$. Stellar and wind parameters can be obtained by adjusting the synthetic spectrum until it matches the observed spectra simultaneously. This also means that the abundance of a specific element (e.g. H, C, N, O) can be adjusted if needed to match the strength of observed lines.

3.4.2. Resulting spectroscopic parameters

Deriving stellar and wind parameters from stellar spectra in which lines are blended by two stars of a binary is a difficult task. The following subsections describe the strategy employed and the final parameters that are listed in Table 3.4.2.

3.4.2.1. Rotation rates

Before starting the spectral fitting process, accurate values for the projected rotational velocities ($v \sin i$) of each component are needed. These impact the depth and shape of all synthetic lines and hence conclusions drawn from the spectroscopic fit. We employ the IACOB-BROAD tool (Simón-Díaz & Herrero 2014) which uses a combination of a Fourier transform (FT) and a goodness of fit (GOF) method to obtain accurate measurements of $v \sin i$.

When obtaining projected rotation rates, the preference is to use metal lines over helium lines as the latter are, in addition to the rotational broadening, also pressure broadened. For the primary, we use the N IV λ 4057 as well as the N IV λ 6381 line. As there are no metal lines that solely can be attributed to the secondary, we use the prominent He I λ 6875 and the He I λ 7065 line. The projected rotational velocities of the primary and secondary component are best described with $v_1 \sin i = 135 \pm 10$ km s^{-1} and $v_2 \sin i = 185 \pm 10$ km s^{-1}, respectively.

Most of the observed lines are formed in the rotating photosphere of a star, while fewer but still important lines in the UV are formed within the static (non-rotating) wind. To account for this, the synthetic PoWR models used

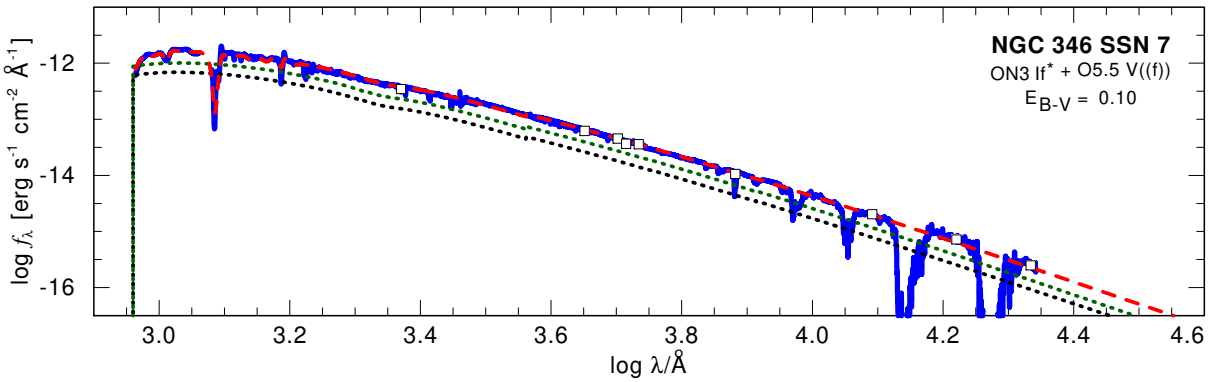

Fig. 3.4.1. Observed (blue) and combined synthetic (red) SED. The individual synthetic SEDs of the primary and secondary are shown as the dotted black and green line, respectively. The photometry, listed in Table 3.2.1, is shown as open squares.

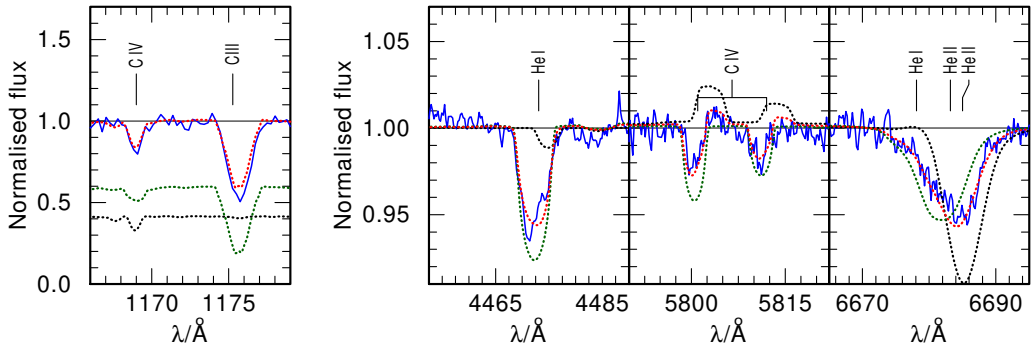

Fig. 3.4.2. Close-ups on the carbon and helium lines used to constrain the luminosity ratio (solid blue) compared to the combined synthetic model (dotted red). *Left:* Observed FUSE spectra (ID 01). The weighted synthetic spectra of the primary and secondary components are shown as a dotted black and green line. *Right:* Observed X-Shooter spectra (ID 09 and 31). The unweighted synthetic spectra of the primary and secondary components are shown as a dotted black and green line.

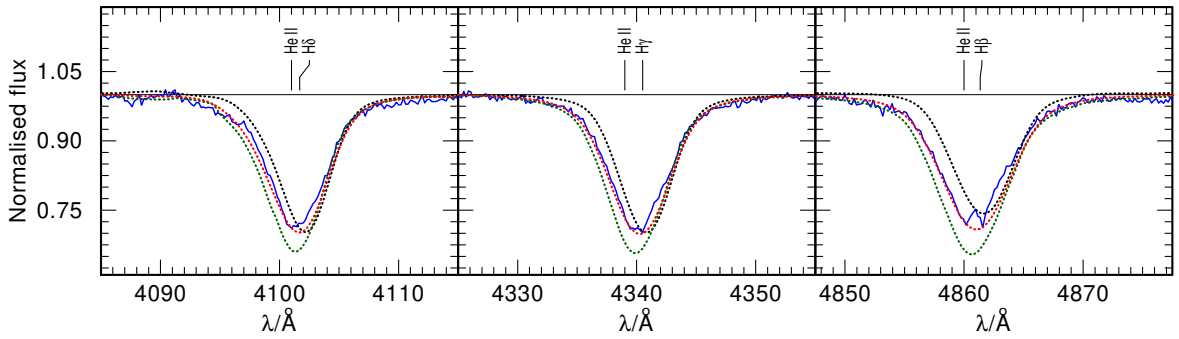

Fig. 3.4.3. Close-ups on the Balmer lines in the X-Shooter spectrum (ID 09; solid blue) compared to the combined synthetic model (dotted red). The unweighted synthetic spectra of the primary and secondary components are shown as dotted black and green line.

in this work are calculated with a rigidly rotating photosphere and a non-rotating wind, as described in Shenar et al. (2014).

3.4.2.2. Luminosity, temperature, and surface gravity

To constrain the luminosity of each binary component, we carefully looked at the ratios of isolated and blended helium and metal lines. One of the key diagnostic lines was the C III λ 1175 in the UV, which originates purely from the secondary, giving an extra constraint on the luminosity ratio. A selected set of the lines used is illustrated in Fig. 3.4.2. Determining the luminosity ratio is an iterative process and is revisited after each modelling change, as changes in temperature and surface gravity also affect the shape of key diagnostic lines. The luminosity of each component is $\log(L_1 / L_\odot) = 5.75$ and $\log(L_1 / L_\odot) = 5.78$ for the primary and secondary, respectively.

Table 3.4.1. Abundances and ionisation stages employed in the PoWR models.

Element	Primary		Secondary	
	mass fr.	ion. stages	mass fr.	ion. stages
H	0.60	I, II	0.7375	I, II
He	0.39	I, II, III	0.26	I, II, III
C	1×10^{-5}	II – V	21×10^{-5}	II – V
N	138×10^{-5}	II – VI	40×10^{-5}	II – VI
O	4×10^{-5}	II – VII	110×10^{-5}	II – VII
Mg	10×10^{-5}	II, III, IV	10×10^{-5}	II, III, IV
Si	1.3×10^{-5}	III – VIII	1.3×10^{-5}	III – VI
P	8.3×10^{-7}	IV, V, VI	8.3×10^{-7}	IV, V, VI
S	4.4×10^{-5}	III – VI	4.4×10^{-5}	III – VI
Fe	3.5×10^{-4}	II – IX	3.5×10^{-4}	II – IX

The surface gravity of each of the component stars is determined by fitting the wings of the Balmer lines in the spectra with the biggest RV shifts. We find that the primary and the secondary have similar surface gravities of $\log g = 3.7 \pm 0.1$ (see Fig. 3.4.3).

The temperatures of the stars are derived using the ratio between the He I and He II lines associated with each component (see Table B.1.3). To get a more accurate constraint on the primary's temperature, the ratio between the different observed nitrogen lines are used, namely N IV $\lambda\lambda\lambda$ 3479, 3483, 3485, N IV λ 4058, N V $\lambda\lambda$ 4604, 4620, N III $\lambda\lambda$ 4634, 4641, and N IV $\lambda\lambda\lambda$ 6212, 6216, 6220. We find for the primary $T_{\mathrm{eff},1} = 43.6 \pm 2.0$ kK, while the secondary is best fit with $T_{\mathrm{eff},2} = 38.7 \pm 2.0$ kK.

3.4.2.3. Surface abundances

During the determination of the temperature of the primary, we find that it is possible to match the ratio of the He I and He II lines, but these lines are systematically too weak. Hence, we lowered the primary's surface hydrogen abundance to $X_{\mathrm{H},1} = 0.60 \pm 0.1$. Furthermore, to fit the observed nitrogen lines, which are also crucial for the temperature determination, we find that the nitrogen abundance of the primary is enhanced to $X_{\mathrm{N},1} = 138^{+10}_{-30} \times 10^{-5}$ (i.e. $2\,N_\odot$).

In addition, the spectrum contains carbon and oxygen lines that show clear contributions from the primary. To constrain its surface oxygen abundance, we used the O IV $\lambda\lambda\lambda$ 1337-1343-1344 triplet in the UV, the O IV multiplet around $\sim$ 3000 Å, and the O III lines in the range from 1409 Å – 1412 Å. We find that oxygen in the primary's atmosphere is depleted with $X_{\mathrm{O},1} = 4^{+6}_{-3} \times 10^{-5}$. Regarding the carbon abundance, we used C IV λ 1169 in the UV and the C IV $\lambda\lambda$ 5801, 5812 doublet in the optical, yielding a surface carbon abundance of $X_{\mathrm{C},1} = 1^{+9}_{-0} \times 10^{-5}$ in the primary.

Determining the surface abundance of the secondary is more complicated as it shows little contribution to the observed metal lines. We can see in some spectra that the secondary contributes to the N III $\lambda\lambda$ 4634, 4641 doublet. Hence, we tried to use this as a constraint on its surface nitrogen abundance and find the best fit with $X_{\mathrm{N},2} = 60^{+20}_{-10} \times 10^{-5}$. We can also see a contribution to the C IV $\lambda\lambda$ 5801, 5812 doublet in the optical, and the C III λ 1175 in the UV. These lines can be well reproduced with the initial carbon abundance of $X_{\mathrm{C},2} = 21^{+0}_{-5} \times 10^{-5}$. Unfortunately, we cannot see a clear contribution of the secondary to the oxygen lines. As the nitrogen abundance is increased and theory predicts that the amount of CNO material should be $X_{\mathrm{CNO}} \approx 137 \times 10^{-5}$ for stars in the SMC (Kurt & Dufour 1998), we scaled down the oxygen abundance of the secondary to $X_{\mathrm{O},2} = 80 \times 10^{-5}$. We note that this does not have any impact on the quality of our fit.

Figure 3.4.5 shows the all-important metal lines used to fit the abundances of the primary and secondary. The changed surface abundances of the primary, especially the lower surface hydrogen abundance and the increased nitrogen, hint at previous binary interaction that stripped off parts of the envelope (see Sect. 3.6).

3.4.2.4. Spectroscopic stellar masses

Given the fundamental stellar parameters (T_{eff}, $\log g$, L) of each binary component, we can calculate the spectroscopic masses. We find that the mass of the primary component is $M_{\mathrm{spec},1} = 32^{+19}_{-13}\,M_\odot$, surprisingly low for

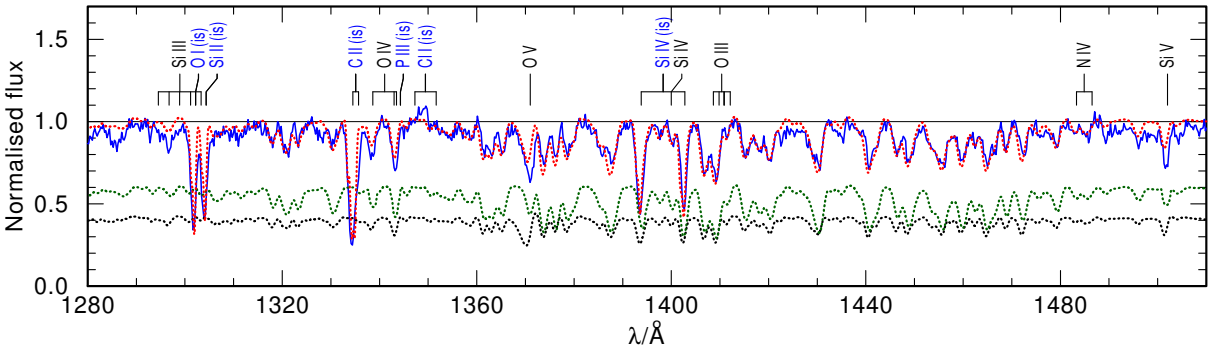

Fig. 3.4.4. Close-up on the iron forest of the HST FOS (ID 03) spectrum (solid blue) compared to the combined synthetic model flux (dashed red). The weighted synthetic model spectra of the primary and secondary are shown as a dotted black and green line, respectively. The iron forest is used to check the iron abundance and to constrain the microturbulence within the stellar atmosphere.

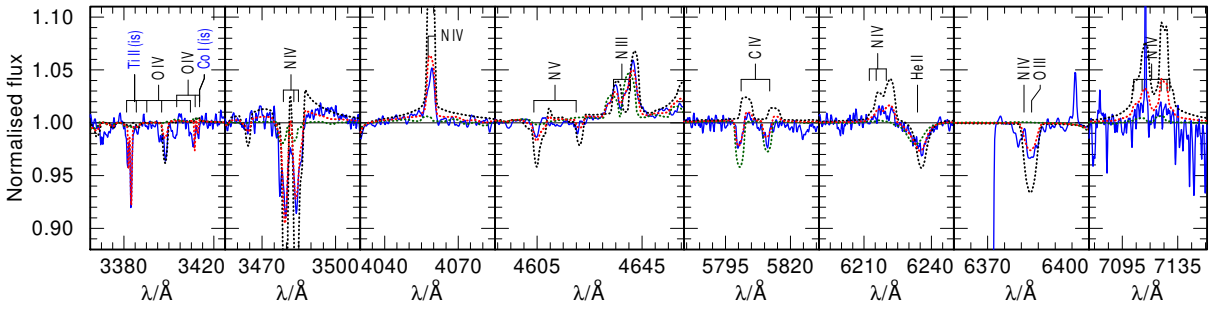

Fig. 3.4.5. Close-ups on the metal lines in the X-Shooter spectrum (ID 09 and 31; solid blue) compared to the combined synthetic spectrum (dashed red). The unweighted synthetic spectra of the primary and the secondary component are shown as a dotted black and green line, respectively.

its luminosity. The mass of the secondary is $M_{\mathrm{spec},2} = 55^{+32}_{-21}\,M_\odot$. The low mass of the primary strengthens our argument that the binary components must have interacted in the past.

To further strengthen this hypothesis, we calculated the Roche radius, using the results from the orbital analysis in combination with the spectroscopic masses and find that both stars are currently slightly overfilling their Roche lobe with $R_1/R_{\mathrm{RL}} = 1.01$ and $R_2/R_{\mathrm{RL}} = 1.03$. This strongly suggests that the system interacted in the past, and that both stars are still currently in contact.

3.4.2.5. Wind velocities and mass-loss rates

So far only photospheric lines were considered in the spectroscopic analysis. However, in the spectra there are several lines that are sensitive to wind parameters, like the N v $\lambda\lambda$ 1239, 1243 and C iv $\lambda\lambda$ 1548, 1551 doublets in the UV, and Hα and He ii λ 4686 in the optical. Both stars are very bright, massive, and hot, meaning that both of them are expected to contribute to the wind diagnostic lines. Within the FUV FUSE observation, no measurable P v or S iv wind resonance lines are present. This is consistent with our composite model.

The primary motion is reflected by the emission parts of Hα and He ii λ 4686, while the secondary's motion is evident from the absorption components of the same lines. We conclude that the primary must have a stronger mass-loss rate compared to the secondary. We used the Hα and He ii λ 4686, in combination with N v $\lambda\lambda$ 1239, 1243 and C iv $\lambda\lambda$ 1548, 1551, to calibrate the primary's mass-loss rate to $\log(\dot{M}_1/(\,M_\odot\,\mathrm{yr}^{-1})) = -5.4 \pm 0.1$. With this mass-loss rate, the resonance doublets in the UV were fully saturated in the synthetic spectrum of the primary, yet the observed profiles were not fully saturated. The secondary contributes roughly 60% of the UV flux, so we fit the combined spectra with a partially saturated secondary wind. The secondary is fit with a mass-loss rate of $\log(\dot{M}_2\ /\ (\,M_\odot\,\mathrm{yr}^{-1})) = -7.3 \pm 0.1$, which results in the combined synthetic spectrum matching the observed spectrum (Fig. 3.4.6).

The terminal wind velocity of the primary is adjusted to match the blue edge of the N v $\lambda\lambda$ 1239, 1243 absorption trough, giving $v_{\infty,1} = 2500 \pm 100\,\mathrm{km\,s^{-1}}$. For the secondary, we experimented with different values of v_∞ to see how the slope of the C iv λ 1548,1551 resonance doublet changes. The best fit that matches the profile in the STIS and FOS spectrum was obtained when using the same terminal wind velocity for the secondary as for the primary ($v_{\infty,2} = 2500 \pm 300\,\mathrm{km\,s^{-1}}$).

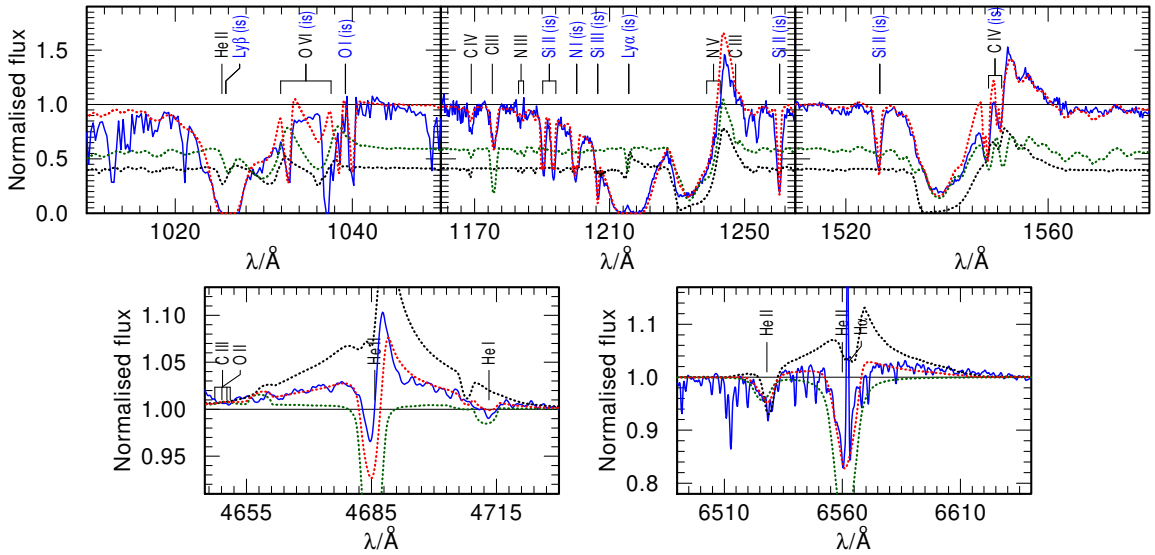

Fig. 3.4.6. Close-ups on the key wind diagnostic lines (solid blue) in the FUV, UV and optical spectra overplotted by the combined synthetic model (dashed red). In the upper panels the weighted and in the lower panels the unweighted synthetic spectra of the primary and secondary components are shown as dotted black and green line, respectively. *Upper left:* The O VI line of the FUSE (ID 1) spectrum. This line is sensitive to X-rays. *Upper middle:* The N V resonance doublet in the HST FOS (ID 3) spectrum. *Upper right:* The C IV resonance doublet in the HST FOS (ID 3) spectrum. *Lower left:* The He II λ 4686 line in the X-Shooter spectrum (ID 9), showing strong wind emission features from the primary. *Lower right:* Hα of the X-Shooter spectrum (ID 31), again, the primary dominates the wind emission of this line.

3.4.2.6. Required X-ray flux

The O VI $\lambda\lambda$ 1032, 1038 resonance doublet in the FUV shows weak indications of a P Cygni profile, which cannot be modelled by default in a stellar atmosphere model. Cassinelli & Olson (1979) were the first to suggest that these high ionisation stages must be 'super-ionised' by a hot X-ray plasma that originates from within the wind.

We include, in our primary and secondary, a hot plasma that is smoothly distributed throughout the wind, starting at 1.1 R_* and having a temperature of $T_X = 3$ MK. We find that the O VI $\lambda\lambda$ 1032, 1038 resonance doublet (Fig. 3.4.6) can be explained with an X-ray luminosity of $\log(L_{X,1}/(\mathrm{erg\,s^{-1}})) = 32.4$ and $\log(L_{X,2}/(\mathrm{erg\,s^{-1}})) = 32.1$ for the primary and secondary, respectively. This is much lower than the X-Ray luminosity observed from the core of NGC 346 and comparable to X-rays needed for other O stars (Nebot Gómez-Morán & Oskinova 2018).

3.5. Stellar evolution modelling

In the previous sections we determine the stellar and wind parameters of the binary components, and refine the binary period, and we establish that the system is most likely in contact. With this information at hand, we proceed to model the past, present, and future evolution of this remarkable system.

The evolution of SSN 7 in this work is modelled using the Modules for Experiments in Stellar Astrophysics (MESA; Paxton et al. 2011, 2013, 2015, 2018, 2019) code (v.15140). Our aim is to understand, from the predictions of the stellar evolutionary models, the current evolutionary stage of our target rather than finding a perfect fine-tuned fit for our empirically derived parameters. The orbital and spectroscopic parameters (Sect. 3.4.1 and Sect. 3.3.1) limit the possible previous evolutionary paths. To find a fitting model, we explore a parameter space in the following ranges: donor masses in the range $M_{1,i} = 45\,M_\odot - 65\,M_\odot$, initial accretor masses with $M_{2,i} = 30\,M_\odot - 55\,M_\odot$, and initial orbital periods in the range $P_i = 2\,d - 7\,d$.

3.5.1. Stellar and binary input physics

The employed binary evolutionary models are constructed using the input files provided by Marchant et al. (2016).[1] A brief summary of the assumed input physics follows.

In the binary models, following the work of Brott et al. (2011), tailored initial abundances are used. The initial abundances are $X_H = 0.7460$, $X_{He} = 0.2518$, and $Z = 0.0022$, with Z being the total metal fraction. The individual

[1] https://github.com/orlox/mesa_input_data/tree/master/2016_binary_models

Table 3.4.2. Stellar parameters derived from the spectroscopic analysis, compared to those of the best-fitting MESA model

	Spectroscopic fit		MESA model		Unit
	SSN 7a	SSN 7b	mass donor	mass gainer	
$\log L$	5.75 ± 0.15	5.78 ± 0.15	5.76 ± 0.1	5.74 ± 0.1	$[L_\odot]$
$T_{\rm eff}$	43.6 ± 1.0	38.7 ± 1.0	43.6 ± 1.5	38.8 ± 1.5	[kK]
$\log g$	3.7 ± 0.1	3.7 ± 0.1	3.68 ± 0.05	3.7 ± 0.05	$[\mathrm{cm\,s^{-2}}]$
$v \sin i$	135 ± 10	150 ± 10	-	-	$[\mathrm{km\,s^{-1}}]$
$v_{\rm rot}$	-	-	222 ± 10	274 ± 10	$[\mathrm{km\,s^{-1}}]$
$\log \dot{M}$	-5.4 ± 0.1	-7.3 ± 0.4	-5.87 ± 0.1 [a]	-5.75 ± 0.1 [a]	$[M_\odot\,\mathrm{yr^{-1}}]$
v_∞	2500 ± 100	2500 ± 300	-	-	$[\mathrm{km\,s^{-1}}]$
R	13.2 ± 1.7	17.3 ± 2.1	13.5 ± 0.3	16.3 ± 0.5	$[R_\odot]$
$R_{\rm RL}$ [b]	$13.1^{+3.8}_{-2.3}$	$16.8^{+4.8}_{-3.3}$	13.5 ± 0.3	16.3 ± 0.5	$[R_\odot]$
$R/R_{\rm RL}$	1.01	1.03	1	1	
M	32^{+19}_{-13}	55^{+32}_{-21}	33 ± 2	50 ± 5	$[M_\odot]$
$X_{\rm H}$	0.60 ± 0.05	0.7375	0.51 ± 0.1	0.71 ± 0.02	[mass fr.]
$X_{\rm He}$	0.39 ± 0.05	0.26	0.50 ± 0.1	0.28 ± 0.02	[mass fr.]
$X_{\rm C} \times 10^5$	1^{+1}_{-0}	21 ± 5	2 ± 2	26 ± 2	[mass fr.]
$X_{\rm N} \times 10^5$	138^{+10}_{-30}	40^{+20}_{-10}	138 ± 2	43 ± 5	[mass fr.]
$X_{\rm O} \times 10^5$	4^{+6}_{-1}	80 [c]	4 ± 2	80 ± 5	[mass fr.]

Notes. [a] Only wind mass-loss rates, according to the wind recipe used in our calculations. [b] Calculated using the period $P = 3.07$ d, as from the orbital analysis (see Sect. 3.3), and using the spectroscopic mass ratio. [c] Set to fulfil $\Sigma\,\mathrm{CNO_i} \approx \mathrm{const.} = 137 \times 10^{-5}$.

Table 3.5.1. Initial chemical abundances of our stellar evolutionary models.

element	mass fraction	reference
C	20.82×10^{-5}	Kurt & Dufour (1998)
N	3.28×10^{-5}	Kurt & Dufour (1998)
O	113.07×10^{-5}	Kurt & Dufour (1998)
Mg	9.32×10^{-5}	Trundle et al. (2007) Hunter et al. (2007)
Si	1.30×10^{-5}	Trundle et al. (2007) Hunter et al. (2007)
Fe	33.74×10^{-5}	Venn (1999)

Notes. All elements that are not listed here correspond to the solar abundances from Asplund et al. (2005) scaled down by a factor of 1/5.

initial metal abundances are listed in Table 3.5.1. The abundances are comparable to fit in our atmospheric model (see Table 3.4.1).

Mixing is included as follows. Convection is modelled as standard mixing length theory (MLT, Böhm-Vitense 1958) using the Ledoux criterion and $\alpha_{\rm mlt} = 1.5$. Semiconvective mixing is assumed to be efficient with $\alpha_{\rm sc} = 1$ (Langer et al. 1983; Schootemeijer et al. 2019). For core hydrogen-burning stars, the step overshooting is assumed to be up to $0.335 H_{\rm P}$ (Brott et al. 2011; Schootemeijer et al. 2019). Furthermore, rotational mixing is included as a diffuse process, including dynamical shear, secular shear, and Goldreich-Schubert-Fricke instabilities, as well as Eddington-Sweet circulations Heger et al. (2000). The efficiency parameters are set to $f_c = 1/30$ and $f_\mu = 0.1$. Thermohaline mixing is modelled with $\alpha_{\rm th} = 1$ (Kippenhahn et al. 1980). Lastly, the models take into account momentum transport originating from a magnetic field as expected from a Taylor-Spruit dynamo (Spruit 2002).

To avoid numerical complications in the late evolutionary stages of the star, the evolution of both components is only modelled until core helium depletion. Furthermore, for core helium burning stars with core masses above $> 14\,M_\odot$ a more efficient mixing theory, MLT++ (section 7.2 of Paxton et al. 2013), is employed.

Mass-loss via a stellar wind is included in the models in the following way. For hydrogen-rich ($X_\mathrm{H} \geq 0.7$) OB stars, the recipe of Vink et al. (2001) is used. As soon as the temperature of any model drops below the bi-stability jump (Vink et al. 2001, their equations 14 and 15), the maximum of the mass-loss rate of Vink et al. (2001) or Nieuwenhuijzen & de Jager (1990) is taken. During the WR stage, when the surface hydrogen abundance drops below $X_\mathrm{H} \leq 0.4$, the mass loss rates of Shenar et al. (2019, 2020c) are used. For surface abundances between $0.7 > X_\mathrm{H} > 0.4$, the mass-loss rate is linearly interpolated between the mass-loss rates of Vink et al. (2001) and Shenar et al. (2019, 2020c).

To reduce the free parameter space, it is presumed that the components of SSN 7 are initially tidally locked and that the orbit is circularised. This is a reasonable approach for a binary with a period as short as 3.1 d.

Mass transfer by Roche-lobe overflow is modelled implicitly using the contact scheme of the MESA code. The mass transfer is modelled conservatively as long as the mass-gainer is below critical rotation. Whenever the mass-gainer spins up to critical rotation, it will stop the accretion, and we assume that the material is directly lost from the system. In addition to the mass transfer by Roche-lobe overflow, mass accretion from the stellar wind is taken into account.

At the instance of time when the donor star depletes helium in its core, its model is stopped. It is assumed that the primary directly collapses into a BH without a supernova explosion and without a kick. Further mass transfer via Roche-lobe overflow and wind from the companion onto the BH accretion onto the BH is limited by the Eddington accretion rate.

3.5.2. Resulting binary models

The best fit of the empirically derived fundamental stellar parameters of both binary components is achieved with an initial primary mass of $52\,M_\odot$, an initial secondary mass of $38\,M_\odot$, and an initial orbital period of 2.7 d. The corresponding tracks of the mass donor and mass gainer in the Hertzsprung–Russell diagram (HRD) are shown in Fig. 3.5.1. The binary evolutionary model that matches the spectral fit parameters best predicts that the observed stars are currently in contact in a slow Case A mass-transfer phase. This prediction would make SSN 7 the most massive Algol-like system known so far, making it an ideal laboratory to study the ongoing effects and efficiencies of mass transfer in binaries hosting massive stars.

The parameters of the closest fitting binary evolution model are listed in Table 3.4.2. Errors quoted are sophisticated guesses on the uncertainties of the binary evolutionary models from the experiences we gained when tailoring the evolutionary models to match the empirically derived stellar parameters. For more accurate error margins, a fine grid of detailed stellar evolution models is needed.

The empirically derived fundamental stellar parameters as well as the observed period of 3.1 d can be explained by our binary evolutionary model. Our favourite model predicts that the binary has an age of 4.2 Myr. The only discrepancy found is between the predicted and observed rotation rates. We discuss this in detail in Sect. 3.6.2.2.

It is predicted that the primary, after it depletes the hydrogen in its core, expands and initiates another more rapid mass-transfer phase, also called Case AB mass-transfer. During this phase it strips off large fractions of its H-rich envelope and evolves bluewards in the HRD towards the regime where WR stars can be found. During its WR phase, our model is predicted to have some H remaining in the envelope ($X_\mathrm{H} \sim 0.2$). During this time, the secondary, which will be rejuvenated from mass accretion, is still core hydrogen burning.

After the primary, which is the current mass donor, depletes the helium in its core, we assume that it directly collapses into a BH. The formed BH has a mass of $25.5\,M_\odot$, which should be considered as an upper limit since we assumed a direct collapse. However, this assumption allows us to make predictions about the future evolution of the secondary. Our model predicts that the secondary will evolve off the main sequence and will initiate mass transfer on the BH, stripping parts of its H-rich envelope ($X_\mathrm{H} \sim 0.4$). This star does not evolve bluewards to the WR regime and the Of/WNh population. This is linked to the increased envelope-to-core mass ratio, leading to the formation of a steep chemical gradient (Pauli et al. 2023; Schootemeijer & Langer 2018). After a short time (of the order of a few hundred thousand years), the remaining star will also collapse to a BH with a mass of $25\,M_\odot$. The two black holes orbit each other every 4.85 d. Following Peters (1964) we calculated the merger timescale of the binary to be $\tau_\mathrm{merger} = 18.5$ Gyr. This is longer than the age of the Universe. We note that our estimated value should be considered a lower limit as the BH masses of the individual components could be lower, which would result in even longer merger timescales.

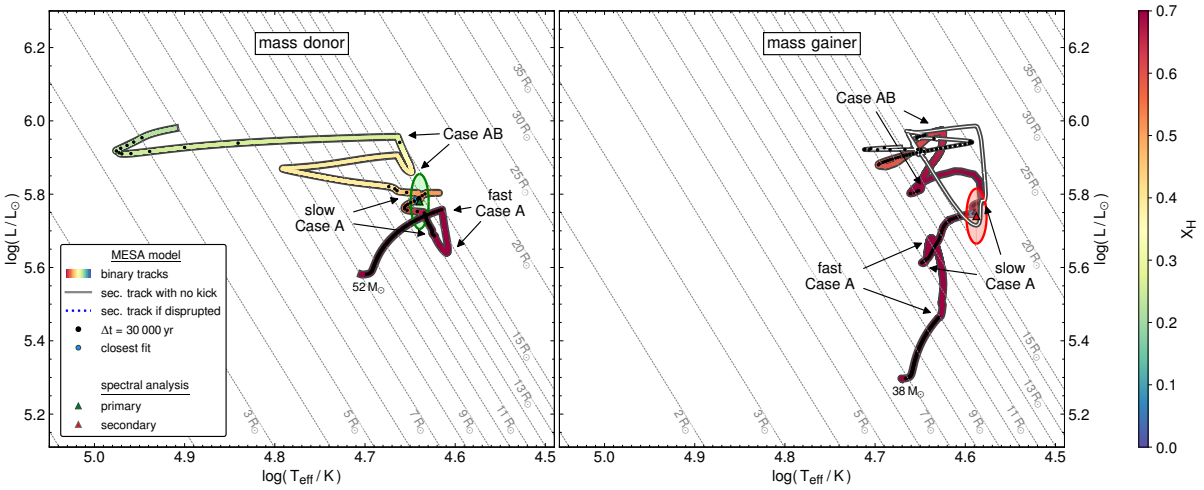

Fig. 3.5.1. Evolutionary tracks of the donor (left) and the accretor (right) colour-coded by their surface H-abundance. The track of the mass gainer is only colour-coded until the primary dies and then continues as a solid white line, assuming that the binary is not disrupted by a supernova explosion. The tracks are overlayed by black dots that show equidistant time steps of 30 000 yr to highlight phases in which the stars spend most of their time. The spectroscopic results are shown as green and red triangles surrounded by error ellipses. Start and end phases of fast and slow Case A, as well as Case AB mass-transfer are indicated by arrows. The iso-contours of equal radii are indicated in the background as dashed grey lines.

3.6. Discussion

3.6.1. Orbital, spectroscopic, and stellar evolutionary masses

The most reliable mass estimate is the projected orbital mass of the system (see Sect. 3.3). Since we do not have a light curve available, it is only possible to compare it with the spectroscopic result by choosing an inclination. However, this introduces additional uncertainties and makes the orbital masses inaccurate. A better way to compare the results is by using the derived mass ratios.

In Section 3.3 we obtained $q_{\mathrm{wilson}} = 1.34 \pm 0.07$ using the fitting method from Wilson (1941) and $q_{\mathrm{PHOEBE}} = 1.47^{+0.13}_{-0.09}$ when modelling the RV curve in detail with the PHOEBE code. From our spectroscopic analysis, we derived a somewhat higher mass ratio of $q_{\mathrm{spec}} = 1.7^{+2.9}_{-1.0}$. The large error margins arise from the uncertainties from fitting the surface gravity and from the uncertainties introduced in the multiple solutions that can be found for the luminosity ratio (i.e. $M_{\mathrm{spec}} \propto R^2 \propto L$). Hence, it could be that the spectroscopic mass ratio is overestimated. However, the conclusion that the primary component is more massive than the secondary component remains.

During the tailoring process of our evolutionary model towards the empirically derived stellar parameters, we exploited various combinations of the mass ratio of the two components. In these models, the mass and the position of the primary were always only explainable when it was in a slow Case A mass-transfer phase. The secondary in these models had different initial masses, and thus the mass during the Case A mass transfer was also different (i.e. lower) compared to our best-fitting model.

3.6.2. Effects of the inclination on the final parameters

3.6.2.1. Fundamental stellar and wind parameters

As discussed in the previous section, the orbital mass ratio and the spectroscopic mass ratio agree within their respective uncertainties. This agreement enabled us to estimate the inclination of the system to be $i_{\mathrm{orb}} = 16 \pm 1\,^{\circ}$ (see Sect. 3.3.3.2). This implies that we must be looking at the system pole-on. Given our estimates on the rotational velocities and the fact that the two stars are in contact, they must be oblate and deformed. Hence, the stellar parameters of these stars might no longer be uniform over the surface of the star.

Under the assumption of a star rotating close to break-up velocity, the effective surface gravity at the equator is $g_{\mathrm{equator}} \approx 0$ as the gravitational and centrifugal forces cancel each other out. On the other hand, the effective surface gravity on the pole must be rather unperturbed and is mostly affected by gravity. Since we are looking at

the pole region of the star, we conclude that our estimate on the surface gravity is reliable within its uncertainties, and hence also our estimate on the inclination.

Due to the effect of gravity darkening, an ellipsoidal star is cooler at the equator and hotter at the poles. Abdul-Masih (2023) studied the effect of rotation and inclination on the determined effective temperature by using synthetic models created with the SPAMMS code on a three-dimensional surface. He concluded that in the case of rapid rotation and low inclination, the star's temperature can be overestimated by 10%. This means that both of our stars actually might be 3 kK – 4 kK cooler. Furthermore, Abdul-Masih (2023) finds that the surface helium abundance of a rapidly rotating pole-on star can be underestimated by as much as 60%, which would account for the discrepancy between the observed helium abundance and the helium abundance from the binary evolutionary models.

Given the ellipsoidal shape and hence the different radii and temperatures, it might be evident that the star's luminosity also depends on the inclination angle. We calculated the expected luminosity of our target at the pole and the equator and find a difference $\Delta \log L/L_\odot \approx 0.15$, which is within our given uncertainties. The impact of a somewhat lower luminosity on our final results is too small to impact our final conclusions.

Due to the different effective surface gravities between the poles and the equator, wind parameters vary with inclination. The wind is slower and weaker in the equatorial regions, while it is faster and more powerful at the poles. An average mass-loss rate for the whole star would thus be lower than any measured from a low inclination angle, such as in our case. We would therefore treat our stated mass-loss rates as upper limits.

3.6.2.2. Discrepancy between observed and predicted rotation velocity

The binary evolutionary models agree with almost all spectroscopically derived stellar parameters, except the rotational velocity. Under the assumption that the inclination determined from the orbital analysis (see Sect. 3.3) is reliable, the observed rotation velocities of the binary components ($v_1 = 490 \pm 47\,\mathrm{km\,s^{-1}}$ and $v_2 = 544 \pm 49\,\mathrm{km\,s^{-1}}$) are a factor of two higher than those predicted by the binary evolutionary models.

Given that we are looking at the binary pole-on, and that both stars are deformed due to their fast rotation, this means that the assumption of spherical symmetry breaks down in the evolutionary models. Zahn et al. (2010) have shown this for a uniformly rapidly rotating star $R_{\mathrm{equator}} \approx 1.5 R_{\mathrm{pole}}$. Hence, under the assumption that $R \approx R_{\mathrm{pole}}$, the rotation rates of the binary model need to be corrected to $v_{\mathrm{mod,\,1}} \approx 325 \pm 45\,\mathrm{km\,s^{-1}}$ and $v_{\mathrm{mod,\,2}} \approx 425 \pm 50\,\mathrm{km\,s^{-1}}$. This brings observations and predictions closer together, but still shows some discrepancy. We note that our target is a contact binary, meaning that the stars are tear-drop shaped rather than ellipsoidal. This makes an estimate of the rotation rates even more complicated.

On the other hand, it is worth mentioning that in our stellar atmosphere calculations we neglect additional broadening mechanisms such as macroturbulence and asynchronous rotation (e.g. introduced by differential rotation). These effects are compensated for in our estimate of the projected rotational velocity $v \sin i$, and hence might lead to an overestimation, which can explain the observed discrepancy.

3.6.3. Empirical mass-loss rates

From our spectroscopic analysis (Sect. 3.4.2.5) we derived that the primary dominates most of the wind lines ($\log(\dot{M}_1 / (M_\odot\,\mathrm{yr^{-1}})) = -5.4$), while the secondary still has a significant and noticeable contribution in the wind UV lines ($\log(\dot{M}_2 / (M_\odot\,\mathrm{yr^{-1}})) = -7.3$). In the following we want to determine whether the chosen mass-loss rates agree with observations and theoretical expectations.

Following Rickard et al. (2022), we would expect from a star that has evolved in isolation and has a current luminosity of $\log(L/L_\odot) = 5.75$ a mass-loss rate of only $\log(\dot{M}_{\mathrm{Rickard}} / (M_\odot\,\mathrm{yr^{-1}})) = -7.35$. This is two orders of magnitude lower than that derived for the primary from empirically spectroscopic analysis. However, the primary has lost a huge amount of mass and has an unusual L/M ratio that is not considered in their relation. On the other hand, theoretical mass-loss recipes take into account several parameters, such as luminosity, mass, temperature and metallicity. For comparison, we calculated the mass-loss rate predicted with the frequently used Vink et al. (2001) to be $\log(\dot{M}_{\mathrm{Vink,\,1}} / (M_\odot\,\mathrm{yr^{-1}})) = -5.9$. A more updated recipe for O-type stars is from Björklund et al. (2022). Their mass-loss recipe predicts $\log(\dot{M}_{\mathrm{Bjrklund\ 2022,\,1}} / (M_\odot\,\mathrm{yr^{-1}})) = -6.6$, which is one order of magnitude lower than the observed mass-loss rate. However, these mass-loss rates are calculated for H-rich ($X_{\mathrm{H}} > 0.7$). The primary has already lost a significant amount of its envelope, and its surface H-abundance already dropped to $X_{\mathrm{H}} \approx 0.6$ (see Table 3.4.2). For completeness, we calculated the corresponding WR mass-loss rates according to Shenar et al. (2019, 2020c) for stars with $X_{\mathrm{H}} > 0.4$, yielding $\log(\dot{M}_{\mathrm{Shenar,\,1}} / (M_\odot\,\mathrm{yr^{-1}})) = -5.5$ and being in agreement with the empirically derived values.

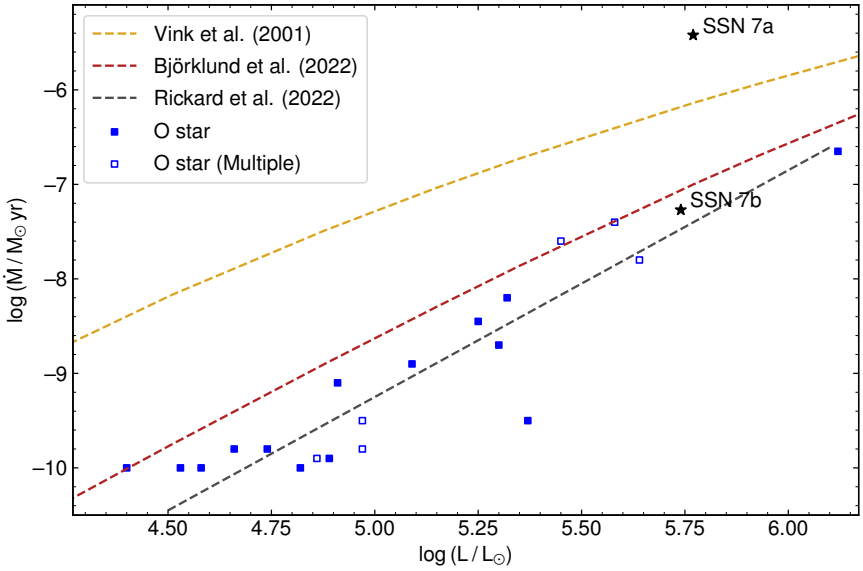

Fig. 3.6.1. Observed mass-loss rates of O stars in NGC 346 (including SSN 7) as a function of stellar luminosity compared to theoretical and empirical relations. The position of both binary components of SSN 7 are marked by black stars. The data is complemented by O stars from Rickard et al. (2022). Apparently single stars are shown as filled blue squares and known muliple systems as open blue squares. In the background the empirical relation of main-sequence O-type stars from Rickard et al. (2022) is included as dashed black line. In addition, we show the theoretical relations of Vink et al. (2001) and Björklund et al. (2022) for main-sequence stars as dashed yellow and dashed red line, respectively.

The secondary seems to be more well behaved. Its empirically derived mass-loss rates agrees well with the expectations from other O stars in the SMC (Rickard et al. 2022). The theoretical predicted rates from Vink et al. (2001) and Björklund et al. (2022) are $\log(\dot{M}_{\mathrm{Vink,\,2}} / (M_\odot\,\mathrm{yr}^{-1})) = -6.2$ and $\log(\dot{M}_{\mathrm{Bjrklund\ 2022,\,1}} / (M_\odot\,\mathrm{yr}^{-1})) = -7.1$, respectively. Only the latter agrees within the error margins of the observed mass-loss rates. For comparison, we illustrate in Fig. 3.6.1 the expected mass-loss rates from other O-type stars in NGC 346 compared to our spectroscopically fit values, alongside theoretical prescriptions.

3.6.4. SSN 7 and its role in NGC346

In the recent paper of Rickard et al. (2022), it is noted that the massive giant NGC 346 SSN 9 (MPG 355, O2III(f*), Walborn et al. 2000) is the major ionising source of the core region. In their work it is stated that the star outshines the remaining O-star population and is responsible for 50% of the hydrogen ionising flux ((log $Q_{\mathrm{H,\,SSN\,9}} = 49.98$). However, in their analysis SSN 7 was neglected because of its binary nature. According to our stellar atmosphere models, we find that the two early-type stars in the binary have a combined hydrogen ionising flux of $\log Q_{H,\,\mathrm{SSN7\,a+b}} = 49.88$. This makes SSN 7 one of the two major contributors to the H ionising flux of the core of NGC 346. We stated in Rickard et al. (2022) that the morphology of the ionising front within images of NGC 346 centre upon SSN 9. The location of SSN 7 is directly 'behind' SSN 9 from the position of the ionising front (Fig. 3.1.1).

We compared the calculated H ionising photon count of both components of SSN 7 to other massive stars within both the SMC and LMC (Fig. 3.6.2). The predicted ionising flux is consistent with the spectral types assigned to each component by Walborn et al. (2000), even though the primary has an outstanding L/M ratio and the secondary that is suspected to have accreted several solar masses.

For helium ionising photons, the model of the primary gives $\log Q_{\mathrm{He\,I,\,SSN\,7a}} = 48.98$ and $\log Q_{\mathrm{HeII,\,SSN\,7a}} = 40.81$, while the secondary model gives $\log Q_{\mathrm{He\,I,\,SSN\,7b}} = 48.58$ and $\log Q_{\mathrm{HeII,\,SSN\,7b}} = 43.14$. Combined, the helium ionising fluxes of the two components of the binary combined are $\log Q_{\mathrm{HeI,\,SSN7\,a+b}} = 49.12$ and $\log Q_{\mathrm{HeI,\,SSN7\,a+b}} = 43.14$, or 25% and 0.04% of the total of the O stars analysed in the core of NGC 346 between this paper and Rickard et al. (2022). This is compared to $\log Q_{\mathrm{HeI,\,SSN\ 9}} = 49.41$ and $\log Q_{\mathrm{HeII,\,SSN\ 9}} = 46.50$, or 31% and 99%. This is notable because the combined He I ionising flux for the binary is comparable to that of SSN 9, but not for the He II ionising flux, where SSN 9 dominates.

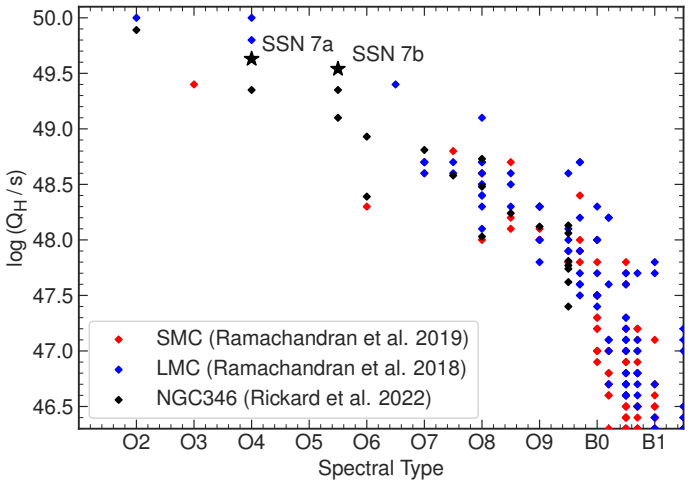

Fig. 3.6.2. log Q_H to spectral type. SMC sample stars analysed by Ramachandran et al. (2019) are included (red diamonds) as well as LMC stars from Ramachandran et al. (2018b) (blue diamonds) and O stars from the core of NGC 346 from Rickard et al. (2022) (black diamonds). The two components of the SSN 7 binary are shown separately.

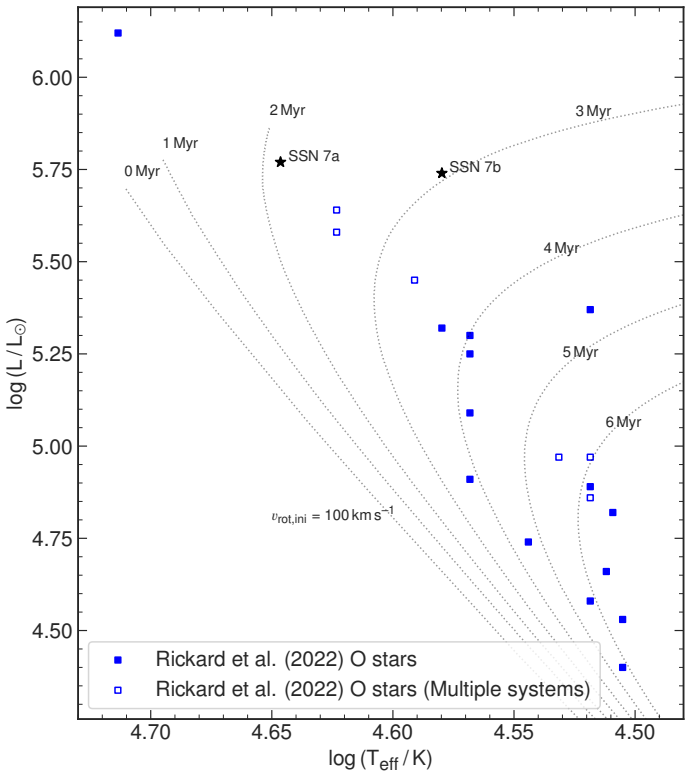

Fig. 3.6.3. HR diagram showing the position of the two components of SSN 7 as determined by our spectrographic analysis. Black stars are the two SSN 7 components. Blue symbols are the other O stars within the central core of NGC 346 (Rickard et al. 2022). Open symbols are noted spectral binaries (Dufton et al. 2019). Dotted lines are isochrones with $Z = 0.002$ (Georgy et al. 2013) and an initial rotation of 100 km s^{-1}.

3.6.5. Age of the NGC 346 O-star population

During our evolutionary analysis it was revealed that the system of SSN 7 has an age of 4.2 Myr (see Sect. 3.5.2). Meanwhile, much younger ages for NGC346 have been estimated in previous works, such as 1 – 2.6 Myr (Dufton et al. 2019) and 1 – 2 Myr (Walborn et al. 2000). In Fig. 3.6.3 we compare the empirically derived stellar parameters of SSN 7 and other O stars (Rickard et al. 2022) to isochrones from Georgy et al. (2013). According to these isochrones, the age of the primary should be 2 Myr, while the secondary would be 3 Myr old. This mismatch

between the age predicted through evolutionary modelling and the age compared to single-star isochrones is not an isolated example and could lead to false conclusions on the age of the cluster.

When inspecting Fig. 3.6.3 in more detail we can see that most of the luminous O stars in NGC 346 are known binaries, or higher order multiple systems, with the one exception of SSN 9. However, this star is unusually luminous and hot and undermassive for its position in the HRD, hinting towards a binary nature. Taking into account only the apparent single O stars in this cluster, we conlcude the age of the O-star population, according to single-star evolution isochromes, to be 4 Myr, which is consistent with the age derived from our binary models.

With evidence that the core of NGC 346 has not yet been affected by any supernova explosion (Danforth et al. 2003), the fate of more massive stars within NGC 346 comes into question. Either none had formed yet, or those that did have imploded into BHs directly.

3.6.6. Luminosity class and spectral type

In the previous work of Walborn (1978), SSN 7 was classified as O4 III(n)(f), but it was not known to be a binary. In a recent work, Dufton et al. (2019) propose that the presence of He I λ 4471 absorption and weak He II λ 4686 emission suggest that the primary should be a O4 If star. With the new insights gained from the detailed multi-epoch observations, we assign the He I λ 4471 absorption mainly to the secondary component, meaning that the primary has an earlier type.

Here we want to use the newly gained insights from the spectral analysis to reclassify the primary and secondary star. It is evident that the primary in our model shows only a very weak contribution to the He I λ 4471 line (see Fig. 3.4.2), meaning that it must be of very early type (O2-3.5). Following Walborn et al. (2002) it is suggested to use for such early-type stars the ratio of N IV λ 4058 to N III λ 4640 emission. The multi-epoch observations have shown that the N III λ 4640 emission line is a blend of the primary and secondary components, while the N IV λ 4058 purely originates from the primary (see Fig. 3.4.5 and Table B.1.3). Guided by our stellar atmosphere models we find that N IV λ 4058 > N III λ 4640, while we see very weak or no absorption in He I λ 4471, implying a spectral type of O3.

According to our spectral analysis we find that in the primary nitrogen is enhanced, while carbon and oxygen are deficient. Therefore, we add the qualifier 'N' to the spectral type. Following the classification criteria of Sota et al. (2011) and taking into account that the N IV λ 4058 emission feature is greater than the N III λ 4640 emission and that the He II λ 4686 is also in emission we suggest adding the suffix 'f*'. In Sota et al. (2014) the luminosity classes are linked to the spectral type as a function of the f phenomenon, suggesting a luminosity class I for the primary. Because of the high temperature of the star, combined with the low Si IV abundance ($\sim$ 2% solar), no Si IV $\lambda\lambda$ 1394, 1403 P Cygni lines are observed (Crowther et al. 2002), so the presence or absence of this line cannot contribute to our luminosity classification. The final spectral type we assign to the primary is ON3 If*.

Observational counterparts with similar spectral type at low metallicity are sparse. Galactic examples are Cyg OB2-7 and Cyg OB2-22A. By comparison of their observed spectra to the synthetic spectrum of our primary we find a good agreement between the morphology of the lines, supporting our choice on the spectral type.

For the secondary, we limit its spectral type to O4-8 as it shows He I λ 4471 in absorption, while He II λ 4542 > He I λ 4388 and He II λ 4200 > He I λ 4144, and it lacks Si III λ4552, which can be seen in the earliest O-type stars. Hence, we follow Conti & Alschuler (1971) and use the logarithmic ratio of the equivalent widths of He I λ 4471 and He II λ 4542. Unfortunately, the He II λ 4542 line is blended by the companion. Therefore, we decided to use the equivalent widths of the synthetic spectrum of the secondary, yielding log(EW(4471)/EW(4542)) = -0.45. This corresponds to a spectral type of O5.5. As mentioned above, the N III λ 4640 emission line is a blend from the primary and secondary component. As the secondary does not contribute to the N IV λ 4058 line and shows strong He II λ 4686 absorption we add the suffix '((f))' (Sota et al. 2011). Following Sota et al. (2014), given the spectral type and the f phenomenon, the star should have a luminosity class V. We use the criterion for the luminosity class estimation introduced by Martins (2018). The criterion is based on the equivalent width of He II λ 4686 absorption line in the synthetic model of the secondary. With an equivalent with of EW(4868)) = 0.74, this star is confirmed to have a luminosity class V. The final spectroscopic classification of the binary is ON3 If*+O5.5 V((f)).

3.7. Conclusions

We have conducted the first consistent multi-wavelength multi-epoch spectral analysis of the SB 2 contact binary SSN 7 located in the NGC 346 cluster in the SMC. The detailed analysis revealed that SSN 7 is a system with two binary components that have comparable luminosity ($\log(L/L_\odot) \approx 5.75$), while having divergent stellar and wind parameters. The primary is the hotter ($T_{\rm eff,1} = 43.6$ kK) but less massive ($M_1 = 32\,M_\odot$) component. We revealed that the surface hydrogen abundance is $X_{\rm H} = 0.6$, and that it has CNO values close to those of the

CNO equilibrium. The mass-loss rate of the primary, $\log(\dot{M}_1 / (M_\odot\,\mathrm{yr}^{-1})) = -5.4$, is exceptionally high for its luminosity. The secondary is slightly cooler ($T_{\mathrm{eff},2} = 38.7\,\mathrm{kK}$), but more massive ($M_2 = 55\,M_\odot$). The secondary has a mass-loss rate of $\log(\dot{M}_2 / (M_\odot\,\mathrm{yr}^{-1})) = -7.3$, which is in agreement with other O stars within the SMC that have similar luminosity. The findings suggest that the two binary components exchange mass. Based on the newly gained insights we reclassified the system as ON3 If*+O5.5 V((f)).

The multi-epoch RV analysis of 19 separated observations, including 11 spaced over ten days, allowed us to constrain the orbital parameters. The best fit is achieved with a period of $P = 3.07\,\mathrm{d}$ and a circular orbit. The orbital analysis confirms a mass ratio of $q_{\mathrm{orb}} = 1.5$, favouring the secondary to be more massive and supporting the theory of a binary interaction. Furthermore, given the orbital and stellar parameters, we calculated the Roche radius and found that both components are filling their Roche lobes and must be in contact.

From initial abundances consistent with NGC 346, we have modelled possible stellar evolution pathways that explain the empirically derived stellar and orbital parameters of SSN 7. Our favourite model predicts that the system has an age of $\sim$ 4 Myr. In this context, we review the age of the O-star population within the core of NGC 346 and see that no single star (except for the peculiar massive object SSN 9) is to the left of the 4 Myr isochrone. We postulate that the age of the O-star population within the core of NGC 346 is older than $\gtrsim 4$ Myr.

The binary evolutionary models are capable of explaining the currently observed contact phase and predict that both stars are still undergoing slow Case A mass transfer. This makes SSN 7 the most massive Algol-like system known to date, enabling the study of the physics of binary interactions in a way previously unavailable. This will shape our understanding of post-interaction massive binaries, binary BHs, and ultimately, the progenitors of GW events.

Acknowledgments: DP acknowledges financial support by the Deutsches Zentrum für Luft und Raumfahrt (DLR) grant FKZ 50 OR 2005. MJR and DP acknowledge Prof. Wolf-Rainer Hamann, Prof. Lida Oskinova, Dr. Rainer Hainich, and Dr. Heldge Todt of the Institut für Physik und Astronomie, Universität Potsdam. Dr. Andreas Sander and Dr. Varsha Ramachandran of Zentrum für Astronomie der Universität Heidelberg, Astronomisches Rechen-Institut, and Dr. Tomer Shenar of the Institut for Astronomy, University of Amsterdam, and all other contributors to the PoWR code. This publication has benefited from a discussion at a team meeting sponsored by the International Space Science Institute at Bern, Switzerland.

Chapter 4

Manuscript III: Spectroscopic and evolutionary analyses of the binary system AzV 14 outline paths toward the WR stage at low metallicity

D. Pauli, L. M. Oskinova, W.-R. Hamann, D. M. Bowman, H. Todt, T. Shenar, A. A. C. Sander, C. Erba, V. M. A. Gómez-González, C. Kehrig, J. Klencki, R. Kuiper, A. Mehner, S. E. de Mink, M. S. Oey, V. Ramachandran, A. Schootemeijer, S. Reyero Serantes, A. Wofford

Astronomy & Astrophysics, 2023, Volume: 673, ID: A40, 19 pp.

Abstract

The origin of the observed population of Wolf-Rayet (WR) stars in low-metallicity galaxies, such as the Small Magellanic Cloud (SMC), is not yet understood. Standard, single-star evolutionary models predict that WR stars should stem from very massive O-type star progenitors, but these are very rare. On the other hand, binary evolutionary models predict that WR stars could originate from primary stars in close binaries. We conduct an analysis of the massive O star, AzV 14, to spectroscopically determine its fundamental and stellar wind parameters, which are then used to investigate evolutionary paths from the O-type to the WR stage with stellar evolutionary models. Multi-epoch UV and optical spectra of AzV 14 are analyzed using the non-local thermodynamic equilibrium (LTE) stellar atmosphere code PoWR. An optical TESS light curve was extracted and analyzed using the PHOEBE code. The obtained parameters are put into an evolutionary context, using the MESA code. AzV 14 is a close binary system with a period of $P = 3.7058 \pm 0.0013$ d. The binary consists of two similar main sequence stars with masses of $M_{1,2} \approx 32\,M_{\odot}$. Both stars have weak stellar winds with mass-loss rates of $\log \dot{M}/(\,M_{\odot}\,\mathrm{yr}^{-1}) = -7.7 \pm 0.2$. Binary evolutionary models can explain the empirically derived stellar and orbital parameters, including the position of the AzV 14 components on the Hertzsprung-Russell diagram, revealing its current age of 3.3 Myr. The model predicts that the primary will evolve into a WR star with $T_{\mathrm{eff}} \approx 100$ kK, while the secondary, which will accrete significant amounts of mass during the first mass transfer phase, will become a cooler WR star with $T_{\mathrm{eff}} \approx 50$ kK. Furthermore, WR stars that descend from binary components that have accreted significant amount of mass are predicted to have increased oxygen abundances compared to other WR stars. This model prediction is supported by a spectroscopic analysis of a WR star in the SMC. Inspired by the binary evolutionary models, we hypothesize that the populations of WR stars in low-metallicity galaxies may have bimodal temperature distributions. Hotter WR stars might originate from primary stars, while cooler WR stars are the evolutionary descendants of the secondary stars if they accreted a significant amount of mass. These results may have wide-ranging implications for our understanding of massive star feedback and binary evolution channels at low metallicity.

4.1. Introduction

Massive stars ($M_{\rm initial} > 8\,M_{\odot}$) in all evolutionary phases strongly affect their galactic neighborhood via stellar winds and ionizing fluxes. During core-H burning on the main sequence, they have spectral types O and early B. As massive stars evolve, their outer hydrogen (H) rich envelopes could be removed by stellar winds. The majority of massive stars are born in binary systems (e.g Sana et al. 2012, 2014; Moe & Di Stefano 2017), and interactions with a companion star may also lead to a removal of the outer envelope. Highly evolved massive stars that lost a large portion of their outer H-rich layers and have optically thick winds are spectroscopically classified as Wolf-Rayet (WR) stars. The WR stars are typically hotter and have stronger, optically thick winds when compared with their evolutionary predecessors. These stars come in two major subtypes, WN and WC, which are spectroscopically identified by strong emission lines of nitrogen and carbon, respectively. WR stars end their lives with a core-collapse event, likely leading to the formation of black holes (BHs; e.g., Sukhbold et al. 2016; Gal-Yam et al. 2022). Understanding the formation pathways of WR stars in nearby low-metallicity galaxies is needed for quantifying stellar feedback and compact object populations in conditions resembling the early Universe.

The Small Magellanic Cloud (SMC) galaxy has a metallicity of $Z \approx 1/7\,Z_{\odot}$ (Hunter et al. 2007; Trundle et al. 2007) and is nearby ($d \approx 61$ kpc; Hilditch et al. 2005), thus providing an excellent test bed for investigating stars at low metallicity. The proximity of the SMC and its low foreground and intrinsic extinction allows for a detailed study of stellar and wind parameters of low-metallicity populations of O and WR stars. This enables us to obtain a realistic understanding of massive star evolution and feedback at low metallicity in general.

Yet what we have learned so far is perplexing. Only 12 WR stars exist in the SMC. All of them are very luminous and (except for one WO-type star) contain some hydrogen (Hainich et al. 2015; Shenar et al. 2016). According to the standard, single-star evolutionary tracks, their progenitors are O-type stars with masses $\gtrsim 40\,M_{\odot}$ (Shenar et al. 2020b, and references therein). For an order of magnitude estimate, one can assume that a massive star spends 10 % of its life in a WR stage. This implies that a galaxy containing approximately ten WR stars should contain approximately one-hundred massive O stars. However, there is a severe paucity of such O-stars in the SMC (Ramachandran et al. 2019; Schootemeijer et al. 2021).

Close binary evolution is expected to play a principal role in the formation of WR stars (Paczyński 1967; Kippenhahn & Weigert 1967). However, the importance of binarity is still under debate and different studies have come to different conclusions (e.g., Vanbeveren et al. 2007; Eldridge et al. 2017; Shenar et al. 2020b; Pauli et al. 2022a). Up to now, the evolution toward the WR stage in binaries has chiefly been studied for primary stars, while the evolution of secondary stars has been largely neglected. In this paper, we aim to gain insights into the evolution of both components in a binary with well-established stellar parameters.

One of the youngest and earliest O-type stars in the SMC is AzV 14, the main ionizing source of the H II region NGC 261 (see Fig. 4.1.1). Previously, single epoch optical spectra of AzV 14 have been analyzed by Massey

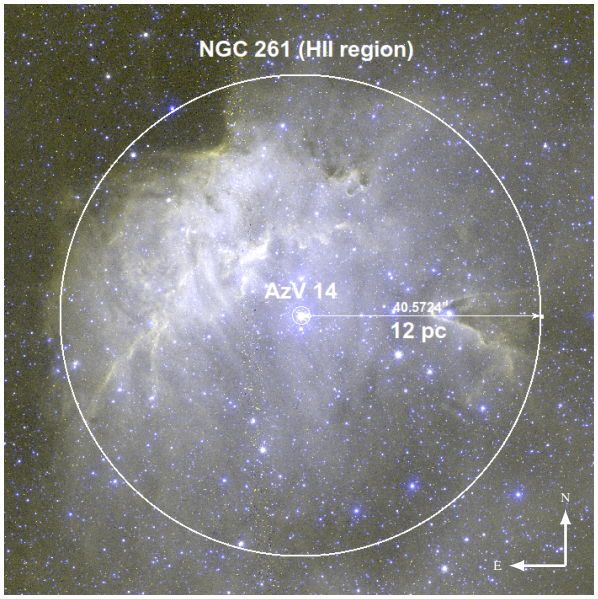

Fig. 4.1.1. False-color HST image composed of the images in the F475W (blue) and F657N (yellow) filters. The position of AzV 14 and the approximate size of the NGC 261 H II region are indicated by white circles.

et al. (2004) and Mokiem et al. (2006). The star was classified as O5 V with a reported spectroscopic mass of $74\,M_\odot - 90\,M_\odot$ being in the mass range of potential WR single-star progenitors. From a newly obtained light curve, we know now that AzV 14 is in fact a binary. In this paper, we complement recently obtained spectra of AzV 14 in the UV and optical by archival data, aiming at securely determining stellar parameters and, on this basis, to model the evolution of the AzV 14 components toward WR stages.

4.2. Observations

Presently, six spectra of AzV 14 obtained at different epochs covering the far-UV, UV and optical wavelength ranges exist in telescope archives. One far-UV spectrum was taken with the Far Ultraviolet Spectroscopic Explorer (FUSE; Oegerle et al. 2000), two UV spectra with the Hubble Space Telescope's (HST) Faint Object Spectrograph (FOS; Keyes et al. 1995) and Space Telescope Imaging Spectrograph (STIS; Branton et al. 2021), and three optical spectra with the European Southern Observatory (ESO) Very Large Telescopes (VLT) Ultraviolet and Visual Echelle Spectrograph (UVES; Dekker et al. 2000) and the X-Shooter (Vernet et al. 2011) spectrograph. One X-Shooter spectrum was taken as part of the XShootU project[1] (from here on "X-Shooter (2020)") and one as part of our program, ID 109.22V0.001 (from here on "X-Shooter (2022)"). A detailed description of the individual spectra and photometry can be found in Appendix C.1.

AzV 14 is close to the SMC bar, thus we adopt a distance modulus of $DM = 18.9$ mag (Westerlund 1997; Harries et al. 2003; Hilditch et al. 2005). The radial velocities (RV) of the different regions in the SMC are not uniform (e.g., De Propris et al. 2010). We estimate the RV shift of the NGC 261 complex by fitting Gaussians to interstellar absorption lines as $v_{\mathrm{NGC\,261}} = 148 \pm 2\,\mathrm{km\,s^{-1}}$. All spectra shown in this work are in the rest frame of NGC 261.

AzV 14 was observed by the NASA Transiting Exoplanet Survey Satellite (TESS; Ricker et al. 2015) mission (TIC 180206579) during its sectors 1, 27 and 28 in full-frame image (FFI) mode with a cadence of 30, 10 and 10 min, respectively. TESS has a low spatial resolution of $21''\,\mathrm{px}^{-1}$. However, since AzV 14 is the brightest optical object in this region we can extract its light curve (see Appendix C.3). Furthermore, AzV 14 was detected by the *Chandra* X-ray telescope (Weisskopf et al. 2000).

4.3. Spectral analysis

4.3.1. Spectral line variability reveals AzV 14 as a close binary

The multi-epoch spectroscopy allows us to search for signs of binarity. In Fig. 4.3.1, we show selected He I and He II lines in the UVES and X-Shooter spectra, taken at different epochs. Massey et al. (2004) and Mokiem et al. (2006) attributed the apparent emission feature in the middle of helium absorption lines of the UVES to a nebular contamination. New multi-epoch X-Shooter spectra clearly show that the profiles of helium lines are complex and variable. They are well explained as composite lines originating from two components of a binary system. The UVES and X-Shooter (2022) spectra must have been taken at a comparable orbital phase, as the line profile is similar in both spectra, while the X-Shooter (2020) spectrum must have been obtained close to conjunction. This is confirmed by the binary ephemeris derived in the Sect. 4.4.

[1] https://massivestars.org/xshootu/

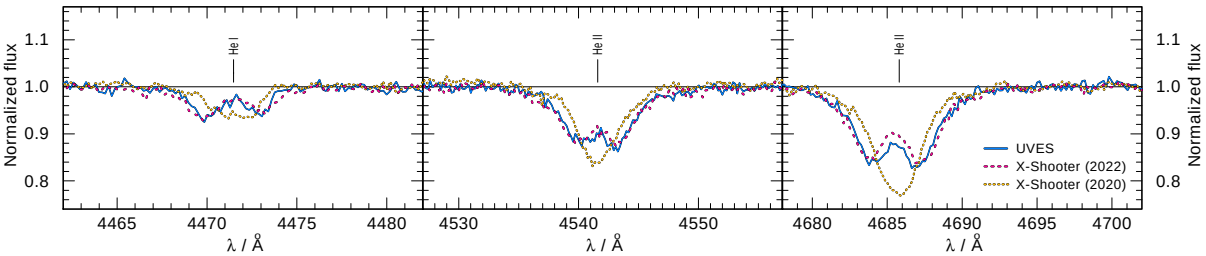

Fig. 4.3.1. Comparison of selected lines in the UVES (solid blue) and the X-Shooter (dashed pink and dotted yellow) optical spectra. The high resolution UVES spectrum is binned by 0.15 Å to match the X-Shooter spectra. All spectra are convolved with a Gaussian having a FWHM = 0.05 Å for a better comparison. The lines in the UVES and X-Shooter (2022) spectra are separated, while they are blended in the X-Shooter (2020) spectrum. This provides a clear indication for binarity.

4.3.2. Establishing projected rotation velocity and RVs

The projected rotation velocity as well as the RV shifts of the individual binary components are necessary ingredients of spectral modeling. In the following we describe how we derived these quantities.

4.3.2.1. Projected rotation velocities

The helium lines in UVES and X-Shooter (2022) spectra are resolved into two components with lines of similar depths and widths, indicating that the components of the binary system are similar stars. We employ the `iacob broad` tool (Simón-Díaz & Herrero 2014) to measure the projected rotational velocities for each binary component. For the fitting procedure the lines He II λ4200, He I λ4471, He II λ4542, and He II λ4686 were used, while cutting off the parts of the lines that are blended by the companion. Although helium lines are not only rotationally, but also pressure broadened, they were analyzed because of the lack of available metal lines. The `iacob broad` tool derives two different values for the projected rotational velocities, one from a Fourier transformation (FT) and one from the goodness of the fit (GoF). We quote the average value obtained by the different methods. As the estimates on the projected rotation velocities are based on blended lines, we adopt conservative error margins. We find that both binary components have similar projected rotational velocities of $v_{\rm rot} \sin i = 90 \pm 20\,{\rm km\,s^{-1}}$.

4.3.2.2. RVs of the binary components in each spectrum

The RVs of all spectra are determined by shifting the synthetic spectra until they fit the observations using a Markov chain Monte Carlo method combined with a least square fitting (Pauli et al. 2022b, their section 3.1.2 and their appendix A).

The UVES spectrum shows RVs of $v_1 = -101.9 \pm 2.6\,{\rm km\,s^{-1}}$ and $v_2 = 80.5 \pm 3.2\,{\rm km\,s^{-1}}$ for the primary and the secondary, respectively. This is comparable to those of the X-Shooter (2022) spectrum, yielding RV shifts of $v_1 = -112.4 \pm 2.6\,{\rm km\,s^{-1}}$ and $v_2 = 98.6 \pm 2.9\,{\rm km\,s^{-1}}$. In the X-Shooter (2020) spectrum the lines are not split due to an orbital phase close to conjunction. We estimated $v_1 = -46.1 \pm 5.8\,{\rm km\,s^{-1}}$ and $v_2 = 22.3 \pm 5.9\,{\rm km\,s^{-1}}$ for the primary and secondary, respectively. Accurate measurements of RV shifts in the optical spectra allow us to estimate the temperature and surface gravity of the individual binary components (see Sect. 4.3.3.1).

In the STIS spectrum, the He II λ1640 line is split into two individual components of similar strength (see Fig. C.4.4), yielding RVs of $v_1 = -128.6 \pm 2.5\,{\rm km\,s^{-1}}$ for the primary and $v_2 = 113.2 \pm 2.3\,{\rm km\,s^{-1}}$ for the secondary. Measuring RVs in the UV spectra allows to determine the terminal wind velocity (v_∞) and thus the mass-loss rate ($\dot{M}$) more precisely (see Sect. 4.3.3.4). We estimated the RVs in the low resolution FOS spectrum such that the width of the oxygen lines in the range of 1330 Å – 1420 Å can be matched, arriving at $v_1 = 92.9 \pm 6.2\,{\rm km\,s^{-1}}$ for the primary and $v_2 = 113.2 \pm 2.8\,{\rm km\,s^{-1}}$ for the secondary.

4.3.3. Stellar atmosphere modeling

To analyze the spectra, we employ the Potsdam Wolf-Rayet (PoWR) model atmosphere code (Gräfener et al. 2002; Hamann & Gräfener 2003, 2004; Todt et al. 2015b; Sander et al. 2015). A short characterization of the code is given in Appendix C.2.

4.3.3.1. Temperatures and surface gravities

We measure the stellar temperatures using the ratio between He I to He II lines (see Fig. C.4.1). To constrain the surface gravities, we used the wings of the Balmer, Hβ, Hγ, and Hδ lines in the UVES and X-Shooter (2022) spectra. For the primary we obtained an effective temperature of $T_1 = 43 \pm 2\,{\rm kK}$, while the secondary is slightly cooler with $T_2 = 42 \pm 2\,{\rm kK}$. The surface gravity is $\log g = 4.0 \pm 0.2$ for both binary components.

4.3.3.2. Stellar luminosities and spectroscopic masses

Luminosity L and color excess $E_{\rm B-V}$ are determined by fitting the composite spectral energy distribution (SED) — containing the synthetic flux of both stellar components — to photometry (see Fig. C.4.2). The color excess is modeled as a combined effect of Galactic foreground, using the reddening law by Seaton (1979) with $E_{\rm B-V,\,Gal} = 0.03$ mag, and SMC background, using the reddening law by Bouchet et al. (1985) with $E_{\rm B-V,\,SMC} = 0.11$ mag.

Table 4.3.1. Summary of the stellar parameters of both binary components obtained from spectroscopic analysis conducted with the PoWR code.

parameter	primary	secondary	unit
$T_{\rm eff}$ [a]	42.8 ± 2.0	41.8 ± 2.0	[kK]
$\log g$	4.0 ± 0.2	4.0 ± 0.2	[cm s^{-2}]
$\log L$	5.41 ± 0.15	5.38 ± 0.15	[$L_\odot$]
R	9.3 ± 0.5	9.2 ± 0.5	[$R_\odot$]
$R_{\rm RL}$ [b]	15.6 ± 0.8	15.2 ± 0.7	[$R_\odot$]
$R/R_{\rm RL}$	0.60 ± 0.04	0.61 ± 0.04	
$M_{\rm spec}$	32^{+8}_{-7}	31^{+8}_{-7}	[$M_\odot$]
$\log \dot{M}$	-7.7 ± 0.2	-7.7 ± 0.2	[$M_\odot$ yr^{-1}]
v_∞	1600 ± 200	1600 ± 200	[km s^{-1}]
$v_{\rm rot} \sin i$ [c]	90 ± 20	90 ± 20	[km s^{-1}]
$v_{\rm rot}$ [d]	157 ± 40	157 ± 40	[km s^{-1}]
$P_{\rm rot}$ [d]	3.0 ± 0.8	3.0 ± 0.8	[d]
$\log Q_{\rm H}$	49.13	49.10	[s^{-1}]
$\log Q_{\rm He\,I}$	48.41	48.35	[s^{-1}]
$\log Q_{\rm He\,II}$	43.41	43.27	[s^{-1}]

[a] For a definition, see Appendix C.2. [b] Calculated using the orbital parameters obtained with the PHOEBE code (see Sect. 4.4) and the formula of Eggleton (1983). [c] Obtained with the `iacob broad` tool. [d] Based on the inclination $i = 35°$ obtained with the PHOEBE code (see Sect. 4.4).

The luminosities of the two binary components are chosen such that the ratio of the depths of the synthetic helium lines match all spectra. Additionally, we use the C III λ1175 line in the UV, which is sensitive to changes in the light ratio. Both stars have comparable luminosities in the optical and UV. The final luminosities are $\log(L_1/L_\odot) = 5.41 \pm 0.15$ and $\log(L_2/L_\odot) = 5.38 \pm 0.15$ for the primary and secondary, respectively. Accordingly, the masses of the primary and secondary are $M_{\rm spec,\,1} = 32^{+8}_{-7}\,M_\odot$ and $M_{\rm spec,\,2} = 31^{+8}_{-7}\,M_\odot$. The spectroscopic mass ratio is $q_{\rm spec} = 0.97$. When employing the method of Wilson (1941), one can derive an independent measure of the mass ratio from the RVs. This yields $q_{\rm Wilson} = 0.95 \pm 0.02$ which is in agreement with the spectroscopic results.

4.3.3.3. CNO surface abundances

All metal lines are well-matched with standard initial abundances of the SMC (see Table C.2.1 and Fig. C.4.3). The only line which is not well reproduced is the N IV λ3479 line, which is deeper than predicted by the synthetic spectrum. This absorption line is quite narrow, suggesting that the N IV λ3479 line might be blended with an unidentified ISM line. Pristine abundances prompt us to conclude that the AzV 14 components are young unevolved stars which have not yet interacted.

4.3.3.4. Wind mass-loss rates

In the optical spectra of AzV 14, Hα and He II λ4686 do not show any contribution from winds. However, in the UV one can see wind lines with P Cygni profiles. Key diagnostic lines are the N V $\lambda\lambda$1239, 1243 and C IV $\lambda\lambda$1548, 1551 resonance doublets and the He II λ1640 line. By fitting the observed N V and C IV resonance doublets in the STIS and FOS spectra consistently yields a terminal wind velocity of $v_\infty = 1600 \pm 200\,{\rm km\,s^{-1}}$ and a mass loss rate of $\log(\dot{M}/(\,M_\odot\,{\rm yr^{-1}})) = -7.7$ for each of the stars (see Fig. C.4.4).

To match the O VI $\lambda\lambda$1032, 1038 resonance doublet in the FUSE spectrum, we include in the model a hot plasma component with $T_{\rm X} = 3\,{\rm MK}$ emitting X-rays with $L_{\rm X,mod} = 2 \times 10^{30}\,{\rm erg\,s^{-1}}$. According to the *Chandra* Point Source Catalog v.2.0 (Evans et al. 2010), the X-ray flux of AzV 14 in the $0.5\,{\rm keV} - 7.0\,{\rm keV}$ band is $F_{\rm X} = 7.3 \times 10^{-16}\,{\rm erg\,s^{-1}\,cm^{-2}}$, corresponding to an X-ray luminosity corrected for reddening (see Fig. C.4.2) $L_{\rm X} \approx 5 \times 10^{32}\,{\rm erg\,s^{-1}}$ or $\log(L_{\rm X}/L_{\rm bol}) \approx -6$. We suggest that the majority of the observed X-rays originate from

a colliding wind zone between two binary components in common with O-type binaries in the Galaxy (Rauw & Nazé 2016). A summary of the empirically determined stellar parameters is given in Table 4.3.1.

4.4. Orbital analysis

The TESS light curve of AzV 14 displays periodic variability (originating from ellipsoidal variability, see Fig. 4.3.2). We employed a frequency analysis and phase folding techniques to determine the dominant periodicity in the TESS light curve, yielding an orbital period of $P_{\rm orb} = 3.7058 \pm 0.0013$ d (see Appendix C.3).

Orbital parameters from the light and RV curve are determined consistently with the Physics of Eclipsing Binaries (PHOEBE) code version 2.4.5 (Prša & Zwitter 2005; Prša 2011; Prša et al. 2016; Horvat et al. 2018; Jones et al. 2020; Conroy et al. 2020). The input parameters are provided by the spectral analysis (Table 4.3.1). To reduce the free parameter space, the orbital period is fixed to the period measured from the TESS light curve. Since the light curve is sinusoidal and has minima at phases $\Phi = 0.0$ and $\Phi = 0.5$, the binary orbit must be close to circular ($e = 0$). We fit the remaining orbital parameters, including the inclination. A more detailed description can be found in Appendix C.5.

The best fit is achieved with an inclination of $i = 35 \pm 5\,^\circ$ and an epoch of the primary eclipse of $T_0 = 2\,459\,036.101 \pm 0.004$ HJD. The orbital masses are $M_{\rm orb,\,1} = 33.6^{+5.0}_{-3.7}$ and $M_{\rm orb,\,1} = 31.9^{+4.8}_{-3.5}$, being in agreement with the spectroscopic analysis. The remaining orbital parameters are listed in Table C.5.1 and C.5.2. The best fitting light and RV curves are shown in Fig. 4.3.2, including the phases at which each spectrum was taken. The X-Shooter (2020) spectrum was obtained in the orbital phase close to conjunction, while the UVES and X-Shooter (2022) spectra were measured at comparable phases out of conjunction.

Given the inclination of the system, the rotation velocities of the two components are $v_{\rm rot} = 157 \pm 40\,{\rm km\,s^{-1}}$. Hence, the rotation period of each star is $P_{\rm rot} = 3.0 \pm 0.8$ d which is close to the orbital period, implying that the binary is tidally locked.

Using the orbital period and the mass-ratio, we calculated the Roche radii for each star (see Table 4.3.1). By comparison to the previously determined stellar radii we conclude that both stars are underfilling their Roche lobe ($R/R_{\rm RL} = 0.6$), further supporting our conclusion that both stars have not interacted yet.

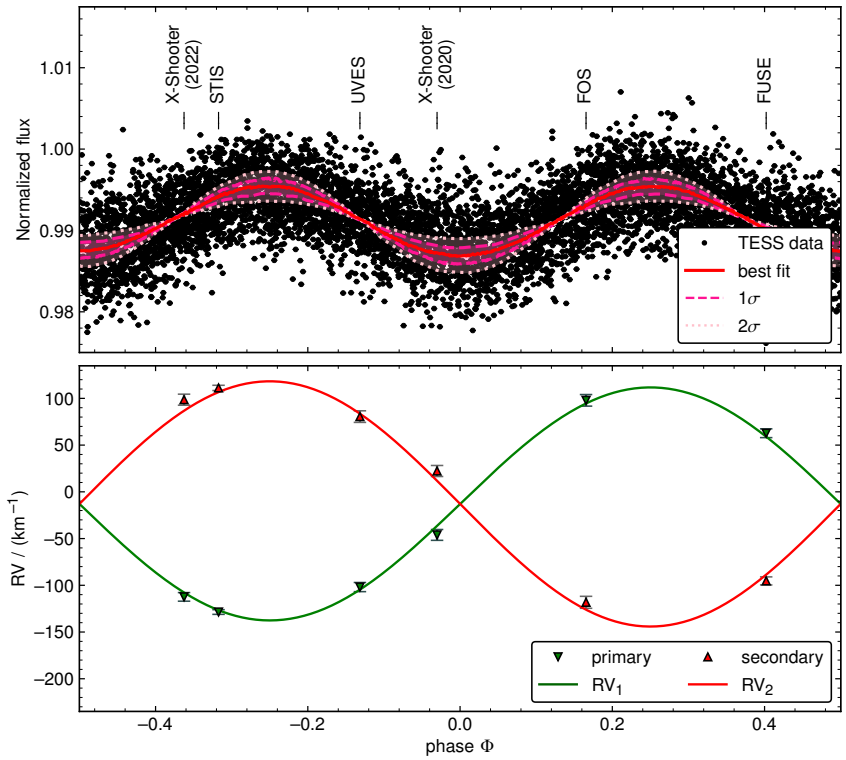

Fig. 4.3.2. Comparison of the phased observed and synthetic light and RV curve of AzV 14. *Upper panel*: Phased TESS light curve (dots) and best fit obtained with the PHOEBE code (red line). For the PHOEBE model we show the 1σ and 2σ deviations as pink shaded areas. *Lower panel*: Observed (triangles) and fitted RV curves (solid lines) of the primary (green) and secondary (red) component.

4.5. Binary evolution models predict the formation of WR stars

Empirically derived stellar parameters of the binary components of AzV 14 (Table 4.3.1) are used to anchor the position of the system on the Hertzsprung–Russell diagram (HRD), and on this basis to investigate their possible future evolution. We calculated binary evolution models with the Modules for Experiments in Stellar Astrophysics (MESA) code (Paxton et al. 2011, 2013, 2015, 2018, 2019). The methods and basic assumptions made in our models are described in Appendix C.6. In our models, a star enters WR evolutionary stages when the optical depth at its surface is $\tau \geq 0.2$. For further information we refer to Appendix C.7.

The current positions of the binary components in the HRD can be explained best by a binary evolutionary model with initial masses of $M_{1,\mathrm{ini}} = 35.0\,M_\odot$ and $M_{2,\mathrm{ini}} = 33.5\,M_\odot$, and an initial period of $P_{\mathrm{orb,ini}} = 3.7$ d. The model predicts that AzV 14 formed 3.3 Myr ago. The corresponding evolutionary tracks are shown in Fig. 4.5.1. According to the evolutionary model the binary components have not interacted yet, but will exchange mass in the future. During the future mass-transfer event, it is predicted that the secondary will accrete about $15\,M_\odot$. Both binary components evolve successively into WR stars.

Both components will become H-poor WN type stars similar to WN stars observed in the SMC. For comparison the HRD shown in Fig. 4.5.1 includes the positions of the apparently single WR stars SMC AB 10 and AB 4. The primary will enter the WN stage at an age of 5.9 Myr and spends most of its WR lifetime (0.35 Myr) close to the helium zero-age main sequence, which is roughly at $\log(T_{\mathrm{eff}}/\mathrm{K}) \approx 5.0$ (SMC AB 10 matches this position). During the WR stage, the primary will have a mass of $17\,M_\odot$, while being accompanied by a $50\,M_\odot$ main sequence star in an ≈ 8.5 d orbit. The mass ratio has only a second-order effect on the amount of mass removed during the mass-transfer phase (e.g., Pauli et al. 2022a, their section 3.2), meaning that the primary would be located (if it goes through a stable mass-transfer event) at a comparable position in the HRD, even if it had a less massive companion that could prevent or complicate a detection. We presume that at the end of its evolution, the primary will directly collapse into a BH and remains bound.

The remaining secondary star, will continue its evolution on the main sequence. Shortly after that stage, it will initiate mass-transfer onto the BH, stripping off parts of its H-rich envelope and entering the WR phase at an age of 6.9 Myr. The resulting secondary WR star will spend most of its lifetime (also 0.35 Myr) at much lower temperatures ($\log(T_{\mathrm{eff}}/\mathrm{K}) \approx 4.75$) than the primary WR star while being similarly massive with $25\,M_\odot$ (SMC

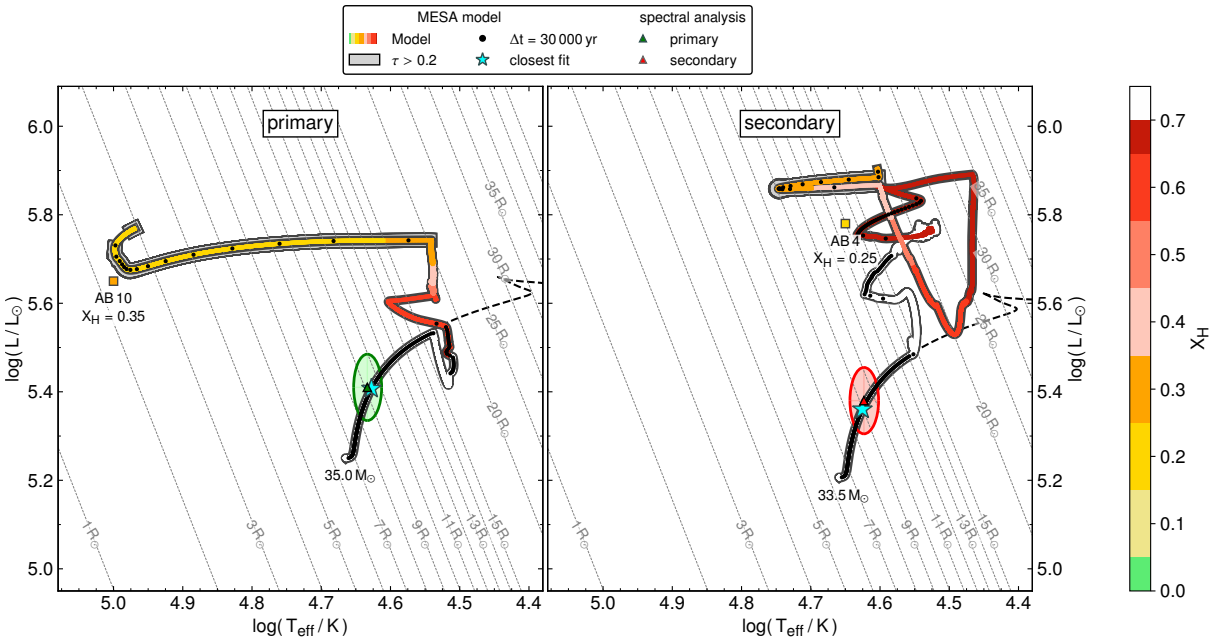

Fig. 4.5.1. Evolutionary tracks of the primary (left) and secondary (right) compared to the empirical positions of AzV 14 (triangles with error ellipses). The evolutionary tracks are color-coded by the surface hydrogen abundance of the model and are overlayed by black dots corresponding to equidistant time-steps of 0.3 Myr. In the background, single star tracks are shown as dashed black lines. The instance of time in which the model is closest to the observations is marked by blue stars. The tracks are labeled by their initial stellar masses. The phases during which the model is expected to be observed as WR star, this is where $\tau \geq 0.2$, are highlighted by bold black frames. In addition, the positions of the WR stars AB 10 and AB 4, are marked by squares which are color-coded according to their observed surface-hydrogen abundances.

Table 4.5.1. Summary of the stellar parameters of both binary components reproduced with the MESA stellar evolution code.

parameter	primary	secondary	unit
$T_{\rm eff}$	42.5	42.2	[kK]
log g	4.04	4.05	[cm s^{-2}]
log L	5.41	5.36	[$L_\odot$]
R	9.5	9.1	[$R_\odot$]
$M_{\rm ini}$	35.0	33.5	[$M_\odot$]
$M_{\rm evo}$	33.7	32.4	[$M_\odot$]
log $\dot{M}^{(a)}$	−6.5	−6.6	[$M_\odot$ yr^{-1}]
$v_{\rm rot}$	129	123	[km s^{-1}]

$^{(a)}$ According to the mass-loss recipes used in our evolutionary models (see Appendix C.6).

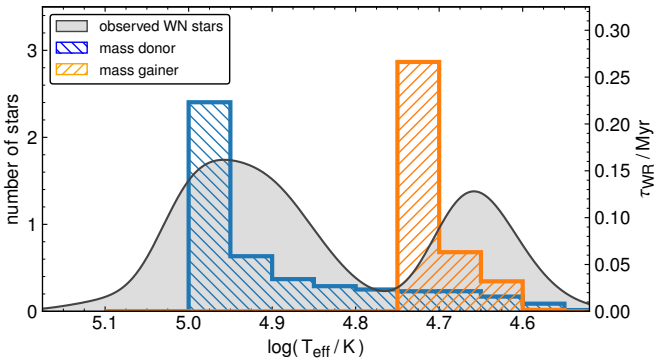

Fig. 4.5.2. Observed temperature distribution of the WR stars in the SMC (gray area) compared to the time our evolutionary model of the primary (blue) and secondary (orange) are predicted to spend in the different temperature ranges during their WR phase. The observations are shown as Gaussians that have standard deviations corresponding to the observational uncertainties (see Table C.7.1). We excluded the binary SMC AB5 from this plot, as it has a different evolutionary origin.

AB 4 is at this position). This relatively cool WR star is accompanied by a BH with a mass of 16 $M_\odot$ in an orbit of 3.3 d.

Our binary evolutionary models of AzV 14 predict the formation of WR stars with different temperatures. Indeed, the WR population in the SMC (Hainich et al. 2015; Shenar et al. 2016, 2018) has a bimodal temperature distribution which is comparable to the predicted temperature regimes of the evolutionary models of AzV 14 (see Fig. 4.5.2). In the following, we elaborate on this idea further and discuss the implications and robustness of our findings.

4.6. Discussion

4.6.1. Exploring the parameter space by computing a small grid of binary evolutionary models

Inspired by the insights gained from the binary evolutionary models of AzV 14 (see Sect. 4.5), we explore if the bimodal temperature distribution of WR stars at low metallicity is also predicted by binary evolutionary models with different initial masses and initial orbital periods. Therefore, we calculated a small grid covering initial primary masses of 30, 45, and 60 $M_\odot$, while having a fixed mass ratio of $q = 0.85$. The initial primary masses are chosen to roughly represent the full luminosity distribution of the observed WR population of the SMC. The models are calculated for initial orbital periods of 5, 50, and 500 d. A HRD containing the evolutionary tracks of all the models is shown in Fig. 4.6.1.

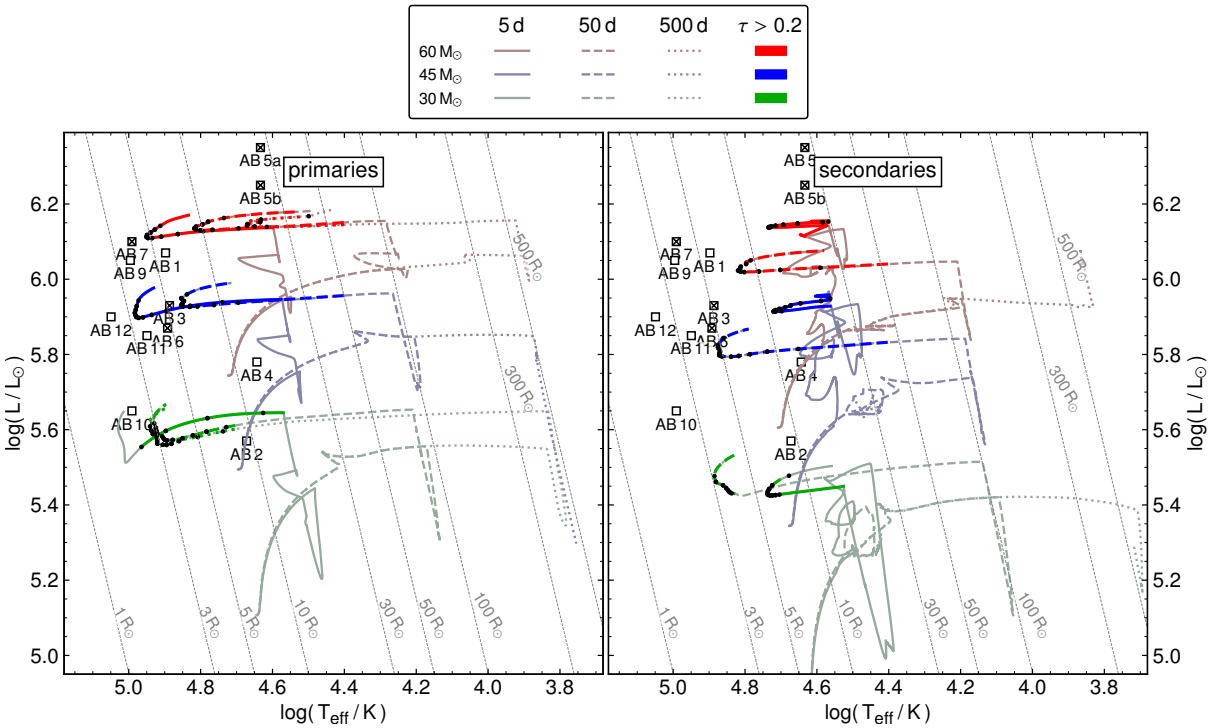

Fig. 4.6.1. Evolutionary tracks of primary (left) and secondary (right) models with initial primary masses of 30 (green gray), 45 (blue gray), and 60 $M_\odot$ (red gray), fixed mass ratio $q = 0.85$ and initial orbital periods of 5 (solid), 50 (dashed), and 500 d (dotted). We highlighted the WR phase (i.e., $\tau \geq 0.2$) in bold colors. Equidistant time steps of 0.3 Myr are marked by black dots during the WR stage. In the background, we marked the positions of all observed WR stars in the SMC.

Figure 4.6.2 depicts a simplified picture of the different formation channels of hotter and cooler WR stars. The flow chart is based on those models in our small grid that have a stable mass-transfer phase.

The evolutionary tracks of the primaries with initial masses of 30 $M_\odot$ are similar to those of AzV 14. All of the primary stars expand and initiate mass-transfer events, during which they lose most of the H-rich envelope, resulting in the formation of hotter WR stars ($\log T_{\rm eff} > 4.9$). The evolution of the secondaries depends on the initial parameters. The secondary in the system with initial period of 5 d accretes about $\sim 5\,M_\odot$ of material, leading to a rejuvenation of the core. After hydrogen is depleted in its core, the stellar model expands and quickly initiates mass transfer, stripping off parts of the accreted envelope. After the mass-transfer event the secondary has a temperature of $\log T_{\rm eff} \approx 4.7$ and a high surface H-abundance of $X_{\rm H} = 0.5$ (left side of Fig. 4.6.2). On the other hand, the secondary in the system with initial period of 50 d accretes less than 0.5 $M_\odot$. This is a big difference to the short-period model, which is explained by the fact that in our models accretion is only allowed when the accretor can avoid rapid rotation. In the short-period binaries, the stars are tidally locked, slowing down the rotation sufficiently for the accretor to stay below critical rotation during the accretion process. In a long-period binary, the star spins up quickly, limiting the amount of mass that can be accreted (Petrovic et al. 2005; de Mink et al. 2007; Shao & Li 2016). In such long-period systems (right side of Fig. 4.6.2) the secondary initiates mass transfer after core-H burning during its evolution toward the blue (BSG) and yellow supergiant (YSG) phase, leading to the formation of a hotter WR star with $\log T_{\rm eff} \approx 4.9$ (i.e., the same temperature regime that is also populated by the primary models). In even longer period systems ($P = 500$ d) mass transfer is initiates when the star is evolving toward a red supergiant (RSG). The model has already formed a large convective envelope which expands adiabatically, making mass-transfer unstable. Potentially, this leads to a common envelope evolution which is not modeled here.

The models with initial primary masses of 45 $M_\odot$ and initial periods of 5 and 50 d also predict the formation of hotter WR stars ($\log T_{\rm eff} > 4.85$). However, the primary model with initial period of 500 d is on its way to becoming a RSG and has already formed a large outer convection region. Similar to the models presented above, this leads to an unstable mass transfer and possibly a common envelope evolution. In the model with an initial period of 5 d the secondary accretes a significant amount of mass ($> 10\,M_\odot$) and initiates mass transfer after its main sequence evolution. After the mass transfer event the surface H fraction drops to $X_{\rm H} = 0.35$ and the temperature is $\log T_{\rm eff} > 4.7$. The secondary will end its life as a cooler WR (left side of Fig. 4.6.2). For an initially wider orbit (50 d) the secondary accretes only negligible amounts of material and, similar to the primary models, evolves into a hotter WR star (right side of Fig. 4.6.2).

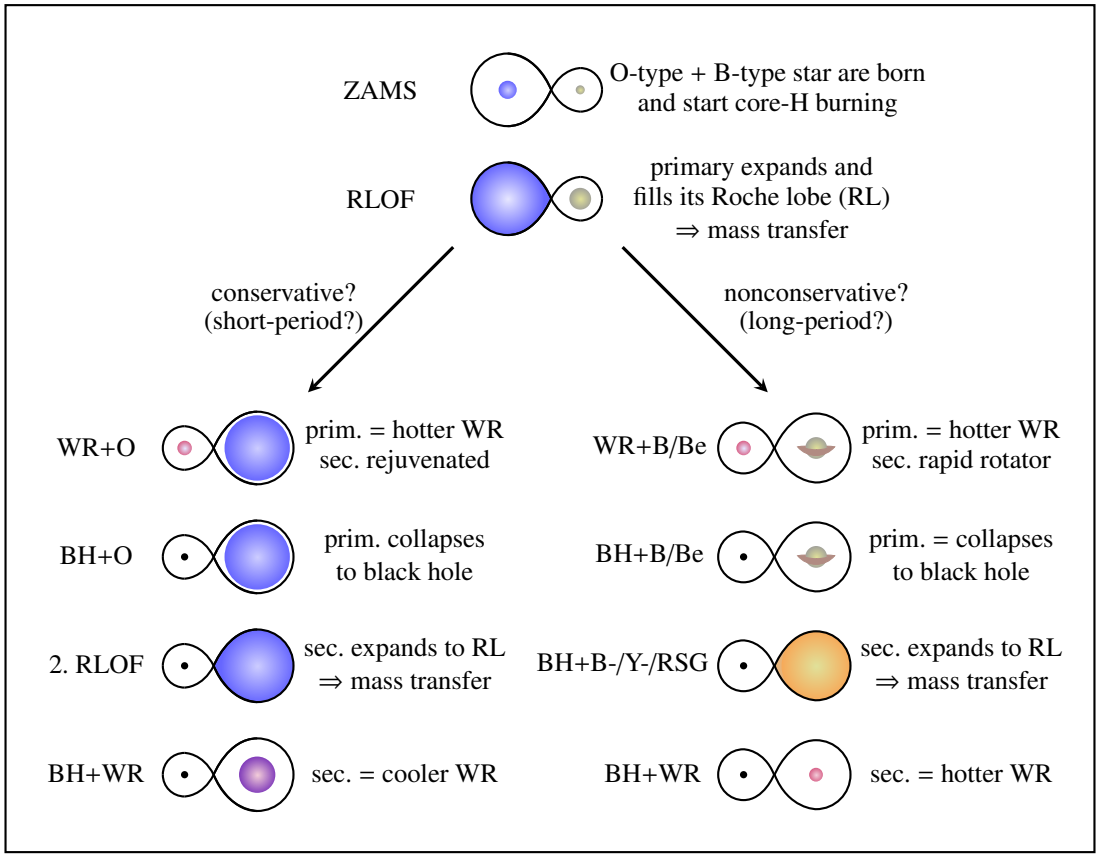

Fig. 4.6.2. Sketch of the evolutionary stages for possible formation channels of hotter and cooler WR stars under the assumption of stable mass transfer.

The primary models with initial masses of $60\,M_\odot$ populate a wide range of effective temperatures ($\log T_{\rm eff} = 4.65 - 5.0$). The broad temperature range can be explained by the changing efficiency of envelope stripping and its dependence on initial period and mass ratio. The efficiency is linked to the point in the primary's evolution when it transitions into the core-He burning stage, which happens before or during the mass transfer (see also Klencki et al. 2022, their figure 3). In the primary model of the system with initial period of 5 d the mass transfer is very efficient in removing the H-rich envelope and with the help of the strong WR winds the model is able to remove a significant amount of the envelope, making the star appear hot. On the other hand, in the primary model with initial period of 500 d the mass-transfer is less efficient, making the WR star appear cooler. The secondary in the system with an initial period of 5 d accretes a significant amount of mass ($> 10\,M_\odot$). It initiates mass transfer after the main sequence, stripping off parts of the accreted envelope, resulting in the formation of a cooler WR. The secondary in the system with an initial period of 50 d behaves similarly to its corresponding primary model and forms a hotter WR star. The secondary in the system with initial period 500 d initiates mass transfer when it is on its way to becoming a RSG and has already formed an extended outer convection zone. Mass-transfer in this model is unstable.

4.6.2. Bimodal temperature distribution of WR stars at low metallicity

From considering different evolutionary pathways probed by our exploratory model grid, we learned that primaries and secondaries which have not accreted a significant amount of material evolve to hotter WR stars. Only secondaries that have accreted a fair amount of mass (i.e., those with the shortest periods) evolve into cooler WR stars. There are two main factors that may be responsible for this behavior. Firstly, evolved accretors are characterized by a steep chemical gradient at the core-envelope boundary, producing cooler WR stars once the outer envelope is lost (Schootemeijer & Langer 2018, their figure 9). Secondly, accretors that are not fully rejuvenated tend to remain compact after the end of MS and begin the core-He burning phase as BSGs (Vanbeveren et al. 2013; Justham et al. 2014). Mass transfer from such stars leads to less efficient envelope stripping and cooler WR products (Klencki et al. 2022). This is different from the single star models (e.g., Georgy et al. 2012; Choi et al. 2016; Eldridge et al. 2017; Limongi & Chieffi 2018) which can only explain the hottest and most luminous WR stars.

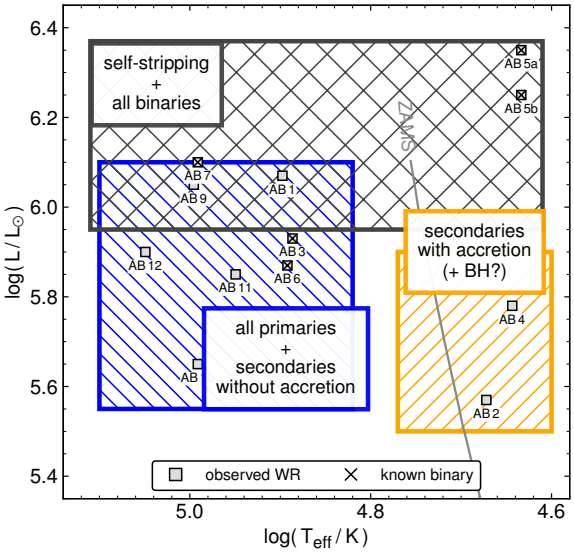

Fig. 4.6.3. HRD containing the positions of the observed WR stars in the SMC, over-plotted by a sketch stating the different evolutionary channels of single stars and binaries undergoing stable mass transfer, leading to the different marked regions.

Based on our models, we hypothesize that there must be a bimodal temperature distribution of faint WR stars at low metallicity. First, hotter WR stars of any luminosity can be well explained by the primary models as well as by the secondary models that did accrete negligible amounts of material (i.e., those in wide orbits). Second, cool and faint WR stars ($\log T_{\rm eff} = 4.65-4.7$ and $\log(L/L_\odot) \simeq 5.5-5.9$) must arise from secondaries that have accreted a significant amount of material, leading to a rejuvenation and high envelope-to-core mass ratios. Third, hotter and luminous WR stars ($\log T_{\rm eff} = 4.65-4.7$ and $\log(L/L_\odot) \simeq 5.9-6.2$) can be explained by primary, secondary, and single star models. We note that according to our models the cool and faint WR stars should all be accompanied by a compact companion, which can avoid detection and can help to explain observed apparently single cooler WR stars. We sketched the morphology of the WR population in the SMC in Fig. 4.6.3.

It is less clear whether cooler WR stars at higher metallicities are formed in the same way as in low-metallcity galaxies. Two reasons should be considered. First, at high metallicity, the observed effective temperatures of WR stars can be lower, due to stronger winds (e.g., Sander & Vink 2020; Sander et al. 2023), also termed "dynamic inflation" (Grassitelli et al. 2018). Second, at higher metallicity WR stars additionally suffer from the effect of hydrostatically inflated envelopes (e.g., Gräfener et al. 2012; Sanyal et al. 2015), yielding again lower effective temperatures. Third, the stellar winds in the pre-WR stage at higher metallicity are stronger, stripping off more of the H-rich envelope, which is left after mass transfer. While the latter leads to the formation of hotter WR stars (as shown in Sect. 4.6.4.1), the effect on the observed temperature might partially be counter-balanced by the higher wind densities. All these effects make it difficult to distinguish between WR stars formed from stars which have accreted significant amounts of material in the past and intrinsically inflated WR stars.

Hence, in order to clearly see a bimodal temperature distribution of WR stars originating from post interaction binaries, populations at low metallcity must be considered. However, the number of WR stars decreases with decreasing metallicity (e.g., Shenar et al. 2020b), enforcing us to rely on small number statistics. In the SMC, the sample of WR stars is complete which minimizes selection biases. Therefore, despite the small number statistics, it remains the best representative sample of an WR population at low metallicity. In order to confirm or falsify our predictions, further observations of complete populations of WR stars in other low metallicity galaxies in combination with calculations of binary evolutionary models are necessary.

Our findings and other recent results (Renzo & Götberg 2021; Renzo et al. 2022) indicate that evolution of past accretors may be systematically different to those of normal (primary) stars. This impacts our understanding of stellar evolution and feedback. For instance, in the SMC hotter WR stars like AB 10 ($\log(Q_{\rm He\,II}/{\rm s}^{-1}) = 48.1$), have strong He II ionizing fluxes, while cooler WR stars like AB 4 ($\log(Q_{\rm He\,II}/{\rm s}^{-1}) = 37.5$) have five orders of magnitude lower ionizing flux. Broader implications for binary evolution channels, proposed in this work, are yet to be explored.

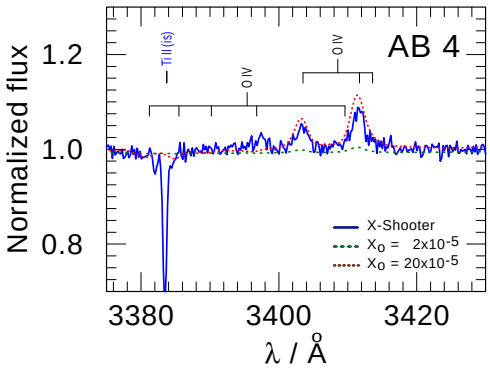

Fig. 4.6.4. Close-up view of the O IV multiplet in the X-Shooter spectrum of the WR star SMC AB 4. The observed spectrum is shown as a blue solid line, the synthetic spectra are calculated with an oxygen abundance of $X_O = 2 \times 10^{-5}$ and $X_O = 20 \times 10^{-5}$ and are shown as green dotted and red dotted lines, respectively.

4.6.3. Observational fingerprints of previous evolutionary channels

Our model predicts that the observed effective temperature is one of the key diagnostics to differentiate between the evolutionary origin of WN type stars at low metallicity, as explained in Sect. 4.6.2. However, for WN stars originating from past accretors, a low effective temperature is not the only diagnostic.

The surface H-abundance can be considered as another clue, as all of our rejuvenated secondary model show $X_H \gtrsim 0.3$, while for their corresponding primary models the surface H-abundance are noticeably lower $X_H \sim 0.2$. However, for our most luminous models ($M_{ini,1} = 60\,M_\odot$) in the systems with the widest orbits, the primaries have low temperatures and the H-abundances are comparable to those of the rejuvenated secondaries. Hence, a high hydrogen abundance and a low temperature are not a robust criterion to identify the previous evolutionary path.

In our search for additional fingerprints to detect past accretors, we identified a difference in the predicted CNO surface composition of normal (primary) stars and the rejuvenated secondaries. It is expected that both, the primaries and nonrejuvenated secondaries, have CNO equilibrium composition ($X_C = 1-2 \times 10^{-5}$, $X_N = 139 \times 10^{-5}$, and $X_O = 1-3 \times 10^{-5}$). In a direct comparison, the models of the rejuvenated secondaries have a decreased surface N-abundance, while the surface O-abundance is increased by about one order of magnitude ($X_C = 1-2 \times 10^{-5}$, $X_N \approx 120 \times 10^{-5}$, and $X_O = 10-25 \times 10^{-5}$), due to the formation of a shallow chemical gradient extending through the accreted envelope. Therefore, we predict that oxygen lines should be present in spectra of cooler WN stars formed from past accretors.

For the analysis of larger WN samples (e.g., Hamann et al. 2006; Sana et al. 2014; Hainich et al. 2015; Shenar et al. 2016), traditionally the N-abundance has been fixed to a value reflecting CNO equilibrium, while oxygen has not been included at all, due to its weak or absent spectral imprint in the optical regime. To predict the spectral appearance of WN stars which originate from stars that have accreted significant amounts of material in the past, synthetic spectra now need to include oxygen as well. Given the temperatures of WR stars O IV and O V are expected to be dominant ions.

In order to check this prediction, we select the WR star SMC AB 4 (WN6h), as its empirical position in the HRD can only be explained by our models of secondaries that have accreted material during mass transfer. A spectrum of AB4 taken with X-Shooter at the ESO-VLT within the ESO program 106.211Z (PI J. S. Vink) is available from the archive. We re-calculated the stellar atmosphere model of AB 4, from Hainich et al. (2015) with an enhanced O-abundances of $X_O = 20 \times 10^{-5}$ as well as with the CNO equilibrium value of $X_O = 2 \times 10^{-5}$. Indeed, the model with ten times enhanced oxygen abundance reproduces the O IV lines at wavelengths 3403 Å and 3414 Å just as observed, while the CNO equilibrium abundance fails by far (see Fig. 4.6.4).

As illustrated by this example, WN stars with enhanced oxygen abundance, such as AB 4, may be explained by the evolutionary models assuming that they accreted a significant amount of matter in the past. We suggest that the oxygen abundance of WN type stars is an important diagnostic which can help to identify WR stars originating from binary components that have accreted significant amounts of material in the past.

4.6.4. Sensitivity of the evolutionary model to different parameters

Estimating uncertainties in stellar evolution models is a nontrivial task, as it does not only depend on the numerical uncertainty but also on the physical assumptions made within the model itself. Stellar evolution models rely on many free parameters that can alter the evolution of a star, for instance mass-loss and mixing processes. Exploring the impact of all free parameters, quickly opens a large parameter space and needs intensive computational

power. Such an investigation is far beyond the scope of the present paper. In the following, we briefly discuss two examples of how these parameters can impact our predictions on the temperature distribution of WR stars in low-metallicity environments.

4.6.4.1. Example 1: Enhanced mass-loss rates

In the binary model presented in this paper, the mass-transfer takes place while the primary is still core-H burning. Therefore, the evolution of the secondary is not really sensitive to the mass-loss rates of O stars. However, both stars spend a significant amount of their lifetime in the WR stage. Hence, we decided to test how the evolution would be affected if the WR mass-loss rate is increased by a factor of 3.

Figure 4.6.5 shows the resulting tracks. By comparison to Fig. 4.5.1, the predicted temperature regimes and the surface chemical composition during the WR phases changes. The primary loses a larger fraction of its H-poor envelope and spends more time at higher temperatures. At the end of core-He burning the stellar evolution model starts to contract instead of expanding. On the other hand, the stellar evolution model of the secondary shows even stronger response to the increased mass-loss rate. Instead of becoming a cooler WR star with plenty of hydrogen in the envelope, it is now able to remove large fractions of this envelope and position itself at higher temperatures in the HRD. We note that the region in the HRD where the stellar evolution model of the secondary is located is not populated by an observational counterpart.

The above example shows that the choice of the mass-loss recipe during different evolutionary phases can have a drastic impact on the evolution of massive stars. Only when using adequate mass-loss recipes, one can explain the cooler WR stars observed in the SMC. We note that in the case of WR winds being weaker than we assume in this work, the prediction on the morphology of the temperature distribution of WR stars would shift to lower metallicities.

4.6.4.2. Example 2: More efficient mixing

There are several mixing processes within stellar interiors, including convective mixing, semiconvective mixing, overshooting, rotational mixing, pulsational mixing, etc. Typically, these mixing processes are parameterized by free parameters, for example the mean free path a photon can travel, or the efficiency of a specific mixing process which cannot be predicted by theory. In the literature there are many works trying to limit the parameter space of the different free parameters (e.g., Schootemeijer et al. 2019; Higgins & Vink 2019; Gilkis et al. 2021; Michielsen et al. 2021). In this section, we want to showcase how changing one of the free parameters can impact the evolution of a star.

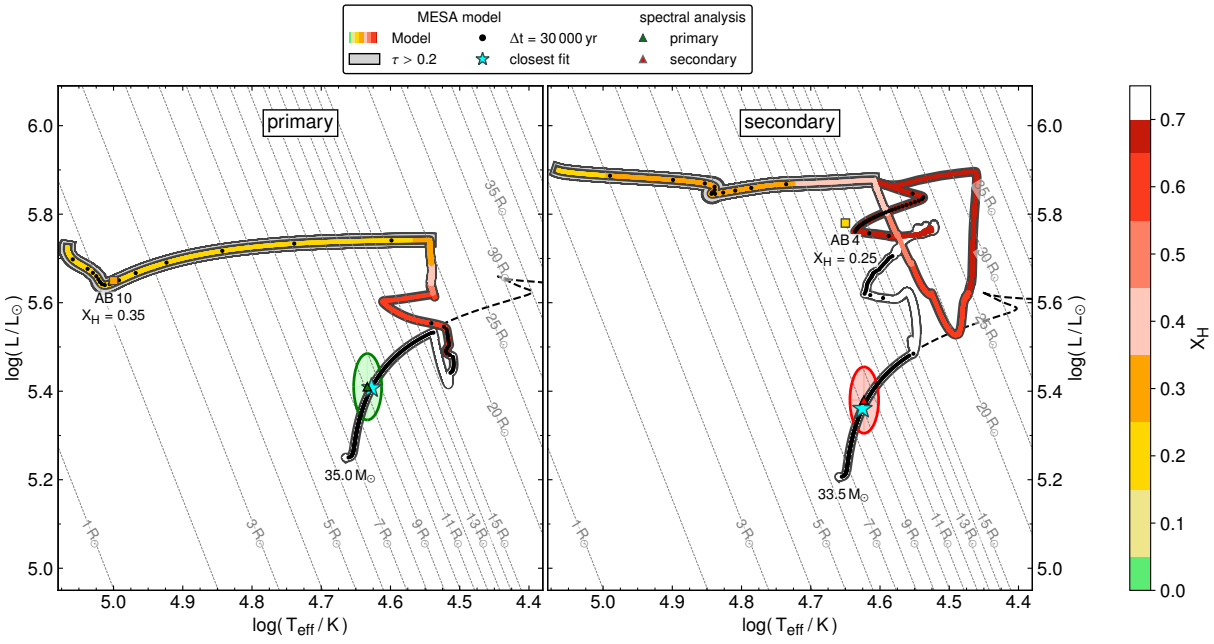

Fig. 4.6.5. Same as Fig. 4.5.1, but now with the WR mass-loss rates enhanced by a factor 3.

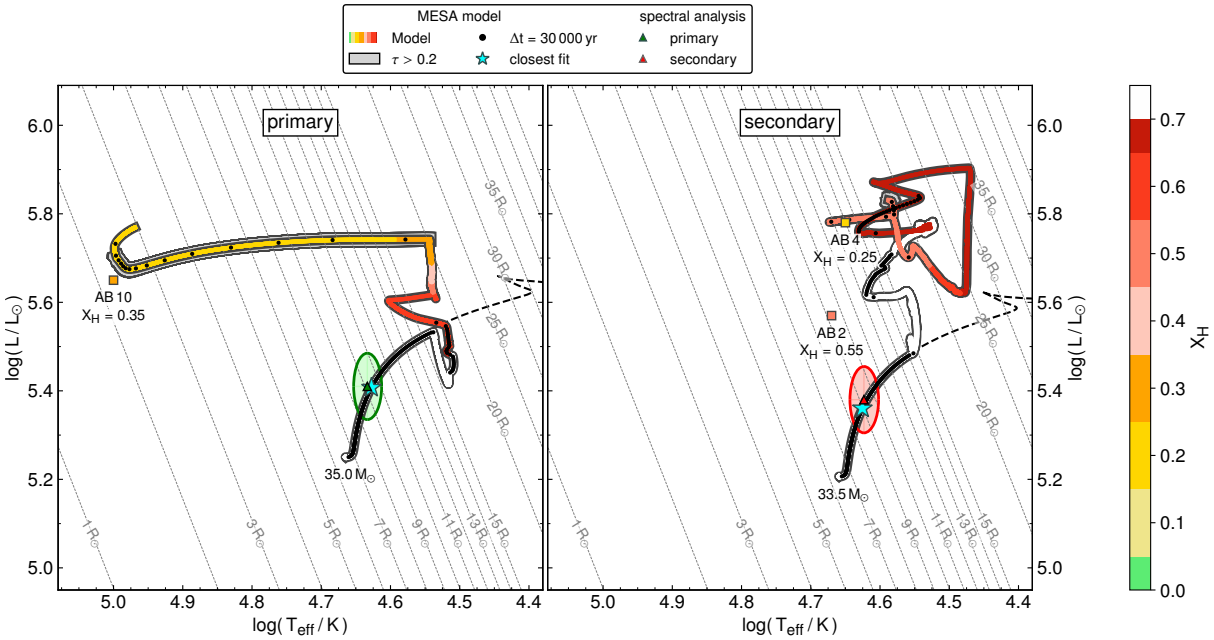

Fig. 4.6.6. Same as Fig. 4.5.1, but now with an increased efficiency of semiconvection.

One of the least constrained , yet important, mixing process is the efficiency of semiconvective mixing. Schootemeijer et al. (2019) used the population of the BSGs and RGSs to constrain semiconvective mixing efficiencies, but were able only to limit it to $\alpha_{\rm sc} \gtrsim 1$. They report that higher values only barely impact the number ratio of blue and red supergiants in galaxies. In our models presented above we used $\alpha_{\rm sc} = 1$. For the models presented in this section, however, we increased the efficiency to $\alpha_{\rm sc} = 10$ in order to see how it changes our understanding of the evolution of the binary.

The evolutionary tracks of the primary and secondary with the more efficient semiconvective mixing are shown in Fig. 4.6.6. By comparing these tracks to those shown in Fig. 4.5.1, one can see that the evolution of the primary barely changes. Semiconvective mixing becomes important only in evolutionary stages after the main sequence. The primary begins mass transfer already during its main sequence evolution and spends its post-main sequence evolution as a WR star, leaving the semiconvective mixing no time to impact the evolution. On the other hand, the evolution of the secondary changes because during the accretion phase it forms extensive convective and semiconvective regions in its envelope. The secondary initiates mass-transfer after the main sequence evolution, giving semiconvection some time to efficiently mix material. In addition, due to more efficient semiconvection, the secondary expands less in the transition to the core-He burning phase and initiates mass transfer at a somewhat more advanced evolutionary stage, consequently losing less mass during mass-transfer and producing a cooler WR star with an even higher surface H abundance. This is reflected in the higher surface H-abundance and the cooler temperature. Klencki et al. (2022) recently reported something similar: Binary models at low metallicity with highly efficient semiconvective mixing will not become WR/helium stars after Case B mass transfer. Their models managed to stay at the position in the HRD at which they initiated the mass transfer and hence are core-He burning stars, disguised as O- or B-type stars. It is worth mentioning that according to our criterion based on the optical depth, the secondary of the binary evolutionary model with efficient semiconvective mixing would spend only a short time as a WR star at low temperature.

These two examples illustrate that binary evolution models are quite sensitive to the input parameters. A more detailed study based on grids of detailed binary evolutionary models and population synthesis are needed to confirm or disprove our predictions on the morphology of WR populations at low metallicity.

4.7. Summary and conclusions

A consistent analysis of multi-epoch optical and UV spectra of one of the earlierst O-type stars in the SMC, AzV 14, reveals its binary nature. Furthermore, our analysis uncovered that the systems' two components are very similar. The primary and secondary have temperatures of $T_{\rm eff,1} = 42.8 \pm 2.0$ kK and $T_{\rm eff,2} = 41.8 \pm 2.0$ kK, luminosities of $\log(L_1/L_\odot) = 5.41 \pm 0.15$ and $\log(L_2/L_\odot) = 5.38 \pm 0.15$ and surface gravities of $\log(g_{1,2}/(\mathrm{cm\,s^{-2}})) = 4.0 \pm 0.2$, respectively. The analysis of a TESS light curve confirms the binary na-

ture of AzV 14 with an orbital period of 3.7058 ± 0.0013 d. Their spectroscopic masses of $M_1 = 32 \pm 8\,M_\odot$ and $M_2 = 31 \pm 8\,M_\odot$ are confirmed by the orbital analysis. Both binary components drive weak stellar winds with mass-loss rates of about $\log(\dot{M}/(\,M_\odot\,\mathrm{yr}^{-1})) = -7.7 \pm 0.2$. The relatively high observed X-ray emission of AzV 14 is attributed to colliding winds.

The new empirically derived stellar parameters and the current orbital period of AzV 14 are well explained by our evolutionary models. In particular, the spectroscopic and orbital masses of the binary components are in agreement with the evolutionary ones. According to the evolutionary models, the components of AzV 14 did not yet exchange mass. Most interestingly, the binary evolutionary model of AzV 14 predicts that the primary will evolve into a hotter WR star, while the secondary is destined to evolve into a cooler WR star.

Inspired by these results we calculated a small evolutionary model grid to investigate the conditions for the formation of hotter and cooler WR stars. Guided by these calculations, we anticipate that WR populations in low metallicity galaxies should show bimodal temperature distributions. According to our models, stars born in long-period binaries both evolve to hotter WR stars. On the other hand, for stars born in short-period binaries only the primary is destined to become a hot WR star, while the secondary evolves into a cooler WR star. In our models we assume that accretion in short-period binaries is efficient, leading to a rejuvenation of the core and a different envelope-to-core mass ratio. This eventually allows the past accretors to stay at lower temperatures during their WR stage.

These results are sensitive to the input physics, but if turned out to be correct they would have a vast impact on our understanding of binary evolution at low metallicity, stellar feedback, and, hence, on galaxy formation and evolution. To test if our models are reliable and cooler WR stars originate from past accretors we introduced an additional criterion: the surface oxygen abundance. From standard evolutionary models one expects that a WR star has a surface composition which corresponds to the CNO equilibrium value. However, in our models the cooler WR stars, formed by stars that accreted a significant amount of material in the past, all have surface oxygen abundance which are increased by a factor of about ten. We tested this prediction with archival spectra of the apparently single WN star AB4 in the SMC. We detect oxygen lines in its optical spectrum, and measure the high oxygen abundance which is in agreement with our evolutionary model predictions. This empirically supports the new evolutionary pathway to the formation of WR stars at low metallcity proposed in this paper.

Acknowledgments: The authors are appreciative to the reviewer for useful comments which helped to improve the paper, and for their suggestions. The results presented in this paper are based on observations obtained with the NASA/ESA Hubble Space Telescope, retrieved from MAST at the Space Telescope Science Institute (STScI). STScI is operated by the Association of Universities for Research in Astronomy, Inc. under NASA contract NAS 5-26555. Support to MAST for these data are provided by the NASA Office of Space Science via grant NAG5-7584 and by other grants and contracts. The TESS data presented in this paper were obtained from MAST at the STScI. Funding for the TESS mission was provided by the NASA Explorer Program. Furthermore, its conclusions are based on observations collected at the European Southern Observatory (ESO) under the program 098.A-0049. The authors thank the managing committee of XShootU and Andrea Mehner for preparing the OBs of the XShootU project. This work has made use of data from the European Space Agency (ESA) mission *Gaia* (https://www.cosmos.esa.int/gaia), processed by the *Gaia* Data Processing and Analysis Consortium (DPAC, https://www.cosmos.esa.int/web/gaia/dpac/consortium). Funding for the DPAC has been provided by national institutions, in particular the institutions participating in the *Gaia* Multilateral Agreement. DP and SRS acknowledge financial support by the Deutsches Zentrum für Luft und Raumfahrt (DLR) grants FKZ 50OR2005 and 50OR2108. AACS and VR acknowledge support by the Deutsche Forschungsgemeinschaft (DFG, German Research Foundation) in the form of an Emmy Noether Research Group – Project-ID 445674056 (SA4064/1-1, PI Sander). DMB gratefully acknowledges a senior postdoctoral fellowship from the Research Foundation Flanders (FWO) with grant agreement number 1286521N. RK acknowledges financial support via the Heisenberg Research Grant funded by the German Research Foundation (DFG) under grant no. KU 2849/9. CK acknowledges financial support from the Spanish Ministerio de Economía y Competitividad under grants AYA2016-79724-C4-4-P and PID2019-107408GB-C44, from Junta de Andalucía Excellence Project P18-FR-2664, and from the State Agency for Research of the Spanish MCIU through the 'Center of Excellence Severo Ochoa' award for the Instituto de Astrofísica de Andalucía (SEV-2017-0709). TS acknowledges support from the European Union's Horizon 2020 under the Marie Skłodowska-Curie grant agreement No 101024605. The collaboration of coauthors was facilitated by support from the International Space Science Institute (ISSI, Bern). The authors are grateful to the Lorentz Center (Leiden) for organizing a stimulating workshop. We thank Paul Crowther for useful discussions as well as advice regarding the UVES spectrum and for providing the updated IR photometry.

Chapter 5

Manuscript IV: A partially stripped massive star in a Be binary at low metallicity: A missing link towards Be X-ray binaries and double neutron star mergers

V. Ramachandran, J. Klencki, A. A. C. Sander, **D. Pauli**, T. Shenar, L. M. Oskinova, W.-R. Hamann

Astronomy & Astrophysics, 2023, Volume: 674, ID: L12, 11 pp.

Abstract

Standard binary evolutionary models predict a significant population of core helium-burning stars that lost their hydrogen-rich envelope after mass transfer via Roche-lobe overflow. However, there is a scarcity of observations of such stripped stars in the intermediate-mass regime ($\sim 1.5 - 8\,M_{\odot}$), which are thought to be prominent progenitors of SN Ib/c. Especially at low metallicity, a significant fraction of these stars are expected to be only partially stripped, retaining a significant amount of hydrogen on their surfaces. For the first time, we discovered a partially stripped massive star in a binary with a Be-type companion located in the Small Magellanic Cloud (SMC) using a detailed spectroscopic analysis. The stripped-star nature of the primary is revealed by the extreme CNO abundance pattern and very high luminosity-to-mass ratio, which suggest that the primary is likely shell-hydrogen burning. Our target SMCSGS-FS 69 is the most luminous and most massive system among the known stripped star + Be binaries, with $M_{\rm stripped} \sim 3\,M_{\odot}$ and $M_{\rm Be} \sim 17\,M_{\odot}$. Binary evolutionary tracks suggest an initial mass of $M_{\rm ini} \gtrsim 12\,M_{\odot}$ for the stripped star and predict it to be in a transition phase towards a hot compact He star, which will eventually produce a stripped-envelope supernova. Our target marks the first representative of an as-yet-missing evolutionary stage in the formation pathway of Be X-ray binaries and double neutron star mergers.

5.1. Introduction

Massive stars are frequently found in binary or multiple systems where components are in close proximity to one another, making the interaction between the two stars inevitable as the primary grows and evolves (Sana et al. 2012, 2014; Moe & Di Stefano 2017). The components will be subjected to substantial interactions involving the transfer of mass and angular momentum, which will have profound effects on the fundamental parameters and final fates of both stars. Such interactions frequently lead to the stripping of the primary's envelope (Kippenhahn & Weigert 1967; Paczyński 1967), which can produce hot and compact He-core stars with a thin layer of hydrogen on top (see, e.g., Yoon & Cantiello 2010; Yoon 2017; Claeys et al. 2011). Depending on their initial masses, the stripped-envelope primaries would have spectral characteristics ranging from hot subdwarfs to Wolf-Rayet (WR) stars (e.g., Paczyński 1967; Vanbeveren 1991; Eldridge et al. 2008; Götberg et al. 2017). Secondaries, on the other hand, would evolve into rapidly rotating stars (e.g., de Mink et al. 2013b; Renzo & Götberg 2021), which can have disk emission features similar to Be stars (Pols et al. 1991; Shao & Li 2014; Bodensteiner et al. 2020b; Hastings et al. 2021).

Interestingly, stripped-envelope stars with masses between low-mass subdwarfs and classical WR stars are rarely observed. This intermediate-mass regime $\sim 1.5 - 8\,M_\odot$ at solar metallicity (Götberg et al. 2017) gets wider up to $\lesssim 17\,M_\odot$ at SMC metallicity (Z=0.2 $Z_\odot$; Shenar et al. 2020b). Moreover, the intermediate-mass stripped-envelope stars (hereafter stripped stars) are predicted to be a long-lived core He-burning phase. They are considered to be the progenitors of Ib/c supernovae and major sources of far-UV ionizing flux (Götberg et al. 2017). The only known intermediate-mass hot He star is the qWR star HD 45166 (Groh et al. 2008), whereas other hot and compact stripped star candidates in the Galaxy are in the subdwarf mass range of $< 1.5\,M_\odot$ (Wang et al. 2021; Schootemeijer & Langer 2018; Gilkis & Shenar 2023). For HD 45166, a new study yields a strong magnetic field, meaning that this star likely does not follow standard binary evolution (Shenar et al. 2023).

In recent literature, there is growing evidence for stripped stars, but many of them are partially stripped OB-type giants of a few solar radii, often with a significant residual H-layer ($X_\mathrm{H} > 50\%$) on their surface. These include originally proposed X-ray quiet black hole + Be binaries, such as LB1 and HR6819 (Liu et al. 2019; Rivinius et al. 2020), which have later been disputed (e.g., Abdul-Masih et al. 2020; Bodensteiner et al. 2020a; Shenar et al. 2020a; El-Badry & Quataert 2021) or were revealed to be partially stripped star + Be binaries (Frost et al. 2022). Another similar object is HD 15124, which is currently undergoing mass transfer (El-Badry et al. 2022b). All these objects are in the Milky Way and have masses $\lesssim 1.5\,M_\odot$. In contrast, Irrgang et al. (2022) reported γ Columbae to be a partially stripped pulsating core ($\sim 4 - 5\,M_\odot$) of a massive star that has a spectral appearance similar to that of a B subgiant but with altered surface abundances. However, there is no evidence of a mass-accreted secondary in this system. In the Large Magellanic Cloud (LMC), notable systems are NGC1850 BH1 (El-Badry & Burdge 2022; Saracino et al. 2023) and NGC 2004#115 (Lennon et al. 2022; El-Badry et al. 2022a), which are speculated to contain a black hole or low-mass stripped star. Growing observational evidence for these partially stripped stars compared to the apparent absence of fully stripped He stars in the intermediate-mass regime raises questions about our understanding of binary evolution.

Recent evolutionary models by Klencki et al. (2022) suggest that binary evolution at low metallicity favors partial envelope stripping and slow mass transfer, leading to a large population of partially stripped donors. Due to their predicted surface properties, these systems are likely hiding among OB binaries as apparent main sequence (MS) or supergiant stars (e.g., Pauli et al. 2022b). Identifying and characterizing such systems at low metallicity would yield sharp constraints on binary evolution and, in turn, on the origin of gravitational wave sources, ultra-luminous X-ray sources, stripped-envelope supernovae, and ionization in the early Universe. In this paper we report the first observational evidence of a partially stripped star + Be binary at low metallicity.

5.2. Observations

In a previous study (Ramachandran et al. 2019) we analyzed the optical spectra of OB stars in the Wing of the SMC taken in 2010 with the Fiber Large Array Multi-Element Spectrograph (FLAMES) on the ESO Very Large Telescope (VLT). Three of the standard settings of the Giraffe spectrograph LR02 (resolving power $R = 6000$, 3960–4567 Å), LR03 ($R = 7500$, 4501–5071 Å), and HR15N ($R = 19200$, 6442–6817 Å) were used for this survey. Details of the observation, data reduction, and extraction of the spectra are described in Ramachandran et al. (2019). As a spectroscopic follow-up, we collected additional epochs in 2019 for most of this sample.

In this work we carefully inspected the spectra of Be stars and other fast rotators in this sample and discovered that SMCSGS-FS 69 shows significant radial velocity (RV) variations up to $45\,\mathrm{km\,s^{-1}}$ (see Fig. 5.2.1 and more details in Appendix D.1). Based on a single epoch optical spectrum the star was initially classified as B0.5 (II)e (Ramachandran et al. 2019). With a detailed inspection of the spectra, we found that SMCSGS-FS 69 is a double-line spectroscopic binary, consisting of both broad- and narrow-line components (Fig. 5.2.2), indicating that it is a potential post-mass-transfer binary. In addition, high-resolution H-band (1.51-1.70 μm) spectra from the Apache Point Observatory Galactic Evolution Experiment (APOGEE) survey (Majewski et al. 2017) are available in the archive, which we used to study the Be companion. Furthermore, our target was observed with Gaia and has listed proper motions and parallaxes. The radial velocities from the optical spectra and the Gaia proper motions agree well with that of SMC Wing. The negative values for the Gaia parallaxes support that this object is not a foreground Galactic star.

In addition to the spectra, we used various photometric data (from UV to infrared) from VizieR to construct the spectral energy distribution (SED). We also utilized data from the Transiting Exoplanet Survey Satellite (TESS) for this system. We ex-

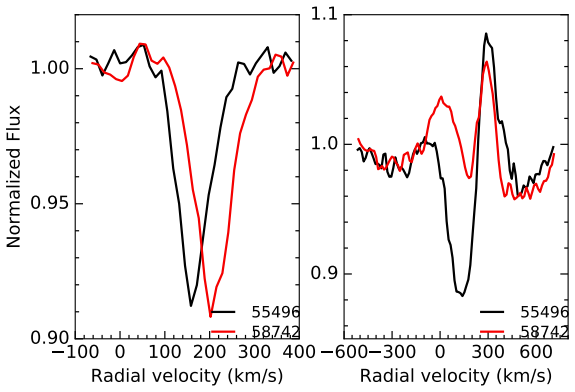

Fig. 5.2.1. Radial velocity variation in Si IIIλ4553 (left) and Hβ (right). The colors indicate the two observation epochs in Julian dates (see legend).

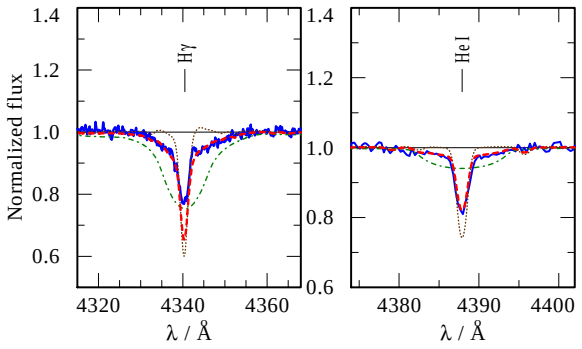

Fig. 5.2.2. Observed spectra of SMCSGS-FS 69 (blue solid lines) displaying narrow and broad components. The composite model (dashed red) is the weighted sum of the stripped star primary (dotted brown) and the rapidly rotating Be star secondary (dashed green) model spectra with effective temperatures of 24 kK and 28 kK, respectively. The weaker absorption core in Hγ likely results from filled-in disk emission.

tracted the light curves and found that the variability cannot be consistent with the orbital period, but rather indicates rotational modulations induced by the Be star (see Appendix D.2 for details).

5.3. Analysis

In the optical range the overall spectrum of SMCSGS-FS 69 resembles an early B-type supergiant except for the following a) disk emission features in Hα and Hβ ; b) the presence of extended broad wings and narrow absorption in Hγ and Hδ ; c) a combination of strong narrow absorption and weak broad components in multiple He I lines; and d) the strength of CNO absorption lines different from typical supergiant spectra. These features imply that the observed spectrum is a composite of a slowly rotating partially stripped B supergiant-like star and a fast-rotating MS star with disk emission (Fig. 5.2.2). All the metal lines are narrow, suggesting they are mainly from the stripped star. Although Hα is in emission, it is not clear whether this is entirely from the Be secondary or if there is a contribution from the stripped primary. Despite the low S/N, all the Brackett series lines in the APOGEE spectra (Fig. D.3.3) display broad disk emission with multiple peaks, which are mostly from the secondary Be star.

We performed the spectral analysis of SMCSGS-FS 69 using the PoWR model atmosphere code (see Gräfener et al. 2002; Hamann & Gräfener 2004; Sander et al. 2015, for more details). Initially, we chose PoWR SMC grid models (Hainich et al. 2019) as a starting point for the investigation and further computed additional models with tailored parameters for the primary and secondary. The full spectral and SED fit is shown in Fig. D.3.1.

In the spectral fitting method, we started with the analysis of the primary since it has a major contribution in the optical. First, we estimated the projected rotation velocity ($v \sin i$) of narrow-lined primary from metal absorption lines. We used a combined Fourier transform (FT) and goodness-of-fit (GOF) analysis employing the `iacob-broad` tool (Simón-Díaz & Herrero 2014). We applied this method to several metal lines and found the overall mean to deduce $v \sin i$ and macro-turbulent ($v_{\rm mac}$) velocities. Subsequently, these values, along with instrumental broadening, were used to convolve the model spectra to match the observations.

The main diagnostic we use to constrain the temperature of the primary is the He and Si ionization balance based on He I / He II and Si III / Si IV line ratios. The pressure-broadened wings of the Balmer lines are the primary diagnostics for the surface gravity. We considered Hγ and Hδ since they are less impacted by wind and disk emissions. However, in our case the Hγ and Hδ have contributions from both primary and secondary. Thus we simultaneously adjusted the luminosity ratios and surface gravities in the primary and the secondary models to match the observations. Since the ionization balance also reacts to gravity, we simultaneously re-adjusted T_* and log g_* to achieve a good fit to the observed spectra. The final uncertainty in the primary parameters reflects the overall fit quality and is limited by the model grid resolution. Constraining the secondary parameters is challenging, but we find that assuming cooler temperatures results in stronger broader components in the metal and He I lines, whereas hotter temperatures lead to pronounced He II lines in the composite spectra. To account for the broad lines from the secondary, we had to use a very high $v \sin i$.

Although we initially used grid models computed with typical SMC abundances (Trundle et al. 2007), they do not reproduce satisfactorily the observed CNO lines. To match the observed strength of CNO absorption lines, we had to drastically increase N and decrease C and O in the primary model. Most B supergiants in the SMC do not show such pronounced abundance variations. This is illustrated in Fig 5.3.1, where we compare the optical spectra of SMCSGS-FS 69 to that of an SMC B supergiant. The N abundance is determined by analyzing multiple N II and N III lines, while the CO abundance is just an upper

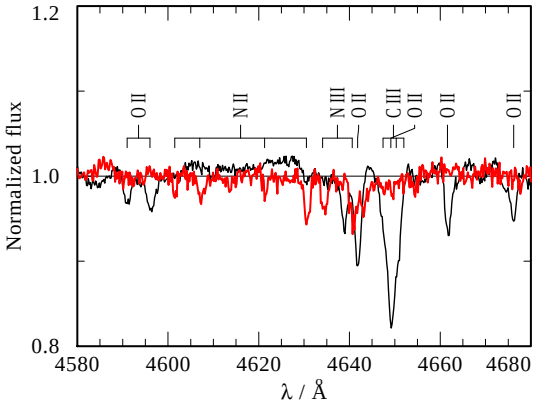

Fig. 5.3.1. Comparison of CNO lines in the spectra of SMCSGS-FS 69 (red) and an SMC B supergiant (AV 242) of similar $T_{\rm eff}$ (black). The spectra demonstrate that carbon and oxygen are substantially reduced, while nitrogen is highly enriched in SMCSGS-FS 69.

limit as most of the CO lines are either very faint or within the noise. In addition to the CNO abundances, we varied the H mass fraction ($X_{\rm H}$) in the primary models between 0.5 and 0.73 and found that slightly He-enriched models better represent the observations. The remaining elements either had their abundance values scaled to one-fifth of solar or adopted typical SMC abundances derived from OB stars (Trundle et al. 2007). We also checked for the overall broadening of metal lines by varying the micro-turbulence ξ in the range of 10-20 km s^{-1}.

Since a UV spectrum is not available for this object, we can only constrain the wind parameters ($\dot{M}$ and v_∞) from Hα. The Hα profile shows a single but asymmetric emission peak (Fig. D.3.2). If this emission is only contributed by the primary stripped star, it can be modeled as a result of a strong and slow stellar wind ($\log \dot{M} \approx -6.2$ and $v_\infty \approx 600\,{\rm km\,s^{-1}}$), as illustrated in Fig. D.3.2 (left). However, since infrared spectra (Fig. D.3.3) clearly showcase multi-peak disk emission features, we cannot exclude disk emission components in Hα. We can alternatively reproduce the asymmetric Hα profile with a combination of strong disk emission from the Be star and a weak absorption component ($\log \dot{M} = -7.2$) from the stripped star. Consequently, the wind mass-loss rate could be lower or higher depending on the Be disk emission strength. To precisely constrain the wind parameters, it is necessary to obtain UV spectra and to disentangle the components using multi-epoch optical spectra.

We determine the luminosity L and color excess $E_{\rm B-V}$ by fitting the composite model SED to the photometry (first panel of Fig. D.3.1). The model flux is diluted with the SMC Wing distance modulus of 18.7 mag (Cignoni et al. 2009). By fitting the normalized spectra, we are able to place constraints on the luminosity ratio, thus the SED fitting by composite model yields both primary and secondary luminosities. Both components were found to have the same luminosity, even though the primary stripped star contributes approximately 60-65% of the light in the optical range.

5.4. Results and discussion

Our spectroscopic analysis reveals that while the estimated temperature and gravity of the primary are in the range of B supergiants, the luminosity, radius, and consequently mass are considerably lower. The spectroscopic mass of the primary ($2-4.3 M_\odot$) is strikingly low compared to what is expected for an early B supergiant. Notably, the partially stripped star's He II flux contribution is much smaller than expected from fully stripped stars (e.g., Götberg et al. 2017), which is mainly due to the much lower temperature. The spectroscopic mass of the Be star secondary is less constrained ($10-26 M_\odot$) but consistent with a MS star. A complete overview of the derived parameters of both the primary and the secondary is given in Table 5.4.1.

In Fig. 5.4.1, we illustrate that, unlike other SMC B stars including supergiants, our primary star shows an extreme surface abundance pattern that cannot be explained via rotational mixing (e.g., as calculated in the tracks by Brott et al. 2011). The derived nitrogen abundance is a factor of 4 higher than for typical SMC B supergiants and ten times that for average B stars (Dufton et al. 2005; Hunter et al. 2007). On the other hand, carbon and oxygen are depleted by more than a factor of ~ 15 compared to typical SMC stars. While silicon abundances are in agreement, a slight enrichment in magnesium is detected. A comparison of the derived surface abundances with typical B stars and B supergiants in the SMC is given in the Appendix Table D.4.1.

The unusual abundance pattern can be explained by the removal of external layers via mass transfer, exposing the inner CNO-processed layers of the star. This would be in line with the exceptionally high luminosity-to-mass ratio of the primary, which we illustrate in Fig. 5.4.2 and compare it to relations of pure He stars and (early) MS stars. Notably, its luminosity ($\log L/L_\odot \sim 4.7$) is much higher than that of a pure He star of the same mass ($\log L/L_\odot \sim 4.0$), which suggests that most of the luminosity is produced in a leftover envelope layer via H-shell burning. Our primary is located in the upper left corner of Fig. 5.4.2, close to the Eddington limit, which is characteristic for stars that have lost a significant amount of mass via mass transfer. Altogether, these clues indicate a partially stripped star nature for the primary.

In the Hertzsprung–Russell (HR) diagram in Fig. 5.4.3 we compare SMCSGS-FS 69 with the other stripped star candidates reported in the literature, including fully and partially stripped objects. The newly discovered SMCSGS-FS 69 stands out as

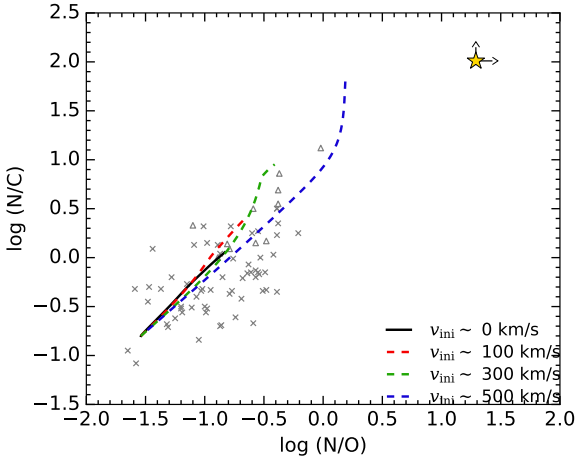

Fig. 5.4.1. N/C vs. N/O abundances of the stripped star (yellow star) compared to SMC B stars (triangles for giants and crosses for main sequence) from Hunter et al. (2009). The dashed lines are tracks from Brott et al. (2011) for the SMC with different initial rotations for $M_{ini} = 12$. The location of the stripped star at the top right corner demonstrates that its surface CNO pattern is too extreme to be explained by standard stellar evolution.

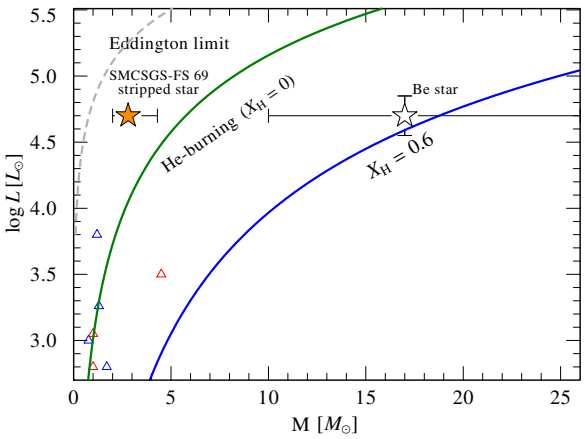

Fig. 5.4.2. Location of the SMCSGS-FS 69 components compared to mass-luminosity relations for pure He stars (green line) and early MS stars ($X_H = 0.6$, blue line), from Gräfener et al. (2011). The position of the partially stripped primary is shown by a filled star, while the Be secondary is shown by an open star along with their respective uncertainties. For comparison, Galactic hot subdwarfs in binaries (blue triangles) and partially stripped stars (red triangles) are indicated. The stripped primary is located in the upper left corner, which is a characteristic of a star that has lost most of its envelope via mass transfer.

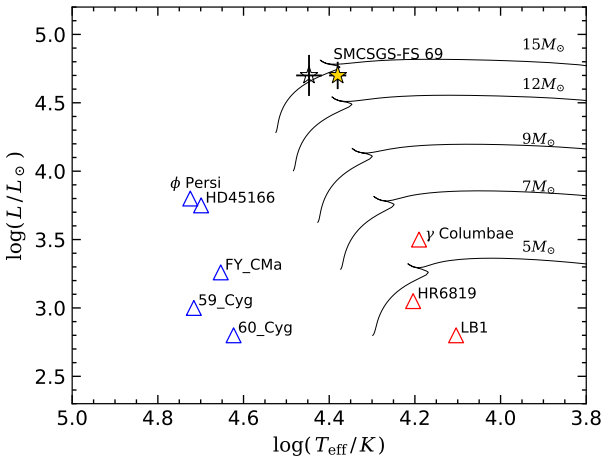

Fig. 5.4.3. Location of SMCSGS-FS 69 on the HR diagram compared to other stripped star candidates from the literature. Bonn SMC tracks are plotted for comparison (Brott et al. 2011). The symbols are the same as in Fig. 5.4.2

the most luminous (and massive) of all and is the first one detected at SMC metallicity. The HRD in Fig. 5.4.3 shows again that its mass is much lower than that of a MS star with a similar luminosity ($\sim 15 M_\odot$).

To interpret the evolutionary status of the system, we employed the stellar evolution code MESA (Paxton et al. 2015, 2018, 2019) to compute a binary model for SMCSGS-FS 69 (see Appendix D.5 for details). We found several solutions that are able to reproduce several of the observed parameters. Notably, based on a grid of $\sim$ 2300 binary evolution models, we find that the luminosity of the stripped primary can only be reproduced by models with the current mass stripped star$\gtrsim 3 M_\odot$. The closest match can be obtained with a Case B model in which the primary has an initial mass of $12.2 M_\odot$ and is stripped via Case B mass transfer to produce a partially stripped star of $4.6 M_\odot$ (with a He core of $3.6 M_\odot$). This is illustrated by the magenta line in Figures 5.4.4 and D.5.3. The Case B model (marginally) matches most of the properties derived in our spectral analysis, except for the surface O abundance (which is a factor of $\sim$ 3 too large). In order to reproduce the luminosity of the Be star companion, we find that at least $\sim$ 40% of the mass transferred during a Case B interaction needs to be accreted by the secondary. (see the example of an $11.7 M_\odot$ secondary accreting $3 M_\odot$ in Fig. D.5.1). This may be in tension with models where the accretion efficiency is regulated via surface rotation of the accretor, which generally predicts negligible accretion during Case B evolution (Sen et al. 2022; Pauli et al. 2022b), but may reach higher values depending on the assumed angular momentum budget ($\sim$ 30% in the model by Renzo & Götberg 2021). We find that an alternative solution in which no mass accretion is strictly required could

Table 5.4.1. Fundamental parameters and abundances derived for SMCSGS-FS 69 using spectroscopic analysis.

	Stripped star	Be star
T_* (kK)	24^{+2}_{-1}	28^{+2}_{-3}
$T_{2/3}$ (kK)	21^{+2}_{-1}	28^{+2}_{-3}
$\log g_*$ (cm s^{-2})	$2.65^{+0.2}_{-0.1}$	$3.7^{+0.2}_{-0.2}$
$\log g_{2/3}$ (cm s^{-2})	$2.4^{+0.2}_{-0.1}$	$3.7^{+0.2}_{-0.2}$
flux $f/f_{\rm tot}$ (V)	0.65	0.35
$\log L$ ($L_\odot$)	$4.7^{+0.1}_{-0.1}$	$4.7^{+0.15}_{-0.15}$
R_* ($R_\odot$)	$13^{+1}_{-1.5}$	$8.7^{+2}_{-1.5}$
$R_{2/3}$ ($R_\odot$)	$17^{+1.5}_{-2}$	$8.7^{+2}_{-1.5}$
$v \sin i$ (km s^{-1})	50^{+10}_{-10}	400^{+100}_{-100}
$v_{\rm mac}$ (km s^{-1})	20^{+20}_{-10}	50 (fixed)
ξ (km s^{-1})	12^{+3}_{-2}	14 (fixed)
$X_{\rm H}$ (mass fr.)	$0.59^{+0.1}_{-0.1}$	0.737*
$X_{\rm He}$ (mass fr.)	$0.40^{+0.1}_{-0.1}$	0.26*
$X_{\rm C}/10^{-5}$ (mass fr.)	$\lesssim 1$	21*
$X_{\rm N}/10^{-5}$ (mass fr.)	120^{+20}_{-20}	3*
$X_{\rm O}/10^{-5}$ (mass fr.)	$\lesssim 7$	113*
$X_{\rm Si}/10^{-5}$ (mass fr.)	11^{+2}_{-2}	13*
$X_{\rm Mg}/10^{-5}$ (mass fr.)	19^{+3}_{-3}	10*
$E_{\rm B-V}$ (mag)	$0.13^{+0.03}_{-0.03}$	
$M_{\rm spec}$ ($M_\odot$)	$2.8^{+1.5}_{-0.8}$	17^{+9}_{-7}
$\log Q_{\rm H}$ (s^{-1})	47.3	47.5
$\log Q_{\rm He\,II}$ (s^{-1})	32.9	37.5

Notes. (*) Abundances of the Be star are adopted from Trundle et al. (2007) which corresponds to typical values for OB stars in the SMC

possibly be obtained if the stripped star originates from a more massive primary ($16.5 M_\odot$) that interacts already during the MS (i.e., Case A mass transfer), and we observe the stripped product while it is still core-H burning. This scenario is illustrated by the green line in Fig. 5.4.4 and in Fig. D.5.2. The Case A model matches the observed surface abundances and rotation velocity of the stripped star very well, but is inconsistent regarding the current mass (by $\gtrsim 4 M_\odot$) and surface gravity (by $\gtrsim 0.45$ dex). While the determination of the surface gravity is affected by the rotationally broadened lines of secondary, the discrepancy in $\log g$ is so large that we consider the Case A scenario (under the current evolutionary calculation scheme) to be less likely. We estimate the relative rate of the two scenarios to be comparable in the population of the SMC within a factor of ~2 (see Appendix D.5).

Regardless of whether the stripped star in SMCSGS-FS 69 is a product of Case A or Case B mass transfer evolution, its pre-interaction mass of $\gtrsim 12 M_\odot$ guarantees that it sits firmly in the mass regime for the formation of neutron stars (NSs), making it the first such stripped star found to date. Our binary evolution models suggest that in 1−1.5 Myr the primary will explode as a type IIb/Ib supernova (with $\sim 0.02 M_\odot$ of H left at the surface) and form a NS. If the system remains bound, it will later evolve into a Be X-ray binary. The favored Case B model tentatively suggests a long orbital period of hundreds of days at this stage. Such wide Be X-ray binaries are thought to be the direct progenitors of common-envelope events, leading to double NS mergers (Tauris et al. 2017; Vigna-Gómez et al. 2020; Klencki et al. 2021). The properties of Be X-ray binaries in the SMC seem to point toward moderate accretion efficiencies in their prior mass transfer evolution (Vinciguerra et al. 2020;

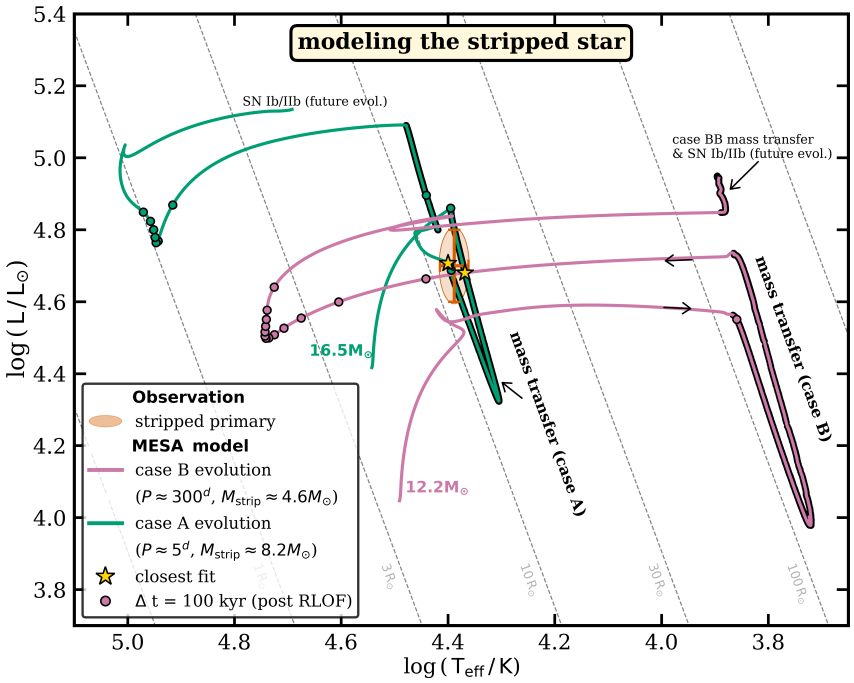

Fig. 5.4.4. Two potential binary evolution pathways leading to the formation of a stripped star in SMCSGS-FS 69. The Case B mass transfer evolution roughly matches most of the derived surface properties, though it notably requires $\gtrsim$ 40% accretion efficiency to reproduce the secondary (Fig. D.5.1). The Case A mass transfer evolution does not have that requirement, but it overpredicts the current mass of the stripped star.

Igoshev et al. 2021), in agreement with our Case B evolutionary model for SMCSGS-FS 69. These considerations emphasize the significance of SMCSGS-FS 69 as a newly discovered intermediate evolutionary stage in the formation pathway of Be X-ray binaries and double NS mergers.

The discovery of a massive stripped star + Be binary in a transition phase allows binary evolution to be constrained and hints at the existence of more such binaries at low metallicity. Moreover, SMCSGS-FS 69 can act as a template for identifying hidden systems in typical OB populations. These partially stripped transition stages are more luminous due to their H-shell burning and are visible in the optical due to the cooler surface temperatures. Even though the transition phase is short-lived ($\lesssim$ 10% He burning lifetime), binary evolution models predict tens or more of similar objects to be hiding among the known OB star population of the SMC (Klencki et al., in prep), motivating a large-scale search for binary-interaction products in this low-metallicity environment.

The growing population of partially stripped stars, including SMCSGS-FS 69, further raises the question of why we discover systems during a short transition stage, but so far do not observe intermediate-mass stripped stars in their hot, compact stage. Evolutionary models usually predict that stripped stars settle at hotter temperatures, but with lower luminosities (see, e.g., Fig. 5.4.4). It is presently unclear whether these objects are just very hard to observe or this stage might not be regularly reached by binary evolution, contrary to current predictions. The presence or absence of such a compact stripped-star population will have a severe impact on population synthesis predictions, for example, due to the different evolutionary fates and ionizing fluxes.

Acknowledgments: We thank the anonymous referee for useful suggestions. We would like to thank Ylva Götberg and Cole Johnston for helpful discussions. VR and AACS are supported by the Deutsche Forschungsgemeinschaft (DFG - German Research Foundation) in the form of an Emmy Noether Research Group – Project-ID 445674056 (SA4064/1-1, PI Sander) and funding from the Federal Ministry of Education and Research (BMBF) and the Baden-Württemberg Ministry of Science as part of the Excellence Strategy of the German Federal and State Governments. JK acknowledges support from the ESO Fellowship. DP acknowledges financial support by the Deutsches Zentrum für Luft und Raumfahrt (DLR) grant FKZ 50OR2005. TS acknowledges support from the European Union's Horizon 2020 under the Marie Skłodowska-Curie grant agreement No 101024605. This research was supported by the International Space Science Institute (ISSI) in Bern, through ISSI International Team project #512 "Multiwavelength view on massive stars in the era of multimessenger astronomy".

Chapter 6

Manuscript V: X-Shooting ULLYSES: Massive Stars at low metallicity VIII. Stellar and wind parameters of newly revealed stripped stars in Be binaries

V. Ramachandran, A.A.C. Sander, **D. Pauli**, J. Klencki, F. Backs, F. Tramper, M. Bernini-Peron, P. Crowther, W.-R. Hamann, R. Ignace, R. Kuiper, S. Oey, L. M. Oskinova, T. Shenar, H. Todt, J.S. Vink, L. Wang, A. Wofford, and the XShootU collaboration

accepted by Astronomy & Astrophysics, 2024

Abstract

On the route toward merging neutron stars and stripped-envelope supernovae, binary population synthesis predicts a large number of post-interaction systems with massive stars that have been stripped of their outer layers. However, observations of such stars in the intermediate-mass regime below the Wolf-Rayet masses are rare. Using X-Shooting ULLYSES (XShootU) data, we have discovered three partially stripped star + Be/Oe binaries in the Magellanic Clouds. We analyzed the UV and optical spectra using the Potsdam Wolf-Rayet (PoWR) model atmosphere code by superimposing model spectra that correspond to each component. The estimated current masses of the partially stripped stars fall within the intermediate-mass range of $\approx 4 - 8\,M_{\odot}$. These objects are found to be over-luminous for their corresponding stellar masses, which aligns with the luminosities during core He-burning. Their accompanying Be/Oe secondaries are found to have much higher masses than their stripped primaries (mass ratio $\gtrsim 2$). The surfaces of all three partially stripped stars exhibit clear indications of significant nitrogen enrichment as well as a depletion of carbon and oxygen. Furthermore, one of our sample stars shows signs of substantial helium enrichment. Our study provides the first comprehensive determination of the wind parameters of partially stripped stars in the intermediate-mass range. The wind mass-loss rates of these stars are estimated to be on the order of $10^{-7}\,M_{\odot}\,\mathrm{yr}^{-1}$, which is more than ten times higher than that of OB stars with the same luminosity. The current mass-loss recipes commonly employed in evolutionary models to characterize this phase are based on OB or WR mass-loss rates, and they significantly underestimate or overestimate the observed mass-loss rates of (partially) stripped stars by an order of magnitude. Binary evolution models suggest that the observed primaries had initial masses in the range of 12–17 $M_{\odot}$, and are potential candidates for stripped-envelope supernovae resulting in the formation of a neutron star. If these systems survive the explosion, they will likely evolve to become Be X-ray binaries and later double neutron stars.

6.1. Introduction

Massive stars are key players in the evolution of the Universe as they produce heavy elements, emit ionizing radiation, explode as supernovae, and collapse into compact objects. However, there are still major gaps in our understanding on their evolution, fate, and impact to their surroundings, especially at low metallicity, which hampers our view on the formation of gravitational wave sources and the re-ionization of the Universe.

One of the key factors affecting the evolution and final remnant mass of massive stars is binary interaction. Most massive stars are not isolated, but belong to binary or multiple systems, where they can exchange mass and angular momentum with their companions (Sana et al. 2012, 2014). Binary evolution can lead to the formation of a significant population of core helium-burning stars that have lost a significant part of their hydrogen-rich envelope after mass transfer via Roche-lobe overflow. These stars are known as stripped-envelope stars, and their spectral characteristics vary from hot subdwarfs to Wolf-Rayet (WR) stars, depending on their masses (e.g., Paczyński 1967; Vanbeveren 1991; Eldridge et al. 2008; Götberg et al. 2017). However, stripped-envelope stars with masses between the regimes of low-mass subdwarfs ($\lesssim 1.5\,M_{\odot}$) and classical WR stars ($\gtrsim 8\,M_{\odot}$) are rarely observed. Furthermore, the minimum mass of WR stars is found to increase with lower metallicities ($\gtrsim 17\,M_{\odot}$ at Z=0.2 $Z_{\odot}$; Shenar et al. 2020b) expanding the range of intermediate masses. Drout et al. (2023) used UV photometry and follow-up optical spectroscopy in the Magellanic Clouds to specifically look for hot and compact phases of stripped stars. Götberg et al. (2023) carried out a spectroscopic analysis of a subsample of these stripped stars, which revealed seven hot He stars in the intermediate-mass regime. However, they found that the contribution from the secondary companion (mass gainer) to the optical spectra in their subsample is negligible. They thus suggest that these hot stripped He stars are the result of either common envelope ejection in case the secondary is a main-sequence star, or – in the case of compact companions – stable mass transfer or common envelope ejection, whereas in the lower mass range a handful of subdwarf O + Be binaries have been observed in the Galaxy (e.g., Schootemeijer & Langer 2018; Wang et al. 2021).

Binary evolution models predict that these stripped He stars are typically fainter than their main-sequence companions, and hence can be easily outshined (e.g., Yungelson et al. 2024). This makes their identification not easily achieved without the use of detailed quantitative spectroscopy. There have been a few recent detections suggesting that the predicted population of stripped-envelope stars, which has so far been mostly absent in observations, may actually be present within the known population of OB stars. Systems originally proposed to be X-ray quiet black hole + Be binaries such as LB1 and HR6819 (Liu et al. 2019; Rivinius et al. 2020) have been revealed as partially stripped star + Be binaries (e.g., Abdul-Masih et al. 2020; Bodensteiner et al. 2020a; Shenar et al. 2020a; El-Badry & Quataert 2021; Frost et al. 2022). Ramachandran et al. (2023) recently discovered the first partially stripped massive star in a binary with a massive Be-type companion located in the low-metallicity environment of the Small Magellanic Cloud (SMC). Villaseñor et al. (2023) has identified a similarly bloated stripped star with an early B-type companion in the Large Magellanic Cloud (LMC). However, most of these discovered stripped stars in binaries seem to not reside in the predicted long-lived stage of core He burning on the He-Zero age main sequence, where they are hot and fully stripped. To the contrary, observations find cooler, partially stripped stars, which are associated with short transition phases.

Recent evolutionary models by Klencki et al. (2022) suggest that binary evolution at low metallicity might favor partial envelope stripping and mass transfer on a long nuclear timescale. The presence or absence of a compact stripped-star population would have a severe impact on population synthesis predictions, for example, due to the different evolutionary fates and ionizing fluxes. Accurate knowledge about the evolution of massive binary stars is needed to explain observed gravitational wave mergers. However, there is a significant lack of observations for binary systems containing a massive main-sequence star with a stripped-star companion. Whether this is due to observational challenges or errors in the underlying evolutionary models is one of the key questions in massive star research. A particularly decisive, but essentially unknown, ingredient is the wind mass-loss rate of these intermediate-mass partially stripped stars, which can only be constrained with UV spectroscopy. There are currently no studies on the winds of stripped stars, due to the reliance on optical spectra in the newly discovered systems, which lack UV spectra.

In this paper, we report the discovery of three partially stripped stars with Oe/Be companions in the Magellanic Clouds using multi-epoch and multi-wavelength spectroscopy. We refer to the mass donor, the stripped star, as the "primary" throughout this work, and the mass gainer, the spun-up star, as the "secondary". To search for hidden stripped stars among the known OB population, we used both UV and optical spectra provided by the X-Shooting ULLYSES (XShootU) project.[1] The XShootU data cover hundreds of hot massive stars in the Magellanic Clouds, providing a good sample to identify and characterize stripped stars in binaries among the OB populations at low metallicity.

As a result of binary interaction (stable mass transfer), the secondary (i.e., the initially less massive) component gains mass and angular momentum (Kriz & Harmanec 1975; Pols et al. 1991; Langer et al. 2020). Such secondaries would evolve into rapidly rotating stars (e.g., de Mink et al. 2013a; Renzo & Götberg 2021), which can have disk emission features and appear as Be stars (Pols et al. 1991; Shao & Li 2014; Bodensteiner et al. 2020b). Moreover, the lack of main-sequence companions to Be stars (Bodensteiner et al. 2020b), the evidence from SEDs for a tidal truncation of the Be disk by a companion (Klement et al. 2019), as well as population synthesis predictions (Shao & Li 2014; Hastings et al. 2021) indicate that Be stars are part of post-interaction binaries, and are the best candidates to look for stripped-star companions. We thus focused on objects within the XShootU sample that show disk emission features (Oe/Be) in their optical spectra. We looked for the spectral characteristics of binaries with stripped stars and Be stars, as suggested by Ramachandran et al. (2023). We carefully inspected narrow and broad components of stellar absorption lines in such systems and looked for radial velocity variations if multi-epoch observations were available. In a subsample of these systems, we carried out the spectral analysis and confirmed the detection of three

[1] https://massivestars.org/xshootu/

systems consisting of a partially stripped star and a Be/Oe star which we present in this work. By analyzing both the UV and optical spectra, we are providing the empirical wind parameters of the stripped stars for the first time. The observations used in this study are described in Sect. 6.2. The details on the spectroscopic analysis and parameters derived for each system are covered in Sect. 6.3.2, 6.3.3 and 6.3.4. Discussions on mass, chemical abundances, wind, and evolution of the stripped stars are presented in Sect. 6.4, followed by our conclusions in Sect. 6.5. In Sects. E.2 to E.5 details of the orbital analysis, evolution models, and additional plots are given.

6.2. Observations

The objects are part of the XShootU sample. The details of the project, observations, and data are explained in (Vink et al. 2023; Roman-Duval et al. 2020). For two of the sample stars (2dFS 163 and Sk -71° 35) UV spectra are taken with the *Hubble* Space Telescope's Cosmic Origins Spectrograph (HST/COS) with the G130M/1291 and G160M/1611 gratings. For 2dFS 2553, the UV spectrum is obtained using the Space Telescope Imaging Spectrograph (HST/STIS) with the E140M/1425. Additionally, we utilized the available HST/COS spectra taken with the G130M/1096 at three different epochs for this particular object.

Optical spectra of each star were obtained with X-Shooter at the ESO's Very Large Telescope (VLT). Data reduction and normalization methods are described by Sana et al. (2024). The spectral coverage includes both the UBV and VIS arms. In addition, low-resolution archival optical spectroscopy is available for two SMC targets as a part of the 2dF SMC survey (see Evans et al. 2004, for more details). VLT/FLAMES spectra of Sk -71° 35 are also utilized in this study (details on the observations and data reduction are in Ramachandran et al. 2018a,b). Here, the spectra are taken with three of the standard settings of the Giraffe spectrograph: LR02, LR03, and HR15N. Details of the available spectra for each source are summarized in Table 6.2.1.

In addition to the flux-calibrated UV spectra, we used various photometric data (from UV to infrared) to construct the spectral energy distribution (SED). The UBV and JHK magnitudes of all sources are taken from Table B.1 in Vink et al. (2023). Additionally, we included Gaia G magnitudes from Gaia Collaboration (2022). We also utilized data from the Transiting Exoplanet Survey Satellite (TESS) for Sk -71° 35. We extracted the light curves and used them to understand the binary period of the system. The light curves of the two remaining stars are contaminated by bright sources visible in their full frame images (FFIs) since they are fainter in optical (by 2 mag). Therefore, we did not utilize them to determine periods.

Table 6.2.1. Spectroscopic data used in this study

Object	Telescope	Instrument	grating	λ (Å)	R	Date (yy/mm/dd)	Exposure (s)	PI
2dFS 163	HST	COS	G130M	1132–1433	12000–17000	2020/10/09	2084	Roman-Duval, J
	HST	COS	G160M	1419–1790	13000–20000	2020/10/09	4815	Roman-Duval, J
	VLT	X-shooter	UBV	3100–5600	6700	2020/10/28	2×1655	Vink, J
	VLT	X-shooter	VIS	5600–10240	11400	2020/10/28	2×1725	Vink, J
	AAT	2dF		3900–4900	1600	1998/09/25	1800	Evans, C.J.
2dFS 2553	HST	COS	G130M	900–1236	13000	2022/06/14	2907	Roman-Duval, J
	HST	COS	G130M	900–1236	13000	2022/07/01	6963	Roman-Duval, J
	HST	COS	G130M	900–1236	13000	2022/05/19	1828	Roman-Duval, J
	HST	STIS	E140M	1144–1710	45800	2020/06/24	2755	Mahy, L
	VLT	X-shooter	UBV	3100–5600	6700	2020/11/08	3×1655	Vink, J
	VLT	X-shooter	VIS	5600–10240	11400	2020/11/08	2×1725	Vink, J
	VLT	X-shooter	UBV	3100–5600	6700	2022/08/14	2000	Pauli, D
	VLT	X-shooter	VIS	5600–10240	8935	2022/08/14	2000	Pauli, D
	AAT	2dF		3900–4900	1600	1998/09/28	1800	Evans, C.J.
SK -71 35	HST	COS	G130M	1132–1433	12000–17000	2022/04/20	488	Roman-Duval, J
	HST	COS	G160M	1419–1790	13000–20000	2022/04/20	816	Roman-Duval, J
	VLT	X-shooter	UBV	3100–5600	6700	2021/03/12	540	Vink, J
	VLT	X-shooter	VIS	5600–10240	11400	2021/03/12	610	Vink, J
	VLT	GIRAFFE	LR02	3960–4570	6300	2015/12/19	5400	Oskinova, L.M
	VLT	GIRAFFE	LR03	4500-5070	7500	2015/12/19	5400	Oskinova, L.M
	VLT	GIRAFFE	LR03	6445–6820	17000	2015/12/19	3600	Oskinova, L.M

6.3. Analysis

6.3.1. Atmosphere models

We performed the spectral analysis of the binaries discussed in this paper using the PoWR model atmosphere code. PoWR is a state-of-the-art stellar atmosphere code suitable for the spectroscopic analysis of hot stars with and without winds, across a broad range of metallicities (Hainich et al. 2014, 2015; Oskinova et al. 2011). The PoWR code solves the radiative transfer equation for a spherically expanding atmosphere and the statistical equilibrium equations simultaneously under the constraint of energy conservation. Stellar parameters were determined iteratively. Details of the PoWR code are described in Gräfener

et al. (2002), Hamann & Gräfener (2003), Hamann & Gräfener (2004), Sander et al. (2015), and Todt et al. (2015a). PoWR models have been used to analyze a large sample of WR stars (e.g., Hainich et al. 2015, 2014; Shenar et al. 2016, 2019), OB stars (e.g., Ramachandran et al. 2018b, 2019; Rickard et al. 2022), and a few stripped stars in binaries (Ramachandran et al. 2023; Pauli et al. 2022b; Rickard & Pauli 2023) in the Magellanic Clouds. In the discussions, we compare the results from the analysis of our newly discovered stripped star binaries to the above literature as well as other studies.

The main parameters that specify a PoWR model are the stellar luminosity L, stellar temperature T_*, and surface gravity g_*, as well as mass-loss rate $\dot{M}$ and terminal velocity v_∞ for the wind. The stellar temperature relates to stellar radius R_* and L via the Stefan-Boltzmann law $L = 4\pi\sigma_{\rm SB} R_*^2 T_*^4$. In this case the "stellar temperature" T_* is the effective temperature $T_{\rm eff}$ corresponding to the stellar radius R_* that marks the inner boundary of the model atmosphere. In our models, the inner boundary and thus R_* is located at a Rosseland continuum optical depth of 20. Contrary to OB stars, stripped stars may have a slight difference between their stellar temperature T_* and the photospheric effective temperature $T_{2/3}$, defined correspondingly to $R_{2/3}$ at $\tau_{\rm Ross} = 2/3$. In the derived parameters of our sample, we provide $T_{2/3}$, $\log g_{2/3}$, and $R_{2/3}$, as well as T_*, $\log g_*$, and R_*.

In the subsonic region of the stellar atmosphere, a velocity field is defined such that a hydrostatic density stratification is approached (Sander et al. 2015). In the supersonic region, the prespecified wind velocity field $v(r)$ is assumed to follow the so-called β-law (Castor et al. 1975)

$$v(r) = v_\infty \left(1 - \frac{r_0}{r}\right)^\beta . \tag{6.3.1}$$

In this work, we adopt $\beta = 0.8$, for OB-type secondaries (Kudritzki et al. 1989) and we explore different values for stripped stars.

In the non-LTE iteration in the co-moving frame, the line opacity and emissivity profiles are treated as Gaussians with a width following from a constant Doppler velocity $v_{\rm Dop} = 30\,{\rm km\,s^{-1}}$. In the formal integral for the calculation of the emergent spectrum, the Doppler velocity is split into the depth-dependent thermal velocity and a "microturbulence velocity" $\xi(r)$. We assume $\xi(r) = \max(\xi_{\rm min}, 0.1v(r))$ for the models, where the photospheric microturbulent velocity $\xi_{\rm min} = 14\,{\rm km\,s^{-1}}$ is fixed for OB-type secondaries (Hainich et al. 2019) and varied as a fit parameter for stripped stars. The pressure broadening is also taken into account in the formal integral.

Optically thin inhomogeneities in the model iterations are described by the "clumping factor" D by which the density in the clumps is enhanced compared to a homogeneous wind of the same $\dot{M}$ (Hamann & Koesterke 1998b). For all stars in our study, we account for depth-dependent clumping assuming that clumping begins at the sonic point, increases outward, and reaches a density contrast of D at a radius of $R_{\rm D}$ (Runacres & Owocki 2002). If necessary, we adjusted the values of D and $R_{\rm D}$ for stripped stars, otherwise we set them to $D = 10$ and $R_{\rm D} = 10\,R_*$.

The PoWR code can account for additional ionization due to X-rays. To match the observations (especially N V lines in the UV), X-rays were integrated into the model for certain objects in this study. The X-ray emission is modeled using the Baum et al. (1992) approach, assuming only free–free transitions contribute to the flux. A more recent description of the inclusion of X-rays in the PoWR is given in Sander et al. (2018). Comparisons to CMFGEN and FASTWIND are provided in appendix D of Bernini-Peron et al. (2023) and appendix B.4 of Sander et al. (2024), respectively. Since the current generation of PoWR models is limited to spherical symmetry, the X-rays are assumed to arise from an optically thin spherical shell around the star. The X-ray emission is specified by three free parameters: fiducial temperature of the X-ray emitting plasma $T_{\rm X}$, the onset radius of the X-ray emission R_0 ($R_0 > R_*$), and a filling factor $X_{\rm fill}$. We set the onset radius to $1.1R_*$ and $T_{\rm X}$ to 1 MK. The X-ray filling factor is adjusted such that the UV lines are reproduced by the model.

The models are calculated using complex atomic data of H, He, C, N, O, Mg, Si, P, S, and the Fe group elements. The iron group elements are treated with the so-called superlevel approach as described in Gräfener et al. (2002). The initial chemical abundances of C, N, O, Mg, Si, and Fe are adopted from Trundle et al. (2007) and Hunter et al. (2007). The abundance of the remaining elements in LMC stars is fixed at $1/2\,Z_\odot$, while in SMC stars it is fixed at $1/5\,Z_\odot$. The mass fractions of carbon (C), nitrogen (N), and oxygen (O) are adjusted as needed for each object to achieve the best possible match with their observed spectra.

The PoWR code is used to calculate models for individual stars. To analyze composite spectra originating from binaries, we compute individual models tailored to each component of the binary and merge them (based on their luminosity ratio) such that we match the composite observed spectra. Our models are limited to spherical symmetry, which may not hold for some binary systems. In particular for the case of fast-rotating Oe/Be secondaries, rotation modifies the shape of the star and leads to a deviation from spherical symmetry, thereby influencing the derived stellar parameters such as effective gravity, effective temperature, and radiative flux (von Zeipel 1924). The pole-to-equator temperature and gravity can differ by a few kK and few dex, respectively, resulting in an uncertainty of about ≈2 kK in T_* and ≈0.2 dex in $\log g$ for early main-sequence B stars that are close to critically rotating $\Omega/\Omega_C = 0.8$ (Frémat et al. 2005).

6.3.2. 2dFS 163

2dFS 163 was previously classified as an O8 supergiant by Evans et al. (2004) as a part of 2dF SMC survey. The object's optical and UV spectra are primarily characterized by the prevalence of narrow absorption lines, with the exception of weak broad components observed in the He I and Balmer lines (see Fig. 6.3.1). The optical spectrum can be classified as O7.5 based on the intensities of He I λ4471 and He II λ4542, using the O type standards from Sota et al. (2011). Additionally, the luminosity class can be determined as Ib(f) by considering the intensity of He II λ4686, as suggested by Evans et al. (2004). When solely focusing on the narrow He lines, the intensity ratio between He I λ4471 to He II λ4542 suggests a slightly earlier subtype than

O7, in line with the strength of N III $\lambda\lambda$4634-4640 emission lines. Hence, we classified the primary as O6.5 Ib(f). We determine the radial velocity (RV) at different epochs as described in Appendix E.1. The narrow absorption lines show an RV variation of $\sim 28\,\mathrm{km\,s^{-1}}$ between the recently obtained X-shooter spectra and archival 2dF spectra. In addition, the narrow photospheric lines in the UV spectra (e.g., N III, Si V) show an RV variation of $\sim$43 $\mathrm{km\,s^{-1}}$ relative to X-shooter spectra, indicating its binary nature. Furthermore, the observed RV variations indicate that the narrow-line star moves faster ($\delta RV \sim 43\,\mathrm{km\,s^{-1}}$) than the less prominent broad-line star ($\delta RV \sim 15\,\mathrm{km\,s^{-1}}$), indicating that the O supergiant-like star (partially stripped) likely possesses a significantly lower mass than its rapidly rotating companion. Moreover, double peak disk emission profiles are visible in Hα, Hβ, and across all members of the Paschen series. These lines are likely coming from the fast-rotating companion rather than the slow-rotating O supergiant-like star. In conclusion, the spectral features suggest that 2dFS 163 is a post-interaction binary system consisting of a star that has been stripped of its outer layers and rapidly rotating early Be star companion.

We chose PoWR SMC grid models (Hainich et al. 2019) as a starting point for the analysis and further computed additional models with tailored parameters. As an initial approach, we try to fit the spectra as a single star since the primary contributes to most of the light. One can approximately fit the spectra with models assuming a range of stellar temperatures $T_* \sim 34 - 38$ kK. For the cooler models, we used a lower log g_* (3.5) while a higher log g_* (3.9) is used for the hotter models. The cooler models were unable to reproduce the N III emission lines and the N IV absorption lines in the optical as well as the unsaturated C IV and weak He II line in the UV. On the other hand, the hotter models result in weaker He I lines and broader He II lines in the optical as well as weaker C IV and stronger He II in the UV than observed. Despite the differences, all these single-star models suggested much lower stellar masses than expected for an O supergiant, namely in the range of $\sim 7 - 12 M_\odot$.

After these initial considerations, we proceed with a two-model approach representing each of the components. To determine the temperature of the stripped star, we utilized the N III $\lambda\lambda$4634–4642 emission lines and various absorption lines including N IV $\lambda\lambda$3460-3485, Si IV λ4089, and He II lines in the optical spectrum. These lines are exclusively originating from the stripped primary, making them suitable for constraining its temperature. Simultaneously, the C IV λ1169 to C III λ1175 and O IV to O V line ratios are employed in the ultraviolet spectra to constrain the temperature of the primary.

In order to account for the influence of gravity on the ionization balance, we made simultaneous adjustments to both the effective temperature (T_*) and the surface gravity (log g_*) to obtain a satisfactory agreement with the observed spectra. A major constraint on log g_* of the primary is the need to align with the profiles of the He II spectral lines. The Balmer lines are not a good diagnostic in this case as they are influenced by contributions from both the secondary and primary star as well as the disk contribution. Along with T_* and log g_*, we also varied the micro-turbulence ξ velocity in the range of 10-20 $\mathrm{km\,s^{-1}}$ to match the metal line profiles.

The secondary star is not making any significant contribution to the metal lines or the He II lines in the optical (no broad components visible in the spectra), suggesting that its temperature is unlikely to exceed 30,000 K, as otherwise there would be observable contributions in the He II lines. Similarly, there should be Si III lines in the optical near 4550-4570 Å if the secondary is cooler than 24,000 K. Simultaneously, the secondary component exhibits noticeable effects on the absorption lines of He I, specifically at wavelengths 4387, 4471, and 4922 Å. Based on these, we could estimate the temperature range and subsequently make adjustments to the luminosity ratio. The luminosity ratios, surface gravities, and temperatures in the primary and secondary models were adjusted concurrently to match the observations.

The projected rotation velocity ($v \sin i$) of the narrow-lined primary was estimated using N III emission lines, as well as absorption lines of N III, N IV, and He I. In our study, we employed a combined approach of Fourier transform (FT) and goodness-of-fit (GOF) analysis using the `iacob-broad` tool (Simón-Díaz & Herrero 2014). The method was applied to various lines and the average values are adopted for $v \sin i$ and the macro-turbulent (v_{mac}) velocity. In the secondary analysis, a high rotational velocity was applied to the model in order to accommodate the broad core of the He I lines. In this case, we fixed v_{mac} while varying $v \sin i$ to achieve the best fit of these lines. These velocities were then used, along with instrumental broadening, to convolve the model spectra such that they match the observations.

We initially computed models with typical SMC abundances (Trundle et al. 2007). However, they fail to reproduce all the observed CNO lines satisfactorily. In order to match the observed intensity of the CNO lines, the abundance of N is increased by a factor of 50 in the stripped-star model, while the abundances of C and O are decreased by a factor of 20 and 5, respectively. The N abundance is determined by analyzing multiple N IV and N III lines in both the UV and the optical range. The optical range exhibits a notable absence of the majority of C and O absorption lines (see Fig. 6.3.1) which is usually not expected in an O star spectrum. This absence suggests a strong depletion in the abundance of these elements. For the C abundance, we rely on the C IV λ1169 and C III λ1175 absorption lines in the UV. We deduce the O abundance from O IV and O III lines near 3350Å and O IV lines in the UV. In addition to the CNO abundances, we varied the H mass fraction (X_{H}) in the primary model between 0.2 and 0.73 and found that H-depleted (He-enriched) models better represent the observations. At this hot temperature, the strength of narrow components in He I and He II lines can only be simultaneously reproduced with a high He abundance. A standard He abundance would result in very weak or absent He I lines at 4388, 4713, 4922 Å for the stripped star. Additionally, in the UV spectrum, He II λ1640 line is found to be better reproduced with this higher He abundance. Strong He and N enrichment, along with C and O depletion, are in agreement with the primary's stripped envelope.

Once the stellar parameters are adjusted, we proceed to modify the wind parameters in the primary model in order to accurately match the UV P Cygni profiles, and wind lines observed in the optical spectrum. We measured v_∞ from the blue edge of C IV $\lambda\lambda$1548–1551 and N V $\lambda\lambda$1238–1242 (see Fig. 6.3.2). The mass-loss rate ($\dot{M}$) is estimated from the C IV, N V and Si IV profiles. Nevertheless, an accurate reproduction of N V can only be achieved by incorporating an X-ray field into our model, where the X-ray luminosity is $\log L_{\mathrm{X}} = 31.5\,\mathrm{erg\,s^{-1}}$. X-rays have a significant impact on the ionization structure, particularly in enhancing the N V line (Cassinelli & Olson 1979; Baum et al. 1992). Figure 6.3.3 demonstrates the influence of incorporating X-rays on the population of nitrogen ions. Specifically, the incorporation of X-rays leads to an increase in the

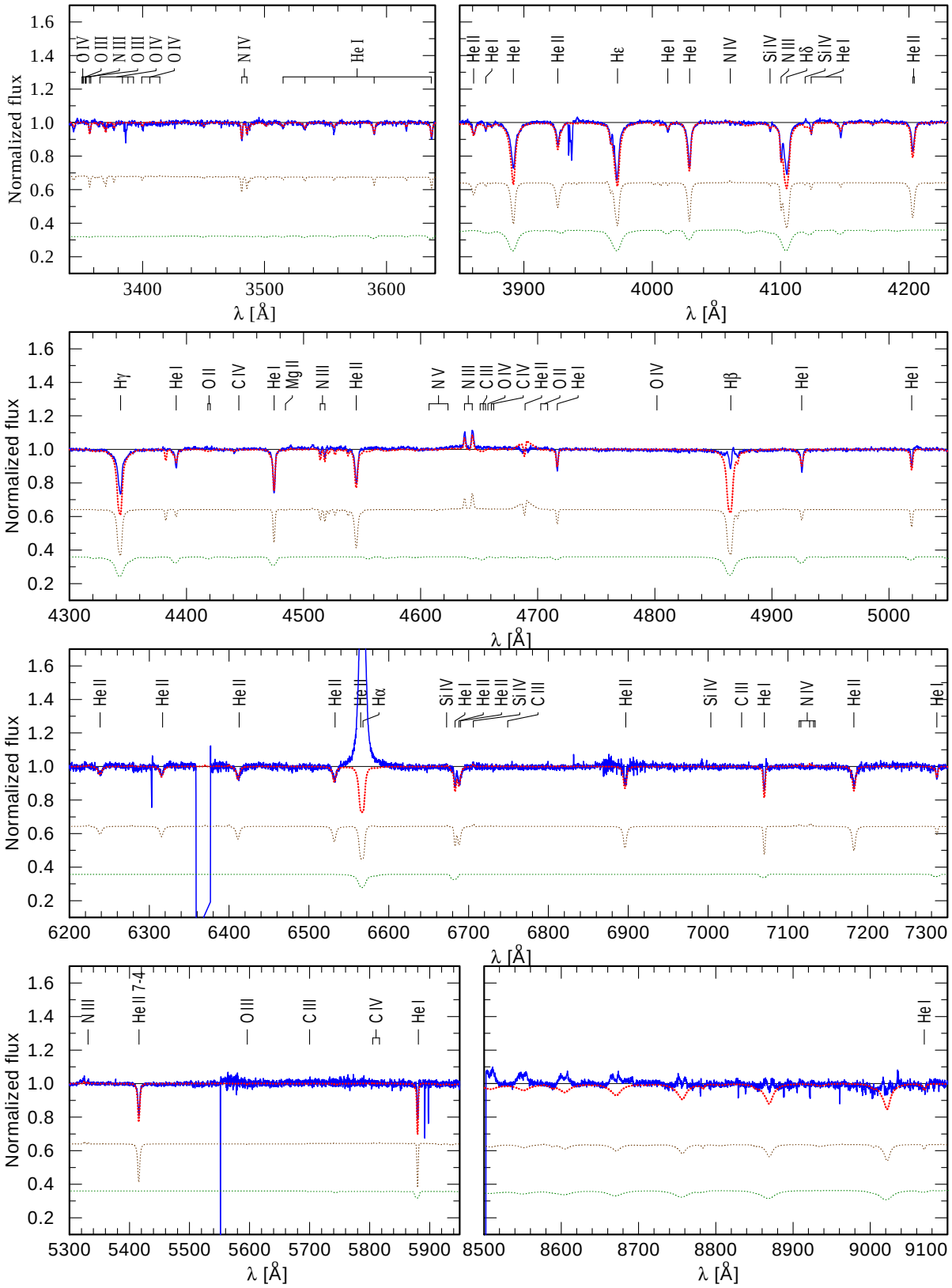

Fig. 6.3.1. Observed spectra of 2dFS 163 (solid blue) compared to the model spectra. The composite model (dotted red) is the weighted sum of the stripped star (dotted brown) and rapidly rotating Be star (dotted green) model spectra.

population of N v in the outer wind. It should be noted that the sensitivity of existing X-ray surveys is not sufficient to detect the star. Using current X-ray catalogs, the upper limit on X-ray luminosity of 2dFS 163 in the 0.2-12.0 keV band is $\log L_X < 36.5$.

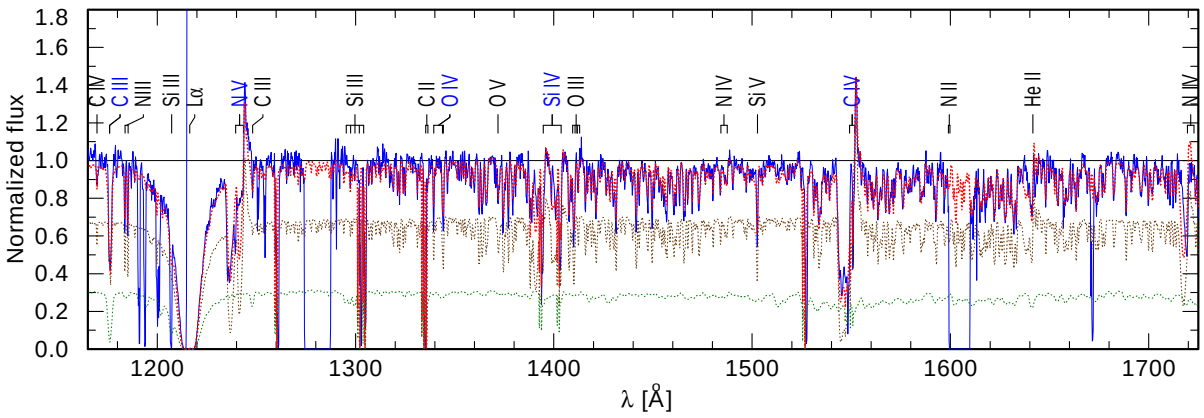

Fig. 6.3.2. Observed HST UV spectra of 2dFS 163 (solid blue) compared to the model spectra. The composite model (dotted red) is the weighted sum of the stripped star (dotted brown) and rapidly rotating Be star (dotted green) model spectra

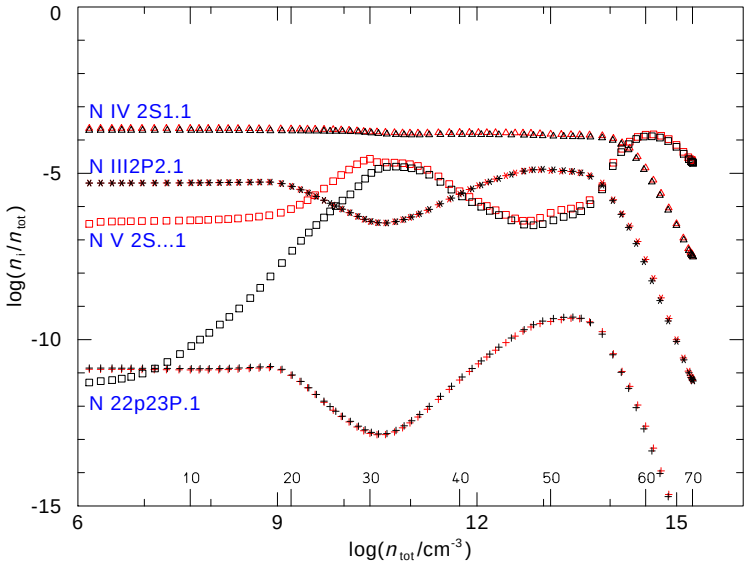

Fig. 6.3.3. Change in nitrogen level population in the model when including X-rays (red) and without X-rays (black). The levels of nitrogen ions N II, N III, N IV, N V are denoted by a plus sign, asterisk, triangle, and square, respectively.

Along with $\dot{M}$, we also adjusted the wind velocity law exponent. Assuming $\beta = 1.1$ is found to be in best agreement with the observed P Cygni profiles. Because clumping enhances the emission in optical wind lines such as Hα and He II λ4686, we varied the clumping factor and the onset of clumping to best match these lines. In this system, since Hα is filled with disk emission from the companion, we had to solely rely on He II λ4686, which nearly matches the continuum due to filled-in emission. This line is best reproduced by a model with a density contrast of $D = 20$ where the clumping starts at a radius of $1.12\,R_*$ and reaches the maximum value of D at $R_D = 5\,R_*$. Given the limited contribution of the secondary component to the UV lines and the relatively weak wind of B dwarfs in the SMC, we assumed a fixed low $\dot{M}$ and other wind parameters for the model. The only impact of the secondary star on the composite UV spectra is the dilution of lines from the primary. One such noticeable feature is the unsaturated C IV P Cygni profile with a flat bottom. The non-zero flux in the absorption trough of the C IV $\lambda\lambda$1548–1551 line suggests that the stripped star wind does not substantially occult the secondary. Thus, the binary system may be widely separated.

We determine the luminosity L and color excess E_{B-V} by fitting the composite model SED to the photometry and flux-calibrated UV spectra (Fig. 6.3.4). The model flux is diluted with the adopted SMC distance modulus of 18.98 mag (Graczyk et al. 2020). The reddening encompassed contributions from an internal SMC component and the Galactic foreground. For the Galactic component we used the reddening law published by Seaton (1979) and a color excess of E_{B-V}= 0.04 mag. For the SMC component, the color excess is varied as a free parameter, while the reddening law is adopted from Bouchet et al. (1985). By fitting the normalized spectra, we can place constraints on the luminosity ratio, thus the SED fitting by the composite model yields both primary and secondary luminosities. For 2dFS 163, the primary stripped star contributes approximately 70% of the light in the UV and 65% in the optical.

The final, best-fit composite models for 2dFS 163 are shown in Figs. 6.3.1, 6.3.2, and 6.3.4 respectively. The resulting stellar and wind parameters as well as the derived surface abundances for both primary and secondary components are given in Table 6.3.1.

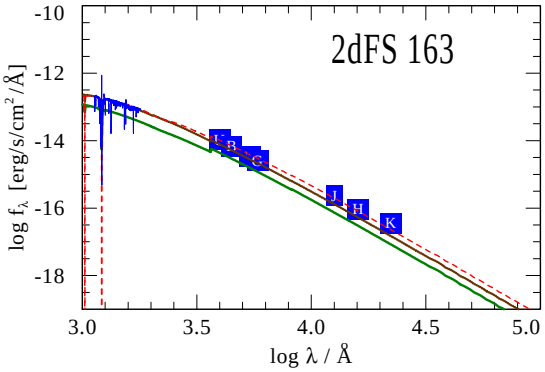

Fig. 6.3.4. Observed flux calibrated UV spectra and photometry of 2dFS 163 (blue) compared to the model SED. The composite model (dashed red) is the weighted sum of the stripped star (brown) and rapidly rotating Be star (green) models.

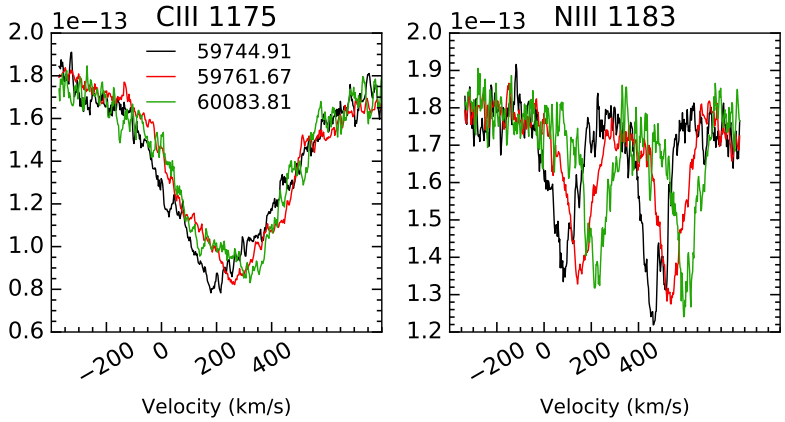

Fig. 6.3.5. UV spectra of 2dFS 2553 taken at different epochs showing radial velocity shift in C III λ1175 and N III λ1183,1185 lines.

6.3.3. 2dFS 2553

Evans et al. (2004) classified the star as O6.5II(f) using the 2dFS survey. Based on multi-epoch UV and optical spectra, we found that 2dFS 2553 shows RV variations (see Figs. 6.3.5, 6.3.6). Both the UV and optical spectra are dominated by narrow absorption and emission lines from the primary star. The N III $\lambda\lambda$4634–4642 and N IV λ4057 emission lines as well as the N IV $\lambda\lambda$3460-3485 absorption lines and all He II lines stem exclusively from the hot primary. Based N IV to N III ratio, we reclassify the primary as O4 III (f). Narrow lines in the UV spectra such as N III λ1183 and C IV λ1169 show RVs in the range of ~80-210 km s^{-1} (see Fig. 6.3.5). In the optical, N III and N IV emission lines show RVs in the range of ~130-260 km^{-1} (see Fig. 6.3.6).

The weak broad-line components from the secondary are visible in the X-shooter spectra, mainly in the He I lines. Specifically, the He I lines at 4144 and 4388Å are exclusively from the secondary (no narrow component). The secondary also shows disk emission line contribution to the Balmer and Paschen lines as well as to the He I lines in the red optical part. It is further evident from Fig. 6.3.6 that the emission part in He I λ5876 and Hβ are moving in the opposite direction compared to the narrow absorption part and the N III emission lines. All this suggests that the secondary is a fast-rotating, early-type Be star. We measured an RV separation of $\approx$ 90 km/s between primary and secondary lines in the X-shooter spectra. Between two epochs of X-shooter spectra, the secondary's lines are moving $\approx$ 70 km/s in the opposite direction of the primary. The C III λ1175 line in the UV range also shows strong contributions from the broad components of the secondary, but the RV variations in the line are much smaller than that found in narrow N III λ1183 lines (see Fig. 6.3.5). In conclusion, the luminous primary is moving faster than the Be secondary, indicating that the mass of the primary is smaller than that of the secondary star.

Details of the RV measurements are given in Appendix E.2.1. Since the narrow lines are prominent in both the UV and optical spectra, we measured the RV of the primary from 7 epochs, as listed in Table E.2.1. An additional RV value for the star is reported by Lamb et al. (2016). Using all this information, we searched for possible orbital periods of the system with *The Joker* (Price-Whelan et al. 2017), a custom Monte Carlo sampler for sparse RV datasets. In addition, we employed PHOEBE to derive the period and to determine orbital parameters. The most likely period of the system is found to be 93.6 days (see more details in Appendices E.2.2 and E.2.3).

The spectral analysis of 2dFS 2553 is carried out in the same manner as that of 2dFS 163 since the composite spectra look similar. The main differences include the presence of the N IV λ4057 emission line in the optical range and a stronger C IV λ1169 to C III λ1175 ratio in the UV. To account for this, we had to increase the temperature of the primary along with increasing log g_*. Since the primary is much hotter here, the weak, broad He I lines are found to be exclusively from the

Table 6.3.1. Fundamental parameters and abundances derived for 2dFS 163 using spectroscopic analysis.

	Stripped star	Be star
Spectral type	O6.5 Ib (f)	B0-1 Ve
T_* (kK)	37^{+1}_{-2}	26^{+3}_{-4}
$T_{2/3}$ (kK)	35.9^{+1}_{-2}	25.8^{+3}_{-4}
$\log g_*$ (cm s^{-2})	$3.5^{+0.1}_{-0.2}$	$3.8^{+0.2}_{-0.2}$
$\log g_{2/3}$ (cm s^{-2})	$3.45^{+0.1}_{-0.2}$	$3.79^{+0.2}_{-0.2}$
$\log g_{\rm true}{}^{\dagger}$ (cm s^{-2})	$3.51^{+0.1}_{-0.2}$	$3.89^{+0.2}_{-0.2}$
$\log L$ ($L_\odot$)	$4.75^{+0.1}_{-0.1}$	$4.18^{+0.2}_{-0.2}$
R_* ($R_\odot$)	$5.8^{+1}_{-0.7}$	$6.1^{+2.5}_{-2}$
$R_{2/3}$ ($R_\odot$)	$6.1^{+1}_{-0.7}$	$6.15^{+2.5}_{-2}$
$\log \dot{M}$ ($M_\odot$yr^{-1})	$-6.9^{+0.1}_{-0.2}$	-10 (fixed)
v_∞ (km s^{-1})	1000^{+100}_{-100}	1500 (fixed)
β	1.1	0.8 (fixed)
D	20	10 (fixed)
$v \sin i$ (km s^{-1})	60^{+10}_{-10}	250^{+80}_{-80}
$v_{\rm mac}$ (km s^{-1})	50^{+10}_{-10}	50 (fixed)
$v/v_{\rm crit}$	$\gtrsim 0.2$	$\gtrsim 0.53$
ξ (km s^{-1})	15^{+5}_{-5}	14 (fixed)
$X_{\rm H}$ (mass fr.)	$0.33^{+0.1}_{-0.05}$	0.737*
$X_{\rm He}$ (mass fr.)	$0.67^{+0.05}_{-0.1}$	0.26*
$X_{\rm C}/10^{-5}$ (mass fr.)	$1^{+1}_{-0.5}$	21*
$X_{\rm N}/10^{-5}$ (mass fr.)	160^{+20}_{-20}	3*
$X_{\rm O}/10^{-5}$ (mass fr.)	20^{+10}_{-10}	113*
$E_{\rm B-V}$ (mag)	$0.08^{+0.02}_{-0.02}$	
$M_{\rm spec}$ ($M_\odot$)	$3.96^{+1.8}_{-1.5}$	10.5^{+5}_{-4}
$\log\ Q_{\rm H}$ (s^{-1})	48.4	46.4
$\log\ Q_{\rm He\,II}$ (s^{-1})	39.8	34.7

Notes. $^{(\dagger)}$ $\log(g_* + (v \sin i)^2/R_*)$ $^{(*)}$ Abundances of the Be star are adopted from Trundle et al. (2007) which corresponds to typical values for OB stars in the SMC

secondary. This allows us to adjust the luminosity ratios in the composite spectral fit. Again, we found a plausible temperature range for the secondary, as it does not contribute to the He II or Si III lines in the optical spectra similar to 2dFS 163. The final parameters determined in Table 6.3.2 correspond to the best fit-composite model for the observations.

We varied the CNO abundance in the stripped-star model to accurately replicate the observed intensity of the CNO lines in the optical and UV spectra. The N enrichment is found to be stronger in 2dFS 2553 than in 2dFS 163. However, it is difficult to match the strength of the N lines of different ionization stages simultaneously. The emission lines of N IV and N III in the optical spectrum, as well as the absorption lines of N III, and the N V P Cygni profile in the ultraviolet spectrum, are in good agreement with the final nitrogen abundance employed in the model. Conversely, the model slightly under-predicts the strength of the N IV $\lambda\lambda$3460-3485 absorption lines in the optical. Interestingly, we see a complete absence of C and O absorption lines

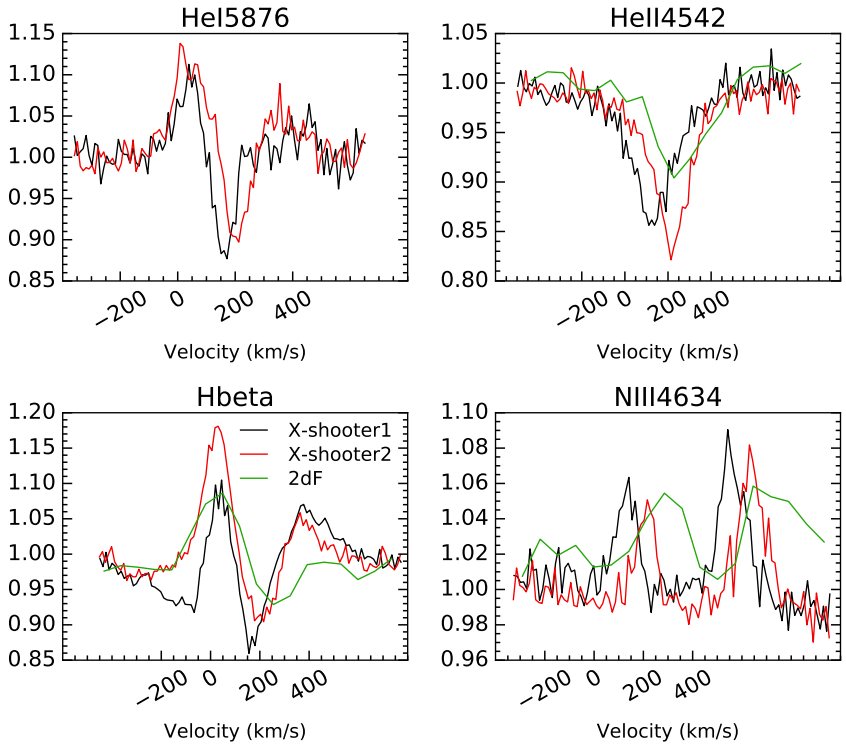

Fig. 6.3.6. Radial velocity shift between 2dF and two X-shooter spectra of 2dFS 2553. The narrow primary lines are moving in opposite directions to the broad and disk emission components.

in the optical spectra (see Fig. 6.3.1), even in the bluest part where we found a few O lines in 2dFS 163. Hence, we need to rely on UV absorption lines to determine the C and O abundances. Since the secondary also contributes to the C III λ1175 line, we could constrain the C abundance in the Be star model, which is also found to be significantly depleted compared to the initial value. Unlike 2dFS 163, there are no obvious indications in the observed spectra for He enrichment. We varied the H mass fraction ($X_{\rm H}$) in the primary model between 0.5 and 0.73 and found the best fit at $X_{\rm H} = 0.6$.

The wind parameters of the stripped star are determined by analyzing the C IV $\lambda\lambda$1548–1551 and N V $\lambda\lambda$1238–1242 P Cygni lines (see Fig. E.5.2). The v_∞ is measured from the blue edge of the profiles, and the mass-loss rate is estimated from the overall strength of the P Cygni profiles. Since the stripped star in 2dFS 2553 is much hotter than 2dFS 163, we can accurately replicate the N V line profile without incorporating any X-rays into the model. The default clumping parameters from the SMC OB grid model (Hainich et al. 2019) give a reasonable fit to the phosphorus lines at 1118, 1128 Å in the UV. Similar to 2dFS 163, the contribution of the secondary component to the UV spectra is very low, especially to the wind lines. Hence, we assumed fixed wind parameters for the secondary model as described in Sect. 6.3.2. The only impact of the secondary star on the composite UV spectra is the dilution of the primary's wind lines and its contribution to the C III absorption line.

As described in Sect. 6.3.2, the luminosity L and color excess $E_{\rm B-V}$ are estimated by fitting the composite model SED to the photometry and flux calibrated UV spectra (Fig. E.5.3). In this system, the stripped star contributes approximately 60% of the light in the UV and the optical. The final best-fit model and SED for 2dFS 2553 are shown in Figs. E.5.1, E.5.2, and E.5.3 respectively. The stellar and wind parameters as well as surface abundances derived for both the stripped star and the Be star are given in Table 6.3.2. Based on the parameters derived from spectroscopic analysis and orbital analysis (see Appendix E.2) we calculated the Roche lobes surrounding each component using

$$\frac{R_{\rm RL1}}{a} = \frac{0.49q^{2/3}}{0.6q^{2/3} + \ln(1 + q^{1/3})}$$

; where $q = M_1/M_2$ (Eggleton 1983). Subsequently, the Roche lobe filling factor $f_{\rm RL} = R_*/R_{\rm RL}$ is calculated. The radius of both components of 2dFS 2553 are much smaller than their Roche lobes, indicating it is a detached binary.

6.3.4. Sk -71 35

This LMC star was classified as a B1 II in Ramachandran et al. (2018b) and analyzed using a single epoch GIRAFFE spectrum. Although the spectra show B supergiant-like features, it also consists of double peak disk emission features similar to the newly identified partially stripped binary SMCSGS-FS 69 (Ramachandran et al. 2023). The optical spectra are primarily characterized by narrow absorption lines originating from the B supergiant-like star. Nevertheless, we have detected absorption lines of He II λ4686 and He II λ5412 in the spectra. These He II lines are significantly broader than the metal lines in the spectra and can

Table 6.3.2. Fundamental parameters and abundances derived for 2dFS 2553

	Stripped star	Be star
Spectral type	O4 III (f)	B0-1 Ve
T_* (kK)	42^{+1}_{-2}	27^{+3}_{-3}
$T_{2/3}$ (kK)	41.3^{+1}_{-2}	26.8^{+3}_{-3}
$\log g_*$ (cm s^{-2})	$3.8^{+0.1}_{-0.2}$	$3.8^{+0.2}_{-0.2}$
$\log g_{2/3}$ (cm s^{-2})	$3.77^{+0.1}_{-0.2}$	$3.79^{+0.2}_{-0.2}$
$\log g_{\rm true}{}^{\dagger}$ (cm s^{-2})	$3.81^{+0.1}_{-0.2}$	$3.91^{+0.2}_{-0.2}$
$\log L$ ($L_\odot$)	$4.91^{+0.1}_{-0.1}$	$4.34^{+0.2}_{-0.2}$
R_* ($R_\odot$)	$5.4^{+1}_{-0.7}$	$6.8^{+2}_{-1.6}$
$R_{2/3}$ ($R_\odot$)	$5.59^{+1}_{-0.7}$	$6.86^{+2}_{-1.6}$
$\log \dot{M}$ ($M_\odot$yr^{-1})	$-7.3^{+0.2}_{-0.2}$	-10 (fixed)
v_∞ (km s^{-1})	1350^{+100}_{-100}	1500 (fixed)
β	1	0.8 (fixed)
D	20	10 (fixed)
$v \sin i$ (km s^{-1})	80^{+10}_{-10}	300^{+100}_{-50}
$v_{\rm mac}$ (km s^{-1})	30^{+10}_{-10}	50 (fixed)
$v/v_{\rm crit}$	$\gtrsim 0.2$	$\gtrsim 0.59$
ξ (km s^{-1})	15^{+5}_{-5}	14 (fixed)
$X_{\rm H}$ (mass fr.)	$0.6^{+0.1}_{-0.05}$	0.737*
$X_{\rm He}$ (mass fr.)	$0.39^{+0.05}_{-0.1}$	0.26*
$X_{\rm C}/10^{-5}$ (mass fr.)	2^{+1}_{-1}	4^{+2}_{-2}
$X_{\rm N}/10^{-5}$ (mass fr.)	200^{+80}_{-40}	3*
$X_{\rm O}/10^{-5}$ (mass fr.)	40^{+20}_{-20}	113*
$E_{\rm B-V}$ (mag)	$0.10^{+0.02}_{-0.02}$	
$M_{\rm spec}$ ($M_\odot$)	$6.86^{+3.3}_{-2.8}$	$13.8^{+5}_{-3.5}$
$\log Q_{\rm H}$ (s^{-1})	48.4	46.4
$\log Q_{\rm He\,II}$ (s^{-1})	43.1	35.9
$P_{\rm orb}$ (days)	93.6	
$R_{\rm RL}$ ($R_\odot$)	81.2^{+38}_{-30}	99.7^{+47}_{-38}
$f_{\rm RL}$	$0.07^{+0.035}_{-0.03}$	$0.07^{+0.035}_{-0.03}$

Notes. $^{(\dagger)}$ $\log(g_* + (v \sin i)^2/R_*)$ $^{(*)}$ Abundances of the Be star are adopted from Trundle et al. (2007) which corresponds to typical values for OB stars in the SMC

only be attributed to a star with a hotter temperature. In addition, the existence of disk emission characteristics in the Balmer and Paschen series indicates the presence of a rapidly rotating Oe star as the secondary companion in the system. The primary, on the other hand, is a slowly rotating, partially stripped star with a substantial H-rich envelope. Following Fitzpatrick's LMC B supergiant scheme the primary supergiant can be classified as B1 based on the relative strengths of Si IV λ4089 to Si III $\lambda\lambda$4552-

4575. The luminosity class is unclear given the narrow core + broad wings of Hγ, nevertheless, we suggest Ia luminosity class for primary following the new B supergiant Milky Way template scheme of Negueruela et al. (2024) assuming the broad component is from secondary. Based on the intensity ratio of the broad component of He I λ4388 to He II λ4542 lines and Balmer emissions suggest that the secondary is O9 e star.

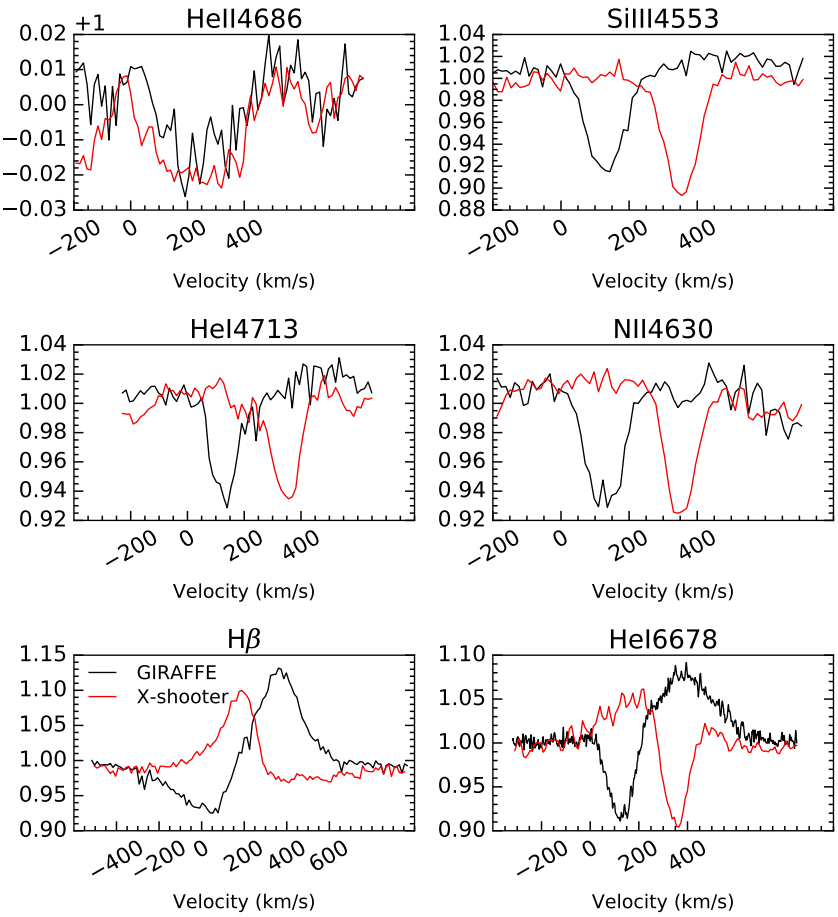

Fig. 6.3.7. Radial velocity shift between Flames/GIRAFFE and X-shooter spectra of Sk -71 35.

We checked for RV variations in the spectra by comparing the X-shooter and GIRAFFE spectra as shown in Fig. 6.3.7. The narrow absorption lines show an RV variation of $\approx$ 215 km s^{-1} between the two epochs. The UV spectra also exhibit RV shifts relative to the optical spectra. For the primary star, the maximum $\delta_{\rm RV}$ from the available observations is $\approx$ 290 km s^{-1}. On the other hand, the RV variations in the broad He II lines are much smaller. The maximum $\Delta_{\rm RV}$ for the secondary from the UV and optical spectra is $<$ 70 km s^{-1}, indicating that the partially stripped star has a much lower mass than the Oe star.

The disk emissions in Hα and Hβ are found to be moving in the opposite direction to the narrow lines, confirming their secondary origin. Moreover, asymmetric double peak-like emissions are visible in He I lines in the red part of the optical spectra. For example, He I λ6678 shows both narrow absorption (from the stripped primary) and disk emission component (from the Oe star) moving in opposite directions (see Fig. 6.3.7). This kind of emission plus absorption features from both components are also imprinted in the Paschen lines. In all these cases, the RV shifts between two stars are in agreement with the measure from the He I absorption lines in the blue part of the optical spectra where we can see both narrow and broad components.

Only three epochs of spectra are available for Sk -71° 35. The details of the RV measurements are given in Appendix E.3.1. However, since it is a bright star, we looked at the TESS light curves to determine the orbital period. The light curve exhibits ellipsoidal modulation, suggesting that it is likely caused by the gravitational distortion of one of the two stars–likely the partially stripped primary star, which is puffier and more prone to distortion. We derived a binary orbital period of $\approx$ 9.4 days for the system. Details of the light curve analysis can be found in Appendix E.3.2. Using the period derived from the TESS light curve and using 3 RV measurements we carried out the orbital analysis of the system using `rvfit` code (see Appendix E.3.3).

We performed the spectral analysis of Sk -71° 35 by following a similar method described in Ramachandran et al. (2023). The main diagnostic to constrain the temperature of the primary in Sk -71° 35 is the He and Si ionization balance based on He I / He II and Si III / Si IV line ratios. The secondary star is much hotter than the primary in this system, as indicated by the broad He II lines in the optical and N V lines in the UV. From the broad components of the He I and He II lines, we constrained the temperature of the Oe star. For the surface gravity, the pressure-broadened wings of the Balmer lines are the primary diagnostics. We considered Hγ and Hδ since they are less impacted by wind and disk emissions. Nevertheless, both Hγ and Hδ contain primary and secondary contributions. As a result, the luminosity ratios and surface gravities in the primary and

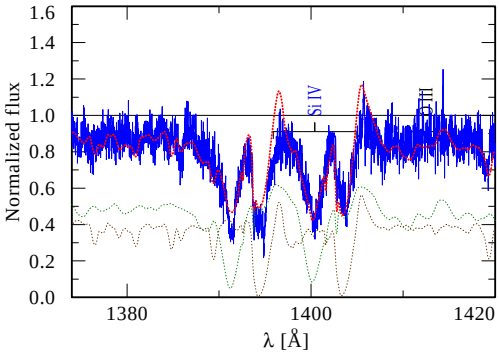

Fig. 6.3.8. Si IV P Cygni line of Sk -71° 35. The composite model (dashed red) is the weighted sum of the stripped star (dotted brown) and Oe star (dashed green) model spectra with an RV shift.

secondary models were concurrently modified to match with the observations. Since the ionization balance also reacts to gravity, we simultaneously re-adjusted T_* and log g_* to achieve a good fit to the observed spectra.

Unlike the other two systems discussed before, the secondary component in Sk -71° 35 has a stronger contribution to the UV spectrum. Moreover, we can clearly distinguish the wind components from both primary and secondary due to the temperature and RV differences. The P Cygni lines of C IV $\lambda\lambda$1548–1551 and N V $\lambda\lambda$1238–1242 are coming from the hotter secondary. On the other hand, Si IV $\lambda\lambda$1393–1403 P Cygni profiles are visible from both components and well-separated with an RV difference of $\approx$ 200 km s^{-1} (see Fig. 6.3.8). We measure v_∞ from the blue edge of these lines for both the primary and secondary. For the secondary, this measurement of v_∞ is consistent with the value from the N V and C IV profiles. The mass-loss rate ($\dot{M}$) is estimated for both components from the strength of the P Cygni profiles. For the secondary, we have to incorporate an additional X-ray field into the model with an X-ray luminosity of log L_X = 32.8 erg s^{-1} to reproduce N V. This is in agreement with the upper limit on X-ray luminosity of Sk -71° 35, log L_X < 34 in 0.2-12.0 keV.

We constrained the CNO abundances for the primary and secondary components in the system. For the primary, we use CNO lines in the optical spectra. The N abundance is determined by analyzing multiple N II and N III lines. Although we found an enrichment by a factor of 16 compared to the LMC baseline value, the enrichment is actually much lower than in the other two newly found stripped stars. The C and O abundances are estimated from several C III and O II lines in the optical spectra. The CNO abundances for the secondary are constrained from the UV lines (C III, N III, N IV, and O IV). In addition to the CNO abundances, we varied the H mass fraction (X_H) in the primary models between 0.5 and 0.73. Our best-fit model to the observations suggests X_H = 0.7, does not favor any signs of surface-He enrichment or H depletion.

In Sk -71° 35, the partially stripped star contributes approximately 65% of the light in the optical, but only 30% in the UV. We adjusted the luminosities of primary and secondary models such that the composite model SED matches the photometry and flux-calibrated UV spectra (Fig. E.5.6). Here the model flux is diluted with the adopted LMC distance modulus of 18.48 mag (Pietrzyński et al. 2019). The final best-fit model and SED for 2dFS 2553 are shown in Figs. E.5.4, E.5.5, and E.5.6 respectively. The stellar and wind parameters as well as surface abundances derived for both the stripped star and the Oe star are given in Table 6.3.3. The system Sk -71° 35 is found to be semi-detached where the less massive partially stripped star is filling its Roche lobe and transferring mass.

6.4. Discussions

6.4.1. Stellar masses

We determined the spectroscopic mass from gravity and stellar radius using the relation $g_{\rm true} = G\,M_*\,R_*^{-2}$ for each of the components in our sample binaries. Here $g_{\rm true}$ is determined via the measured log g_* from the analysis, after accounting for centrifugal acceleration using the relation $\log(g_* + (v \sin i)^2/R_*)$(Repolust et al. 2004). The mass of the primary in 2dFS 163 is determined to be only half of the mass of the secondary, which contributes significantly less to the observed spectra compared to the primary. The mass of the primary is estimated to be ~4 $M_\odot$, making it a candidate for an intermediate-mass stripped star.The spectroscopic masses of the stripped stars in 2dFS 2553 and Sk -71° 35 are relatively high, approximately 7 $M_\odot$. Both 2dFS 163 and 2dFS 2553 exhibit spectral characteristics similar to early-type O stars which usually have masses greater than 30 $M_\odot$ (e.g., Martins et al. 2005). However, the estimated masses of these primaries are considerably smaller, suggesting He-core burning and substantial removal of their outer layers. In addition, their smaller radii ($R < 6\,R_\odot$) suggest that they might be in an ongoing contracting phase. Similarly, the mass of the stripped star in Sk -71° 35 is way lower than expected for an early B supergiant. In this case, the stripped star has a much larger radius and short orbital period, with a Roche lobe filling factor > 1, indicating an ongoing mass transfer phase. This is in agreement with the observed ellipsoidal modulations in the light curve.

The secondary Be star in 2dFS 2553 is twice as massive as the stripped star. For 2dFS 2553 the mass ratio determined through orbital analysis using PHOEBE (see Appendix E.2.3) is lower, but it falls within the range of error and is consistent. In Sk -71° 35, the Oe star is found to be 4.6 times more massive than the stripped star, and the orbital analysis is also in agreement with a high mass-ratio (see Appendix E.3.3). It should be noted that since the lines of secondaries are weaker in the observed spectra, the true uncertainty in the estimated masses of these objects may be higher. For stripped primaries, we found

Table 6.3.3. Fundamental parameters and abundances derived for Sk -71 35

	Stripped star	Oe star
Spectral type	B1 Ia	O9 Ve
T_* (kK)	21^{+2}_{-2}	32^{+3}_{-3}
$T_{2/3}$ (kK)	20^{+2}_{-2}	31.8^{+3}_{-3}
$\log g_*$ (cm s^{-2})	$2.6^{+0.2}_{-0.2}$	$3.8^{+0.2}_{-0.2}$
$\log g_{2/3}$ (cm s^{-2})	$2.51^{+0.1}_{-0.2}$	$3.79^{+0.2}_{-0.2}$
$\log g_{\rm true}{}^{\dagger}$ (cm s^{-2})	$2.65^{+0.1}_{-0.2}$	$3.85^{+0.2}_{-0.2}$
$\log L$ ($L_\odot$)	$4.93^{+0.1}_{-0.1}$	$5.12^{+0.2}_{-0.2}$
R_* ($R_\odot$)	22.1^{+2}_{-2}	11.8^{+2}_{-2}
$R_{2/3}$ ($R_\odot$)	24.3^{+2}_{-2}	11.9^{+2}_{-2}
$\log \dot{M}$ ($M_\odot$yr^{-1})	$-7.0^{+0.2}_{-0.2}$	$-7.1^{+0.2}_{-0.2}$
v_∞ (km s^{-1})	400^{+50}_{-50}	900^{+100}_{-100}
β	0.8	0.8 (fixed)
D	10	10 (fixed)
$v \sin i$ (km s^{-1})	85^{+10}_{-10}	250^{+80}_{-80}
$v_{\rm mac}$ (km s^{-1})	30^{+10}_{-10}	50 (fixed)
$v/v_{\rm crit}$	$\gtrsim 0.4$	$\gtrsim 0.4$
ξ (km s^{-1})	15	15 (fixed)
$X_{\rm H}$ (mass fr.)	$0.7^{+0.04}_{-0.1}$	0.737 (fixed)
$X_{\rm He}$ (mass fr.)	$0.29^{+0.1}_{-0.1}$	0.26 (fixed)
$X_{\rm C}/10^{-5}$ (mass fr.)	10^{+2}_{-2}	3^{+1}_{-1}
$X_{\rm N}/10^{-5}$ (mass fr.)	100^{+10}_{-10}	20^{+7}_{-7}
$X_{\rm O}/10^{-5}$ (mass fr.)	64^{+10}_{-10}	164^{+100}_{-50}
$E_{\rm B-V}$ (mag)	$0.14^{+0.02}_{-0.02}$	
$M_{\rm spec}$ ($M_\odot$)	$7.8^{+3.6}_{-3}$	35.7^{+18}_{-14}
$\log Q_{\rm H}$ (s^{-1})	47.2	48.4
$\log Q_{\rm He\,II}$ (s^{-1})	-	42
$P_{\rm orb}$ (days)	9.398	
$R_{\rm RL}$ ($R_\odot$)	17.0^{+9}_{-7}	33.8^{+19}_{-15}
$f_{\rm RL}$	$1.29^{+0.71}_{-0.56}$	$0.35^{+0.2}_{-0.15}$

Notes. $^{(\dagger)}$ $\log(g_* + (v \sin i)^2/R_*)$

agreement between spectroscopic masses, and those obtained from evolutionary models (see Sect. 6.4.4) and orbital analysis (Appendix E.2.3 and E.3.3).

The positions of the primaries in the mass-luminosity (M-L) diagram shown in Fig. 6.4.1 are also in agreement with envelope stripping. All three stripped stars are over-luminous for their current masses and hence cluster near the curve corresponding to fully stripped, He-burning stars. A similar M-L position is also reported for SMCSGS-FS 69 (Ramachandran et al. 2023). All of the observed characteristics indicate that our discovered systems are post-interaction binaries, wherein the

primary star has undergone significant mass transfer and is burning He in its core, while the secondary star has experienced both mass and angular momentum gain. However, contrary to the usually assumed picture, these stars are not fully stripped, possess a considerable H-rich envelope, and have quite high luminosity and low gravity, hence effectively hiding among the standard OB-type population.

6.4.2. Chemical abundances

All three partially stripped stars show signs of nitrogen enrichment and CO depletion. Noticeably, in the case of two compact stripped stars found in the SMC, the [N/C] and [N/O] ratios are significantly high as shown in Fig. 6.4.2. The CNO abundances are also found to be in alignment with those reported for the previously reported partially stripped star in the SMC, SMCSGS-FS 69 (Ramachandran et al. 2023). On the other hand, the cooler stripped star in the LMC, Sk -71° 35, shows only a rather mild N enrichment and CO depletion. This could be because the system may be undergoing mass transfer. In any case, these CNO abundances are very different than those expected for OB stars based on evolutionary models (e.g., Brott et al. 2011) as well as compared to observations of OB stars in the Magellanic Clouds (Hunter et al. 2009). Even assuming a large initial rotation, which can result in chemical mixing and nitrogen enrichment, is not enough to explain the observed CNO ratios in our sample objects.

The high nitrogen-to-carbon and nitrogen-to-oxygen ratios observed in our sample stars instead suggest that the observed significant chemical evolution is rooted in envelope stripping. Furthermore, strong surface He enrichment is observed in 2dFS 163, indicating that it has undergone intense envelope stripping, exposing the deeper layers.

It is also worth noting that the total CNO abundances of two SMC stars are higher than the baseline values adopted from Hunter et al. (2007); Trundle et al. (2007). For 2dFS 163, ΣCNO (mass fraction) $=1.8\times10^{-3}$ and for 2dFS 2553 this is 2.4×10^{-3}, whereas the baseline value is $\approx 1.4\times10^{-3}$. This is possibly due to a higher scatter in the initial abundances of stars across SMC from the baseline value. Within the XshootU collaboration, Martins et al. (2024, XShootU V) studied the CNO abundance of O stars and found a similar higher total CNO abundance from the baseline values for some of the SMC stars. Furthermore, Ramachandran et al. (2021) have also reported a significant dispersion in CNO abundances among O stars in the SMC Bridge region.

6.4.3. Wind parameters of stripped stars

6.4.3.1. Terminal velocity

Given the absence of prior measurements on the terminal wind velocities of partially stripped stars, it was a priori not clear whether they follow common correlations for OB stars with respect to the effective escape velocity

$$v_{\mathrm{esc},\Gamma} = \sqrt{\frac{2GM}{R}(1-\Gamma_{\mathrm{e}})} \tag{6.4.1}$$

or the stellar temperature. In Fig. 6.4.3, we show the v_∞ to $v_{\mathrm{esc},\Gamma}$ ratio for each of the stripped stars in our sample at their corresponding temperature. The relationship between v_∞ and $v_{\mathrm{esc},\Gamma}$ has been investigated in both theoretical and observational studies for massive stars in our Milky Way and is found to be $v_\infty/v_{\mathrm{esc},\Gamma} \simeq 2.6$ for stars with $T_* \geq 21$ kK, while for stars with $T_* < 21$ kK the ratio is ≈1.3 (Lamers et al. 1995; Kudritzki & Puls 2000). The terminal velocity is also expected to scale

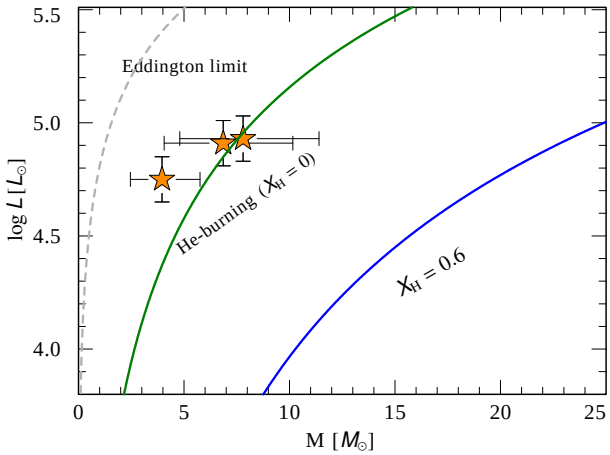

Fig. 6.4.1. Stellar mass vs. luminosity for our newly discovered stripped stars. For comparison, theoretical relations for chemically homogeneous stars with 60% and zero surface hydrogen as well as the Eddington limit are shown as well (Gräfener et al. 2011).

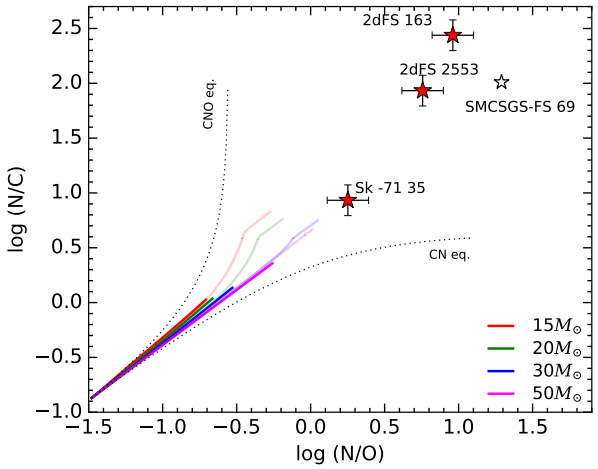

Fig. 6.4.2. log (N/C) vs. log (N/O) abundances (by number) for the stripped primaries in our sample. For comparison the location of the previously reported partially stripped star in the SMC, SMCSGS-FS 69 (Ramachandran et al. 2023) is marked. Dashed lines indicate the expected trends for the case of partial CN and complete CNO equilibrium. Solid lines are based on evolutionary tracks from Brott et al. (2011) for different initial masses and initial rotational velocities corresponding to 0 and 300 km/s.

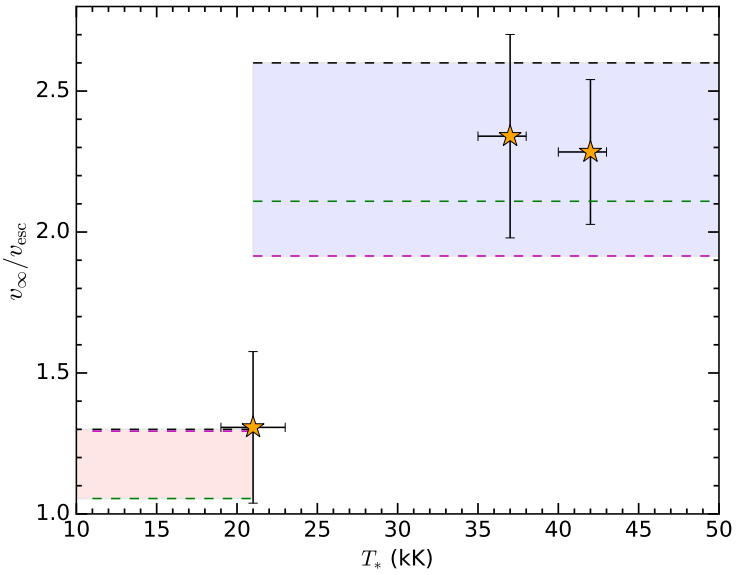

Fig. 6.4.3. Terminal velocity to escape velocity ratio for our sample stripped stars: For comparison, we also plotted the $v_\infty/v_{\rm esc,\Gamma}$ ratios observed for OB stars. The black dashed lines represent $v_\infty/v_{\rm esc,\Gamma}$ for Galactic OB stars as reported in the study by Lamers et al. (1995). The ratios are different for stars with $T_* \gtrsim 21$ kK (blue region) for stars cooler than 21 kK (red region). The green dashed lines represent the same ratio but scaled to SMC metallicity, as described in Leitherer et al. (1992), whereas the magenta dashed lines indicate a steeper metallicity scaling found by Vink & Sander (2021).

with the metallicity, $v_\infty \propto (Z/Z_\odot)^\alpha$, where $\alpha = 0.13$ (Leitherer et al. 1992). Theoretical calculations by Vink & Sander (2021) based on Monte Carlo models employing the Müller & Vink (2008) approach find a difference in the $v_\infty(Z)$-scaling for the two temperature regimes with $\alpha = 0.19$ for the hot side – in line with the empirical findings by Hawcroft et al. (2023) – and an almost vanishing dependency of $\alpha = 0.003$ for the cooler effective temperatures. As evident from Fig. 6.4.3, the hot stripped stars in our study align well with the predictions.

Hawcroft et al. (2023) studied the v_∞ to $v_{\rm esc,\Gamma}$ ratio for the OB stars in the ULLYSES sample and found a significant scatter for both LMC and SMC stars. However, while using their newly determined values for v_∞, the values for $v_{\rm esc,\Gamma}$ was based on a diverse set of literature sources. We thus expect some of the values to change with the availability of the ULLYSES and XShootU data which could give better-quality spectra or reveal previously unknown binaries. Within the XShootU collaboration, Bernini-Peron et al. (2023) recently studied a sample of B supergiants in the SMC, yielding a considerably lower scatter for v_∞ to $v_{\rm esc,\Gamma}$ and only a few, distinct outliers. Moreover, their findings also point toward a rather weak scaling of v_∞ with Z, even above 21 kK, at least for supergiants. The results for our stripped stars, which are more supergiant-like in their surface gravities and winds, seem to align with these findings.

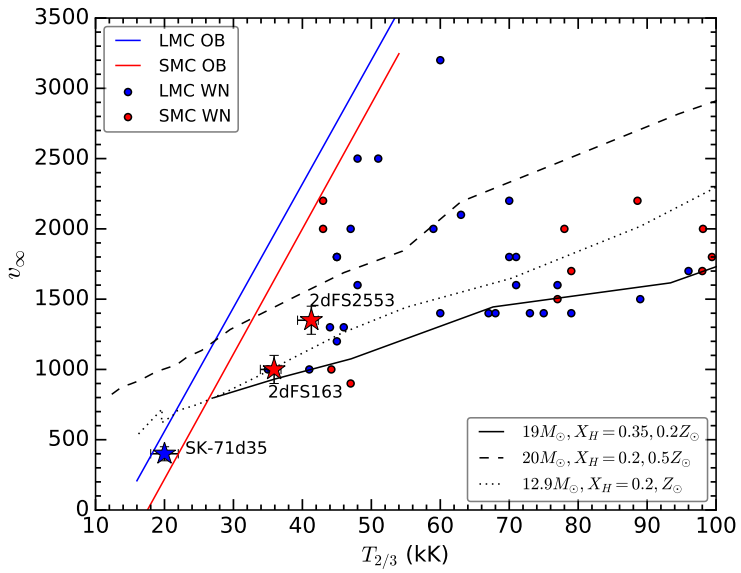

Fig. 6.4.4. Terminal velocity vs. Temperature for our sample stripped stars. The position of WR stars in the Magellanic clouds (Shenar et al. 2016, 2019), theoretical WN model sequences (black lines) from Sander et al. (2023), and the correlation for OB stars from the ULLYSES sample (Hawcroft et al. 2023) are shown for comparison.

Although the v_∞ to $v_{\mathrm{esc},\Gamma}$ ratio of stripped stars is in agreement with OB stars, in particular, the v_∞ for the two hot stripped stars in the SMC is much lower than observed for OB stars of similar temperatures as shown in Fig. 6.4.4. For comparison, we also plot the determined parameters for WN stars in the Magellanic Clouds (Hainich et al. 2014, 2015; Shenar et al. 2016, 2019) and a few theoretical WN model sequences from Sander et al. (2023) including a previously unpublished dataset with SMC-like metallicity ($Z = 0.2\,Z_\odot$) and $X_\mathrm{H} = 0.35$. The optically thick WR winds show a flatter slope with L/M-ratio, metallicity, and hydrogen abundance mainly producing an overall shift. The position of the two hot stripped stars in the v_∞-$T_{2/3}$ plane is clearly shifted toward the locations of the cooler WN stars, but since their winds are not optically thick (cf. discussion below) we would not expect them to follow the scalings for the classical WRs.

6.4.3.2. Mass-loss rates

Multiple studies have determined empirical mass-loss rates for WR and OB stars in the Galaxy and the Magellanic Clouds. Yet, the wind mass-loss rates of intermediate-mass stripped stars have remained unknown for the following reasons: i) Only a small number of potential candidates have been identified so far based on observations. ii) Most of these detections are based on optical spectroscopy, and no UV spectra were available to measure mass-loss rates iii) The winds of these stars are not as powerful as those of WR stars, so typically there are no wind emission lines visible in the optical spectra. iv) Another difficulty in accurately measuring wind mass-loss rates in intermediate-mass stripped stars from optical spectra is the presence of companions with disks, which can contaminate Hα.

In this work, we report the first mass-loss rate estimates for intermediate-mass stripped stars from a combined UV and optical spectral analysis. The derived mass-loss rates are compared with those of WR and OB stars in Fig. 6.4.5, showing the $\dot{M}$-L plane for both the LMC and SMC. The stripped star mass-loss rates found in this study are on the order of $10^{-7}\,M_\odot\mathrm{yr}^{-1}$, considerably higher than the mass-rates observed for "normal" OB stars with a similar luminosity. This is also significantly higher than the reported upper limits for stripped star mass-loss rates in Götberg et al. (2023) based on the optical He IIλ4686 absorption line.

To put their spectral appearance in context to the more massive WR stars, it is helpful to consider quantities that describe the relative strengths of their line emission such as their transformed radii $R_\mathrm{t} = R_*(v_\infty/2500\,\mathrm{kms}^{-1})^{2/3}(\dot{M}\sqrt{D}/10^{-4}M_\odot\mathrm{yr}^{-1})^{-2/3}$(Schmutz et al. 1989) or their transformed mass-loss rate $\dot{M}_\mathrm{t} = \dot{M}\sqrt{D}\cdot(1000\,\mathrm{kms}^{-1}/v_\infty)(10^6 L_\odot/L)^{3/4}$ (Gräfener & Vink 2013). Since R_t was historically derived from observed scalings between different models, larger values actually mean less emission. For our targets, we obtain values of $\log R_\mathrm{t} = 1.97$ (2dFS 163), 2.44 (2dFS 2553), and 2.35 (Sk -71° 35). All of these values are above the limit for which emission-line spectra are expected (see, e.g., Shenar et al. 2020b), although the coolest stripped star Sk -71° 35 shows a P Cygni profile in Hα according to our models. This is also reflected in the slightly more intuitively $\dot{M}_\mathrm{t}$, which describes the mass-loss rate the star would have if it had a smooth wind, a terminal velocity of 1000 km s^{-1} and a luminosity of $10^6\,L_\odot$. Indeed, Sk -71° 35 has the highest value in $\log \dot{M}_\mathrm{t}$, namely -5.1 (compared to -5.3 for 2dFS 163 and -6.1 for 2dFS 2553), indicating the most dense wind of the sample. Still, this is too low to reach the regime of optically thick winds, which starts above $\log \dot{M}_\mathrm{t} \approx -4.5$ for classical WR stars (Sander et al. 2023).

All of our derived mass mass-loss rates are roughly within factors of 2-3, in agreement with the Vink (2017) predictions for stripped stars, despite some objects being considerably cooler than the assumed fixed temperature of 50 kK in their models. The predictions from Vink (2017) yield intermediate values between the empirical WR and OB mass-loss rates in both LMC and SMC. Based on the derived parameters for our three targets, we applied typically used mass-loss recipes such as Nugis & Lamers (2000) for WR stars, and Vink et al. (2000, 2001) for OB stars in addition to Vink (2017) predictions for stripped stars. These values are then compared to the observed mass-loss rates as shown in Fig. 6.4.6. In all cases, Vink et al. (2000, 2001) mass-loss rates underestimate the observed values by roughly an order of magnitude, while Nugis & Lamers (2000) overestimate them by more than a factor of 30. The derived parameters, in particular the optically thin winds and the comparably low temperatures, yield that cWR-wind recipes, including Sander & Vink (2020), are inapplicable for all of our sample stars. On the other hand, during stripped phases, WR or OB mass-loss prescriptions are frequently employed in evolutionary models and population synthesis. Their significant disparities with the observed mass-loss rates will have a substantial impact on the final evolutionary fate and the mass of the compact object. For example, Gilkis et al. (2019) showed that the mass-loss prescriptions for stripped stars assumed in the evolutionary models influence the fraction of stripped supernovae of types IIb and Ibc. Including accurate measurements of wind mass-loss rates of intermediate-mass stripped stars into evolutionary models and population synthesis studies could provide valuable insights into stellar evolution processes at this range of masses.

6.4.4. Evolutionary nature and implications of the discovered systems

In this paper, we discovered three systems with stripped-star primaries and Be/Oe companions. The stripped-star nature of primaries is revealed by their exceptionally low spectroscopic masses (Fig. 6.4.1) and high nitrogen enrichment (Fig. 6.4.2). Their mass transfer origin is supported by fast rotation rates of companions, likely indicative of a recent mass and angular momentum accretion. Interestingly, the discovered stripped stars are all of O/B spectral types and with surface temperatures characteristic for MS stars (i.e., cooler and larger than the canonical He-burn sequence that stretches from subdwarfs to WR stars). Similar stars have previously been referred to as either bloated/puffed-up stripped stars (e.g., Bodensteiner et al. 2020a) or partially-stripped stars (e.g., Ramachandran et al. 2023), signaling that it is the remaining (unstripped) hydrogen envelope that is the cause of larger sizes and cooler surface temperatures compared to "naked" helium stars. If the remaining envelope is particularly massive, such a star may remain of O/B type for the entire core-He burning phase (i.e., ~10% of its total lifetime, Klencki et al. 2022). Otherwise, a puffed-up stripped star is a transitory stage lasting for ~1% the total lifetime (Dutta & Klencki 2023) as the envelope is further depleted and the star contracts to become a hot and UV-bright stripped star (Götberg et al. 2017; Yungelson et al. 2024, see also tracks in Fig. 6.4.7). It may later puff-up again following the end of core-He burning, during a phase of re-expansion lasting for ~0.1% the total lifetime (Laplace et al. 2020). Finally, an OB-type stripped star could be a result of a stellar merger during which most of the envelope has been dynamically ejected, as proposed for the single star γ Columbae by Irrgang et al. (2022).

Here, we model the newly discovered systems in the framework of binary evolution as products of stable mass transfer using the MESA stellar evolution code (Paxton et al. 2011, 2013, 2015, 2018, 2019). We focus on two SMC binaries, 2dFS 163 and 2dFS 2553, and exclude the LMC system, Sk -71° 35 in which the mass transfer might currently still be ongoing. Sk -71° 35

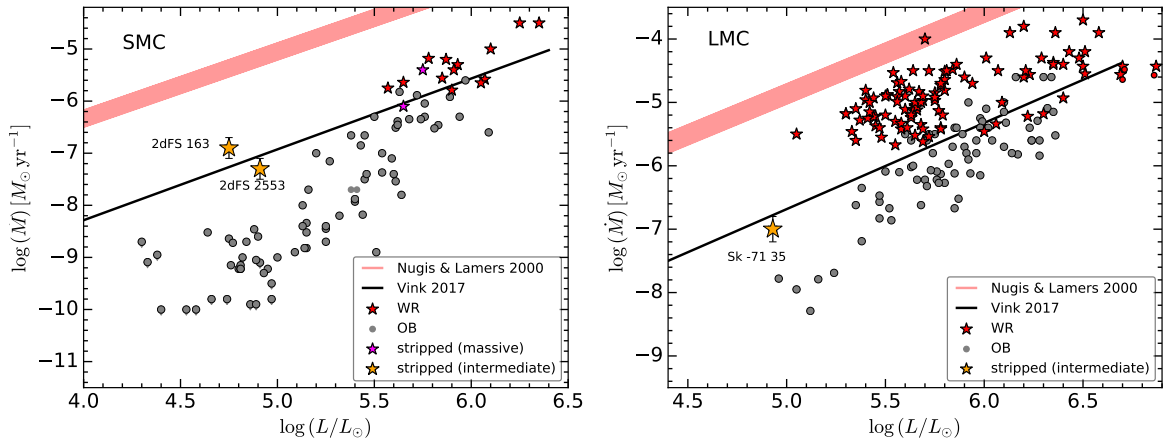

Fig. 6.4.5. Mass-loss rates vs. luminosity relation for stripped stars in the SMC (left) and LMC (right). Stripped stars in the intermediate mass range discovered in this study are shown as orange stars. Massive stripped stars in binaries from Pauli et al. (2022b); Rickard & Pauli (2023) are shown as magenta stars. For comparison, the locations of OB stars (Bouret et al. 2013; Ramachandran et al. 2019; Bouret et al. 2021; Rickard et al. 2022; Brands et al. 2022) and WRs (Hainich et al. 2014, 2015; Shenar et al. 2016, 2019; Bestenlehner et al. 2014) are plotted from the literature. The black solid line shows the mass-loss rate prescriptions for stripped helium stars by Vink (2017) and the red line corresponds to the mass-loss recipe for WR stars based on Nugis & Lamers (2000).

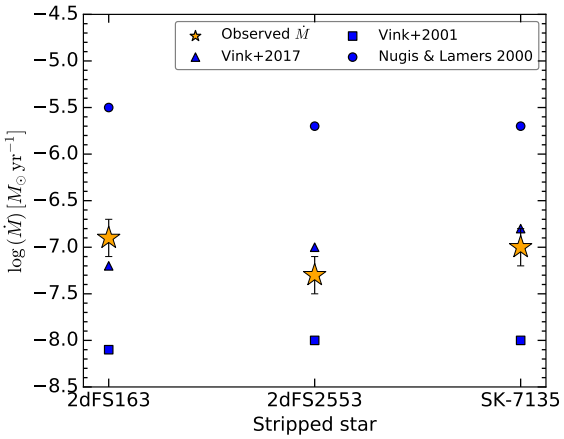

Fig. 6.4.6. Estimated mass-loss rates for stripped stars from the spectral analysis compared to commonly used recipes.

is also an ellipsoidal variable, which offers the possibility for a much more accurate determination of orbital and stellar parameters and tailored detailed modeling in a future work. Comparing 2dFS 163 and 2dFS 2553, we focus in particular on the surface H abundance.

While both primaries have roughly similar temperatures ($\sim 40\,kK$) and comparable luminosities ($\log(L/L_\odot) = 4.75$ and $\log(L/L_\odot) = 4.91$) they have both very distinct surface hydrogen abundances ($X_\mathrm{H} = 0.33$ and $X_\mathrm{H} = 0.6$). For the system with the hydrogen-rich primary, 2dFS 2553, the orbital period is known, and the Roche Lobe filling factor indicates that the system is detached.

As starting parameters for binary models, we set the initial masses as well as the initial orbital period of the system. For the initial primary masses, we calculate tracks with $M_{\mathrm{ini},1} = 12\,M_\odot$, $14\,M_\odot$, and $17\,M_\odot$, corresponding to the observed luminosity range. For the secondary, we fixed the initial mass to $M_{\mathrm{ini},2} = 11\,M_\odot$, which is close to the masses of fast-rotating Be stars in 2dFS 163 and 2dFS 2553. Since the period of 2dFS 2553 is known to be about $P_{\mathrm{orb,\,2dFS\,2553}} = 93.6\,\mathrm{d}$, we choose our initial periods such that the post mass transfer period is about $P_\mathrm{model} = 95 \pm 5\,\mathrm{d}$. To reduce the free parameter space, we assume that the binary is initially tidally synchronized, which fixes the initial rotation of the stars.

Semiconvective mixing is accounted for following Langer et al. (1983). It is one of the processes that will affect the chemical profile of deep envelope layers and, consequently, the surface abundances of stripped stars. Schootemeijer et al. (2019) suggested a semiconvection efficiency of $\alpha_\mathrm{sc} \gtrsim 1$ to reproduce the observed blue/red supergiant ratio of the SMC. Motivated by this, we explore two sets of models: one with $\alpha_\mathrm{sc} = 1$ and one with $\alpha_\mathrm{sc} = 10$. Notably, even higher semiconvection values can lead to partially stripped stars with particularly massive residual envelopes and core-He burning lifetimes (Klencki et al. 2022). Further details on the assumed input physics within our models are provided in Appendix E.4.

Our two sets of binary models are compared with the observed primaries and secondaries are shown in Fig.6.4.7. In both the $\alpha_\mathrm{sc} = 1$ and $\alpha_\mathrm{sc} = 10$ cases, the HRD positions of the partially stripped stars in 2dFS 163 and 2dFS 2553 overlap with the donor tracks of initial masses of $12\,M_\odot$ and $14\,M_\odot$, respectively, observed shortly after the end of mass transfer. The corresponding masses of the stripped donors in models are $4.5\,M_\odot$ and $5.6\,M_\odot$, with good agreement with the determined spectroscopic masses of primaries in 2dFS 163 and 2dFS 2553. The predicted surface H abundances are at around $X_\mathrm{H} \approx 0.3$. While this is in agreement with the primary in 2dFS 163 ($X_\mathrm{H} = 0.33$), it does not fit with the measurement for the primary of 2dFS 2553 ($X_\mathrm{H} = 0.6$). This tension is partly reduced in models with $\alpha_\mathrm{sc} = 10$, which tend to predict higher H abundance and would be consistent with $X_\mathrm{H} \approx 0.6$ for a slightly more massive $17\,M_\odot$ donor.

The discrepancy in X_H may indicate that stellar evolution models are failing to accurately reproduce the abundance profile of deep envelope layers, which in turn affect the exact detachment point and the surface composition of stripped stars formed via mass transfer. Besides semiconvection, multiple other agents are at play, such as rotational mixing, convective-boundary mixing, and gravity-wave induced mixing (Georgy et al. 2013; Kaiser et al. 2020; Klencki et al. 2020; Johnston 2021; Pedersen 2022). The matter is further complicated if the surface abundances of stars in a binary that has only very recently detached from mass transfer are influenced by back-accretion of even a small amount of leftover matter from the circumbinary medium. Interestingly, a surprisingly high surface hydrogen of $X_\mathrm{H} \gtrsim 0.55 - 0.6$ has been measured in most of the known puffed-up/partially stripped stars originating from massive primaries (Ramachandran et al. 2023; Villaseñor et al. 2023; Pauli et al. 2022b), suggesting this to be the norm rather than an exception. From this perspective, 2dFS 163 with $X_\mathrm{H} = 0.33$ stands out as the first of these objects with a significantly reduced surface hydrogen. This might suggest a slightly different evolutionary pathway leading to more efficient envelope stripping, for instance, case A + AB mass transfer rather than case B evolution (to be resolved with follow-up data constraining the orbit). It might also be that 2dFS 163 is observed during a later evolutionary stage of post-He burning re-expansion (Laplace et al. 2020). Although shorter-lived, puffed-up stripped stars of this stage are expected to be more He enhanced and be somewhat closer to the Eddington limit, as is the case for 2dFS 163 (Fig. 6.4.1).

It is worth noting, that due to the usage of the low mass-loss rates of Vink (2017) during the post-mass transfer phase, our models never loose their full hydrogen-rich envelope and they re-expand again following core-He depletion. However, this

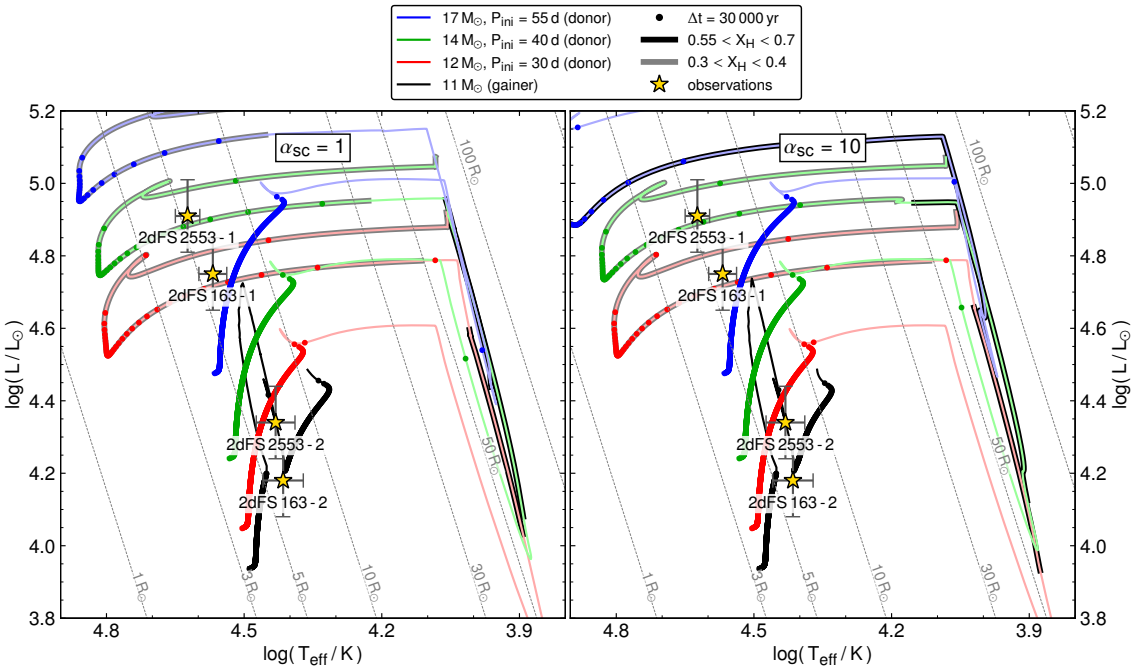

Fig. 6.4.7. HRD showing possible evolutionary pathways of the primary and secondary components for two different sets of semiconvection mixing efficiencies. The donor tracks with initial masses 12 $M_\odot$, 14 $M_\odot$, and 17 $M_\odot$ are shown as red, green, and blue solid lines. The initial orbital periods are chosen, such that the binary has a period of about $P_{\rm model} = 95 \pm 5$ d after the mass-transfer event. The surface hydrogen abundances of our models that are consistent with the one measured for 2dFS 2553 is highlighted by a thick black contour and the one measured for 2dFS 163 as a thick gray contour. As the tracks of the secondary models do not differ drastically, only for clarity the track of the mass gainer of the system with the 17 $M_\odot$ donor is shown as a solid black line. To highlight phases where the stellar models spend most of their time, we overplotted the tracks with dots, equally spaced in time steps of $\Delta t = 30\,000$ yr. The observed positions of the primary and secondary components of the SMC binaries are shown as yellow stars.

might only be the case for models undergoing mass transfer after the main-sequence evolution (Case B) as the removal of the hydrogen-rich envelope in the mass-transfer events during the main sequence (Case A) is more efficient.

The newly discovered systems contribute to the population of post-interaction binaries with intermediate-mass stripped stars. A handful of such systems is now known in the mass range of $\gtrsim 12\,M_\odot$ (pre-interaction), placing them firmly in the mass regime of neutron star progenitors. In their future evolution, the stripped primaries will explode as type Ib/c or IIb supernovae. If the orbit survives the explosion, the systems will likely evolve to become Be X-ray binaries. Those with wide orbits (hundreds of days) may further go through and survive a common-envelope phase (Tauris et al. 2017). Massive post-interaction binaries reported in this work are thus a much needed anchor point for understanding mass transfer evolution in the formation channels of X-ray binaries and gravitational-wave sources. This growing class of objects includes cases in which conservative mass accretion is required, for example, nearly 100% in Villaseñor et al. 2023 and at least 30% in Ramachandran et al. 2023. While the newly discovered Sk -71° 35 is not part of our binary model analysis, the inferred spectroscopic masses $M_1 = 7.8^{+3.6}_{-3}\,M_\odot$ and $M_2 = 35.7^{+18}_{-14}\,M_\odot$ suggest that a significant fraction of the transferred mass has been accreted. On the other hand, both 2dFS 163 and 2dFS 2553 reported here can be reproduced with nearly fully non-conservative mass transfer and agree well with the accretion efficiency being limited by critical rotation (as adopted in the models in Fig. 6.4.7). Notably, the secondaries in models with $\alpha_{\rm sc} = 1$ rotate with rotation velocities close to their breakup velocity, while secondaries in models with $\alpha_{\rm sc} = 10$ slow down to only about 80% of their breakup velocity after detachment. The latter is in better agreement with observations.

The stripped star binaries detected to date may still be just the tip of the iceberg (see HRD in Fig. 6.4.8). Dutta & Klencki (2023) estimate that at least ~0.5 − 1% of O/B/A stars may in fact be post-interaction systems with puffed-up stripped stars originating from primaries with $M_{\rm ini} > 3\,M_\odot$. This corresponds to ~ 100 systems in the SMC alone and about 5-10 in the luminosity range $4.6 < \log(L/L_\odot) < 5.0$. Combining the 2 new SMC systems reported here as well as SMCSGS-FS 69 from Ramachandran et al. (2023), we already have 3 post-interaction binaries in that luminosity range. While this number is currently consistent with the prediction, there is a good chance that the underlying population is at least a few times larger as the search so far has been limited to only a small fraction of the overall population of ~1000 OB stars in the SMC. If that turns out to be the case, binary evolution models may need to be refined to at least sometimes produce long-lived partially stripped stars: whether through inefficient envelope stripping (Klencki et al. 2022) or an unknown mechanism causing premature detachment from mass transfer, stellar mergers with substantial mass loss (Irrgang et al. 2022), or something else entirely.

On the other hand, binary evolutionary models predict a large fraction of stripped stars to be on the He ZAMS, spanning almost 10% of their total lifetime (Götberg et al. 2023; Yungelson et al. 2024). Thus, we would expect to observe at least 10

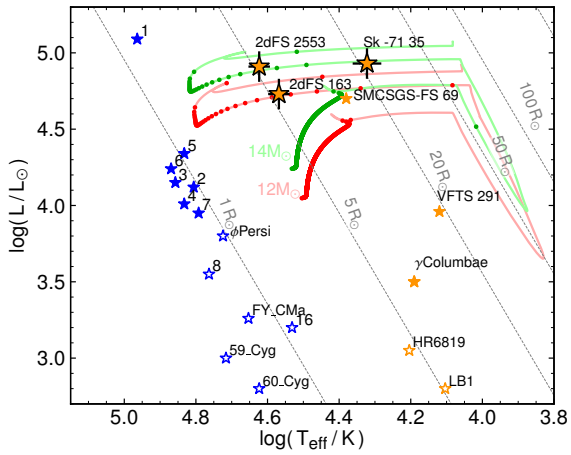

Fig. 6.4.8. HRD for stripped stars including objects discovered in this work and those from literature (Götberg et al. 2023; Ramachandran et al. 2023; Villaseñor et al. 2023; Irrgang et al. 2022; Bodensteiner et al. 2020a; Shenar et al. 2020a; Schootemeijer & Langer 2018). Orange star symbols represent partially stripped stars, while blue are compact stripped He stars. The open star symbols denote low-mass stars in the subdwarf regime, while the filled ones correspond to intermediate masses. Blue stars with numbers 1-8, and 16 are stripped stars located in the Magellanic Clouds (Götberg et al. 2023), VFTS 291 is part of the LMC, and SMCSGS-FS 69 is in the SMC. The rest of the samples are Galactic sources. The evolutionary tracks in the background have the same meaning as in Fig. 6.4.7.

times more hot and compact stripped He stars than puffed-up stripped stars. As shown in Fig. 6.4.8, we lack observations of such stripped stars on the He ZAMS compared to puffed-up stripped stars in the higher luminosity range of $\log(L/L_\odot) > 4.5$. Our newly discovered luminous, partially stripped stars were initially chosen as potential subjects for further examination due to the existence of a Be/Oe companion. The Be phenomenon is expected to be transient, potentially occurring more frequently in stripped-star binaries that have recently undergone mass transfer while being less common in older, hot stripped star systems. As a result, we anticipate detecting more binary systems with stripped stars that do not necessarily have a Be/Oe companion in the XshootU sample and in the Magellanic Clouds in general, with future studies involving multi-epoch data and with detailed orbital analysis. In the lower luminosity range $3.5 < \log(L/L_\odot) < 4.5$, we do have more observations of hot and compact stripped stars relative to puffed-up stripped stars (e.g., in the Magellanic Clouds the current observed ratio in this regime is 7:1 and thus more in line with evolution model expectations).

Whether or not a considerable number of stripped stars spend a large amount of their post-MS lifetime as a puffed-up O/B star has a significant impact on the role of stripped stars as sources of ionizing radiation. Both the primaries and the secondaries are relevant sources of H I ionizing photons, with their fluxes being similar to O/B MS stars of the same luminosity. However, the cooler temperatures of puffed-up stripped primaries essentially prevent them from being considerable sources of He II ionizing radiation (cf. Tables 6.3.1, 6.3.2, 6.3.3). Even the earliest star in our sample, 2dFS 2553, contributes only $\sim 10^{43}$ photons per second, much less than what would be expected for stripped stars on the He main sequence (e.g., Götberg et al. 2018). Presently, population synthesis models that aim to include binary-stripped stars below the WR regime rely on atmosphere models representing He stars residing in a hot, compact stage (e.g., Götberg et al. 2019; Lecroq et al. 2024). Depending on the total number of detections and the derived parameters of stripped stars, this treatment might need to undergo considerable revision.

6.5. Summary and Conclusions

Using UV and optical spectroscopy, we discovered three partially stripped star + Oe/Be binaries in the XShootU sample. Two of these systems are located in the SMC and one is found in the LMC. We identified distinct spectral characteristics of both the partially stripped primary star, which exhibits comparably narrow lines and prominent nitrogen lines and the secondary star, which displays broad lines and disk emission features. By combining the XShootU data with additional archival spectra, we have confirmed RV variations and observed components moving in anti-phase in all three systems. We carried out a composite spectral analysis of the multi-wavelength spectra using the PoWR model atmospheres. We determined the period of the two systems and performed orbital analysis. The comprehensive analyses lead us to the following conclusions:

- The detected binaries contain partially stripped stars of masses in the range of $\approx 4 - 8\,M_\odot$. The spectroscopic masses are found to be consistent with evolutionary masses and orbital masses, within uncertainty. Our stripped stars are thus of intermediate mass, between the ranges of WR and subdwarf masses, where there is so far a noticeable absence of observations.
- In all three systems, the Be/Oe secondaries are found to be significantly more massive than their partially stripped companions, showing mass ratios of $q \gtrsim 2$.

- The partially stripped stars in 2dFS 163 and 2dFS 2553 are as hot as early O-type stars and have radii similar to those on the ZAMS. On the other hand, Sk -71° 35 is a bloated stripped star with spectral features resembling a B supergiant. Both the light curve and spectroscopic analysis indicate that this system may be currently undergoing mass transfer.
- The partially stripped stars in our sample are over-luminous for their corresponding stellar masses, which is consistent with the luminosities during core He-burning.
- The surfaces of all three partially stripped stars clearly show signs of substantial nitrogen enrichment, along with reduced carbon and oxygen abundances. In addition, 2dFS 163 exhibits significant indications of helium enrichment.
- We find no evidence of an increased ionizing flux contribution (H and He II) in our sample of partially stripped stars compared to OB stars of similar luminosity or temperatures.
- The wind mass-loss rates of the newly found partially stripped stars are determined to be on the order of $10^{-7}\ M_{\odot}\,\mathrm{yr}^{-1}$, which is more than ten times higher than that of (main sequence) OB stars with the same luminosity. The current mass-loss recipes commonly employed in evolutionary models to characterize this phase have been found to be significantly under- or overestimated by an order of magnitude. With considerable scatter, the Vink (2017) description provides the right order of magnitude in $\dot{M}$ for their optically thin winds, at least for our observed sample.
- The v_{∞} to $v_{\mathrm{esc},\Gamma}$ ratio for stripped stars is in agreement with those derived for other OB stars, but their v_{∞} is much lower than observed for single OB stars with similar effective temperatures.
- Binary evolution models can explain the current observed temperatures, luminosities, and stellar masses of the primaries in 2dFS 163 and 2dFS 2553. These models suggest that both primaries are core-helium burning. Their distinct surface hydrogen abundances might indicate that more efficient mixing within the stellar models is needed, which would change our standard picture of intermediate-mass binary evolution. Further follow-up in-depth studies are required to investigate the potential consequences.
- The detection of multiple objects with parameters traditionally associated to a short-living transition stage provides a potential challenge to current binary evolution models. While the current number of systems is still in line with predictions, further detections in larger binary-focused surveys such as BLOeM could significantly increase the number of systems. A considerable number of partially stripped stars hiding among the presumed OB main-sequence parameter space would also have consequences for the integrated parameters from population synthesis models such as their He II ionizing fluxes.
- Our newly discovered partially stripped stars are firmly in the mass regime to produce neutron stars and stripped-envelope supernovae. If these systems survive the explosion, they will likely evolve into Be X-ray binaries.

Acknowledgments: The spectral plots in this work were created with WRplot, developed by W.-R. Hamann. We thank the anonymous referee for providing constructive comments that helped improve the paper. VR, AACS, and MBP are supported by the Deutsche Forschungsgemeinschaft (DFG - German Research Foundation) in the form of an Emmy Noether Research Group – Project-ID 445674056 (SA4064/1-1, PI Sander) and funding from the Federal Ministry of Education and Research (BMBF) and the Baden-Württemberg Ministry of Science as part of the Excellence Strategy of the German Federal and State Governments. JSV is supported by STFC funding under grant number ST/V000233/1. RK acknowledges financial support via the Heisenberg Research Grant funded by the Deutsche Forschungsgemeinschaft (DFG, German Research Foundation) under grant no. KU 2849/9, project no. 445783058. We thank C.J. Evans for providing the reduced 2dF spectra. We acknowledge the use of TESS High Level Science Products (HLSP) produced by the Quick-Look Pipeline (QLP) at the TESS Science Office at MIT, which are publicly available from the Mikulski Archive for Space Telescopes (MAST). Funding for the TESS mission is provided by NASA's Science Mission directorate.

Chapter 7

Discussion

In the following the key results obtained in the course of this thesis are briefly summarized and their broader implications for our understanding of massive star evolution and their impact on our interpretation of the rest-UV spectra of unresolved stellar populations of young high-redshift galaxies are discussed.

7.1. Revisiting massive binary evolution at low metallicity

7.1.1. What can we learn from low-metallicity binaries undergoing slow Case A mass-transfer?

In Chapter 3 we performed a comprehensive spectroscopic and orbital analysis of the binary system NGC 346 SSN 7 (ON3 If*+O5.5 V((f))) – one of the earliest type stars in the entire SMC. This analysis revealed that the systems have a remarkably short orbital period of $P_{\rm orb} \approx 3$ d. The current masses of the primary and secondary stars are estimated to be $M_1 = 32\,M_\odot$ and $M_2 = 55\,M_\odot$, respectively, resulting in an extreme mass ratio of $q = 1.7$. These findings, in combination with the primary's decreased surface hydrogen abundance and its CNO abundances being consistent with the CNO equilibrium values, strongly that the system either recently underwent a mass transfer event or is currently in the phase slow Case A mass transfer. This conclusion is confirmed by our binary evolution calculations, which can only successfully reproduce the observed surface properties of both stars by systems currently undergoing slow Case A mass transfer.

Whether the mass ratio inverts during slow Case A mass transfer or not depends on several factors, including the initial mass of the convective core of the donor compared to the companion, the efficiency of the mass transfer process, and the strength of the mass-loss rates, which depend on metallicity (e.g., see Sen et al. 2023). It is suggested that the maximum initial mass for slow Case A systems with inverted mass ratios increases with increasing metallicity. Therefore, the discovery of NGC 346 SSN 7 presents a unique opportunity to challenge binary evolution models and advance our understanding of the physics of mass transfer.

7.1.2. Do we understand Case B mass-transfer at low metallicity?

In Chapters 2, 5, and 6 we report the discovery of four post-interaction binary systems within the SMC. Light and radial velocity curve fitting for two of these systems revealed orbital periods of several tens to hundreds of days, suggesting that they went through a Case B mass transfer event. The stars in the remaining two systems display similar properties to those with confirmed periods, making a Case A evolutionary history unlikely. Their spectral analysis yielded a surprising result. These donor stars have temperatures and luminosities typical for ordinary OB-type stars, yet their masses are at least a factor of two lower than those of the OB stars and their CNO abundances fall between those of the CN and CNO equilibrium. Standard binary evolution models predict these systems to be in a short-lived contraction phase towards the helium main sequence (He-ZAMS), making them exceptionally rare and difficult to observe (Dutta & Klencki 2023). The discovery of four such systems challenges our understanding of binary evolution at low metallicity.

Our efforts to explain the observed stellar and orbital parameters with standard binary evolution models (see Chapters 2, 5, and 6) failed. While the binary evolution models could explain luminosity, temperature, and mass, they consistently failed to reproduce the observed surface abundances. The evolution models predicted surface hydrogen abundances which are significantly lower compare to the measured ones and they predict that all stars should have CNO surface abundances in agreement with the CNO equilibrium.

Intriguingly, our work on the slow Case A system NGC 346 SSN 7 demonstrated that standard models can effectively reproduce its binary evolution. However, the strong discrepancies observed in post-Case B systems challenge our understanding

and puzzle the stellar evolution community. Simultaneous to the works presented in this thesis (Klencki et al. 2022) investigated the influence of enhanced semiconvective mixing, a process that significantly affects a star's evolution after its main sequence phase, on Case B binary evolution models. They demonstrated that enhanced semiconvective mixing shortens the Hertzsprung gap and can trigger early helium core ignition in stars, leading to a slow Case B mass transfer scenario. However, their models predict that there should be several yellow supergiants in the SMC that are currently in the phase of slow Case B mass transfer, which is not observed. Inspired by these findings, we explored in Chapter 6 the possibility of enhanced semiconvective mixing with less extreme efficiency parameters. We confirm that this mechanism offers a viable explanation for the observed stars. Our binary model calculations with enhanced semiconvective mixing have shown that these stars can maintain a larger fraction of their hydrogen-rich envelope impacting their future evolution and final fate.

7.1.3. Do low-metallicity donor stars lose their entire hydrogen-rich envelope?

Short-period binary systems undergo Case A or Case AB mass transfer, which efficiently removes the hydrogen envelope from the donor star. However, our discoveries presented in Chapters 2, 5, and 6 suggest that at SMC metallicity Case B mass-transfer is less efficient at removing a star's hydrogen-rich envelope. Given the weak winds of SMC stars, one needs to consider if these winds can remove the remaining hydrogen-rich layers of the partially stripped stars after mass-transfer or not.

In Chapter 6 we explored different binary evolution models to explain the partially stripped donor stars of Case B systems, which are thought to be the progenitors of intermediate-mass helium stars. These models incorporate mass-loss rates consistent with observations of post-interaction binaries. Both sets of our evolution models including moderate or efficient semiconvective mixing show that the donor stars end the mass transfer phase with a thin, partially hydrogen-depleted envelope. After detachment, the wind mass-loss rates of the donor are not strong enough to completely remove the remaining hydrogen-poor envelope. All of our donor models are predicted to have after their contraction phase around $T_{\rm eff} \approx 60\,{\rm kK}$ and, hence, are positioned between the area of fully stripped stars and the H-ZAMS.

These results have significant implications on the estimates of the ionizing and mechanical feedback from stripped stars at low-metallicity, and, hence, for our understanding of the feedback processes within galaxies. Firstly, our results suggest that hat these stars do not explode as supernova Type Ib/c, but as supernova Type II. Secondly, fully stripped, hot intermediate-mass helium stars are expected to emit copious amounts of ionizing He II photons due to their high temperatures. In contrast, the partially stripped donor stars reported in our work are too cool to emit large amounts of He II ionizing radiation. At the same time, their extended H-rich atmospheres also effectively trap hydrogen ionizing radiation. This questions the role of binary stripping and significantly improves our understanding of the main feedback agents in low-metallicity environments, as present in the Early Universe.

7.1.4. How does accretion affect the evolution of the secondary?

When considering binary evolution often the evolution of the accreting star after the primary's death is neglected. However, in cases where the system remains bound after the primary exploded as a supernova or directly collapsed into a black hole, the former accretor will at some point initiate a new phase of mass transfer via RLOF onto the now compact companion (the former donor). Traditionally, it is assumed the accretor's response to mass transfer would be similar to a "normal" primary star. However, our study, presented in Chapter 4, challenges this assumption. By investigating the detailed evolution of accretors in binary systems with short initial periods ($\lesssim 10\,{\rm d}$), where mass transfer can occur conservatively, their accretors get rejuvenated changing their internal structure. This altered structure modifies the star's response to the removal of mass during RLOF as it expands more slowly. Since they can maintain noticeable fractions of their hydrogen-rich envelopes, these stars do not wander toward the He-ZAMS.

This discovery suggests that WR star populations in low-metallicity environments might exhibit a bimodal temperature distribution. This bimodality would arise from a combination of "normal" primary stars and non-conservative accretors that produce hot almost fully stripped WR stars, and these newly identified, conservative accretors lead to the formation of cooler WR stars residing close to the H-ZAMS. Gravitational wave events are preferentially observed in low-metallicity environments and are thought to originate from short-period binary systems like those studied here. Consequently, these findings have significant implications for understanding the diversity of WR populations, and the progenitors of gravitational wave events.

7.2. What binaries can tell us about radiation-driven stellar winds

What hinders a comprehensive understanding of massive star winds is the lack of knowledge about evolutionary transition phases and how different driving mechanisms change as a function of stellar parameters. For example, how exactly does a stellar wind change when a star evolves from an OB-type stage with modest wind to the WR stage with a very strong wind? This is where post-interaction binaries come into play and serve as valuable anchor points. The partially stripped stars of the (post) interaction binaries presented in Chapters 2, 3, 5, and 6 all showed, that their mass-loss rates are at least one order of magnitude higher when compared to normal OB-type stars with similar spectral type and luminosity (see Fig. 7.2.1). While the donor stars of the most massive post-interaction binaries (see Chapters 2 and 3), displayed mass-loss rates comparable to

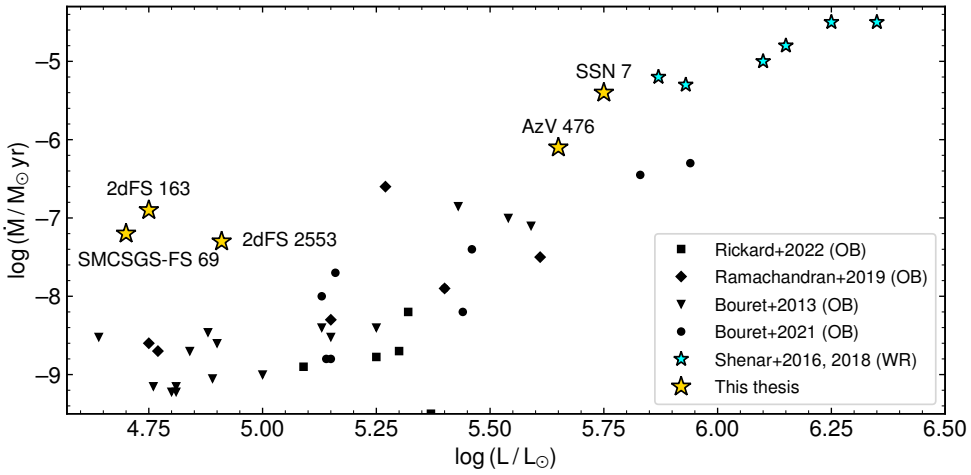

Fig. 7.2.1. Mass-loss rates of SMC stars as a function of luminosity. Apparent single OB stars from various works (Bouret et al. 2013; Ramachandran et al. 2019; Bouret et al. 2021; Rickard et al. 2022) are illustrated as black symbols, WR binaries with known orbital mass (Shenar et al. 2016, 2018) as cyan stars, and the partially stripped stars presented in this thesis (see Chapters 2, 3, and 6) as yellow stars. The partially stripped stars exhibit mass-loss rates at least one order of magnitude higher than stars with similar luminosity.

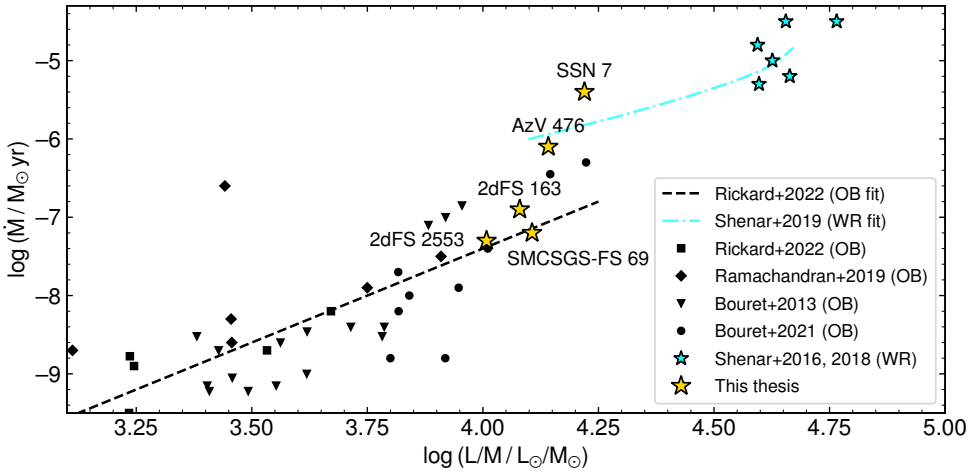

Fig. 7.2.2. Mass-loss rates of SMC stars as a function of the luminosity-to-mass ratio. The symbols are the same as in Fig. 7.2.1. Here the partially stripped stars with the lower luminosity (mass) perfectly group among the OB stars, while the more luminous (massive) stars still seem to have enhanced winds similar to those of the WR stars.

WR stars, the intermediate-mass helium stars (Chapters 5 and 6) exhibit mass-loss rates comparable to those of early O-type stars.

The importance of the donors of post-interaction binaries as reference points becomes evident when plotting the mass-loss rates versus the L/M ratio. Figure 7.2.2 shows the mass-loss rates of partially stripped stars from our analyzed binary systems, alongside those of other OB and WR stars in the SMC with known masses, plotted against their L/M ratio (using their orbital masses when available or, when not, with their masses corrected for centrifugal acceleration; Repolust et al. 2004). A notable increase in mass-loss rates is observed at an L/M ratio of approximately ≈ 4.1, which separates the massive and intermediate-mass donor stars. Whether this phenomenon correlates to another stellar parameter and/or a change in the driving source of the wind is unclear and will be the subject of later follow-up studies. However, this underscores the crucial role of post-interaction binaries and, hence, the significance of this thesis in advancing our understanding of stellar winds.

7.3. Post-interaction binaries and their role in young galaxies

The novel discoveries on the nature of low-metallicity (post) interaction binaries presented in Chapters 2, 3, 5, and 6 of this thesis challenge several long-held assumptions about stars in binaries. It was revealed that i) mass-transfer via RLOF does not necessarily lead to the complete stripping of a star's hydrogen-rich envelope, as previously thought, ii) the partially stripped stars are not strong emitters of He II ionizing radiation, due to their moderate effective temperatures, and iii) the partially stripped stars exhibit surprisingly strong wind features in the UV, sometimes even stronger than those of OB-type stars. These insights have profound implications for our interpretation of the integrated spectra of unresolved galaxies at high redshifts.

7.3.1. Rest-frame UV spectra of young galaxies

The integrated spectra of high-redshift galaxies obtained with HST and JWST typically include only the rest-UV frame of the galaxy which is shifted to the optical or infrared. Since the UV part of a spectrum originates solely from hot stars this puts particular interest on hot massive stars, including post-interaction binaries. There are two simple models describing the stellar content of young galaxies, those that have continuous star formation and those that recently underwent a starburst event where many massive stars have been created. The question is now how the spectral appearance is expected to change when considering our newly gained knowledge about low-metallicity post-interaction binaries.

7.3.1.1. Continuous star formation

In galaxies with continuously ongoing star formation their integrated spectrum, is dominated by the light of the most massive (i.e. brightest) stars. Binary systems are known to play a crucial role in shaping the overall light output of galaxies, particularly those with low metallicity (e.g., Dionne & Robert 2006; Eldridge et al. 2017). However, these calculations often assumed significant mass loss from stars, leading to a substantial contribution from OB-type stars to the integrated spectrum. A recent study by Rickard et al. (2022) examining main-sequence O-type stars in the SMC revealed that these stars exhibit weak or undetectable wind features in their UV spectra. Only luminous stars with a high L/M ratio in longlived evolutionary stages – like very massive stars ($M_{\rm ini} \gtrsim 100\,M_\odot$), giants, supergiants, and Wolf-Rayet stars – are expected to significantly contribute to the UV wind profiles.

The post-interaction binaries reported in this work are part of the ULLYSES sample, which encompasses roughly ~ 100 massive stars. Even without correcting for potential biases in the ULLYSES sample which favors single stars, this suggests that a surprisingly high fraction ($\gtrsim 4\,\%$) of all OB stars in a population might actually be post-interaction binaries. As discussed earlier, we demonstrate that the post-interaction binaries in the SMC are sufficiently luminos, have high L/M ratios, and appear to contract slowly towards the He-ZAMS (see Chapters 2, 3, 5 and 6, as well as the discussions from above) allowing them to leave their imprint on a galaxy's integrated spectrum.

Recent observations of galaxies at high redshifts reveal a surprising phenomenon: their spectra display strong nitrogen features while exhibiting weak lines from carbon and oxygen winds (e.g., Bunker et al. 2023; Cameron et al. 2023; Nagele & Umeda 2023). So far this is an unsolved puzzle, as OB stars are thought to be the primary contributors to these galactic spectra. However, given that the CNO surface abundances of post-interaction binaries correspond to those of the CN or CNO equilibrium, they have increased surface nitrogen and depleted carbon and oxygen abundances. Considering these binaries among the major contributors to low-metallicity spectra of entire galaxies, they are expected to show prominent nitrogen lines. Our results, therefore, offer a compelling solution to the puzzle, potentially providing the missing link towards a more comprehensive understanding of stellar populations within low-metallicity galaxies.

7.3.1.2. Starburst galaxies

In young starburst galaxies, the population of massive stars dwindles over time, leading to a change in the stars that contribute most significantly to the galaxy's integrated spectrum (e.g., Dionne & Robert 2006; Eldridge et al. 2017). The following discussion builds upon the expected stellar populations calculated by Wang et al. (2020) to explain the morphology of young stellar clusters with SMC metallicity. At early stages ($t \approx 2\,$Myr), the integrated spectrum of a starburst galaxy, much like a galaxy with continuous star formation, is dominated by the most massive stars, giants, supergiants, Wolf-Rayet stars, and post-interaction binaries.

As time progresses ($t \approx 10\,$Myr), the most massive stars have already reached the ends of their lives. Consequently, the spectrum becomes dominated by less massive stars ($M_{\rm ini} \approx 20\,M_\odot$). Interestingly, Wang et al. (2020) work demonstrates that the most luminous stars in an aging stellar population transition to giants and supergiants, alongside a growing population of post-interaction binaries. As highlighted throughout this thesis, the UV spectra of intermediate-mass post-interaction binaries (see Chapters 5 and 6) exhibit strong wind signatures, comparable to those of massive OB-type stars. Therefore, neglecting these binaries in spectral analysis can lead to misinterpretations of a galaxy's overall spectrum.

It is evident that incorporating the effects of post-interaction binaries and their unique spectral properties into spectral synthesis models is crucial. Only by doing this, we will be able to decipher the integrated spectra of young high-redshift galaxies.

7.3.2. Feedback within galaxies

The role of massive stars inside galaxies is more than just contributing to the integrated spectrum. With their strong stellar winds, high ionizing fluxes, and enigmatic supernova explosions, they are the main drivers of the chemical enrichment of galaxies and the feedback processes that can regulate star formation (Vink 2006; Rogers & Pittard 2013; Ramachandran et al. 2018b; Crowther 2019). Binary stars are particularly interesting for the ionizing feedback, as after an interaction they have been believed to quickly wander to the He-ZAMS where they emit copious amounts of ionizing photons due to their hot temperatures.

It has been shown that in galaxies with constant star formation, the number of intermediate-mass helium stars increases rapidly with time (e.g., Dionne & Robert 2006; Eldridge et al. 2017; Götberg et al. 2019). Our binary evolution models (Chap-

ter 6), replicating the observed properties of partially stripped donor stars, show that these stars from Case B systems do not reach the He-ZAMS. Instead, they reside near the H-ZAMS with temperatures similar to OB stars. Consequently, they are too cool to produce copious amounts of He II ionizing photons (see our results in Chapters 5 and 5). This has significant implications for our understanding of the feedback processes within galaxies. We must reevaluate the key drivers of the ionization of the Early Cosmos and the regulators of star formation. Furthermore, the weak winds of these partially stripped stars suggest they will retain their hydrogen-rich envelopes, leading to Type II supernovae instead of Type Ib/c. This also necessitates a revision of our understanding of supernova feedback and its impact on chemical enrichment within galaxies.

Chapter 8

Summary and outlook

This thesis focuses on uncovering and characterizing the most massive (post) interaction binary systems within the metal-poor environment of the SMC galaxy. From their analysis we aim to answer i) what the stellar and wind properties of partially stripped stars in the critical evolutionary transition from OB stars to helium stars are, ii) how massive binary stars evolve at metallicities similar to those present in the galaxies of the Early Universe, and iii) how our findings influence the interpretation of spectra and feedback processes within these distant, high-redshift galaxies?

To address these questions, we employ a multifaceted approach: Firstly, we analyze multi-epoch optical and UV data to identify binary systems and measure their stellar and wind properties with the PoWR stellar atmosphere code. Secondly, we use the PHOEBE software to fit light and radial velocity curves of these systems to determine their orbital parameters, information that is crucial to fully comprehend the evolutionary history of the system. Finally, we utilize these results to challenge current binary evolution models and calculate our own binary evolution models with the MESA code to improve our understanding of low-metallicity stellar.

Following this strategy, we discover the first four O-type post-interaction binaries within the SMC galaxy (see Chapters 2, 5, and 6). The detailed spectral analysis reveals that the donor stars in these binaries possess temperatures and luminosities comparable to normal OB-type stars while having significantly lower masses. These partially stripped stars can retain hydrogen-rich envelopes ($X_H \gtrsim 0.5$) after mass transfer, and their CNO abundances align with CN or CNO equilibrium expectations. Surprisingly, these donor stars exhibit strong stellar winds that are at least one order of magnitude higher than those of OB-type stars with similar stellar parameters. While the massive partially stripped stars show mass-loss rates comparable to WR stars, the intermediate-mass ones have mass-loss rates similar to early O-type stars. By comparing their L/M ratios with other well-studied massive stars in the SMC, we found these objects reside near the transition zone from normal OB star's mass-loss rates to those of the WRs, offering unique insights into the physical mechanisms powering the winds of hot stars. These results provide invaluable benchmarks for validating and calibrating theoretical models.

For two of the four newly discovered post-interaction binaries, there was enough data to perform a light and radial velocity curve fit, which revealed their orbital configuration. Our analysis shows that these systems have orbital periods in the range from several tens to hundreds of days, meaning that they previously must have gone through Case B mass transfer. Standard binary evolution models for Case B systems predict that the donor stars shortly after an interaction have thin, hydrogen-poor ($X_H \lesssim 0.4$) envelopes and are in a short-lived contraction phase, meaning that there should be only very few systems in the SMC (Dutta & Klencki 2023). The sheer number of discovered post-interaction binaries within this thesis and the strong discrepancy between measured and predicted stellar properties challenge our understanding of massive binary evolution at low metallicity.

Our binary evolution calculations presented in Chapter 5 show that when incorporating the effects of slightly enhanced semiconvective mixing (which mostly affects the evolution of a star after core hydrogen burning) successfully reproduces the observed stellar and orbital parameters of the post-interaction binaries. Based on these models it is suggested that low-metallicity donor stars in systems undergoing Case B mass transfer contract slower and end up as partially stripped stars with moderate temperatures ($T_{\rm eff} \approx 60\,$kK). Furthermore, the weak stellar winds at the metallicity of the SMC allow these donor stars to retain their leftover partially stripped hydrogen envelopes until the core collapses. This has a critical implication for their ultimate fate: they will explode as Type II supernovae, rather than the Type Ib/c supernovae predicted by current models of fully stripped stars.

In addition to the four post-interaction binaries, our research unveils the so-far most massive binary system observed undergoing mass transfer (Chapter 3), namely NGC 346 SSN 7. This remarkable system has a short orbital period of $P_{\rm orb} \approx 3\,$d and with both stars filling their Roche lobes the observations suggest that it is currently in the phase of slow Case A mass transfer. We determine the current masses of the primary and secondary stars to be $32\,M_\odot$ and $55\,M_\odot$, respectively. Their extreme mass ratio and their stellar parameters suggest a conservative transfer of mass. Our binary evolution models successfully reproduce the observed stellar and orbital parameters of NGC 346 SSN 7 only when considering that the secondary already accreted several solar masses during the still ongoing slow Case A mass transfer, confirming the observations. The

unique properties of this massive interacting binary system present a valuable opportunity to challenge and refine existing models of mass transfer physics.

When discussing the evolution of binary systems often the evolution of the secondary after the primary's death is neglected. Typically it is just assumed that the accretor would respond to the removal of mass via RLOF similarly to a "normal" primary star. With our binary evolution models (Chapter 4) we delve deeper into the evolution of accreting stars. Our models predict, that secondaries in short-period binary systems ($P_{\rm ini} \lesssim 10\,{\rm d}$) accrete mass conservatively, leading to a rejuvenation and a change in the accretors' internal structure and an increased envelope-to-core mass ratio. As a consequence, rejuvenated secondaries can retain a significant portion of their hydrogen-rich envelopes after mass transfer, leading to the formation of partially stripped WR stars with moderate temperatures ($T_{\rm eff} \approx 50\,{\rm kK}$). This novel pathway suggests a potential bimodality in the temperature distribution of WR star populations within low-metallicity environments, which is also seen within the WR population of the SMC. These populations would consist of hot WR stars formed from primary stars and secondaries with highly non-conservative accretion, and cooler, partially stripped WR stars that have been secondaries that got rejuvenated while accreting conservatively.

The altered response of rejuvenated accretors during mass transfer allows them to remain in closer orbits. Consequently, once both stars become compact objects, the binary system requires less time to merge. Our discovery of this novel evolutionary pathway necessitates the incorporation of this effect into models predicting gravitational wave merger rates. This inclusion has the potential to significantly alter our understanding of the frequency of these mergers, particularly in low-metallicity environments where they are frequently observed.

The collective findings of this thesis significantly impact our understanding of massive binary evolution in low-metallicity environments, with far-reaching consequences for interpreting high-redshift galaxies and galactic feedback processes. Post-interaction binaries, with their high luminosities and powerful stellar winds, are predicted to be significant contributors to the UV spectrum of star-forming galaxies, while for galaxies that have recently undergone a starburst, these binaries are expected to dominate the UV spectra entirely. Recent observations reveal high-redshift galaxies with surprisingly strong nitrogen wind features (Bunker et al. 2023; Cameron et al. 2023; Nagele & Umeda 2023), challenging current spectral synthesis models. Our discovery of partially stripped stars in post-interaction binaries offers a compelling explanation. These stars possess both strong stellar winds and CNO abundances consistent with either CN or CNO equilibrium, leading to prominent nitrogen lines in their spectra. This supports that post-interaction binaries are significant contributors to the spectra of young, low-metallicity galaxies.

Traditionally, post-interaction binaries have been considered the primary drivers of a galaxy's feedback through their copious amounts of He II ionizing radiation and energetic supernovae. Our research challenges this paradigm. We demonstrate that partially stripped stars in low-metallicity post-interaction binaries can retain significant, hydrogen-rich envelopes, leading to moderate effective temperatures and, hence, reduced ionizing radiation and feedback. Furthermore, these partially stripped stars are not expected to lose their hydrogen envelope even after mass transfer and are therefore are predicted to explode as Type II supernovae, injecting different elements into the interstellar medium compared to the Type Ib/c supernovae expected by current binary evolution models. These findings necessitate a reevaluation of the impact of massive binary evolution on a galaxy's chemical enrichment and overall evolution. The discovered post-interaction binaries in this thesis might just mark the tip of the iceberg of a so-far undiscovered stellar population in the SMC. Their presented analysis is the first step toward a comprehensive understanding of the conditions of high-redshift galaxies and the Early Universe.

The growing recognition of the crucial role played by binaries that have recently interacted has started a hunt for additional such systems. These searches are essential for constructing a statistically sound sample for refining binary evolution models. Building upon the discoveries presented in this thesis, we have initiated a multi-epoch ESO observing program (ID: 110.24CU, PI: Pauli) targeting previously assumed single stars with properties strikingly similar to our partially stripped stars, namely extreme L/M ratios and strongly enriched surface nitrogen abundances. In addition to that, the Binaries at LOw Metallicity (BLOeM) collaboration recently started a multi-epoch ESO Large Program (ID: 112.25R7, PI: Shenar, Co-I: Pauli) dedicated to obtaining a nearly unbiased perspective on the stellar and binary properties of roughly 1000 OB-type stars within the SMC. These ongoing projects underline the importance of the milestone achieved in this work and promise to deliver in the coming years an even deeper understanding of post-interaction binaries.

References

Abbott, B. P., Abbott, R., Abbott, T. D., et al. 2016, ApJ, 832, L21

Abbott, B. P., Abbott, R., Abbott, T. D., et al. 2019, Phys. Rev. D, 100, 122002

Abdul-Masih, M. 2023, A&A, 669, L11

Abdul-Masih, M., Banyard, G., Bodensteiner, J., et al. 2020, Nature, 580, E11

Abdul-Masih, M., Sana, H., Hawcroft, C., et al. 2021, arXiv e-prints, arXiv:2104.07621

Aguilera-Dena, D. R., Langer, N., Antoniadis, J., et al. 2022, A&A, 661, A60

Asplund, M., Grevesse, N., & Sauval, A. J. 2005, in Astronomical Society of the Pacific Conference Series, Vol. 336, Cosmic Abundances as Records of Stellar Evolution and Nucleosynthesis, ed. I. Barnes, Thomas G. & F. N. Bash, 25

Azzopardi, M. & Breysacher, J. 1979, A&A, 75, 120

Batten, A. H. 1989, Space Science Reviews, 50, 1

Baum, E., Hamann, W.-R., Koesterke, L., & Wessolowski, U. 1992, A&A, 266, 402

Baym, G., Hatsuda, T., Kojo, T., et al. 2018, Reports on Progress in Physics, 81, 056902

Belczynski, K., Kalogera, V., & Bulik, T. 2002, ApJ, 572, 407

Bernini-Peron, M., Marcolino, W. L. F., Sander, A. A. C., et al. 2023, A&A, 677, A50

Bestenlehner, J. M. 2020, MNRAS, 493, 3938

Bestenlehner, J. M., Gräfener, G., Vink, J. S., et al. 2014, A&A, 570, A38

Bethe, H. A. 1939, Physical Review, 55, 434

Björklund, R., Sundqvist, J. O., Singh, S. M., Puls, J., & Najarro, F. 2022, arXiv e-prints, arXiv:2203.08218

Björklund, R., Sundqvist, J. O., Singh, S. M., Puls, J., & Najarro, F. 2023, A&A, 676, A109

Blaha, C. & Humphreys, R. M. 1989, AJ, 98, 1598

Bodensteiner, J., Shenar, T., Mahy, L., et al. 2020a, A&A, 641, A43

Bodensteiner, J., Shenar, T., & Sana, H. 2020b, A&A, 641, A42

Böhm-Vitense, E. 1958, ZAp, 46, 108

Bonanos, A. Z., Lennon, D. J., Köhlinger, F., et al. 2010, AJ, 140, 416

Bouchet, P., Lequeux, J., Maurice, E., Prevot, L., & Prevot-Burnichon, M. L. 1985, A&A, 149, 330

Bouret, J.-C., Lanz, T., Hillier, D. J., et al. 2003, ApJ, 595, 1182

Bouret, J. C., Lanz, T., Martins, F., et al. 2013, A&A, 555, A1

Bouret, J. C., Martins, F., Hillier, D. J., et al. 2021, A&A, 647, A134

Bowman, D. M., Vandenbussche, B., Sana, H., et al. 2022, A&A, 658, A96

Brands, S. A., de Koter, A., Bestenlehner, J. M., et al. 2022, A&A, 663, A36

Branton, D., Riley, A., et al. 2021, STIS Instrument Handbook, Version 20.0, Baltimore: STScI

Brasseur, C. E., Phillip, C., Fleming, S. W., Mullally, S. E., & White, R. L. 2019, Astrocut: Tools for creating cutouts of TESS images

Brott, I., de Mink, S. E., Cantiello, M., et al. 2011, A&A, 530, A115

Bunker, A. J., Saxena, A., Cameron, A. J., et al. 2023, A&A, 677, A88

Burbidge, E. M., Burbidge, G. R., Fowler, W. A., & Hoyle, F. 1957, Reviews of Modern Physics, 29, 547

Cameron, A. J., Katz, H., Rey, M. P., & Saxena, A. 2023, MNRAS, 523, 3516

Cannon, A. J. & Pickering, E. C. 1918, Annals of Harvard College Observatory, 91, 1

Cassinelli, J. P. & Olson, G. L. 1979, ApJ, 229, 304

Castor, J. I., Abbott, D. C., & Klein, R. I. 1975, ApJ, 195, 157

Cerviño, M. & Mas-Hesse, J. M. 1994, A&A, 284, 749

Cescutti, G. & Chiappini, C. 2010, A&A, 515, A102

Choi, J., Dotter, A., Conroy, C., et al. 2016, ApJ, 823, 102

Cignoni, M., Sabbi, E., Nota, A., et al. 2009, AJ, 137, 3668

Cioni, M. R. L., Clementini, G., Girardi, L., et al. 2011, A&A, 527, A116

Claeys, J. S. W., de Mink, S. E., Pols, O. R., Eldridge, J. J., & Baes, M. 2011, A&A, 528, A131

Conroy, K. E., Kochoska, A., Hey, D., et al. 2020, ApJS, 250, 34

Conti, P. S. & Alschuler, W. R. 1971, ApJ, 170, 325

Crowther, P. A. 2007, ARA&A, 45, 177

Crowther, P. A. 2019, Galaxies, 7, 88

Crowther, P. A., Dessart, L., Hillier, D. J., Abbott, J. B., & Fullerton, A. W. 2002, A&A, 392, 653

Curtis-Lake, E., Carniani, S., Cameron, A., et al. 2023, Nature Astronomy, 7, 622

Cutri, R. M., Skrutskie, M. F., van Dyk, S., et al. 2003, VizieR Online Data Catalog, II/246

Danforth, C. W., Sankrit, R., Blair, W. P., Howk, J. C., & Chu, Y.-H. 2003, ApJ, 586, 1179

de Mink, S. E., Langer, N., Izzard, R. G., Sana, H., & de Koter, A. 2013a, ApJ, 764, 166

de Mink, S. E., Pols, O. R., & Hilditch, R. W. 2007, A&A, 467, 1181

de Mink, S. E., Sana, H., Langer, N., Izzard, R. G., & Schneider, F. R. N. 2013b, ArXiv e-prints [arXiv:1312.3650]

De Propris, R., Rich, R. M., Mallery, R. C., & Howard, C. D. 2010, ApJ, 714, L249

Dekker, H., D'Odorico, S., Kaufer, A., Delabre, B., & Kotzlowski, H. 2000, in Society of Photo-Optical Instrumentation Engineers (SPIE) Conference Series, Vol. 4008, Optical and IR Telescope Instrumentation and Detectors, ed. M. Iye & A. F. Moorwood, 534–545

Dessart, L., Hillier, D. J., Livne, E., et al. 2011, MNRAS, 414, 2985

Diaz-Cordoves, J. & Gimenez, A. 1992, A&A, 259, 227

Dionne, D. & Robert, C. 2006, ApJ, 641, 252

Drout, M. R., Götberg, Y., Ludwig, B. A., et al. 2023, Science, 382, 1287

Dufton, P. L., Evans, C. J., Hunter, I., Lennon, D. J., & Schneider, F. R. N. 2019, A&A, 626, A50

Dufton, P. L., Ryans, R. S. I., Trundle, C., et al. 2005, A&A, 434, 1125

Dutta, D. & Klencki, J. 2023, arXiv e-prints, arXiv:2312.12658

Eggleton, P. P. 1983, ApJ, 268, 368

El-Badry, K. & Burdge, K. B. 2022, MNRAS, 511, 24

El-Badry, K., Burdge, K. B., & Mróz, P. 2022a, MNRAS, 511, 3089

El-Badry, K., Conroy, C., Quataert, E., et al. 2022b, MNRAS, 516, 3602

El-Badry, K. & Quataert, E. 2021, MNRAS, 502, 3436

Eldridge, J. J., Izzard, R. G., & Tout, C. A. 2008, MNRAS, 384, 1109

Eldridge, J. J., Stanway, E. R., Xiao, L., et al. 2017, PASA, 34, e058

Erdim, M. K., Ezer, C., Ünver, O., Hazar, F., & Hudaverdi, M. 2021, Monthly Notices of the Royal Astronomical Society, 508, 3337

Evans, C. J., Howarth, I. D., Irwin, M. J., Burnley, A. W., & Harries, T. J. 2004, MNRAS, 353, 601

Evans, I. N., Primini, F. A., Glotfelty, K. J., et al. 2010, ApJS, 189, 37

Foellmi, C., Moffat, A. F. J., & Guerrero, M. A. 2003, MNRAS, 338, 360

Foreman-Mackey, D., Hogg, D. W., Lang, D., & Goodman, J. 2013, PASP, 125, 306

Frémat, Y., Zorec, J., Hubert, A. M., & Floquet, M. 2005, A&A, 440, 305

Frost, A. J., Bodensteiner, J., Rivinius, T., et al. 2022, A&A, 659, L3

Gaia Collaboration. 2022, VizieR Online Data Catalog, I/355

Gaia Collaboration, Brown, A. G. A., Vallenari, A., et al. 2021, A&A, 649, A1

Gaia Collaboration, Prusti, T., de Bruijne, J. H. J., et al. 2016, A&A, 595, A1

Gaia Collaboration, Vallenari, A., Brown, A. G. A., et al. 2023, A&A, 674, A1

Gal-Yam, A., Bruch, R., Schulze, S., et al. 2022, Nature, 601, 201

Garmany, C. D., Conti, P. S., & Massey, P. 1980, ApJ, 242, 1063

Georgy, C., Ekström, S., Eggenberger, P., et al. 2013, A&A, 558, A103

Georgy, C., Ekström, S., Meynet, G., et al. 2012, A&A, 542, A29

Gilkis, A. & Shenar, T. 2023, MNRAS, 518, 3541

Gilkis, A., Shenar, T., Ramachandran, V., et al. 2021, MNRAS, 503, 1884

Gilkis, A., Vink, J. S., Eldridge, J. J., & Tout, C. A. 2019, MNRAS, 486, 4451

Gomel, R., Faigler, S., & Mazeh, T. 2021, MNRAS, 501, 2822

Götberg, Y., de Mink, S. E., Groh, J. H., et al. 2018, A&A, 615, A78

Götberg, Y., de Mink, S. E., Groh, J. H., Leitherer, C., & Norman, C. 2019, A&A, 629, A134

Götberg, Y., Drout, M. R., Ji, A. P., et al. 2023, ApJ, 959, 125

Götberg, Y., Korol, V., Lamberts, A., et al. 2020, ApJ, 904, 56

Götberg, Y., Mink, S. E. d., & Groh, J. H. 2017, Astronomy & Astrophysics, 608, A11, publisher: EDP Sciences

Graczyk, D., Pietrzyński, G., Thompson, I. B., et al. 2020, ApJ, 904, 13

Gräfener, G. 2021, A&A, 647, A13

Gräfener, G., Koesterke, L., & Hamann, W.-R. 2002, A&A, 387, 244

Gräfener, G., Owocki, S. P., Grassitelli, L., & Langer, N. 2017, A&A, 608, A34

Gräfener, G., Owocki, S. P., & Vink, J. S. 2012, A&A, 538, A40

Gräfener, G. & Vink, J. S. 2013, A&A, 560, A6

Gräfener, G., Vink, J. S., de Koter, A., & Langer, N. 2011, A&A, 535, A56

Grassitelli, L., Langer, N., Grin, N. J., et al. 2018, A&A, 614, A86

Groh, J. H., Oliveira, A. S., & Steiner, J. E. 2008, A&A, 485, 245

Gruner, D., Hainich, R., Sander, A. A. C., et al. 2019, A&A, 621, A63

Hainich, R., Pasemann, D., Todt, H., et al. 2015, A&A, 581, A21

Hainich, R., Ramachandran, V., Shenar, T., et al. 2019, A&A, 621, A85

Hainich, R., Rühling, U., Todt, H., et al. 2014, A&A, 565, A27

Hainich, R., Shenar, T., Sander, A., Hamann, W. R., & Todt, H. 2017, in The Lives and Death-Throes of Massive Stars, ed. J. J. Eldridge, J. C. Bray, L. A. S. McClelland, & L. Xiao, Vol. 329, 171–175

Hamann, W.-R. & Gräfener, G. 2003, A&A, 410, 993

Hamann, W.-R. & Gräfener, G. 2004, A&A, 427, 697

Hamann, W.-R., Gräfener, G., & Liermann, A. 2006, A&A, 457, 1015

Hamann, W.-R., Gräfener, G., Oskinova, L., & Liermann, A. 2008, in Astronomical Society of the Pacific Conference Series, Vol. 388, Mass Loss from Stars and the Evolution of Stellar Clusters, ed. A. de Koter, L. J. Smith, & L. B. F. M. Waters, 171

Hamann, W.-R. & Koesterke, L. 1998a, A&A, 335, 1003

Hamann, W.-R. & Koesterke, L. 1998b, A&A, 333, 251

Hammer, F., Yang, Y. B., Flores, H., Puech, M., & Fouquet, S. 2015, ApJ, 813, 110

Harries, T. J., Hilditch, R. W., & Howarth, I. D. 2003, MNRAS, 339, 157

Hastings, B., Langer, N., Wang, C., Schootemeijer, A., & Milone, A. P. 2021, A&A, 653, A144

Hawcroft, C., Sana, H., Mahy, L., et al. 2023, arXiv e-prints, arXiv:2303.12165

Heger, A., Fryer, C. L., Woosley, S. E., Langer, N., & Hartmann, D. H. 2003, ApJ, 591, 288

Heger, A., Langer, N., & Woosley, S. E. 2000, ApJ, 528, 368

Herrero, A., Kudritzki, R. P., Vilchez, J. M., et al. 1992, A&A, 261, 209

Higgins, E. R. & Vink, J. S. 2019, A&A, 622, A50

Hilditch, R. W., Howarth, I. D., & Harries, T. J. 2005, MNRAS, 357, 304

Hillier, D. J., Koenigsberger, G., Nazé, Y., et al. 2019, MNRAS, 486, 725

Hillier, D. J. & Miller, D. L. 1999, ApJ, 519, 354

Hirschauer, A. S. et al. 2021, Cosmic Origins Spectrograph Instrument Handbook, Version 13.0, Baltimore: STScI

Holgado, G., Simón-Díaz, S., Haemmerlé, L., et al. 2020, A&A, 638, A157

Hollenbach, D. J. & Tielens, A. G. G. M. 1999, Reviews of Modern Physics, 71, 173

Horvat, M., Conroy, K. E., Pablo, H., et al. 2018, ApJS, 237, 26

Huang, C. X., Vanderburg, A., Pál, A., et al. 2020, Research Notes of the American Astronomical Society, 4, 204

Humphreys, R. M. & McElroy, D. B. 1984, ApJ, 284, 565

Hunter, I., Brott, I., Langer, N., et al. 2009, A&A, 496, 841

Hunter, I., Dufton, P. L., Smartt, S. J., et al. 2007, A&A, 466, 277

Hurley, J. R., Tout, C. A., & Pols, O. R. 2002, MNRAS, 329, 897

Hut, P. 1981, A&A, 99, 126

Iglesias-Marzoa, R., López-Morales, M., & Jesús Arévalo Morales, M. 2015, PASP, 127, 567

Igoshev, A. P., Chruslinska, M., Dorozsmai, A., & Toonen, S. 2021, MNRAS, 508, 3345

IJspeert, L. W., Tkachenko, A., Johnston, C., et al. 2021, A&A, 652, A120

Ingber, L. 1996, Adaptive simulated annealing (ASA): Lessons learned, Lester ingber papers, Lester Ingber

Irrgang, A., Przybilla, N., & Meynet, G. 2022, Nature Astronomy, 6, 1414

Jayasinghe, T., Stanek, K. Z., Kochanek, C. S., et al. 2020, MNRAS, 491, 13

Johnston, C. 2021, A&A, 655, A29

Jones, D., Conroy, K. E., Horvat, M., et al. 2020, ApJS, 247, 63

Justham, S., Podsiadlowski, P., & Vink, J. S. 2014, ApJ, 796, 121

Kaiser, E. A., Hirschi, R., Arnett, W. D., et al. 2020, MNRAS, 496, 1967

Kajino, T., Aoki, W., Balantekin, A. B., et al. 2019, Progress in Particle and Nuclear Physics, 107, 109

Kasen, D., Metzger, B., Barnes, J., Quataert, E., & Ramirez-Ruiz, E. 2017, Nature, 551, 80

Kewley, L. J., Nicholls, D. C., & Sutherland, R. S. 2019, ARA&A, 57, 511

Keyes, C. D., Koratkar, A. P., Dahlem, M., et al. 1995, Faint Object Spectrograph Instrument Handbook, Version 6.0

Kippenhahn, R., Ruschenplatt, G., & Thomas, H. C. 1980, A&A, 91, 175

Kippenhahn, R. & Weigert, A. 1967, ZAp, 65, 251

Kipping, D. M. 2013, Monthly Notices of the Royal Astronomical Society: Letters, 434, L51

Klement, R., Carciofi, A. C., Rivinius, T., et al. 2019, ApJ, 885, 147

Klencki, J., Istrate, A., Nelemans, G., & Pols, O. 2022, A&A, 662, A56

Klencki, J., Nelemans, G., Istrate, A. G., & Chruslinska, M. 2021, A&A, 645, A54

Klencki, J., Nelemans, G., Istrate, A. G., & Pols, O. 2020, A&A, 638, A55

Koenigsberger, G., Morrell, N., Hillier, D. J., et al. 2014, AJ, 148, 62

Kohler, K., Langer, N., de Koter, A., et al. 2014, VizieR Online Data Catalog, 357, 30071

Kolb, U. & Ritter, H. 1990, A&A, 236, 385

Kopal, Z. 1955, Annales d'Astrophysique, 18, 379

Kriz, S. & Harmanec, P. 1975, Bulletin of the Astronomical Institutes of Czechoslovakia, 26, 65

Kroupa, P., Weidner, C., Pflamm-Altenburg, J., et al. 2013, in Planets, Stars and Stellar Systems. Volume 5: Galactic Structure and Stellar Populations, ed. T. D. Oswalt & G. Gilmore, Vol. 5, 115

Krtička, J. & Kubát, J. 2018, A&A, 612, A20

Kudritzki, R. & Puls, J. 2000, ARA&A, 38, 613

Kudritzki, R. P., Pauldrach, A., Puls, J., & Abbott, D. C. 1989, A&A, 219, 205

Kurt, C. M. & Dufour, R. J. 1998, in Revista Mexicana de Astronomia y Astrofisica Conference Series, Vol. 7, Revista Mexicana de Astronomia y Astrofisica Conference Series, ed. R. J. Dufour & S. Torres-Peimbert, 202

Lamb, J. B., Oey, M. S., Segura-Cox, D. M., et al. 2016, ApJ, 817, 113

Lamers, H. J. G. L. M. & Cassinelli, J. P. 1999, Introduction to Stellar Winds (Cambridge University Press)

Lamers, H. J. G. L. M., Snow, T. P., & Lindholm, D. M. 1995, ApJ, 455, 269

Langer, N. 1987, A&A, 171, L1

Langer, N. 1989, A&A, 210, 93

Langer, N., Fricke, K. J., & Sugimoto, D. 1983, A&A, 126, 207

Langer, N., Schürmann, C., Stoll, K., et al. 2020, A&A, 638, A39

Laplace, E., Götberg, Y., de Mink, S. E., Justham, S., & Farmer, R. 2020, A&A, 637, A6

Lecroq, M., Charlot, S., Bressan, A., et al. 2024, MNRAS, 527, 9480

Leitherer, C., Robert, C., & Drissen, L. 1992, ApJ, 401, 596

Lennon, D. J., Dufton, P. L., Villaseñor, J. I., et al. 2022, A&A, 665, A180

Lenz, P. & Breger, M. 2005, Communications in Asteroseismology, 146, 53

Li, F. X., Qian, S. B., & Liao, W. P. 2022, AJ, 163, 203

Lightkurve Collaboration, Cardoso, J. V. d. M., Hedges, C., et al. 2018, Lightkurve: Kepler and TESS time series analysis in Python

Limongi, M. & Chieffi, A. 2018, ApJS, 237, 13

Liu, J., Zhang, H., Howard, A. W., et al. 2019, Nature, 575, 618

Mac Low, M.-M., Balsara, D. S., Kim, J., & de Avillez, M. A. 2005, ApJ, 626, 864

Madau, P. & Dickinson, M. 2014, ARA&A, 52, 415

Maeder, A. 2009, Physics, Formation and Evolution of Rotating Stars (Springer Berlin Heidelberg)

Mahy, L., Almeida, L. A., Sana, H., et al. 2020, A&A, 634, A119

Maíz Apellániz, J. 2019, MGB: Interactive spectral classification code

Maíz Apellániz, J., Pellerin, A., Barbá, R. H., et al. 2012, in Astronomical Society of the Pacific Conference Series, Vol. 465, Proceedings of a Scientific Meeting in Honor of Anthony F. J. Moffat, ed. L. Drissen, C. Robert, N. St-Louis, & A. F. J. Moffat, 484

Majewski, S. R., Schiavon, R. P., Frinchaboy, P. M., et al. 2017, AJ, 154, 94

Marchant, P. 2016, PhD thesis, Rheinischen Friedrich-Wilhelms-Universität Bonn

Marchant, P. & Bodensteiner, J. 2023, arXiv e-prints, arXiv:2311.01865

Marchant, P., Langer, N., Podsiadlowski, P., Tauris, T. M., & Moriya, T. J. 2016, A&A, 588, A50

Markova, N. & Puls, J. 2015, in New Windows on Massive Stars, ed. G. Meynet, C. Georgy, J. Groh, & P. Stee, Vol. 307, 117–118

Markova, N., Puls, J., & Langer, N. 2018, A&A, 613, A12

Martins, F. 2018, A&A, 616, A135

Martins, F., Bouret, J. C., Hillier, D. J., et al. 2024, arXiv e-prints, arXiv:2405.01267

Martins, F., Hillier, D. J., Bouret, J. C., et al. 2009, A&A, 495, 257

Martins, F. & Palacios, A. 2021, A&A, 645, A67

Martins, F., Schaerer, D., Hillier, D. J., et al. 2005, A&A, 441, 735

Massa, D., Fullerton, A. W., & Prinja, R. K. 2017, Monthly Notices of the Royal Astronomical Society, 470, 3765

Massey, P., Bresolin, F., Kudritzki, R. P., Puls, J., & Pauldrach, A. W. A. 2004, ApJ, 608, 1001

Massey, P. & Duffy, A. S. 2001, ApJ, 550, 713

Massey, P., Lang, C. C., Degioia-Eastwood, K., & Garmany, C. D. 1995, ApJ, 438, 188

Massey, P., Neugent, K. F., Dorn-Wallenstein, T. Z., et al. 2021, ApJ, 922, 177

Massey, P., Olsen, K. A. G., & Parker, J. W. 2003, PASP, 115, 1265

Massey, P., Parker, J. W., & Garmany, C. D. 1989, AJ, 98, 1305

Massey, P., Puls, J., Pauldrach, A. W. A., et al. 2005, ApJ, 627, 477

Matzner, C. D. 2002, ApJ, 566, 302

Mazeh, T. 2008, in EAS Publications Series, Vol. 29, EAS Publications Series, ed. M. J. Goupil & J. P. Zahn, 1–65

Meyssonnier, N. & Azzopardi, M. 1993, A&AS, 102, 451

Michielsen, M., Aerts, C., & Bowman, D. M. 2021, A&A, 650, A175

Mihalas, D. 1978, Stellar Atmospheres, 2nd edn. (W. H. Freeman and Company, San Francisco)

Miller-Jones, J. C. A., Bahramian, A., Orosz, J. A., et al. 2021, Science, 371, 1046

Moe, M. & Di Stefano, R. 2017, ApJS, 230, 15

Moffat, A. F. J., Niemela, V. S., & Marraco, H. G. 1990, ApJ, 348, 232

Mokiem, M. R., de Koter, A., Evans, C. J., et al. 2007a, A&A, 465, 1003

Mokiem, M. R., de Koter, A., Evans, C. J., et al. 2006, A&A, 456, 1131

Mokiem, M. R., de Koter, A., Vink, J. S., et al. 2007b, A&A, 473, 603

Morgan, D. H., Vassiliadis, E., & Dopita, M. A. 1991, MNRAS, 251, 51P

Morrell, N., Ostrov, P., Massey, P., & Gamen, R. 2003, MNRAS, 341, 583

Müller, P. E. & Vink, J. S. 2008, A&A, 492, 493

Muraoka, K., Homma, A., Onishi, T., et al. 2017, ApJ, 844, 98

Nagele, C. & Umeda, H. 2023, The Astrophysical Journal Letters, 949, L16

Nascimbeni, V., Piotto, G., Ortolani, S., et al. 2016, MNRAS, 463, 4210

Nazé, Y., Hartwell, J. M., Stevens, I. R., et al. 2002, ApJ, 580, 225

Nebot Gómez-Morán, A. & Oskinova, L. M. 2018, A&A, 620, A89

Negueruela, I., Simón-Díaz, S., de Burgos, A., Casasbuenas, A., & Beck, P. G. 2024, arXiv e-prints, arXiv:2407.04163

Nelson, C. A. & Eggleton, P. P. 2001, ApJ, 552, 664

Nidever, D. L., Monachesi, A., Bell, E. F., et al. 2013, ApJ, 779, 145

Niedzielski, A. & Skorzynski, W. 2002, Acta Inf., 52, 81

Niemela, V. & Gamen, R. 2004, New A Rev., 48, 727

Niemela, V. S., Marraco, H. G., & Cabanne, M. L. 1986, PASP, 98, 1133

Nieuwenhuijzen, H. & de Jager, C. 1990, A&A, 231, 134

Nomoto, K., Kobayashi, C., & Tominaga, N. 2013, ARA&A, 51, 457

Nugis, T. & Lamers, H. J. G. L. M. 2000, A&A, 360, 227

Oegerle, W., Murphy, E., & Kriss, J. 2000, The FUSE Data Handbook, Version 1.1

Oesch, P. A., Brammer, G., van Dokkum, P. G., et al. 2016, ApJ, 819, 129

Orosz, J. A., McClintock, J. E., Aufdenberg, J. P., et al. 2011, ApJ, 742, 84

Oskinova, L. M., Todt, H., Ignace, R., et al. 2011, MNRAS, 416, 1456

Packet, W. 1981, A&A, 102, 17

Paczyński, B. 1967, Acta Astron., 17, 355

Paczyński, B. 1971, ARA&A, 9, 183

Pauldrach, A., Puls, J., & Kudritzki, R. P. 1986, A&A, 164, 86

Pauli, D., Langer, N., Aguilera-Dena, D. R., Wang, C., & Marchant, P. 2022a, A&A, 667, A58

Pauli, D., Oskinova, L. M., Hamann, W. R., et al. 2023, arXiv e-prints, arXiv:2303.03989

Pauli, D., Oskinova, L. M., Hamann, W. R., et al. 2022b, A&A, 659, A9

Pawlak, M., Soszyński, I., Udalski, A., et al. 2016, Acta Astron., 66, 421

Paxton, B., Bildsten, L., Dotter, A., et al. 2011, ApJS, 192, 3

Paxton, B., Cantiello, M., Arras, P., et al. 2013, ApJS, 208, 4

Paxton, B., Marchant, P., Schwab, J., et al. 2015, ApJS, 220, 15

Paxton, B., Schwab, J., Bauer, E. B., et al. 2018, ApJS, 234, 34

Paxton, B., Smolec, R., Schwab, J., et al. 2019, ApJS, 243, 10

Payne, C. H. 1924, Harvard College Observatory Circular, 256, 1

Pedersen, M. G. 2022, ApJ, 930, 94

Penny, L. R. & Gies, D. R. 2009, ApJ, 700, 844

Peters, P. C. 1964, Physical Review, 136, 1224

Petrovic, J., Langer, N., Yoon, S.-C., & Heger, A. 2005, A&A, 435, 247

Pietrzyński, G., Graczyk, D., Gallenne, A., et al. 2019, Nature, 567, 200

Pignatari, M., Gallino, R., Heil, M., et al. 2010, ApJ, 710, 1557

Pols. 2009, Stellar Structure and Evolution

Pols, O. R. 1994, A&A, 290, 119

Pols, O. R., Cote, J., Waters, L. B. F. M., & Heise, J. 1991, A&A, 241, 419

Price-Whelan, A. M., Hogg, D. W., Foreman-Mackey, D., & Rix, H.-W. 2017, ApJ, 837, 20

Prša, A. 2011, PHOEBE Scientific Reference, Version 0.30

Prša, A., Conroy, K. E., Horvat, M., et al. 2016, ApJS, 227, 29

Prša, A. & Zwitter, T. 2005, ApJ, 628, 426

Puls, J., Vink, J. S., & Najarro, F. 2008, A&A Rev., 16, 209

Ramachandran, V., Hainich, R., Hamann, W.-R., et al. 2018a, A&A, 609, A7

Ramachandran, V., Hamann, W. R., Hainich, R., et al. 2018b, A&A, 615, A40

Ramachandran, V., Hamann, W. R., Oskinova, L. M., et al. 2019, A&A, 625, A104

Ramachandran, V., Klencki, J., Sander, A. A. C., et al. 2023, A&A, 674, L12

Ramachandran, V., Oskinova, L. M., & Hamann, W. R. 2021, A&A, 646, A16

Ramírez-Agudelo, O. H., Sana, H., de Koter, A., et al. 2017, A&A, 600, A81

Rauw, G. & Nazé, Y. 2016, Advances in Space Research, 58, 761

Reindl, N., Rauch, T., Parthasarathy, M., et al. 2014, A&A, 565, A40

Renzo, M. & Götberg, Y. 2021, ApJ, 923, 277

Renzo, M., Zapartas, E., Justham, S., et al. 2022, arXiv e-prints, arXiv:2206.15338

Repolust, T., Puls, J., & Herrero, A. 2004, A&A, 415, 349

Rickard, M. J., Hainich, R., Hamann, W. R., et al. 2022, A&A, 666, A189

Rickard, M. J. & Pauli, D. 2023, A&A, 674, A56

Ricker, G. R., Winn, J. N., Vanderspek, R., et al. 2015, Journal of Astronomical Telescopes, Instruments, and Systems, 1, 014003

Rivero González, J. G., Puls, J., Massey, P., & Najarro, F. 2012, A&A, 543, A95

Rivinius, T., Baade, D., Hadrava, P., Heida, M., & Klement, R. 2020, A&A, 637, L3

Rogers, H. & Pittard, J. M. 2013, MNRAS, 431, 1337

Rolleston, W. R. J., Trundle, C., & Dufton, P. L. 2002, A&A, 396, 53

Roman-Duval, J., Proffitt, C. R., Taylor, J. M., et al. 2020, Research Notes of the American Astronomical Society, 4, 205

Runacres, M. C. & Owocki, S. P. 2002, A&A, 381, 1015

Sabbi, E., Sirianni, M., Nota, A., et al. 2007, AJ, 133, 44

Sana, H., de Koter, A., de Mink, S. E., et al. 2013, A&A, 550, A107

Sana, H., de Mink, S. E., de Koter, A., et al. 2012, Science, 337, 444

Sana, H., Le Bouquin, J. B., Lacour, S., et al. 2014, ApJS, 215, 15

Sana, H., Tramper, F., Abdul-Masih, M., et al. 2024, A&A, A&A, Forthcoming article

Sander, A., Shenar, T., Hainich, R., et al. 2015, A&A, 577, A13

Sander, A. A. C., Bouret, J. C., Bernini-Peron, M., et al. 2024, arXiv e-prints, arXiv:2407.03137

Sander, A. A. C., Fürst, F., Kretschmar, P., et al. 2018, A&A, 610, A60

Sander, A. A. C., Lefever, R. R., Poniatowski, L. G., et al. 2023, A&A, 670, A83

Sander, A. A. C. & Vink, J. S. 2020, MNRAS, 499, 873

Sanyal, D., Grassitelli, L., Langer, N., & Bestenlehner, J. M. 2015, A&A, 580, A20

Saracino, S., Shenar, T., Kamann, S., et al. 2023, MNRAS, 521, 3162

Schmutz, W., Hamann, W.-R., & Wessolowski, U. 1989, A&A, 210, 236

Schneider, F. R. N., Langer, N., de Koter, A., et al. 2014, A&A, 570, A66

Schootemeijer, A. & Langer, N. 2018, A&A, 611, A75

Schootemeijer, A., Langer, N., Grin, N. J., & Wang, C. 2019, A&A, 625, A132

Schootemeijer, A., Langer, N., Lennon, D., et al. 2021, A&A, 646, A106

Scott, P., Asplund, M., Grevesse, N., Bergemann, M., & Sauval, A. J. 2015a, A&A, 573, A26

Scott, P., Grevesse, N., Asplund, M., et al. 2015b, A&A, 573, A25

Seaton, M. J. 1979, MNRAS, 187, 73P

Sen, K., Langer, N., Marchant, P., et al. 2022, A&A, 659, A98

Sen, K., Langer, N., Pauli, D., et al. 2023, A&A, 672, A198

Shao, Y. & Li, X.-D. 2014, ApJ, 796, 37

Shao, Y. & Li, X.-D. 2016, ApJ, 833, 108

Shara, M. M., Crawford, S. M., Vanbeveren, D., et al. 2020, Monthly Notices of the Royal Astronomical Society, 492, 4430

Shenar, T., Bodensteiner, J., Abdul-Masih, M., et al. 2020a, A&A, 639, L6

Shenar, T., Gilkis, A., Vink, J. S., Sana, H., & Sander, A. A. C. 2020b, A&A, 634, A79

Shenar, T., Hainich, R., Todt, H., et al. 2018, A&A, 616, A103

Shenar, T., Hainich, R., Todt, H., et al. 2016, A&A, 591, A22

Shenar, T., Hamann, W. R., & Todt, H. 2014, A&A, 562, A118

Shenar, T., Oskinova, L., Hamann, W. R., et al. 2015, ApJ, 809, 135

Shenar, T., Sablowski, D. P., Hainich, R., et al. 2019, A&A, 627, A151

Shenar, T., Sablowski, D. P., Hainich, R., et al. 2020c, A&A, 641, C2

Shenar, T., Wade, G. A., Marchant, P., et al. 2023, Science, 381, 761

Simón-Díaz, S. & Herrero, A. 2014, A&A, 562, A135

Smartt, S. J. 2009, ARA&A, 47, 63

Smith, N. 2014, ARA&A, 52, 487

Soker, N. 2000, A&A, 357, 557

Sota, A., Maíz Apellániz, J., Morrell, N. I., et al. 2014, ApJS, 211, 10

Sota, A., Maíz Apellániz, J., Walborn, N. R., et al. 2011, ApJS, 193, 24

Southworth, J. & Bowman, D. M. 2022, MNRAS, 513, 3191

Spruit, H. C. 2002, A&A, 381, 923

St-Louis, N., Moffat, A. F. J., Marchenko, S., & Pittard, J. M. 2005, ApJ, 628, 953

Stanway, E. R. & Eldridge, J. J. 2018, MNRAS, 479, 75

Steidel, C. C., Giavalisco, M., Dickinson, M., & Adelberger, K. L. 1996, AJ, 112, 352

Sukhbold, T., Ertl, T., Woosley, S. E., Brown, J. M., & Janka, H. T. 2016, ApJ, 821, 38

Tanvir, N. R., Le Floc'h, E., Christensen, L., et al. 2021, Experimental Astronomy, 52, 219

Tatton, B. L., van Loon, J. T., Cioni, M. R. L., et al. 2021, MNRAS, 504, 2983

Tauris, T. M., Kramer, M., Freire, P. C. C., et al. 2017, ApJ, 846, 170

Tauris, T. M. & van den Heuvel, E. P. J. 2006, in Compact stellar X-ray sources, Vol. 39, 623–665

Tauris, T. M. & van den Heuvel, E. P. J. 2023, Physics of Binary Star Evolution. From Stars to X-ray Binaries and Gravitational Wave Sources

Tenorio-Tagle, G. & Bodenheimer, P. 1988, ARA&A, 26, 145

Thielemann, F. K., Arcones, A., Käppeli, R., et al. 2011, Progress in Particle and Nuclear Physics, 66, 346

Todt, H., Kniazev, A. Y., Gvaramadze, V. V., et al. 2015a, in Astronomical Society of the Pacific Conference Series, Vol. 493, 19th European Workshop on White Dwarfs, ed. P. Dufour, P. Bergeron, & G. Fontaine, 539

Todt, H., Sander, A., Hainich, R., et al. 2015b, A&A, 579, A75

Tramper, F., Sana, H., & de Koter, A. 2016, ApJ, 833, 133

Trundle, C., Dufton, P. L., Hunter, I., et al. 2007, A&A, 471, 625

Udalski, A., Szymański, M. K., & Szymański, G. 2015, Acta Astron., 65, 1

Vanbeveren, D. 1991, A&A, 252, 159

Vanbeveren, D. & Conti, P. S. 1980, A&A, 88, 230

Vanbeveren, D., De Loore, C., & Van Rensbergen, W. 1998, A&A Rev., 9, 63

Vanbeveren, D., Mennekens, N., Shara, M. M., & Moffat, A. F. J. 2018, A&A, 615, A65

Vanbeveren, D., Mennekens, N., Van Rensbergen, W., & De Loore, C. 2013, A&A, 552, A105

Vanbeveren, D., Van Bever, J., & Belkus, H. 2007, ApJ, 662, L107

Venn, K. A. 1999, ApJ, 518, 405

Vernet, J., Dekker, H., D'Odorico, S., et al. 2011, A&A, 536, A105

Vidaña, I. 2018, European Physical Journal Plus, 133, 445

Vigna-Gómez, A., MacLeod, M., Neijssel, C. J., et al. 2020, PASA, 37, e038

Villaseñor, J. I., Lennon, D. J., Picco, A., et al. 2023, MNRAS, 525, 5121

Vinciguerra, S., Neijssel, C. J., Vigna-Gómez, A., et al. 2020, MNRAS, 498, 4705

Vink, J. S. 2006, in ASP Conf. Ser. 353: Stellar Evolution at Low Metallicity: Mass Loss, Explosions, Cosmology, ed. H. J. G. L. M. Lamers, N. Langer, T. Nugis, & K. Annuk (San Francisco: Astronomical Society of the Pacific), 113

Vink, J. S. 2017, A&A, 607, L8

Vink, J. S., de Koter, A., & Lamers, H. J. G. L. M. 2000, A&A, 362, 295

Vink, J. S., de Koter, A., & Lamers, H. J. G. L. M. 2001, A&A, 369, 574

Vink, J. S., Mehner, A., Crowther, P. A., et al. 2023, A&A, 675, A154

Vink, J. S. & Sander, A. A. C. 2021, Monthly Notices of the Royal Astronomical Society, 504, 2051

von Zeipel, H. 1924, MNRAS, 84, 665

Vos, J., Østensen, R. H., Marchant, P., & Van Winckel, H. 2015, A&A, 579, A49

Walborn, N. R. 1978, ApJ, 224, L133

Walborn, N. R., Howarth, I. D., Lennon, D. J., et al. 2002, AJ, 123, 2754

Walborn, N. R., Lennon, D. J., Heap, S. R., et al. 2000, PASP, 112, 1243

Walborn, N. R., Morrell, N. I., Howarth, I. D., et al. 2004, ApJ, 608, 1028

Walborn, N. R., Sana, H., Simón-Díaz, S., et al. 2014, A&A, 564, A40

Wang, C., Langer, N., Schootemeijer, A., et al. 2020, ApJ, 888, L12

Wang, L., Gies, D. R., Peters, G. J., et al. 2021, AJ, 161, 248

Weaver, R., McCray, R., Castor, J., Shapiro, P., & Moore, R. 1977, ApJ, 218, 377

Weidner, C. & Vink, J. S. 2010, A&A, 524, A98

Weisskopf, M. C., Tananbaum, H. D., Van Speybroeck, L. P., & O'Dell, S. L. 2000, in Society of Photo-Optical Instrumentation Engineers (SPIE) Conference Series, Vol. 4012, X-Ray Optics, Instruments, and Missions III, ed. J. E. Truemper & B. Aschenbach, 2–16

Weizsäcker, C. v. 1937, Physikalische Zeitschrift, 38, 176

Weizsäcker, F. v. 1938, Physikalische Zeitschrift, 39, 633

Wellstein, S. & Langer, N. 1999, A&A, 350, 148

Westerlund, B. E. 1997, The Magellanic Clouds

Wilson, O. C. 1941, ApJ, 93, 29

Wilson, R. E. 1990, ApJ, 356, 613

Wright, J. T. & Eastman, J. D. 2014, PASP, 126, 838

Yoon, S.-C. 2017, MNRAS, 470, 3970

Yoon, S.-C. & Cantiello, M. 2010, ApJ, 717, L62

Yorke, H. W., Tenorio-Tagle, G., Bodenheimer, P., & Rozyczka, M. 1989, A&A, 216, 207

Yungelson, L., Kuranov, A., Postnov, K., et al. 2024, arXiv e-prints, arXiv:2401.00802

Zacharias, N., Finch, C. T., Girard, T. M., et al. 2013, AJ, 145, 44

Zahn, J. P. 1975, A&A, 41, 329

Zahn, J. P. 1977, A&A, 57, 383

Zahn, J. P., Ranc, C., & Morel, P. 2010, A&A, 517, A7

Acknowledgements

I am incredibly grateful to my supervisors, Prof. **Lidia Oksinova** and Prof. **Wolf-Rainer Hamann**, for their unwavering support and guidance throughout my PhD journey. Prof. Oksinova's encouragement and kind words which already in the early days gave me the confidence to share my research on international conferences and to apply for numerous observing programs. Prof. Hamann's patience and expertise, especially with the PoWR code and his willingness to answer my countless questions were invaluable of this research and helped me to become the person I am today.

Special thanks to my office colleague, **Sabela Reyero Serantes**, for her relentless support. She was a constant source of encouragement, a patient ear for my frustrations, and always open to help with any kind of problems.

My sincere appreciation extends to my colleagues Dr. **Helge Todt**, Dr. **Andreas Sander**, Dr. **Varsha Ramachandran**, and Dr. **Tomer Shenar**. Their assistance with the many insightful discussions during seminars or even spontaneous via zoom, helped me so many times to get focussed and do not lose track of the goal. I am also grateful to the other members of the research group who have offered help and stimulating discussions. Beyond that, I am so greatful for all the funny times we had during coffee breaks or seminars.

A big thank you to **Matthew Rickard**, my colleague from UCL, for our fantastic collaboration on NGC 346 SSN 7. It was truly enjoyable to delve into the details and make these fascinating discoveries together.

A special thanks goes to Mrs. **Andrea Brockhaus**, the backbone of the astronomy department. I am so thankfull for all your tireless help, patience, and last minute solutions for all the burocratic problems I encountered through the last years.

Finally, my deepest gratitude goes to **my parents** for their unquestioned love and support throughout my academic career. Their constant encouragement, no matter how small the accomplishment, fueled my passion for science and helped me reach this point.

Lastly, I also extend my thanks to Prof. **Norbert Langer** and Dr. **Götz Gräfener**, who supervised my Bachelor's and Master's studies at Bonn. Without you I would never have developed such a passion for massive stars and would not have been here.

Many thanks to all of you for creating an environment that feels like a second family. Every time we meet at conferences, it truly feels like a family reunion. Without each one of you, this work would not have been possible.

Appendix A

Appendix A.1: RV determination

To determine the RV shift of a star during a specific phase we use a MCMC approach. In our code we use the synthetic spectra obtained from the spectral analysis and shift them until the shifted synthetic spectrum best matches the observed spectrum. In our procedure, we use the method described in the `emcee` documentation[1] with small adjustments such that it fulfills our needs.

The probability function, a measure of how well the synthetic spectrum fits the observed one, consists of the combination of a prior function (i.e., a function that limits the parameter space to reasonable numbers) and a likelihood function. Uniform distributions are used as prior functions to avoid biases towards specific RV shifts,

$$\log p_{\mathrm{prior}}(v_1, v_2, f) = \begin{cases} & \text{if } -50\,\mathrm{km\,s^{-1}} < v_1 < 600\,\mathrm{km\,s^{-1}} \\ 0 & \text{and } -600\,\mathrm{km\,s^{-1}} < v_2 < 50\,\mathrm{km\,s^{-1}} \\ & \text{and } -\infty < \log f < 1.0 \\ -\infty & \text{otherwise.} \end{cases} \tag{A.1.1}$$

For the likelihood function we use the least square function and assume that the variance is underestimated by some fractional amount f,

$$\log p_{\mathrm{likelihood}} = -\frac{1}{2} \sum_n \frac{(y_n - y_{\mathrm{model},n})^2}{s_n^2} + \log 2\pi s_n^2, \tag{A.1.2}$$

where

$$s_n^2 = \sigma_n^2 + f(y_{\mathrm{model},n})^2. \tag{A.1.3}$$

Using the above-mentioned functions, the probability function can be expressed as

$$\log P = \log p_{\mathrm{prior}} + \log p_{\mathrm{likelihood}}. \tag{A.1.4}$$

As recommended in the `emcee` documentation[1] the starting values are initialized as tiny Gaussian balls around $v_1 = 300\,\mathrm{km\,s^{-1}}$, $v_2 = -300\,\mathrm{km\,s^{-1}}$ and $\log f = 0.0$. To ensure a good converged posterior distribution, 32 walkers (i.e., individual Makrov chains) are used and each one is iterated for 5000 steps. We cut off the first 1000 steps to ensure that the chains are "burned-in" such that the remaining distribution resembles the posterior distribution. The uncertainties are based on the 16th, 50th, and 84th percentiles of the samples, corresponding to approximately 1σ deviation. To make these values readable for the PHOEBE code, which requires symmetric error margins, only the larger uncertainty is used.

For each of the components, we take the mean value of the RVs obtained from several absorption lines. The primary is causing most of the He II lines seen in the composite spectrum. Only the He II λ4025 line shows contributions from both components. The secondary contributes the majority of the observed He I absorption lines, but in many of them also the primary can be seen. We use the He II λ4025 line to fit both components and to obtain their RVs simultaneously, such that this line can be used as a cross-check to see if these fits are in agreement with the other lines that are purely from the primary, like He II λ4200, or the lines that are associated with the secondary. This gives us confidence that the RVs of the secondary obtained with this method are trustworthy. The obtained RVs of the primary and secondary can be found in Table A.1.1 and A.1.2.

This fitting procedure turns out to work well even for line complexes with contributions from both stars. Figure A.1.1 shows one of our fits of the He I λ3819 region. The He I λ3819 absorption line is present in both spectra. The absorption line of the primary is shifted redwards and the rotationally broadened absorption line of the secondary is shifted bluewards. This complex is blended by the blueshifted He II λ3813 absorption line of the primary.

[1] https://emcee.readthedocs.io

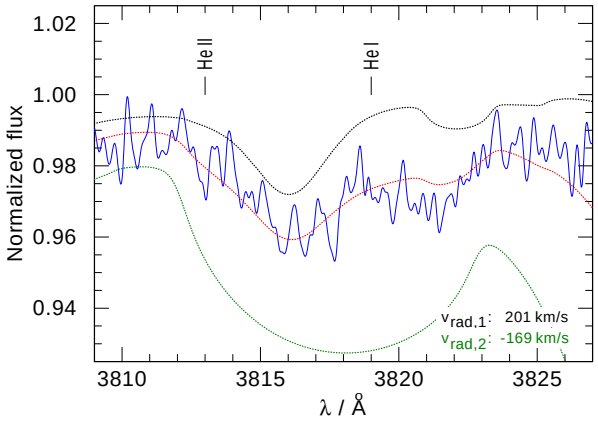

Fig. A.1.1. Radial-velocity fit of the synthetic spectrum to the observed He II λ3813 and He I λ3819 absorption lines of the UVES spectrum with ID 10 (Table 2.2.1). The observed spectrum is shown as a solid blue line, our best fitting model as a dotted red line, the unweighted synthetic spectrum of the primary as a dashed black line, and the unweighted spectrum of the secondary as a dotted green line. The observed spectrum is convolved with a Gaussian with a FWHM = 0.2 Å and is corrected for the velocity of the SMC and the barycentric motion. The line identification marks correspond to the wavelengths of the absorption lines in the rest frame.

Table A.1.1. RVs of the primary determined from different spectral lines.

spectral ID	He I λ3819 [a] [km s^{-1}]	He I λ3935 [km s^{-1}]	He II λ4025 [b] [km s^{-1}]	N IV λ4058 [km s^{-1}]	He II λ4200 [km s^{-1}]	mean value [c] [km s^{-1}]
5	114 ± 63	117 ± 22	120 ± 8	103 ± 7	105 ± 4	112 ± 14
6	—	229 ± 26	236 ± 8	217 ± 21	210 ± 4	223 ± 9
7	48 ± 63	36 ± 47	53 ± 8	46 ± 9	55 ± 8	47 ± 16
8	140 ± 13	115 ± 34	134 ± 11	117 ± 18	122 ± 4	126 ± 8
9	145 ± 59	—	153 ± 10	134 ± 22	131 ± 5	141 ± 16
10	201 ± 53	215 ± 25	209 ± 11	195 ± 18	183 ± 8	201 ± 13
11	223 ± 32	212 ± 26	214 ± 9	192 ± 13	196 ± 4	207 ± 9
12	162 ± 18	167 ± 32	131 ± 14	137 ± 45	144 ± 8	148 ± 12

[a] The He I λ3819 is present in the primary and secondary spectrum. We note that the observed He I λ3819 line also contains the He II λ3813 line from the primary. [b] The He II λ4025 line has a strong contribution from the secondary. [c] The mean value is calculated as $\sum_{i=1}^{i=n} \mathrm{RV}_i/n$ where RV_i is the RV of line i and n is the total number of lines used. The errors of the mean values are calculated via Gaussian error propagation.

This method requires sufficiently high S/N observations. The MCMC code struggles with some of the He I lines that are associated with the secondary. In most cases, the problems emerge when the depth of the absorption lines is of the same order as the noise (i.e., the UVES spectra have a S/N ∼ 25). Moreover, some of the UVES spectra show a wavy pattern from the echelle orders. In some cases, these waves overlap with absorption lines, making an accurate RV determination almost impossible. All fits are inspected by eye and the observations that show the aforementioned issues are discarded from our analysis.

Table A.1.2. RVs of the secondary determined from different spectral lines.

spectral ID	He I λ3819 [a] [km s^{-1}]	He II λ4025 [b] [km s^{-1}]	He I λ4143 [km s^{-1}]	He I λ4387 [km s^{-1}]	He I λ4471 [km s^{-1}]	mean value[c] [km s^{-1}]
5	-88 ± 29	-122 ± 31	—	-117 ± 20	-113 ± 18	-110 ± 13
6	—	-164 ± 22	—	-198 ± 52	-152 ± 24	-171 ± 21
7	-41 ± 83	-33 ± 23	—	-32 ± 35	-35 ± 31	-35 ± 25
8	-137 ± 89	-79 ± 41	-110 ± 55	—	-91 ± 24	-104 ± 29
9	-108 ± 112	—	-95 ± 88	-81 ± 37	-97 ± 24	-95 ± 37
10	-169 ± 52	-199 ± 43	—	—	—	-184 ± 34
11	-194 ± 34	-151 ± 26	-213 ± 121	—	—	-186 ± 43
12	-149 ± 42	-125 ± 79	-146 ± 68	-130 ± 66	132 ± 42	-132 ± 27

Same footnotes as in Table A.1.1.

Appendix A.2: Additional figures

Appendix A.2.1: Additional optical N III and N V lines

Figure A.2.1 shows N III and N V lines in our spectrum with the highest S/N, the X-SHOOTER spectrum (ID 5 in Table 2.2.1, S/N ~ 100). These lines are very weak and therefore barely visible in the spectrum. N V λ4604 is marginally in absorption, while N III $\lambda\lambda$4634, 4641 appears in slight emission. Although nearly hidden in the noise, these weak features are reproduced by our final model (red-dotted).

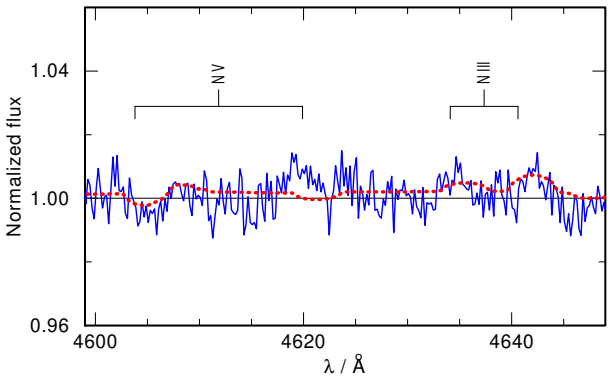

Fig. A.2.1. Same as Fig. 2.4.4, but now zoomed on optical N III and N V lines.

Appendix A.2.2: Optical O IV and N IV lines

Walborn et al. (2004) suggest to use the optical O IV multiplets around 3400 Å and the N IV absorption lines at wavelengths 3463 Å, 3478 Å, 3483 Å and 3485 Å to derive the N and O abundances in hot massive stars. Luckily, the X-SHOOTER spectrum extends to such short wavelengths. Figure A.2.2 shows that the N IV lines of our final model are in agreement with the observation. However, for the O IV multiplet at wavelengths 3403 Å and 3414 Å the synthetic spectrum is in emission and not in absorption as observed. For the O IV λ3414 Å line, there is an ISM contribution from Co I that explains the observed absorption. Regarding the O IV 3403 Å line, we are not aware of any blending lines. However, this particular line is formed close to the onset of the wind and is sensitive to different details within the wind (e.g., temperature stratification, wind velocity law). As the other O IV multiplet $\lambda\lambda$3381 Å – 3389 Å can be well reproduced, we trust our determined O abundance, which is supported by other absorption lines in the UV.

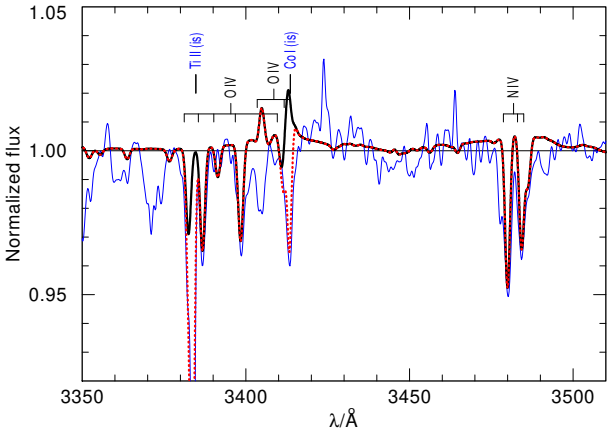

Fig. A.2.2. Observed (X-SHOOTER spectrum; ID 5 in Table 2.2.1) and synthetic spectra of the region around 3400 Å showing the O IV and N IV lines. The observed spectrum (blue) shows clear indications of ISM absorption lines. The black line is the synthetic spectrum without a contribution of ISM lines. The spectrum with the modeled ISM lines is shown as red dotted line. The interstellar absorption arise in the Galactic foreground and in the SMC.

Appendix A.2.3: Additional wind lines

As main diagnostic wind lines, the C IV resonance doublet in the UV and the Hα line in the optical are used. However, the He II λ1640 in the UV and the He II λ4868 in the optical are also sensitive to the stellar wind and are taken into account when adjusting the stellar parameters of our synthetic model. These lines are shown in Fig. C.4.4.

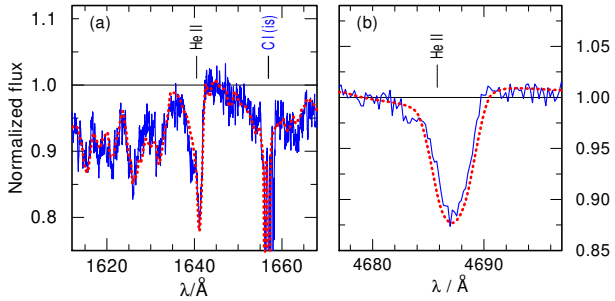

Fig. A.2.3. Observed (blue) and synthetic (red) He II lines that are sensitive to the wind parameters. The sharp interstellar absorptions arise in the Galactic foreground and in the SMC, and are also modeled with their respective RV shifts. (a) He II λ1640 line in the COS spectrum (ID 2 in Table 2.2.1). (b) He II λ4868 line in the X-SHOOTER spectrum (ID 5 in Table 2.2.1).

Appendix A.2.4: Synthetic spectrum calculated with the stellar parameters from the MESA model

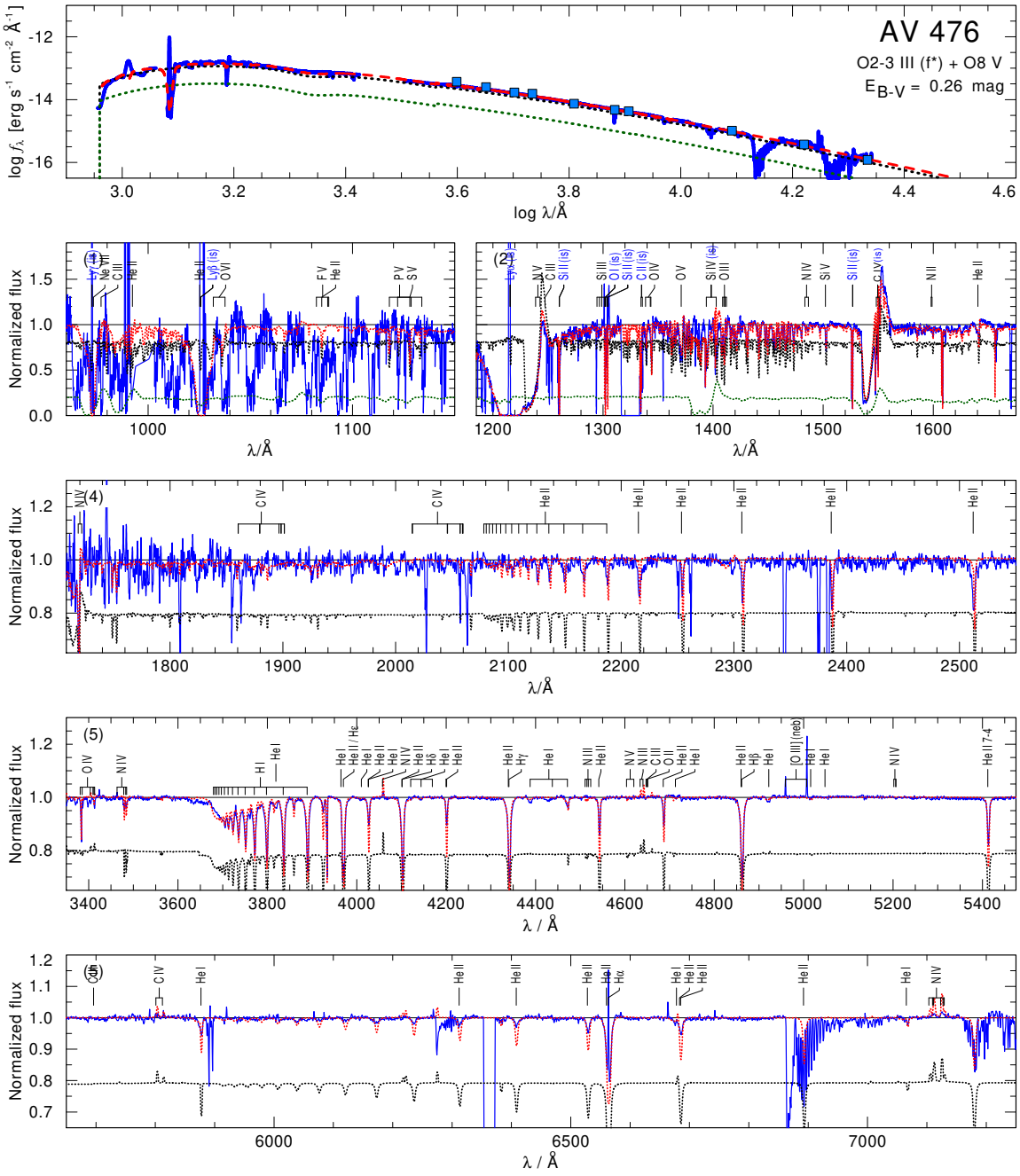

Fig. A.2.4. Spectral model calculated with the stellar parameters of the most favored binary evolutionary model. The plots and line styles are the same as in Figs. 2.4.5 and 2.4.6. In this plot we use a distance of $d = 49$ kpc to compensate the used lower luminosities of the binary components. This plot demonstrates that the predicted surface abundances of the binary evolutionary models are unable to reproduce the observed spectrum. The nitrogen abundance in this model is too strong as it overestimates all optical N IV lines and also predicts unseen N V absorption. The reduced hydrogen abundance leads to an increased helium abundance. This enrichment would produce too deep He II lines in the spectrum of the primary.

Appendix B

Appendix B.1: Additional tables

Table B.1.1. Radial velocities of different lines associated with the primary.

MJD	N IV $\lambda\lambda$ 3478 – 3485 [km s^{-1}]	N IV4058 [km s^{-1}]	N IV6381 [km s^{-1}]	N IV $\lambda\lambda$ 7103 – 7129 [km s^{-1}]	N V $\lambda\lambda$ 4604, 4620 [km s^{-1}]	He II6683$^{(a)}$ [km s^{-1}]	mean RV$^{(b)}$ [km s^{-1}]
52249.01198	7 ± 6	18 ± 7	9 ± 15	—	—	—	11 ± 10
53277.25739	—	56 ± 7	—	—	—	—	56 ± 7
53277.25939	—	51 ± 7	—	—	—	—	51 ± 7
53277.26022	—	42 ± 6	—	—	—	—	42 ± 6
53277.28112	—	48 ± 6	—	—	—	—	48 ± 6
53280.19821	—	—	—	—	18 ± 15	—	18 ± 15
53292.06195	—	—	—	—	−57 ± 15	—	−57 ± 15
57611.32930	—	—	97 ± 15	100 ± 15	—	96 ± 13	98 ± 14
57613.24630	—	—	−74 ± 15	−75 ± 15	—	−86 ± 14	−78 ± 15
57613.28829	—	—	−82 ± 15	−75 ± 15	—	−73 ± 13	−77 ± 14
57617.23463	—	—	54 ± 15	61 ± 14	—	51 ± 8	55 ± 13
57618.10327	—	—	84 ± 15	61 ± 15	—	70 ± 8	72 ± 13
57620.14865	—	—	39 ± 15	38 ± 14	—	31 ± 8	36 ± 13
57620.19042	—	—	40 ± 15	45 ± 14	—	32 ± 8	39 ± 13
57620.23262	—	—	45 ± 15	46 ± 8	—	41 ± 8	43 ± 11
57621.20640	—	—	62 ± 15	68 ± 15	—	62 ± 8	64 ± 13
57621.24834	—	—	55 ± 15	45 ± 10	—	48 ± 8	49 ± 11
57622.14718	—	—	−81 ± 15	−80 ± 15	—	−94 ± 9	−85 ± 13
59216.11133	98 ± 6	97 ± 6	82 ± 22	93 ± 22	92 ± 16	95 ± 8	92 ± 15

Notes. $^{(a)}$ The line shows a clear but distinguishable contribution of the secondary. It can be used as a cross-check for the quality and self-consistency of the secondary's RV fit.

Table B.1.2. Radial velocities of different lines associated with the secondary.

MJD	He I 4471 [km s^{-1}]	He I 4713 [km s^{-1}]	He II 6683$^{(a)}$ [km s^{-1}]	C IV $\lambda\lambda$ 5801, 5812$^{(a)}$ [km s^{-1}]	mean RV$^{(b)}$ [km s^{-1}]
52249.01198	18 ± 9	6 ± 31	—	7 ± 16	10 ± 21
53277.25739	−34 ± 7	—	—	—	−34 ± 7
53277.25939	−32 ± 9	—	—	—	−32 ± 9
53277.26022	−39 ± 7	—	—	—	−39 ± 7
53277.28112	−39 ± 7	—	—	—	−39 ± 7
53280.19821	—	−12 ± 29	—	—	−12 ± 29
53292.06195	—	41 ± 27	—	—	41 ± 27
57611.32930	—	−48 ± 22	−62 ± 20	−60 ± 13	−57 ± 19
57613.24630	—	57 ± 28	69 ± 25	77 ± 14	67 ± 23
57613.28829	—	71 ± 21	71 ± 19	77 ± 23	73 ± 21
57617.23463	—	−19 ± 20	−24 ± 23	−22 ± 14	−22 ± 19
57618.10327	—	−30 ± 25	−35 ± 23	−38 ± 17	−34 ± 22
57620.14865	—	−34 ± 25	−32 ± 23	−35 ± 16	−34 ± 22
57620.19042	—	−32 ± 23	−40 ± 23	−29 ± 14	−34 ± 22
57620.23262	—	−32 ± 18	−31 ± 31	−34 ± 14	−32 ± 22
57621.20640	—	−21 ± 26	−29 ± 22	−22 ± 16	−24 ± 22
57621.24834	—	−28 ± 25	−30 ± 20	−31 ± 16	−30 ± 20
57622.14718	—	71 ± 22	70 ± 25	75 ± 16	72 ± 21
59216.11133	−55 ± 8	−57 ± 25	−55 ± 25	−52 ± 11	−55 ± 19

Notes. $^{(a)}$ The line shows a clear but distinguishable contribution of the primary.

Table B.1.3. List of used lines. Includes which component the lines are attributed to based on relative position to other lines and shifts at different epochs.

Line	Wavelength (Å)	Components source and description
O VI	1031.9, 1037.6	Absorption, predominately from primary
P V	1118.0	Both components show absorption
P V	1128.0	Both components show absorption
C IV	1169.0	Both components show absorption
C III	1175.3	Secondary absorption
N V	1238.8, 1242.8 doublet	Resonance wind lines with absorption and emission for both
O IV	1338.6, 1343.0, 1343.5 triplet	Both components show absorption
O V	1371.0	Both components show absorption
O III	1408.6, 1409.8, 1410.8, 1410.9, 1412.1	Both components show absorption
Fe V-VI	Range ∼ 1412 – 1475	Iron forest lines, both components show absorption
N IV	1483.3, 1486.5	Both components show absorption
Si V	1502.0	Both components show absorption
C IV	1548.2, 1550.8 doublet	Resonant wind line showing contribution of both components
He II	1640.5	Primary P-Cygni with emission, secondary absorption
N IV	3478.7, 3483.0, 3484.9 triplet	Both components show absorption
He I	3964.7	Primary absorption
He II	3970.1	Both components show absorption
He II	4025.6	Overlapping with He I4026.2 for both primary and secondary
He I	4026.2	Overlapping with He II4025.6 for both primary and secondary
N IV	4057.8	Primary emission
He II	4100.7	Both components show absorption
He II	4199.9	Both components show absorption
He II	4338.7	Both components show absorption
He I	4471.5	Secondary absorption
He II	4541.6	Both components show absorption
N V	4603.8, 4619.9 doublet	Absorption, predominately from primary
N III	4634.1, 4640.6 doublet	Both components show emission
O II	4650.0	Primary emission, overlapped by primary He II λ4686Å emission
He II	4685.8	Primary emission, secondary absorption
He I	4713.2	Secondary absorption
He II	4859.3	Both components show absorption
He I	4921.9	Secondary absorption
He I	5015.7	Absorption, predominately secondary
He II	5411.5	Both components show absorption
C IV	5801.3, 5812.0 doublet	Primary emission, secondary absorption
He I	5875.4, 5875.5, 5875.8 triplet	Both components show absorption
He I	6170.7	Both components show absorption
N IV	6212.4, 6215.5, 6219.9 triplet	No observations. Model of primary shows emission
He I	6233.8	Both components show absorption
N IV	6380.8	Primary absorption
He II	6527.1	Both components show absorption
He II	6560.1	Primary emission, secondary absorption
He II	6678.1, 6679.6 doublet	Secondary absorption
He II	6683.2	Both components show absorption
He II	7065.3	Absorption, predominately Secondary
N IV	7102−7129 multiplet	Emission, predominately from primary

Appendix B.2: Light curve modelling with PHOEBE

Although it is in the survey region of the Optical Gravitational Lensing Experiment (OGLE, Udalski et al. 2015) catalogue, to date no light curve of this object has been reported. In addition, the resolution of the Transiting Exoplanet Survey Satellite (TESS) is 21″ pixel^{-1}, not fine enough to disentangle the light curve of our target from the other O stars in NGC 346. To demonstrate if detectable photometric variations based on our results are expected at all, we employed the PHOEBE code (used in Sect. 3.3.3.2) to create a synthetic light curve.

Typically light curves are observed in the optical. Hence, we decided to create the synthetic light curve (shown in Figure B.2.1) in the Johnson V band. In the PHOEBE model we used the stellar parameters of the binary components obtained from our spectroscopic analysis (see Sect. 3.4.1) as input parameters. Furthermore, we assume that gravitational darkening can be approximated by a power law with a coefficient of $\beta_{\rm grav} = 1$, as typically used for hot stars with radiative envelopes. The atmospheres of both components are approximated by a black body, when compared to the SED of our atmospheric model it is a valid approximation for the V-band flux. Limb darkening is modelled by using a quadratic approximation and using coefficients $a_1 = 0.2694$ and $b_1 = -0.003$ for the primary and $a_2 = 0.1751$ and $b_2 = 0.0871$ for the secondary, obtained from the emergent flux distribution of our stellar atmosphere models. The effect of reflections and resulting heating in the binary is modelled using the build in the Horvat scheme that includes Lambert scattering as well as the reflection scheme of Wilson (1990). It is assumed that 90% of the incident flux will be reflected.

For a better understanding on how the different photometric variations are linked to the orbital configuration of the binary, we depict the orbital configurations of the stars in the lower part of Fig. B.2.1. It is evident that the expected maximum photometric variation of the binary components is 18 mmag. The shape of the light curve is only caused by ellipsoidal variability and not by eclipses.

Given the expected low variability, we conclude that only the upcoming powerful telescopes, such as the ELT, will be able to detect this kind of variability. Hence, we can say that our derived low inclination angle is consistent with the lack of published light curve data.

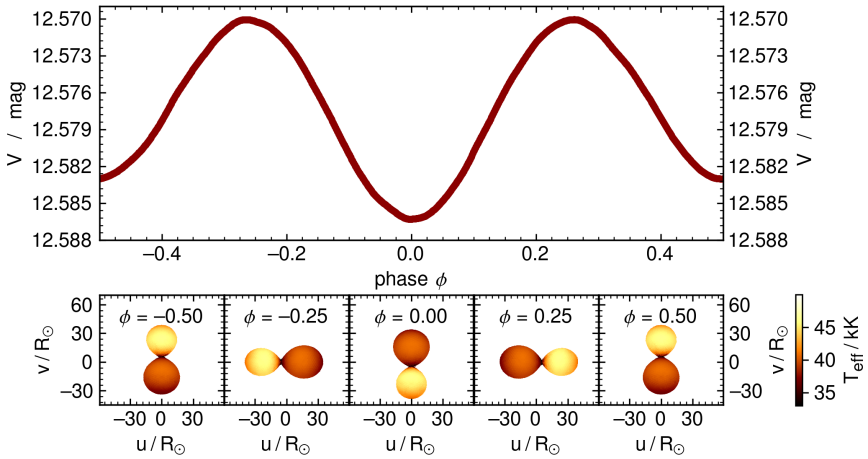

Fig. B.2.1. Synthetic predicted light curves of SSN 7 for an inclination angle of $i = 16^\circ$ and the orbital configuration of the binary components in the plane of sky at different phases. *Upper panel:* Phased synthetic light curve in the Johnson V band. *Lower panel:* Orbital configuration of the binary components at phases $\phi = -0.5, -0.25, 0.0, 0.25$, and 0.5. The models are colour-coded by effective temperature, taking into account the physical effect mentioned in the text.

Appendix C

Appendix C.1: Spectroscopic and photometric data

The information on all observed spectra used in this work is given in Table C.1.1. All spectra are in a reduced state from the individual observatories pipeline. Apart from the UVES spectrum, all other spectra analyzed in this work had been corrected for barycentric motion by the automated extraction pipeline. For the UVES spectrum we had to calculate this correction ourselves. With the help of the tool from Wright & Eastman (2014) we obtained $v_{\rm bary} = -10.6\,{\rm km\,s^{-1}}$. A summary of the estimated RVs and the calculated orbital phases of the individual observed spectra that are used in our analysis are listed in Table C.1.2. The photometric data employed for the SED fitting are listed in Table C.1.3.

Table C.1.1. Spectroscopic observations of AzV 14.

Instrument	Wavelength [Å]	Resolving power	Exposure time [s]	S/N	MJD[(a)] [d]	Program ID	PI
FUSE	950 – 1150	20 000	6770	7.4	51726.5778	p1175301000	J. B. Hutching
HST/FOS	1140 – 1606	250	480	≈ 20	49985.5561	Y25U0101T	C. Robert
HST/STIS	1140 – 1740	45 800	2767	≈ 66	58981.1081	15629	L. Mahy
UVES	3731 – 4999	≈ 41 000	2400	47.3	52180.0263	67.D-0238(A)	P. Crowther
X-Shooter (2020)	3000 – 24 800	≳ 5500	≈ 1000	≳ 100	59156.1955	106.211Z	J. S. Vink
X-Shooter (2022)	3000 – 24 800	≳ 5500	900	≳ 90	59847.3603	109.22V0.001	D. Pauli

[(a)] Mid-exposure time in HJD − 2400000.5.

Table C.1.2. Fitted RV shifts of the binary components of AzV 14 in each spectrum. The given RVs are in addition to the RV of NGC 261 (148 km s^{-1}). The phases are calculated according to our ephemeris (see Sect. 4.4).

Instrument	Phase $\Phi^{(b)}$	RV_1 [km s^{-1}]	RV_2 [km s^{-1}]
FUSE	0.4021	62.7 ± 4.7	−95.3 ± 4.3
HST/FOS	0.1924	92.9 ± 6.2	−113 ± 6.4
HST/STIS	-0.3173	−128.6 ± 2.5	113.2 ± 2.8
UVES	-0.1315	−101.9 ± 2.6	80.5 ± 3.2
X-Shooter (2020)	-0.0302	−46.1 ± 5.8	22.3 ± 5.9
X-Shooter (2022)	-0.3625	−112.4 ± 2.6	98.6 ± 2.9

Table C.1.3. Photometry of AzV 14. The UBI photometry from Bonanos et al. (2010), V-band photometry from Meyssonnier & Azzopardi (1993), JHK photometry from the 2MASS catalog (Cutri et al. 2003), Gaia EDR3 G-band photometry (Gaia Collaboration et al. 2016, 2021), and YJ_sK_s photometry from the VMC survey (Cioni et al. 2011).

Band	Apparent magnitude [mag]
U	12.53 ± 0.03
B	13.59 ± 0.04
V	13.7
G	13.822 ± 0.003
G_{BP}	13.675 ± 0.003
G_{RP}	13.964 ± 0.004
I	13.85 ± 0.04
J	14.193 ± 0.035
H	14.301 ± 0.046
K	14.208 ± 0.067
Y	14.181 ± 0.010
J_s	14.251 ± 0.013
K_s	14.309 ± 0.008

Appendix C.2: Spectral modeling with the PoWR stellar atmosphere code

PoWR assumes that the atmosphere, including the stellar wind, is stationary, spherically symmetric, energy conserving, and in radiative equilibrium. Hot star atmospheres cannot be approximated by LTE. Instead, the equations of radiative transfer and the statistical equilibrium have to be solved consistently in the comoving frame. This is achieved by iteration with the "approximate lambda operator" technique, yielding population numbers of the individual elements.

The stellar atmosphere models which we apply here account for detailed model atoms of the elements: H, He, C, N, O, Mg, Si, P, S. The iron group elements Fe, Sc, Ti, V, Cr, Mn, Co, and Ni are treated as one generic element ("G") using a superlevel approach (see Gräfener et al. 2002). The individual abundances for each element and the considered ionization levels adopted here are listed in Table C.2.1.

To calculate the detailed synthetic spectrum we assume a depth dependent micro-turbulence velocity. In our model calculations it is assumed that the micro-turbulence velocity starts with $\zeta_{\rm ph} = 10\,{\rm km\,s^{-1}}$ in the photosphere and grows linearly with the wind velocity as $0.1\,v(r)$. The density stratification in the photosphere is calculated from the hydrostatic equations, taking the radiation pressure fully into account (Sander et al. 2015). The velocity field in the supersonic regions, is adopted as a β-law (Castor et al. 1975) with the standard exponent of $\beta = 0.8$ (Pauldrach et al. 1986).

The stellar parameters, namely effective temperature $T_{\rm eff}$, surface gravity g, wind mass-loss rate $\dot{M}$, terminal wind velocity v_∞, as well as the chemical composition, are determined by a comparison of the synthetic spectrum to the observation. The effective temperature $T_{\rm eff}$ is defined as referring to the radius where the Rosseland mean continuum optical depth is $\tau = 2/3$.

Stellar winds are inhomogeneous; this is taken into account using the approximation for optically thin clumps (micro-clumping). The clumping factor D describes by how much the density within the clumps is increased compared to a smooth wind with the same mass-loss rate (Hamann & Koesterke 1998b). For our analysis, we adopt depth-dependent clumping that starts at the sonic radius and increases outward, until a clumping factor of $D = 10$ is reached at a radius of $10\,R_*$.

Table C.2.1. Chemical elements and the ionization stages included in the PoWR models for AzV 14.

Element	Abundance [mass frac.]	Ions	Reference
H	0.7375	I, II	Asplund et al. (2005)
He	0.2605	I, II, III	$Y = 1 - X - Z$
C	21×10^{-5}	III - VI	Trundle et al. (2007)
N	3×10^{-5}	III - VI	Trundle et al. (2007)
O	113×10^{-5}	II - VII	Trundle et al. (2007)
Mg	10×10^{-5}	II - V	Trundle et al. (2007)
Si	13×10^{-5}	III - VII	Trundle et al. (2007)
P	8×10^{-7}	IV, V, VI	Scott et al. (2015a)[(a)]
S	4×10^{-5}	IV - VII	Scott et al. (2015a)[(a)]
G	35×10^{-5}	III - IX	Trundle et al. (2007) Scott et al. (2015a)[(a)]

[(a)] We scaled their solar values by a factor of 1/7 to account for the lower metallicity of the SMC.

Appendix C.3: Extraction of the TESS light curve

AzV 14 was observed with TESS, but has no automated pipeline processed light curve yet. Hence, we followed the method of Bowman et al. (2022) and extracted pixel cutouts of size 20×20 using ASTROCUT (Brasseur et al. 2019) provided by MAST[1] to extract a custom light curve and search for photometric variability. We tried differently sized aperture masks for an optimum light curve using the LIGHTCURVE software package (Lightkurve Collaboration et al. 2018). Since AzV 14 is a relatively faint target (V = 13.9 mag) for TESS and because the pixel size of TESS is 21″, the aperture mask that maximized the signal-to-noise of the variability in the light curve and minimized the contribution of contaminating stars was found to be only a single pixel. We note that the field around AzV 14 is quite crowded and that the employed TESS pixel contains several other stars. However, all stars identified by Gaia within this single neighboring pixels have $V \gtrsim 16.5$. This is three orders of magnitude fainter than our target. None of this stars is known to be variable and combined they contribute less than $< 5\%$ of the total measured flux. Pixel masks larger than a single pixel had larger percentage contamination and diminished signal from our target, thus justifying our extraction method. The background flux was estimated by calculating the median observed flux per frame whilst excluding pixels that predominantly contain stellar flux. The background flux was subtracted, and then we normalized the extracted light curve by dividing through the median flux.

TESS sector 1 data are known to be quite noisy and contain problematic systematics. For such a faint target this presented a significant challenge in extracting a reliable light curve. However, the light curves from sectors 27 and 28 are judged to be robust, and span a combined total of 50.8 d.

The variability in the combined sectors 27 and 28 of the TESS data for AzV 14 is well described as periodic. To determine the dominant periodicity we identified the highest-amplitude peak in the amplitude spectrum of the light curve. Next, we optimized the frequency and amplitude and determined uncertainties for this dominant periodicity by fitting a sinusoid to the light curve using nonlinear least-squares methods with the PERIOD04 software tool (Lenz & Breger 2005). We determined the dominant frequency to be $0.539\,69 \pm 0.000\,19\,\mathrm{d}^{-1}$, corresponding to a period of $1.852\,92 \pm 0.000\,65$ d. Yet, as demonstrated from our spectroscopic analysis (see Sect. 4.3.1), AzV 14 contains two similar massive stars. Hence, periodic sinusoidal variability in such a system implies grazing eclipses or ellipsoidal variability. In phase space, however, one expects a symmetric double wave for such variability, meaning that the true dominant frequency is $1.079\,38 \pm 0.000\,38\,\mathrm{d}^{-1}$, and thus the orbital period of the system is $P_{\mathrm{orb}} = 3.7058 \pm 0.0013$ d. The phase-folded light curve on this inferred orbital period is shown in Fig. 4.3.2. We also find this frequency to be significant in the TESS data, but it has a smaller amplitude, hence is not the dominant frequency. It is not uncommon for the (sub)harmonic of the true orbital frequency to have a larger amplitude in the amplitude spectra of (eclipsing) binary star or ellipsoidal variable light curves (see e.g., IJspeert et al. 2021; Southworth & Bowman 2022).

TESS has a low spatial resolution from its large pixel sizes, which when combined with our small aperture mask results in a relatively large scatter in the light curve. Nonetheless, it is possible to use the TESS data to constrain the inclination of the binary. In turn, this allows us to compare inclination dependent parameters, such as the projected rotation velocities to predictions of binary evolutionary models.

[1] https://archive.stsci.edu/

Appendix C.4: Additional figures

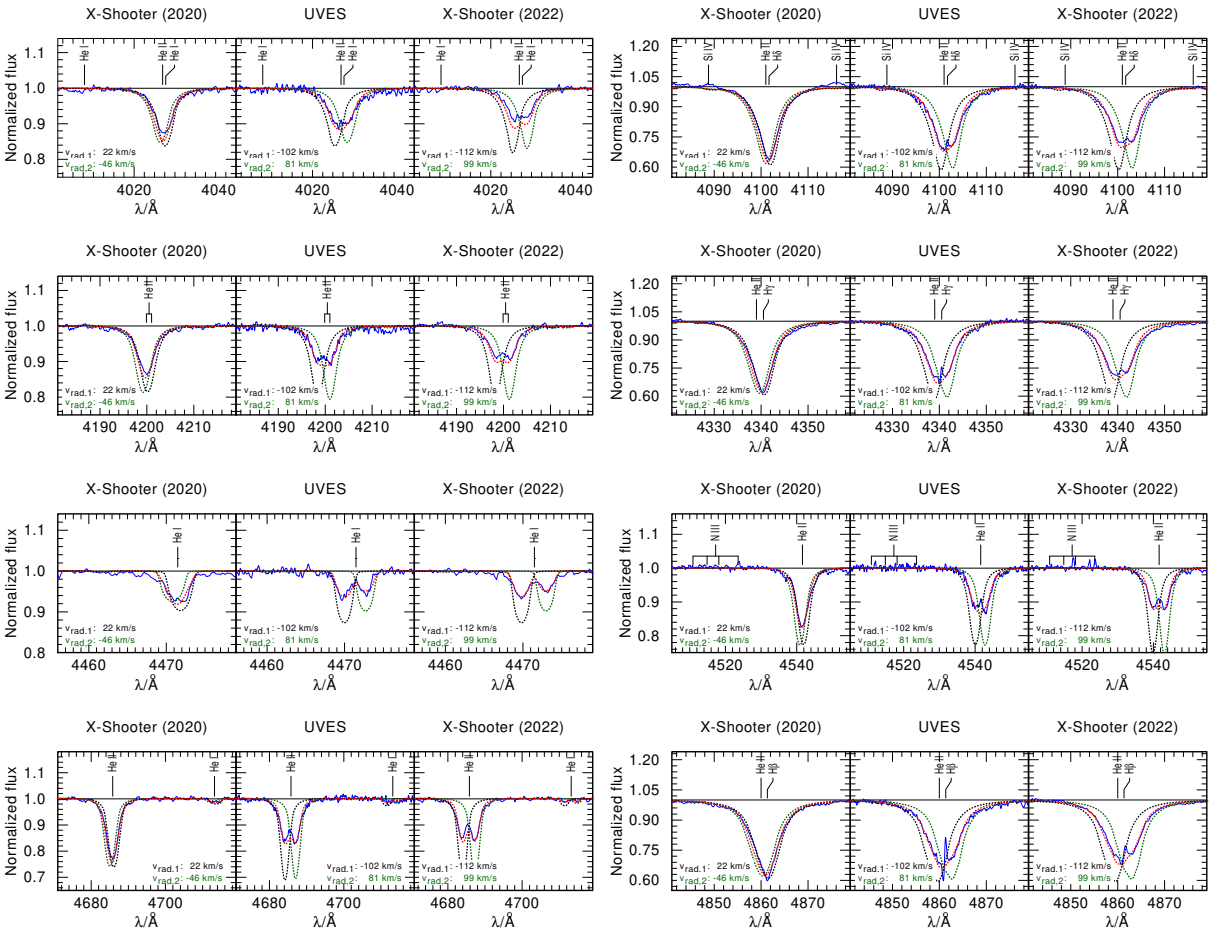

Fig. C.4.1. Hydrogen and helium lines in the two X-Shooter spectra and the UVES spectrum (blue) compared to the combined synthetic spectrum (red). The individual unweighted synthetic spectra of the primary and secondary components are represented as black dotted and green dotted lines, respectively.

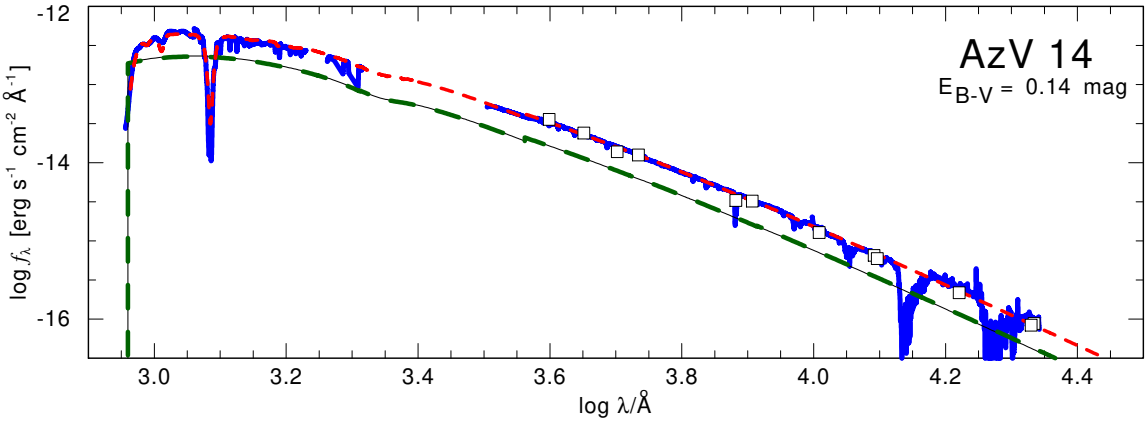

Fig. C.4.2. SED comparing flux-calibrated observations (blue lines) and photometric data (open squares) to the model SED composed of both binary components (red dashed line). The individual synthetic SEDs of the primary and the secondary are shown as thin black and thick green dashed lines, respectively. Due to their similar luminosities these curves are hard to distinguish.

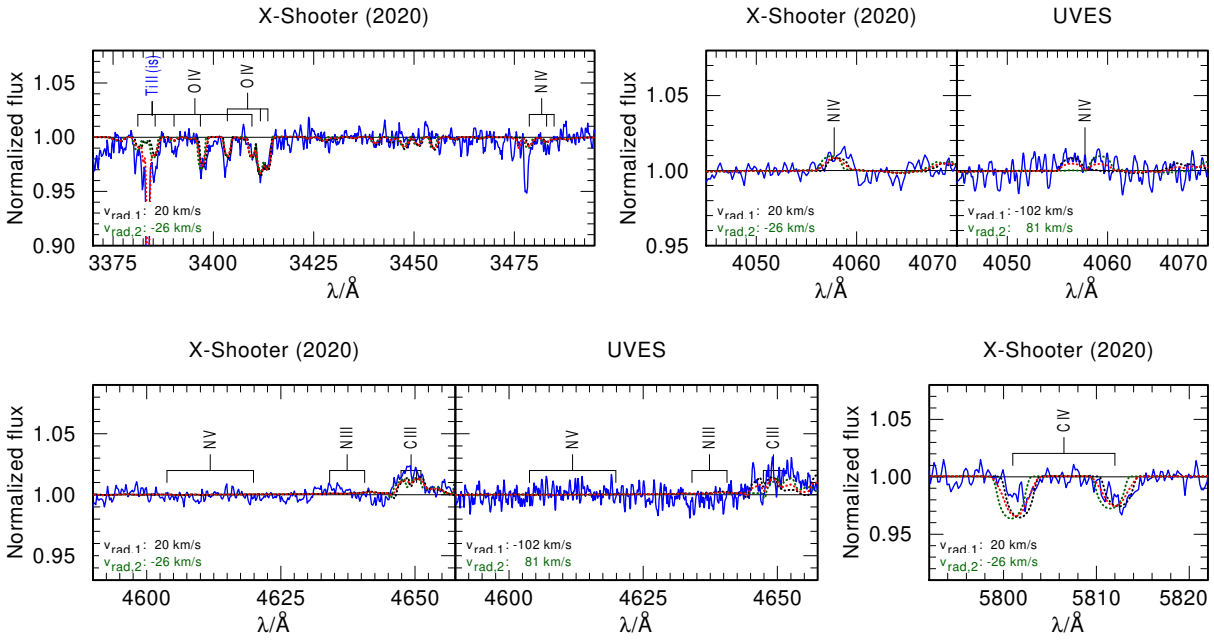

Fig. C.4.3. Close-up view of the metal lines in the X-Shooter (2020) and UVES spectra. The observed spectrum is shown as a solid blue solid line, the individual unweighted synthetic spectra of the primary and the secondary component are represented as black dotted and green dotted lines, respectively and the combined synthetic spectrum as red dashed line. In the combined synthetic spectrum ISM absorption lines, which originate from the Galactic foreground and in the SMC, are included. They are labeled as "(is)".

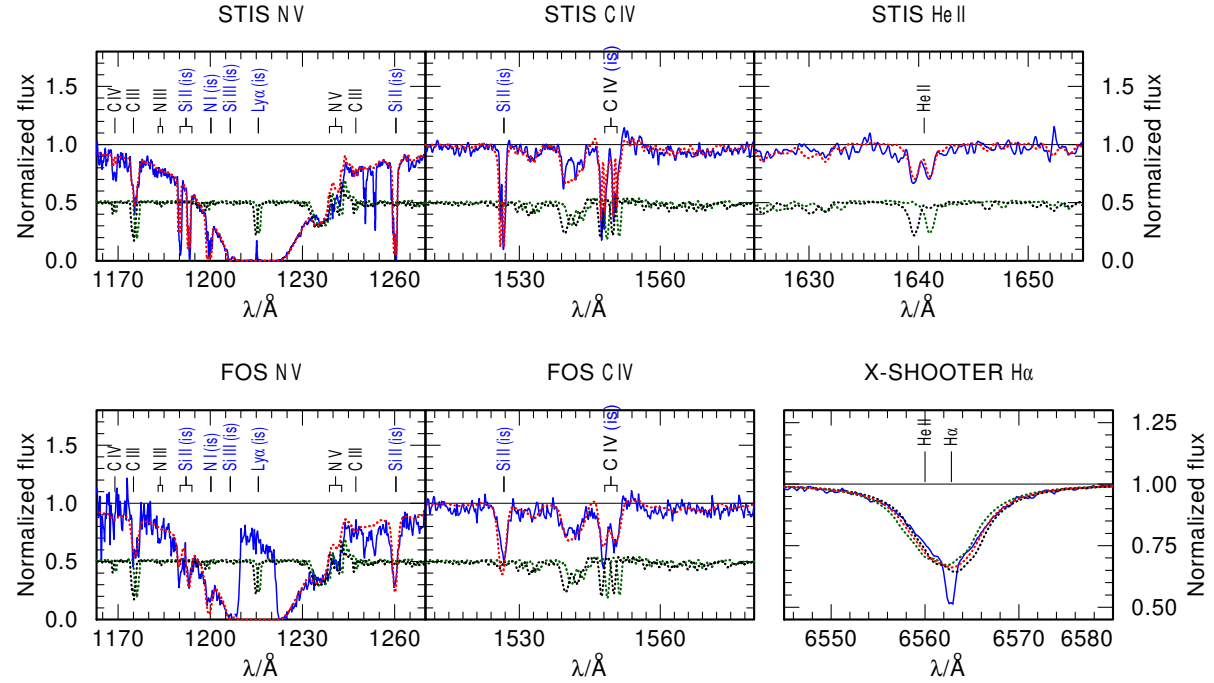

Fig. C.4.4. Close-up view of the wind diagnostic lines in the STIS and FOS spectra, as well as Hα, which is part of the X-Shooter (2020) spectrum. The observed spectrum is shown in blue and needs to be compared to the combined synthetic spectrum, shown in red. In the combined synthetic spectrum ISM absorption lines, which originate from the Galactic foreground and in the SMC, are included and labeled as "(is)". For the STIS and FOS spectrum we plot the weighted synthetic spectra. For the X-Shooter (2020) spectrum we show the unweighted synthetic spectra of the primary and the secondary as black dotted and green dotted lines, respectively. A close-up view of the He II λ4686 wind diagnostic line can be found in Fig. C.4.1.

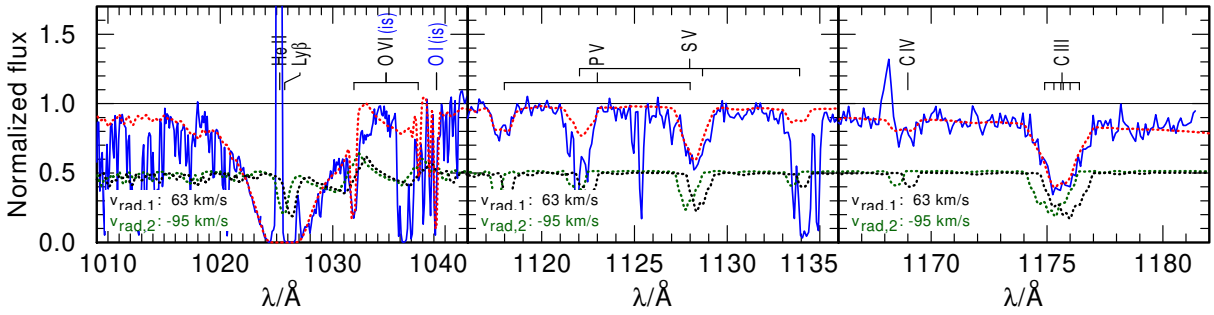

Fig. C.4.5. Close-up view of the important diagnostic lines in the far-UV FUSE spectrum. The observed spectrum is shown as a blue solid line, the weighted synthetic spectrum of the primary and secondary are shown as black dotted and green dotted lines and the combined synthetic spectrum is shown as a dashed red line. In the combined synthetic spectrum ISM absorption lines, which originate from the Galactic foreground and in the SMC, are included. They are labeled as "(is)". We note that not all ISM lines are modeled, and that FUSE spectra are additionally contaminated by absorption lines from molecular hydrogen.

Appendix C.5: Light and RV curve modeling with the PHOEBE code

The PHOEBE code does not contain atmosphere tables for hot stars. Therefore, we approximated the AzV 14 spectrum as a blackbody. From comparison of a blackbody and our synthetic spectrum in the V-band, we find that this is a reasonable approximation. To model the effect of limb-darkening, we adopt a quadratic approximation for the intensity (Diaz-Cordoves & Gimenez 1992)

$$I(\mu) = I(1)[1 - a_i(1-\mu) - b_i(1-\mu)^2], \tag{C.5.1}$$

where $\mu = \cos\theta$ is the cosine of the directional angle and a_i and b_i are the linear and quadratic coefficients of the binary component i. The coefficients are determined by fitting the Eq. (C.5.1) to the emergent intensity distribution in our best fitting PoWR model. For the primary, we derive $a_1 = 0.1474$ and $b_1 = 0.0985$, and for the secondary, $a_2 = 0.1489$ and $b_2 = 0.1025$. The effect of gravitational darkening is approximated by a power-law with exponent $\beta_{\rm grav} = 1$. For simplicity, we assume that both stars are rotating synchronously with the orbit, a reasonable approach for stars in binaries with orbital periods on the order of a few days. In our simulations, the effect of ellipsoidal variability, which is important in short-period binaries, is also included. The reflection effect (Wilson 1990) is modeled with two reflections.

As a fitting routine, we choose the built-in option of the `emcee` sampler (Foreman-Mackey et al. 2013), enabling us to consistently model the light and RV curve. From our PHOEBE model, we conclude that the observed light curve originates purely from ellipsoidal modulations, meaning that the flux during quadrature is the highest and lowest when the stars are aligned. The resulting parameters are listed in Table C.5.1 and C.5.2.

Table C.5.1. Orbital parameters of AzV 14 obtained using the PHOEBE code.

parameter	value	unit
P	3.7058 ± 0.0013 (fixed)[(a)]	[d]
ω_0	0 ± 2	[°]
T_0	$2\,459\,036.101 \pm 0.004$	[d]
v_0	-13 ± 3	[km s^{-1}]
$q_{\rm orb}$	0.95 ± 0.01	
i	35^{+5}_{-5}	[°]
a	40.6 ± 1.8	[$R_\odot$]

[(a)] Adopted from the analysis of the TESS light curve.

Table C.5.2. Orbital parameters of the individual binary components obtained using the PHOEBE code.

parameter	primary	secondary	unit
K	125 ± 5	132 ± 5	[km s^{-1}]
$M_{\rm orb}$	$33.6^{+5.0}_{-3.7}$	$31.9^{+4.8}_{-3.5}$	[$M_\odot$]

Appendix C.6: Input physics in the MESA binary evolutionary model

Our binary evolutionary models are calculated with the MESA version r15140. The chemical composition is adjusted to the SMC. Following Brott et al. (2011), we use tailored abundances for H, He, C, N, O, Mg, Si, and Fe in the evolutionary models. We note that these are similar to those used in the PoWR atmosphere models (see Table C.2.1). As initial parameters, we only set the initial masses of the binary components as well as the initial orbital period. We assume that the binary is initially tidally synchronized, a simplification adopted to reduce the free parameter space.

Our models include rotational mixing and treat it as a diffusive process, which encompasses the effects of dynamical and secular shear instabilities, the Goldreich-Schubert-Fricke instability, as well as Eddington-Sweet circulations (Heger et al. 2000). The efficiency coefficients of rotational mixing are adopted from Brott et al. (2011) and set to $f_c = 1/30$ and $f_\mu = 0.1$. On top of that, we include the angular momentum transport via magnetic fields from a Taylor-Spruit dynamo (Spruit 2002).

We use the standard mixing length theory (Böhm-Vitense 1958) with a mixing length coefficient $\alpha_{\rm mlt} = 1.5$ and the Ledoux criterion to model convection. Our models include the effect of envelope inflation, which occurs in regions within the star that approach the Eddington limit (Sanyal et al. 2015). Semiconvective mixing is taken into account with an efficiency coefficient of $\alpha_{\rm sc} = 1$ (Langer et al. 1983; Schootemeijer et al. 2019) and for core-H burning we include step overshooting in such a way that the convective core is extended by $0.335 H_{\rm P}$ (Brott et al. 2011; Schootemeijer et al. 2019). Thermohaline mixing, which becomes important for late evolutionary stages and during the accretion phase of the companion star, is modeled with an efficiency coefficient of $\alpha_{\rm th} = 1$ (Kippenhahn et al. 1980).

The choice of mass-loss rates is crucial for stellar evolutionary models. In particular, the mass-loss rates during the WR stages are important for those binaries which avoid evolving toward the cool side of the HRD. In the literature a discussion is ongoing on the efficiency of the WR winds at low metallicity. For example, Sander & Vink (2020) argue that below some limiting metallicity the WR winds become inefficient in removing mass. This limiting metallicity is thought to be close to the metallicity of the SMC. Therefore, we adjust the WR mass-loss recipes such that they are adequate for the SMC metallicity. We include mass-loss as follows: for main sequence stars ($X_{\rm H} > 0.7$) we use the mass-loss rates by Vink et al. (2001) (which are an order of magnitude higher than those empirically derived for AzV 14 in this work). For temperatures below the so-called bi-stability jump we use the maximum value of either Vink et al. (2001) or Nieuwenhuijzen & de Jager (1990). And for the WR phase, this is when the surface hydrogen abundance drops below $X_{\rm H} < 0.4$, the recipe of Shenar et al. (2019, 2020c) is used. For surface abundances in the range of $0.7 > X_{\rm H} > 0.4$ we linearly interpolate between Vink et al. (2001) and Shenar et al. (2019, 2020c).

Mass transfer is modeled implicitly using the "contact" scheme of the MESA code. Mass transfer is treated as rotation-dependent mass accretion. This means, in our models mass transfer is conservative as long as the accretor can stay below critical rotation. As soon as it is rotating critically, we assume that all mass is lost from the system. In addition to that, we assume mass accretion from a stellar wind.

The model calculation of a binary component is stopped after core-He depletion. It is assumed that as soon as the primary model depletes helium in its core, it directly collapses into a BH (Dessart et al. 2011). This means that the orbit is not perturbed by a supernova explosion. Under the assumption that we are able to model mass-transfer from the former secondary to the BH produced by the former primary. Recently it was reported that the first supernova originating from a WR progenitor was observed (Gal-Yam et al. 2022). We estimate that in the case of a supernova event the mass of the BH in our models might be overestimated by a factor 2 to 4. However, the main parameter defining the size of the Roche lobe, and thus the start and end of mass transfer is the orbital separation and not the mass ratio (Eggleton 1983, their equation 2). We assume that the impact of this simplification on the evolution of the former secondary is negligible. During the mass-transfer phase, we assume that the BH can only accrete material with the Eddington accretion rate.

Appendix C.7: Identifying WR phases in stellar evolutionary models

We calculated the optical depth at the surface of a star in our evolutionary model calculation with the formula from Langer (1989)

$$\tau = \frac{-\kappa \dot{M}}{4\pi R(v_\infty - v_0)} \ln\left(\frac{v_\infty}{v_0}\right). \tag{C.7.1}$$

In this equation, the opacity κ is approximated by the electron scattering opacity $\kappa_{es} = 0.2\,(1 + X_H)\,\mathrm{cm^2\,g^{-1}}$, $\dot{M}$ is the wind mass-loss rate, R is the radius of the star, v_∞ is the terminal wind velocity, and v_0 is the expansion velocity at the base of the wind, which, for simplicity, is assumed to be constant $v_0 = 20\,\mathrm{km\,s^{-1}}$. Gräfener et al. (2017) found that v_∞ can be linked to the escape velocity v_{esc} by

$$v_\infty = \alpha \cdot v_{esc} = \alpha \cdot \sqrt{\frac{2GM}{R}(1-\Gamma)}, \tag{C.7.2}$$

where Γ is the Eddington factor and α is an evolutionary dependent scaling factor. We assume $\alpha = 1.3$ during the main sequence and WN phase. For factors used in the other phases we refer to Pauli et al. (2022a), their section 2.2.

Ideally the threshold to differentiate between optically thin and thick winds, He-stars or WR stars, is $\tau \geq 1$. However, in the calculation of the optical depth several simplifications are included. Therefore, a calibration to observations is needed. Aguilera-Dena et al. (2022) already did this for H-free WN stars and determined a threshold value of $\tau \geq 1.45$. On the other side, Pauli et al. (2022a) find that for H-poor WN stars a lower threshold might be needed to reproduce observations. In the SMC only H-poor WN stars (and one WO type star) are present. To find a threshold value that can reproduce the observations, we calculated the optical depths of all the H-poor WN stars in the SMC. Their stellar parameters and optical depths are listed in Table C.7.1. We find that all have an optical depth value of $\tau \gtrsim 0.2$, which we set here as our new threshold.

Table C.7.1. Summary of the stellar parameters of the WR stars in the SMC that are used to calibrate the threshold of the optical depth τ.

star id [AB]	T_{eff} [kK]	R_* [$R_\odot$]	log L [$L_\odot$]	log $\dot{M}$ [$M_\odot\,yr^{-1}$]	log $\dot{M}^{(a)}_{Shenar}$ [$M_\odot\,yr^{-1}$]	v_∞ [$km\,s^{-1}$]	X_H [mass fr.]	τ	binary	reference
1	79^{+10}_{-10} [b]	$5.7^{+1.3}_{-1.3}$ [c]	6.07 ± 0.2	−5.58 ± 0.2	-5.33	1700±200	0.50 ± 0.05	0.26	—	Hainich et al. (2015)
2	47^{+3}_{-3}	$9.1^{+1.1}_{-1.1}$ [c]	5.57 ± 0.1	−5.75 ± 0.2	-5.64	900±100	0.55 ± 0.05	0.19	—	Hainich et al. (2015)
3	77^{+5}_{-5}	5.0^{+1}_{-1}	5.93 ± 0.05	−5.30 ± 0.1	-5.23	1500±200	0.25 ± 0.05	0.53	x	Shenar et al. (2016)
4	44^{+3}_{-3}	$13.0^{+1.8}_{-1.8}$ [c]	5.78 ± 0.1	−5.18 ± 0.2	-5.14	1000±100	0.25 ± 0.05	0.37	—	Hainich et al. (2015)
5a	43^{+5}_{-5}	24.0^{+10}_{-7}	6.35 ± 0.1	−4.50 ± 0.1	-4.80	2200±200	0.25 ± 0.05	0.51	x	Shenar et al. (2016)
5b	43^{+10}_{-10}	22.0^{+15}_{-10}	6.25 ± 0.15	−4.50 ± 0.3	-4.86	2000±200	0.25 ± 0.05	0.60	x	Shenar et al. (2016)
6	78^{+20}_{-5}	$4.7^{+1.5}_{-2.3}$	5.87 ± 0.15	−5.20 ± 0.2	-5.27	2000±200	0.25 ± 0.05	0.56	x	Shenar et al. (2018)
7	98^{+20}_{-10}	$3.4^{+1.2}_{-1.2}$	6.10 ± 0.1	−5.00 ± 0.2	-5.28	1700±200	0.15 ± 0.05	1.29	x	Shenar et al. (2016)
9	99^{+10}_{-10} [b]	$3.5^{+0.8}_{-0.8}$ [c]	6.05 ± 0.2	−5.65 ± 0.2	-5.23	1800±200	0.35 ± 0.05	0.31	—	Hainich et al. (2015)
10	98^{+10}_{-10} [b]	$2.2^{+0.5}_{-0.5}$ [c]	5.65 ± 0.2	−5.85 ± 0.2	-5.47	2000±200	0.35 ± 0.05	0.29	—	Hainich et al. (2015)
11	89^{+10}_{-10} [b]	$3.5^{+0.8}_{-0.8}$ [c]	5.85 ± 0.2	−5.56 ± 0.2	-5.52	2200±200	0.40 ± 0.05	0.34	—	Hainich et al. (2015)
12	112^{+10}_{-10} [b]	$2.4^{+0.5}_{-0.5}$ [c]	5.90 ± 0.2	−5.79 ± 0.2	-5.45	1800±200	0.20 ± 0.05	0.30	—	Hainich et al. (2015)

[a] Calculated using the mass-loss recipe of Shenar et al. (2019, 2020c). [b] We adopt a typical uncertainty of 10 kK (i.e., this is equivalent to one step in their used model grid). [c] Calculated using Gaussian error propagation.

Appendix D

Appendix D.1: Radial velocity

Four epochs of spectra are available for SMCSGS-FS 69 ; three of them are taken within one day and one with a gap of nine years. To estimate the RVs, we used a template to cross-correlate selected spectral lines (Si IIIλ4553) or full spectra, and then fit a parabola to the cross-correlation function's maximum region (e.g., Zucker 2003). Initial RV estimates were always calculated using one of the observations as the template. We found a maximum $\delta_{\rm RV} \approx 45\,{\rm km\,s^{-1}}$ for spectra taken in 2010 and 2019, and $\delta_{\rm RV} \lesssim 10\,{\rm km\,s^{-1}}$ for spectra taken within one day.

Appendix D.2: TESS light curve

SMCSGS-FS 69 was observed by the TESS space telescope in 2018 (sectors 1 and 2), 2019 (sector 13), and 2020 (sectors 27 and 28). We created our own light curves from the full frame images (FFIs) by using the Lightkurve package (Lightkurve Collaboration et al. 2018) to download a target pixel file with a 5×5 pixel image with 21 arcsec the projected pixel size, centered on the target for every available TESS sector. Based on cross-correlation with the Gaia DR3 catalog, the region surrounding the star is relatively sparse, with only one bright source one arcmin away. To exclude the contribution from this bright source, we opted for a one-pixel aperture mask centered on the source and further applied background subtraction. The Lightkurve package is also used to remove outliers and to detrend and normalize the light curve. The light curve is shown in Fig.D.2.1 (upper panel); a periodic signal is immediately evident in the light curve and we measure a period of P =0.838 days. The ASAS-SN Variable Stars Database classified the star as an eclipsing binary with a period of 1.675 days based on its photometric variability (Jayasinghe et al. 2020); this is twice the period observed using the TESS light curve. They reported similar variability to W Ursae Majoris-type binary (EW-type), which are known as contact eclipsing binaries. EW binary light curves are characterized by rounded peaks and sharp minima, as well as an overall symmetric shape, and typically have periods of less than one day. Two components in this subclass are expected to have roughly the same temperature, making their primary and secondary minima nearly indistinguishable from one another. Despite the light curve features, the spectra indicate that the two components have different temperatures and properties than EW-type. The inflated stripped star and Be star are just too big to fit into such a short-period system. In addition, three spectra taken within one day only show an RV variability of $\lesssim 10\,{\rm km\,s^{-1}}$.

Rotational variability appears to be the most common type of light variation among B/Be stars (Balona et al.2016, 2019, 2021). Therefore, one possibility is that the observed variability is a result of the fast rotation of the secondary Be star. By plugging in the estimated radius of secondary from spectral analysis and the period from the light curve into $v_{\rm rot} = 2\pi R/P_{\rm rot}$, we found $v_{\rm rot} \sim 480 - 620\,{\rm km\,s^{-1}}$ or $i \sim 35 - 60^{\circ}$. This range of inclination is in agreement with the shape of observed Hα and Brackett series emission line profiles.

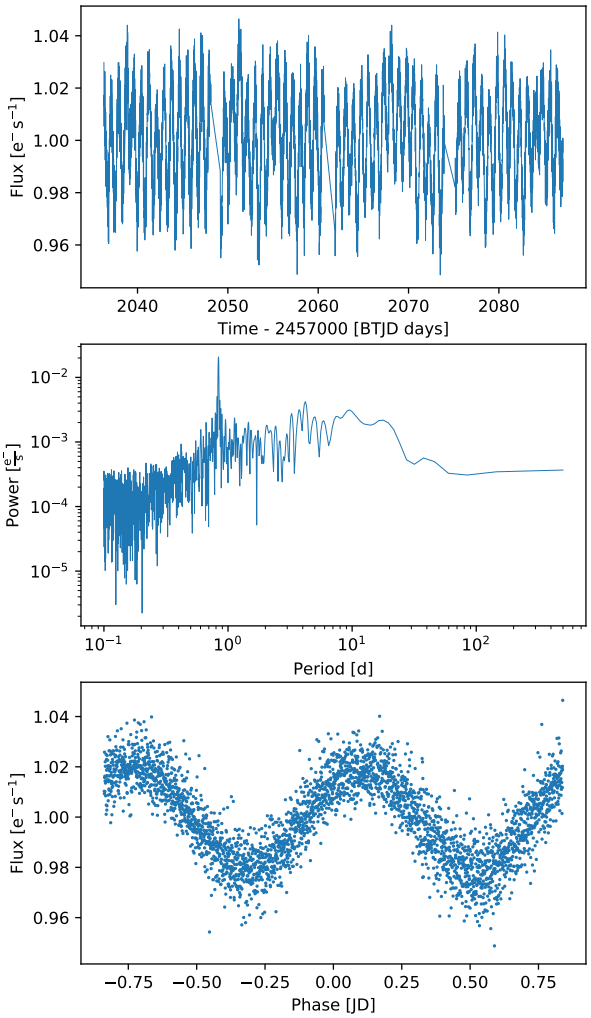

Fig. D.2.1. TESS light curves for SMCSGS-FS 69 extracted from FFIs taken in sectors 27 and 28. The middle panels show the periodograms of the light curve, and the bottom panel includes the phase-folded light curve with a period of 0.838 days.

Appendix D.3: Additional plots

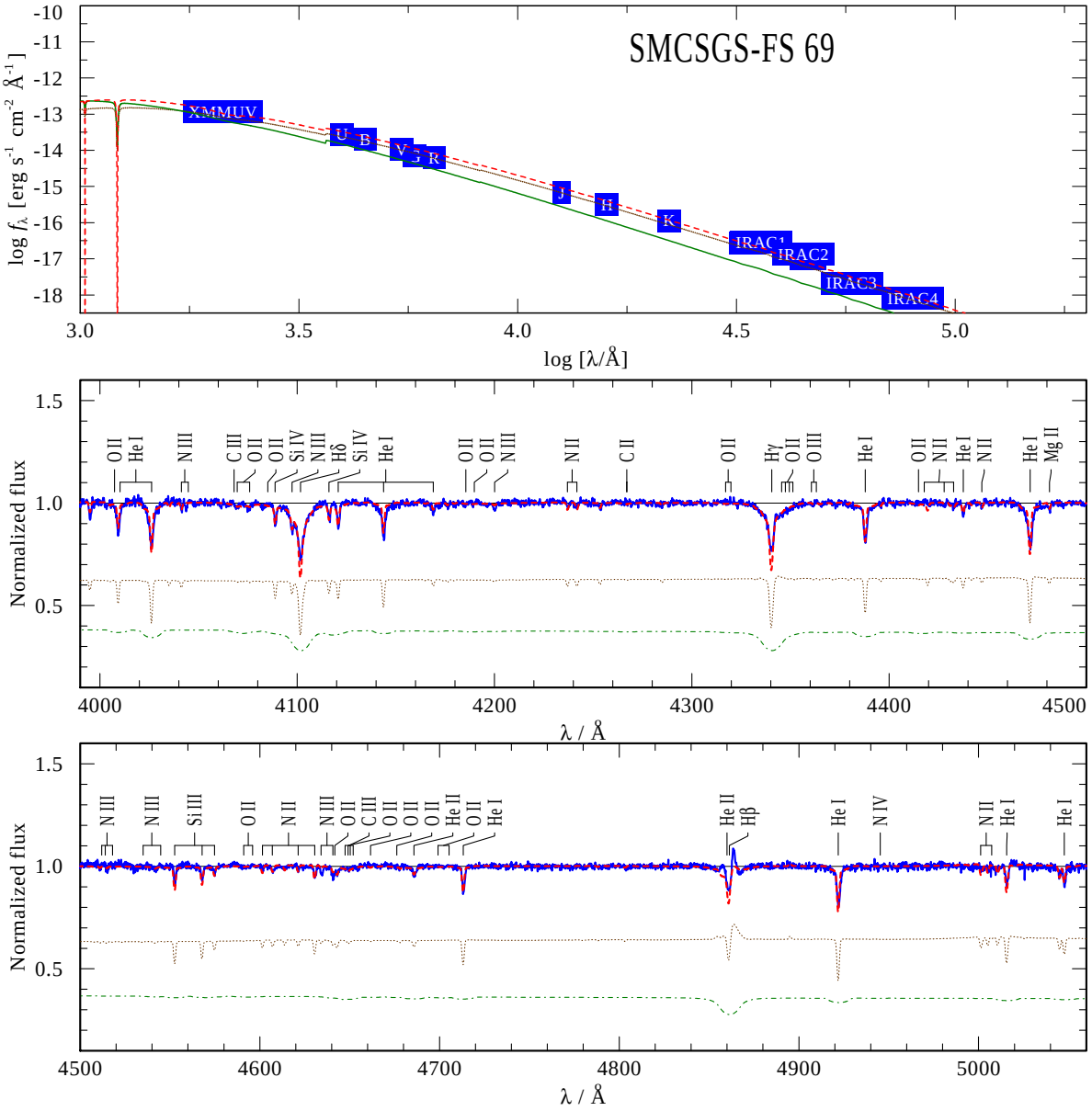

Fig. D.3.1. Observed spectra and photometry of SMCSGS-FS 69 (blue) compared to the model SED and synthetic spectra. The composite model (dashed red) is the weighted sum of the stripped star primary (dotted brown) and rapidly rotating B star secondary (dashed green) model spectra

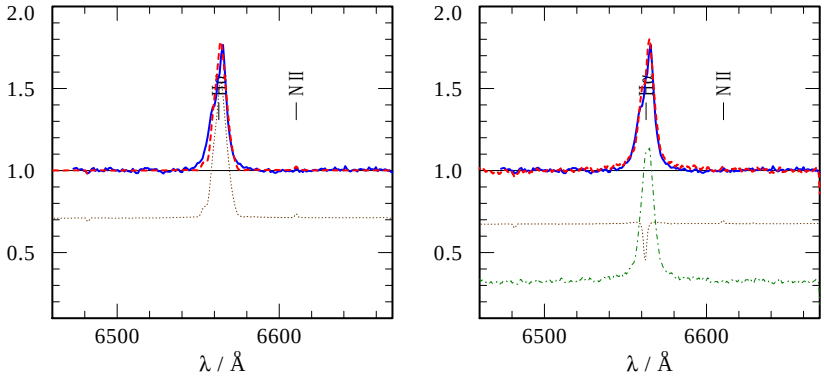

Fig. D.3.2. Comparison of observed Hα profile (blue) with composite PoWR models. (Left) Hα reproduced by a model with strong wind ($\log \dot{M} = -6.2$) assuming it is mostly coming from the stripped star. (Right) Hα feature reproduced by a composite (red dashed) of strong disk emission from the Be star (green dashed) and weak absorption component ($\log \dot{M} = -7.2$) from the stripped star (brown dotted).

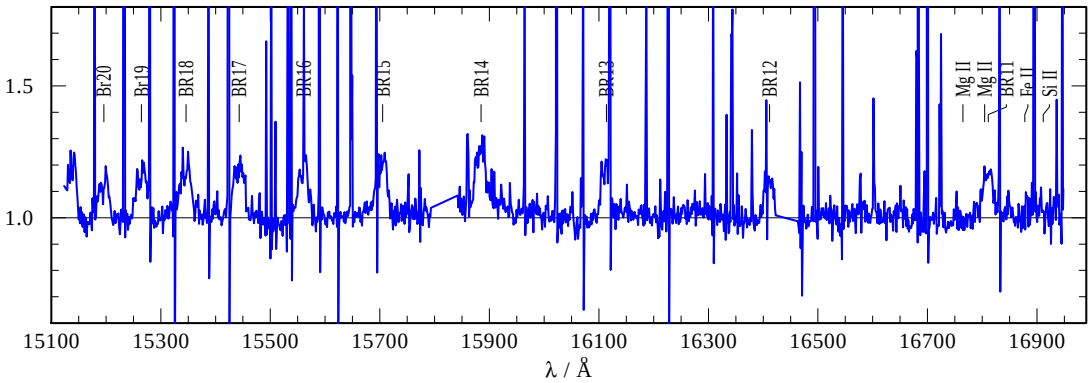

Fig. D.3.3. APOGEE H-band spectra of SMCSGS-FS 69 showing disk emission. The Brackett series lines are labeled

Appendix D.4: Additional tables

Table D.4.1. Absolute abundances in units of 12 + log (X_i/H) for the stripped star compared to SMC B main sequence and supergiants

	C	N	O	Si	Mg
SMCSGS-FS 69	$\lesssim$6.15	8.16	$\lesssim$6.87	6.82	7.12
SMC B supergiants[1]	7.30	7.55	8.11	6.75	6.8
SMC B stars[2]	7.23 (7.35)	7.17 (6.50)	8.06 (8.05)	6.79 (6.80)	6.74 (6.75)

Notes. [(1)] average abundances of SMC B supergiants adopted from Dufton et al. (2005) [(2)] average (and baseline) abundances of SMC B stars adopted from Hunter et al. (2007)

Appendix D.5: Binary evolution modeling

The binary evolution modeling was carried out with the MESA[1] stellar evolution code (Paxton et al. 2015, 2018, 2019). Most of the modeling assumptions follow those of Klencki et al. (2022) for the SMC composition. A notable difference is the use of the convective premixing scheme (introduced in Paxton et al. 2019), which effectively introduces highly effective mixing in semiconvective regions. We model both binary components and finish the evolution once the primary reaches central carbon depletion. In most of our models we do not include stellar rotation in order to retain the option of choosing the accretion efficiency as a free parameter.[2] We explore the parameter range of primary masses from 10 $M_\odot$ to 18 $M_\odot$ (in steps of 0.2 $M_\odot$ around the best-fit model), mass ratios from 0.6 to 0.97, and orbital periods covering the entire range in which mass transfer interaction may occur. We vary mass accretion efficiencies from 0% to 70% in steps of 10%.

To find the best-fitting model, we first try matching the surface properties of both stars derived in spectral analysis (Table 5.4.1), namely: the luminosities, effective temperatures, and surface gravities for both stars, as well as the surface abundances of H, He, C, N, and O for the primary. None of our binary models was able to reproduce all the stripped star properties simultaneously.

Models in which the stripped star was produced following a Case A + Case AB mass transfer evolution were characterized by a surface He abundance $\gtrsim 0.75$ (in tension with the measured 0.3 – 0.5 range). Models of stripped stars produced via Case B mass transfer were generally in better agreement with the measurements. However, we could only marginally reproduce the surface He and H abundances, with most models predicting $X_{\rm He} > 0.5$ and $X_{\rm H} < 0.5$ for the (partially) stripped star stage. Marginal agreement was found in those models where a relatively large amount of envelope was left during mass transfer ($\sim 1 M_\odot$ in our favorite Case B model), which would preferentially occur in wider binaries (periods of hundreds rather than tens of days). The requirement of $X_{\rm He} < 0.5$ and $X_{\rm H} > 0.5$ further prevented us from finding a matching model for the surface O abundance. We found that stripped stars produced in Case B mass transfer would gradually reduce their surface O with increasing surface He abundance, as illustrated by the Case B example in the lower left panel of Fig. D.5.3. However, the exact shape of the relation between the He and the O abundance of the inner envelope layers is subject to large uncertainties related to the extent of internal mixing above the H-burning shell through processes such as overshooting, semiconvection, and rotationally induced mixing. The difficulty in simultaneously reproducing the H, He, and O abundance of the stripped star in SMCSGS-FS 69 is likely a reflection of the limitation of current stellar models in predicting the chemical structure of stars in this complicated inner region.

Altogether, we find that under the assumption of Case B mass transfer evolution, the observed properties of the stripped star are best matched with progenitors of $\sim 12.2 M_\odot$. In reproducing the properties of the secondary, there is a level of degeneracy between the initial mass ratio and the assumed accretion efficiency: the more unequal the initial mass ratio, the higher the accretion efficiency needed to reproduce the current luminosity of the secondary.[3] A particularly interesting solution is a case

[1] MESA version r15140, http://mesa.sourceforge.net/

[2] In MESA, a rotating secondary is unable to accrete any more mass once it is spun up to breakup velocity, which self-regulates the accretion rate during mass transfer.

[3] In principle, additional constraints are offered by the effective temperature of the Be companion. An 8 $M_\odot$ secondary that accretes 7 $M_\odot$ of material would be less evolved and therefore hotter than a 12 $M_\odot$ secondary that accretes 3$M_\odot$ of material. However, since most of our models do not include the fast rotation of the Be star, we most likely somewhat overestimate the temperature of the secondary.

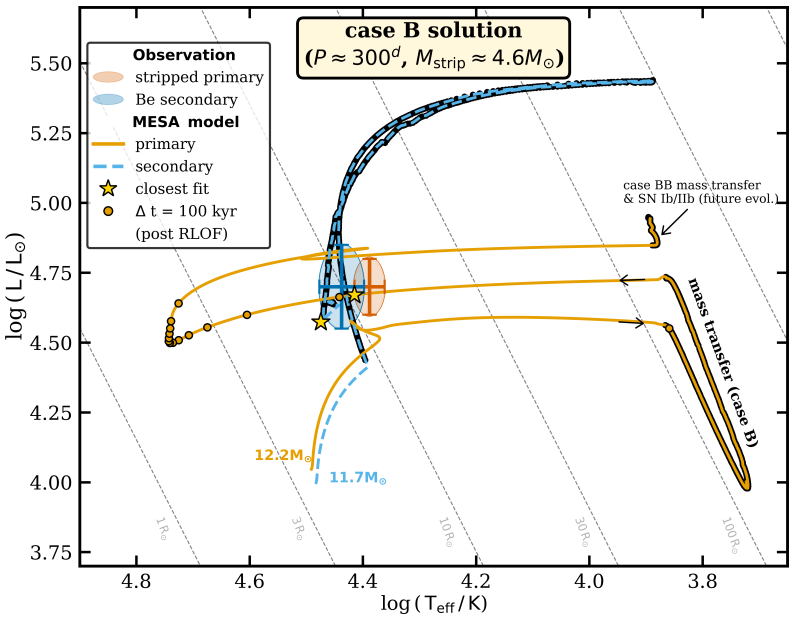

Fig. D.5.1. Best-fitting binary evolution model in which the stripped star is produced as a result of Case B mass transfer. The model requires accretion efficiency of at least ~ 40% to explain the current luminosity of the Be star secondary.

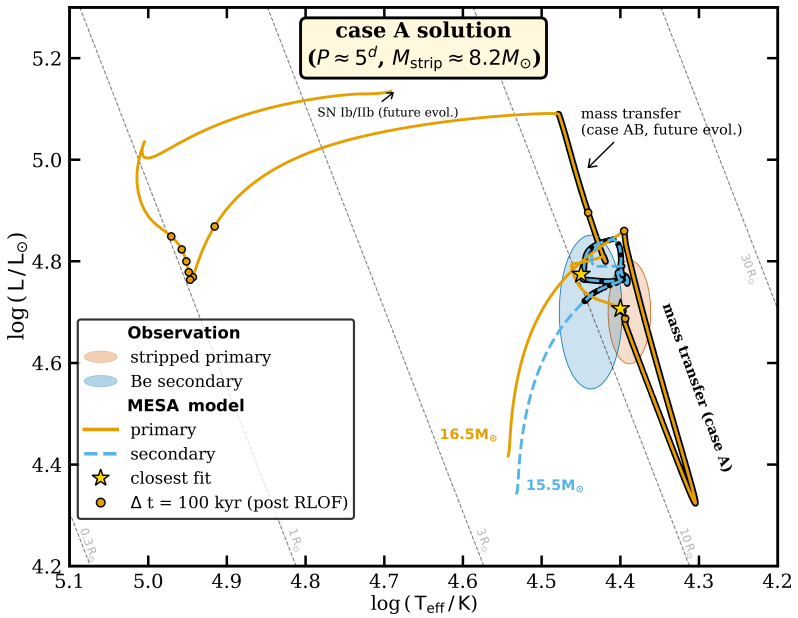

Fig. D.5.2. Best-fitting binary evolution model in which the stripped star is produced as a result of Case A mass transfer and is currently core-H burning.

when the binary is formed with the initial mass ratio very close to unity. In such a system, the amount of mass that is needed to be accreted by the secondary in order to explain its current luminosity can be viewed as the lower limit, placing constraints on the minimum accretion efficiency required to reproduce the observed binary.

This scenario is found in our favorite Case B binary model, shown in Fig. D.5.1, where the system is formed as a $12.2 M_\odot$ primary and an $11.7 M_\odot$ secondary on a 126-day period orbit. The secondary accretes with $\sim 40\%$ efficiency, and once it regains thermal equilibrium at the end of the mass transfer phase it settles back onto the MS with a luminosity of $\log L/L_\odot \sim 4.5$ (i.e., on the lower end of the range measured for the Be star in SMCSGS-FS 69).

As an alternative scenario, we calculated a subgrid of models that include rotation, limiting the amount of material that can be accreted by the secondary. This has severe implications for the Case B models, as it prevents the secondary from accreting enough material to match the observed parameters. However, we were able to find an acceptable solution with a model undergoing Case A mass transfer. This model allows for higher initial primary masses, and hence also higher initial secondary masses without the need for the secondary to accrete a significant amount of material.

Our favorite case A model has an initial primary mass of $16.5\,M_\odot$, an initial secondary mass of $15.5\,M_\odot$, and an initial orbital period of only 4.85 d. The corresponding stellar evolutionary tracks are depicted in Fig. D.5.2. In this model the primary initiates mass transfer close to the terminal-age main-sequence (i.e., shortly before core-H exhaustion). During the mass transfer the secondary only accretes about $\lesssim 1\,M_\odot$ and quickly reaches critical rotation, preventing it from accreting more material. With this model we are able to explain the derived rotation rates of the two binary components, but also the observed surface abundances of H, He, C, N, and O simultaneously (see Fig. D.5.3). Despite the good agreement of the surface properties of the primary component, we are unable to explain the observed low spectroscopic mass and require the primary to be twice as massive as derived. It is worth mentioning, that the envelope mass of the primary in this case makes up roughly 50% of its total mass.

For the future evolution of the system our favorite Case A model predicts that the primary will expand again after all H is exhausted in the core. This will coincide with a new, rapid mass-transfer episode called Case AB, during which most of the H-rich envelope will be removed. The primary is predicted to evolve quickly into a He-star that still has a thin ($\lesssim 0.5\,M_\odot$) H-poor ($X_\mathrm{H} \sim 0.2$) envelope. Similar to the Case B model, the primary will expand again during He-shell burning, and will eventually explode as a supernova, most likely of type IIb/Ib. If the binary survives the explosion, the system will further evolve into a high-mass X-ray binary with a NS accretor. The relatively short-period of the X-ray binary predicted in the Case A scenario (from a few days to a few tens of days) means that in the event of a common-envelope the binary would likely merge and produce a Thorne-Żytkow object.

To estimate the relative rate of the two scenarios, we consider that the case A solution originates from binaries with initial periods between ~2 and ~5 days and initial primary masses between 16 and 17 $M_\odot$. Such systems will interact during the later half of the MS evolution of the primary (at SMC metallicity of $0.2\,Z_\odot$, Klencki et al. 2020), making it possible for the detached donor to match the temperature and luminosity of the stripped star in SMCSGS-FS 69. Similarly, we consider that the case B scenario occurs for binaries with initial primary masses between 11.5 and 12.5 $M_\odot$ and initial periods between 5 and 1000 days (the period range for case B mass transfer evolution in the considered mass range). Based on that, assuming the initial mass function of Kroupa et al. (2013) and the initial period distribution for massive binaries from Sana et al. (2012), we estimate that the formation rate of the progenitors of the case B scenario is about six times higher than that of the case A scenario. On the other hand, the lifetime of the stripped-star stage consistent with SMCSGS-FS 69 is typically about five times longer in

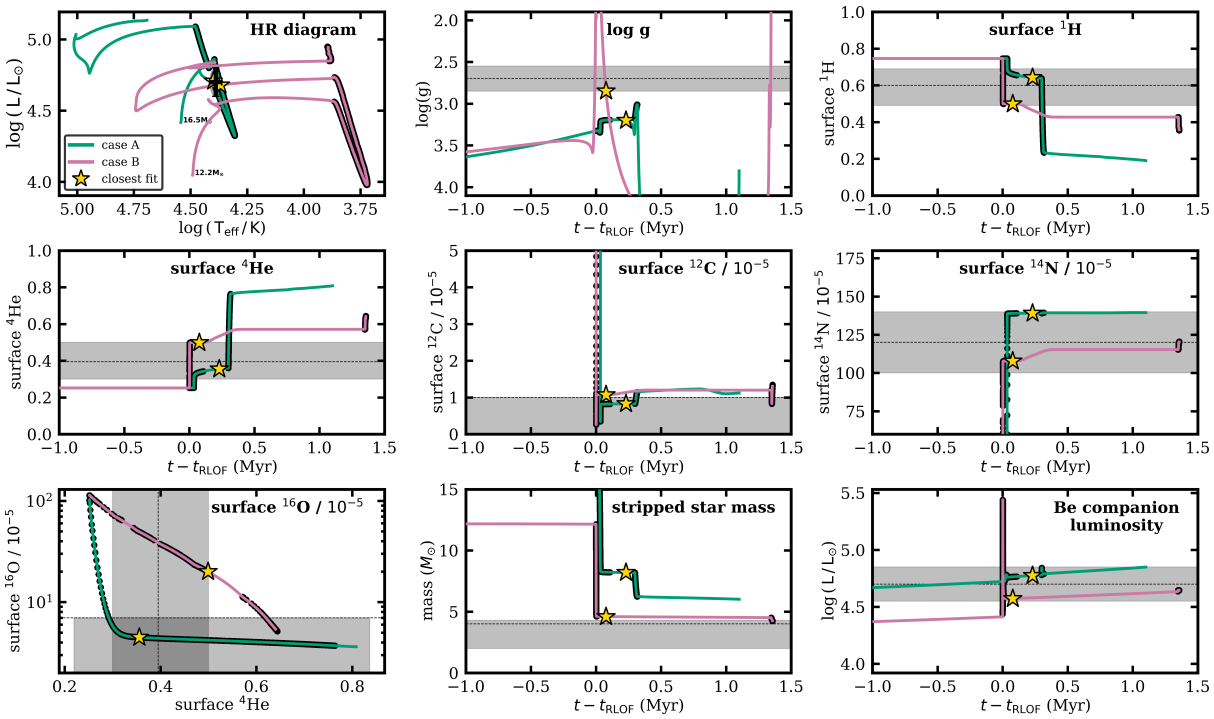

Fig. D.5.3. Stellar parameters and abundances derived spectroscopically (in grey) compared to binary evolutionary model predictions, variants with Case A and Case B mass transfer evolution (see also Fig. 5.4.4). The Case A mass travel model finds better agreement with surface abundances, although it is inconsistent with the measured surface gravity (and correspondingly, the inferred spectroscopic mass of the stripped star).

the case A scenario (~100-200 thousand years) compared to the case B scenario (30 thousand years). Altogether, this crude estimate shows that the relative rate of occurrence of partially stripped stars similar to SMCSGS-FS 69 is comparable for the two scenarios.

Appendix E

Appendix E.1: Radial velocity measurements for 2dFS 163

For 2dFS 163, we only have 3 epochs of available spectra to measure the radial velocities. For the primary (i.e., the slowly rotating stripped star) we derived the RVs by fitting Gaussians to the associated narrow metal lines in the optical and UV spectra. In the Xshooter spectrum, we used the N III $\lambda\lambda$4634–4642 emission lines and absorption lines such as N IV $\lambda\lambda$3460-3485 and He I λ4713 for this purpose. Afterward, we cross-correlated both X-shooter and 2dF spectrum to get the corresponding RV for 2dF. For this, we focused on nitrogen lines, and we got a $\delta_{\rm RV} = 28\,{\rm km\,s^{-1}}$. In the UV spectrum, we used narrow lines such as N III λ1183 and C IV λ1169 to determine the RV of the stripped star. To estimate the secondary's RVs, we fitted the synthetic model spectra of the primary and secondary to the observations while fixing the primary's RV to the values derived with the method described above.

Appendix E.2: Orbital analysis of 2dFS 2553

Appendix E.2.1: Radial velocity measurements

For this binary, we are in the lucky position to have sufficient (> 3) spectra that can be used to perform an orbital analysis, yielding an estimate for possible periods and the mass ratio. For the seven spectra we have at hand, we estimated the RVs following different approaches: For the primary (i.e., the slowly rotating partially stripped star) we derived the RVs by fitting Gaussians to the associated narrow metal lines in the optical and UV spectra. For the secondary (the fast-rotating Be star) we also fitted Gaussians to the broad He I lines in the optical spectra. In the UV spectra the primary is dominating the spectral appearance and the secondary's contribution can only be seen in the C III λ1175 line. To estimate the secondary's RVs, we fitted the synthetic model spectra of the primary and secondary to this line while keeping the primary's RV fixed to the values derived from the other lines. In addition to our estimated RV measurements, Lamb et al. (2016) also analyzed this star and reported a radial velocity shift for the lines associated with our primary star. Since their spectrum is not available in public archives, we adapt their reported RV for our primary. The derived RVs are listed in Table E.2.1.

Appendix E.2.2: Constraining ephemerides with *The Joker*

At first, we employed *The Joker* (Price-Whelan et al. 2017), a custom Monte Carlo sampler designed to derive possible ephemerides for sparse RV datasets. Unfortunately, it is only applicable to the RV of one star, and hence does not yield any information about parameters such as the mass ratio. In order to sample quickly a large parameter space, *The Joker* performs

Table E.1.1. RV estimates for 2dFS 163. All spectra are corrected for the barycentric motion but not for the systemic velocity of the SMC.

Instrument	MJD	RV1	δRV1	RV2	δRV2
2dF	51083	170	20	-	-
X-shooter	59150.0735	142	10	105	30
HST/COS	59131.2654	185	10	120	30

Table E.2.1. RV estimates for 2dFS 2553. Note that all spectra are corrected for the barycentric motion but not for the systemic velocity of the SMC.

Instrument	MJD	RV1	δRV1	RV2	δdRV2
2dF	51083	260	20	150	40
IMACS[(a)]	55069	130	20	—	—
HST/STIS	59024.264	210	10	200	40
HST/COS	59744.9111	80	10	190	30
HST/COS	59761.6678	155	10	190	30
X-shooter	59161.1254	127	10	215	20
X-shooter	59805.2514	214	10	143	20
HST/COS	60083.8085	210	10	120	30

Notes. [(a)] Value adopted from Lamb et al. (2016)

Table E.2.2. Orbital parameters for 2dFS 2553 derived with the PHOEBE code.

parameter	value	unit
$P_{\rm orb}$	$93.66^{+0.07}_{-0.08}$	[d]
ω_0	134^{+107}_{-98}	[°]
t_0	$-424.3^{+7.5}_{-4.5}$	[d]
v_γ	$169.78^{+2.75}_{-6.15}$	[km s^{-1}]
e	$0.03^{+0.14}_{-0.03}$	
$q_{\rm orb}$	$1.30^{+0.55}_{-0.24}$	
$a \sin i$	$211.1^{+51.8}_{-20.2}$	[$R_\odot$]
$i_{\rm orb}$ [(a)]	70	[°]
a [(b)]	$224.7^{+21.5}_{-55.1}$	[$R_\odot$]

Notes. [(a)] Calibrated such that the orbital and spectroscopic masses agree within their uncertainties. [(b)] Calculated using $i_{\rm orb}$.

Table E.2.3. Orbital parameters of the individual components in 2dFS 2553 obtained using the PHOEBE code.

parameter	primary	secondary	unit
K	65^{+3}_{-3}	50^{+4}_{-4}	[km s^{-1}]
$M_{\rm orb} \sin^3 i$	$6.26^{+4.84}_{-1.91}$	$8.14^{+6.17}_{-2.43}$	[$M_\odot$]
$M_{\rm orb}$ [(a)]	$7.5^{+5.8}_{-2.3}$	$9.8^{+7.4}_{-2.9}$	[$M_\odot$]
$R_{\rm RL}$ [(a)]	80^{+18}_{-8}	90^{+24}_{-8}	[$R_\odot$]

Notes. [(a)] Calculated using $i_{\rm orb}$ (see Table E.2.2).

at first a rejection sampling analysis by using prior probability density functions (PDFs) and yields multimodal PDFs of the ephemerides. Within this work, we use the default PDFs as recommended by the manual. As input a log-uniform priors in the range of 0.5 d – 700 d. From this first quick sampling, *The Joker* reports possible periods to be around the order of a few days ($\sim$ 7 d, up to 300 d, with the most likely solution to be around 95 d. We note that the most extreme solutions (i.e., the shortest and longest periods) favor eccentric orbits ($e > 0.2$), while the most likely solution around 95 d favors circular orbits.

After the rejection sampling, a standard MCMC method is used to sample around the most likely solution to fully explore the posterior PDF. Following this procedure, we find that the RVs can be modeled the best with a period of $P = 93.67^{+0.05}_{-0.07}$ d and a circular orbit ($e = 0^{+0.09}$).

Appendix E.2.3: Full orbital analysis with PHOEBE

As a second step, we employ the Physics of Eclipsing Binaries (PHEOBE) code (version 2.3, Prša & Zwitter 2005; Prša et al. 2016; Horvat et al. 2018; Jones et al. 2020; Conroy et al. 2020) to determine all orbital parameters consistently from the primary's and secondary's RVs. For our fitting efforts, we use the built-in option of the MCMC sampler emcee (Foreman-Mackey et al. 2013), allowing us to probe a large parameter space and obtain realistic error margins on the individual orbital parameters.

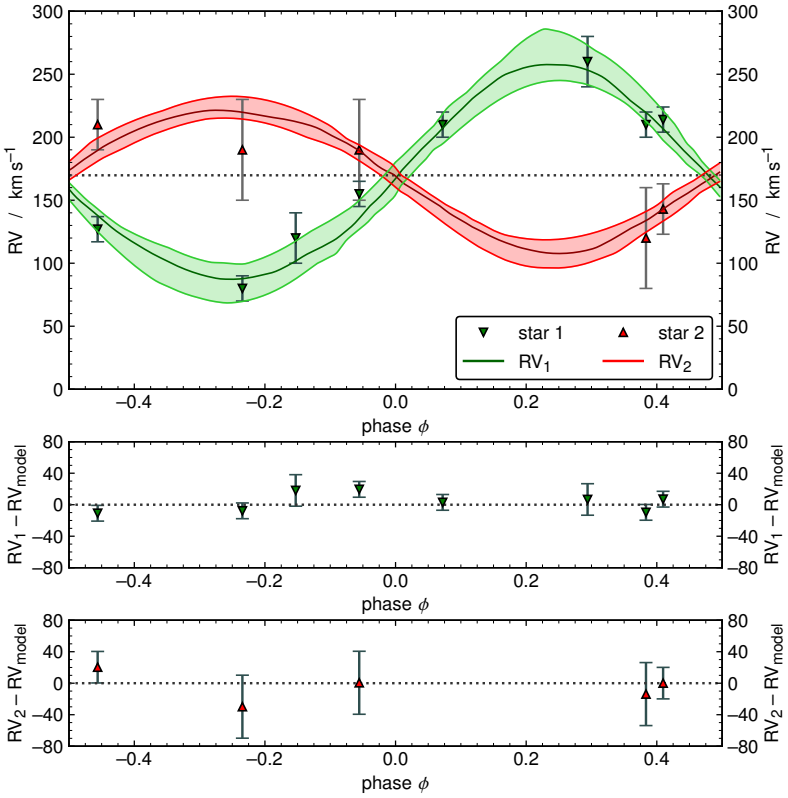

Fig. E.2.1. RVs of both components in 2dFS 2553 as a function of phase. *Upper panel:* Observed (triangles) and synthetic (solid lines) RV curves of the primary (green) and secondary (red) as obtained with the PHOEBE code. The dashed black line indicates the systemic velocity v_γ. *Middle panel:* Residuals of the primary's RVs after subtraction of the model. *Lower panel:* Residuals of the secondary's RVs after subtraction of the model.

To derive the best fitting model, we used as free parameters the orbital period of the star $P_{\rm orb}$, the eccentricity e, the projected orbital separation $a \sin i$, the argument of the periastron ω, the time at which the primary component in our orbit is at superior conjunction t_0, the mass ratio q, and the systemic velocity v_γ. The prior distributions for $P_{\rm orb}$, $a \sin i$, t_0, and v_γ are assumed to have Gaussian shape, centered at the values found by *The Joker*. For the remaining parameters, we assume starting parameters of $e = 0$, $\omega = 0$, and $q = 2$ (the spectroscopic mass ratio) and assume that they are uniformly distributed over the ranges $e = 0 - 0.4$, $\omega = 0 - 2\pi$ rad, and $q = 0.33 - 3.0$.

The best values we quote here are the "mode" values (i.e. the most populated solutions and, hence, the most probable one), and their corresponding error margins are given as one-sigma confidence intervals. Our best RV fit is shown in Fig. E.2.1 the best fitting values are listed in Tables E.2.2 and E.2.3.

The PHOEBE results on the period and eccentricity are comparable with those derived by *The Joker*, but favor a slightly eccentric solution but still consistent with a circular orbit in the error margins. The derived mass ratio is $q_{\rm orb} = 1.3$ a bit lower than the spectroscopically derived one $q = 2^{+1.2}_{-0.96}$. However, both values agree within their respective uncertainties.

We tried to approximate the inclination by matching the projected masses $M_{\rm orb} \sin^3 i$ to the spectroscopic masses, which yields $i \approx 70°$. The spectroscopically derived projected rotation rate of the Be secondary $v_{\rm rot} \sin i = 300^{+100}_{-50}$ km s^{-1} would change to $v_{\rm rot} = 319^{+106}_{-52}$ km s^{-1}, which corresponds to $v/v_{\rm crit} \approx 0.63$.

Appendix E.3: Orbital analysis of Sk -71 35

Appendix E.3.1: Radial velocity measurements

For Sk -71° 35, we only have three epochs of available spectra to measure the radial velocities. For the primary (i.e., the slowly rotating partially stripped star) we derived the RVs by fitting Gaussians to the associated narrow metal lines in the optical and UV spectra. For the secondary (the fast-rotating Oe star) we also fitted Gaussians to the broad He I and He II lines in the optical spectra. Here especially the He II λ4686 and He II λ5412 are only coming from the secondary. In the UV spectra, Si IV $\lambda\lambda$1393–1403 P Cygni profiles are visible from both primary and secondary and are well-separated. So we use this to estimate the RVs by fitting the synthetic model spectra of the primary and secondary to this line. In addition, we also use N V lines in the UV to estimate the RV of the secondary. The derived RVs for Sk -71° 35 are listed in Table E.3.1.

Table E.3.1. RV estimates for Sk -71 35. Note that all spectra are corrected for the barycentric motion but not for the systemic velocity of the LMC.

Instrument	MJD	RV1	δRV1	RV2	δdRV2
GIRAFFE	57375.175	130	10	280	30
X-shooter	59285.02995	345	10	240	30
HST/COS	59689.9703	440	30	230	30

Appendix E.3.2: TESS light curve analysis

To determine the orbital period we make use of TESS light curves. We used the available 31 TESS light curves from the MIT Quick-Look Pipeline (QLP, Huang et al. 2020) taken from 2018 to 2023. Using the Lightkurve package (Lightkurve Collaboration et al. 2018), we concatenate all light curves together, followed by removing outliers (3σ limit) and normalizing all of them at the same time. The resulting light curve is shown in Fig. E.3.1 (upper panel). We performed a period search and found a clear peak at $\approx$ 4.7 days corresponding to a binary orbital period of $\approx$ 9.4 days.

Appendix E.3.3: Orbital analysis with `rvfit`

The RV measurements were analyzed using the `rvfit` code that models the RV curves for double-lined, single-lined binaries, or exoplanets (Iglesias-Marzoa et al. 2015). To do this, it uses an Adaptive Simulated Annealing (ASA) algorithm (Ingber 1996) which fits the following seven Keplerian parameters: the orbital period of the star P, the eccentricity e, the argument of the periastron ω, the time of periastron passage T_p, the systemic velocity γ, and the amplitude of the radial velocity K1 for the primary and K2 for the secondary star.

The period of the system is measured from the TESS light curve. In the analysis, we assume that the system has a circular orbit. Hence, those parameters were fixed during further analysis. The resulting `rvfit` orbital solutions are given in Table E.3.2. The theoretical RV fits to the measurements are shown in Fig. E.3.2.

The mass ratio derived based on the orbital analysis is $q_{\rm orb} = 5.4$, higher than the spectroscopically derived one $q = 4.6^{+3.1}_{-2.5}$. However, both values agree within their respective uncertainties. We tried to approximate the inclination by matching the projected masses $M_{\rm orb} \sin^3 i$ to the spectroscopic masses, which yields $i \approx 37°$. The corresponding orbital masses are $M_1 \approx 7.1\,M_\odot$, $M_2 \approx 38.8\,M_\odot$ and the orbital separation is $67\,R_\odot$. The spectroscopically derived projected rotation rate $v_{\rm rot} \sin i \approx 250\,{\rm km\,s^{-1}}$ would change to $v_{\rm rot} \approx 415\,{\rm km\,s^{-1}}$, which corresponds to $v/v_{\rm crit} \approx 0.67$.

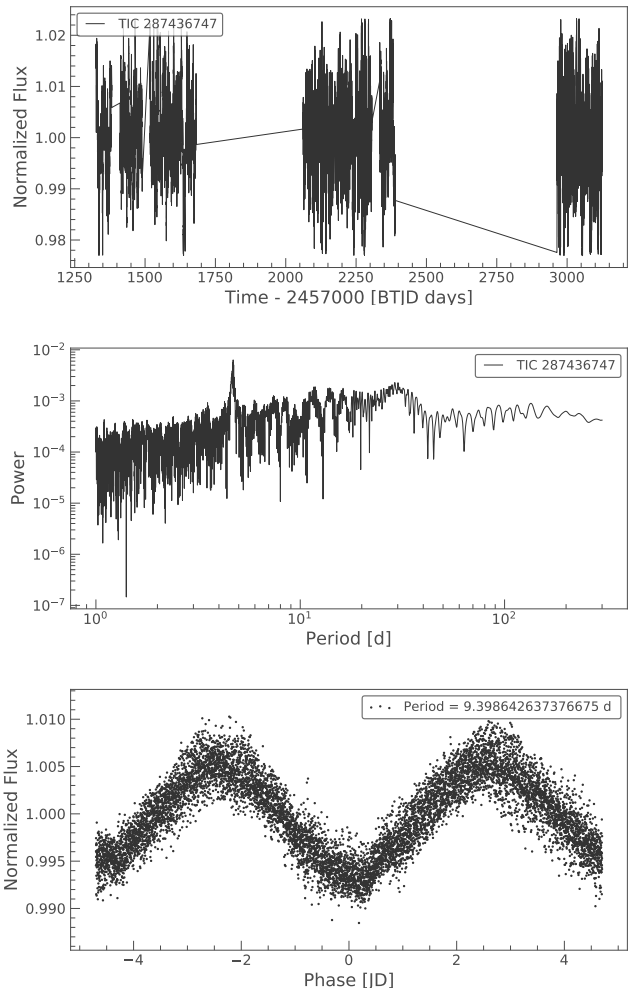

Fig. E.3.1. TESS light curves for Sk -71 35 taken during 2018 to 2023 (upper panel). The middle panels show the periodograms of the light curve, and the bottom panel includes the phase-folded light curve with a period of ≈ 9.4 days.

Table E.3.2. Orbital parameters derived for Sk -71 35 with with `rvfit`

parameter	value	unit
P	$9.39864^{(a)}$	[d]
ω	90	[°]
T_p	59007.02995 ± 0.163	[MJD]
γ	260.24 ± 14.69	[km s^{-1}]
e	$0^{(a)}$	
$K1$	183.95 ± 10.65	[km s^{-1}]
$K2$	33.76 ± 25.03	[km s^{-1}]

Notes. $^{(a)}$ Fixed during the analysis

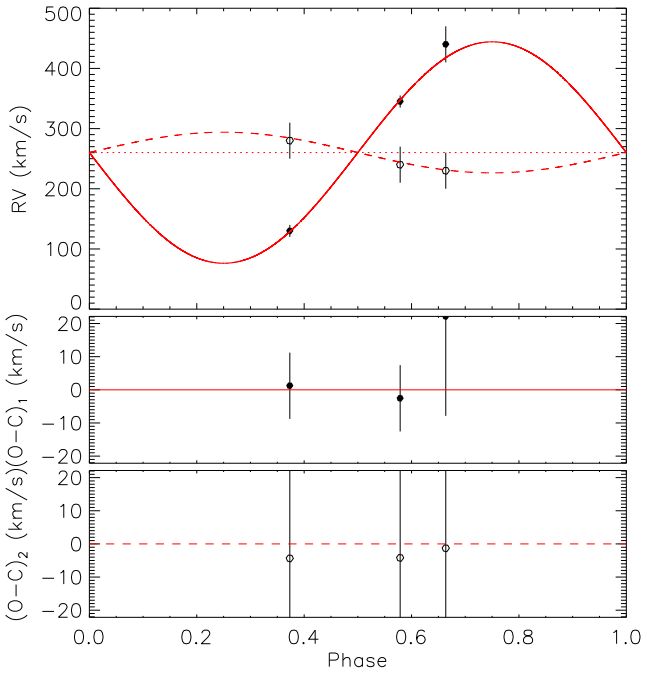

Fig. E.3.2. RV curve fit for primary (filled circles, solid curve) and secondary (open circles, dashed curve) components in Sk -71 35 obtained with `rvfit`. The bottom two panels show the residuals of the fit for the primary and the secondary.

Appendix E.4: Binary evolution calculations with MESA

Our binary evolutionary models presented here are calculated with the MESA code version r23.05.1. Similarly to the stellar evolution model from Brott et al. (2011), we use tailored abundances for H, He, C, N, O, Mg, Si, and Fe that are in accordance with the baseline abundances of the SMC and the ones used for our spectral analysis.

In our models, we employ the standard mixing length theory (Böhm-Vitense 1958) using the Ledoux criterion and a mixing length coefficient of $\alpha_{\rm mlt} = 1.5$ to model convection. Overshooting is included as step overshooting for core-hydrogen burning so that the convective core can extend up to $0.335\,H_{\rm P}$ (Brott et al. 2011; Schootemeijer et al. 2019). Thermohaline mixing is included with a standard coefficient of $\alpha_{\rm th} = 1$ (Kippenhahn et al. 1980). Rotational mixing within our models is treated as a diffusive process taking into account Eddington-Sweet circulations, Goldreich-Schibert-Fricke instabilities, as well as dynamical and shear instabilities (Heger et al. 2000). Following Brott et al. (2011), we set the rotational mixing efficiency coefficients to $f_c = 1/30$ and $f_\mu = 0.1$. Furthermore, angular momentum transport via magnetic fields is described using the Taylor-Spruit dynamo (Spruit 2002).

During the OB phase ($X_{\rm H} > 0.7$) we use the mass-loss recipe of Vink et al. (2001). Inspired from our comparison of the derived mass-loss rates of partially stripped stars to common mass-loss recipes (see Sect. 6.4.3.2), we choose to use the mass-loss recipe of Vink (2017) for stars with $X_{\rm H} < 0.4$ instead of a WR recipe. For stars in the transition phase, we interpolate linearly between the two mass-loss recipes to avoid sudden jumps in the Hertzsprung-Russell diagram (HRD). Since our stars do not evolve to the RSG phase, no mass-loss recipe is needed for this regime.

Mass transfer via Roche Lobe overflow (RLOF) in our MESA models is calculated using the inbuilt implicit scheme the so-called "contact" scheme. During the mass transfer the accretion on the secondary is treated as rotation-dependent, meaning that as soon as a star reaches its breakup velocity, no further mass can be accreted. Additionally, we assume that mass can be accreted from the stellar wind, however, this fraction is marginal compared to the mass-loss rates and mass-transfer rates during RLOF.

Our primary stars are calculated until they reach core-carbon depletion. The evolution of the secondary star continues until core-hydrogen depletion, occurring prior to any potential interaction with the companion.

Appendix E.5: Additional plots

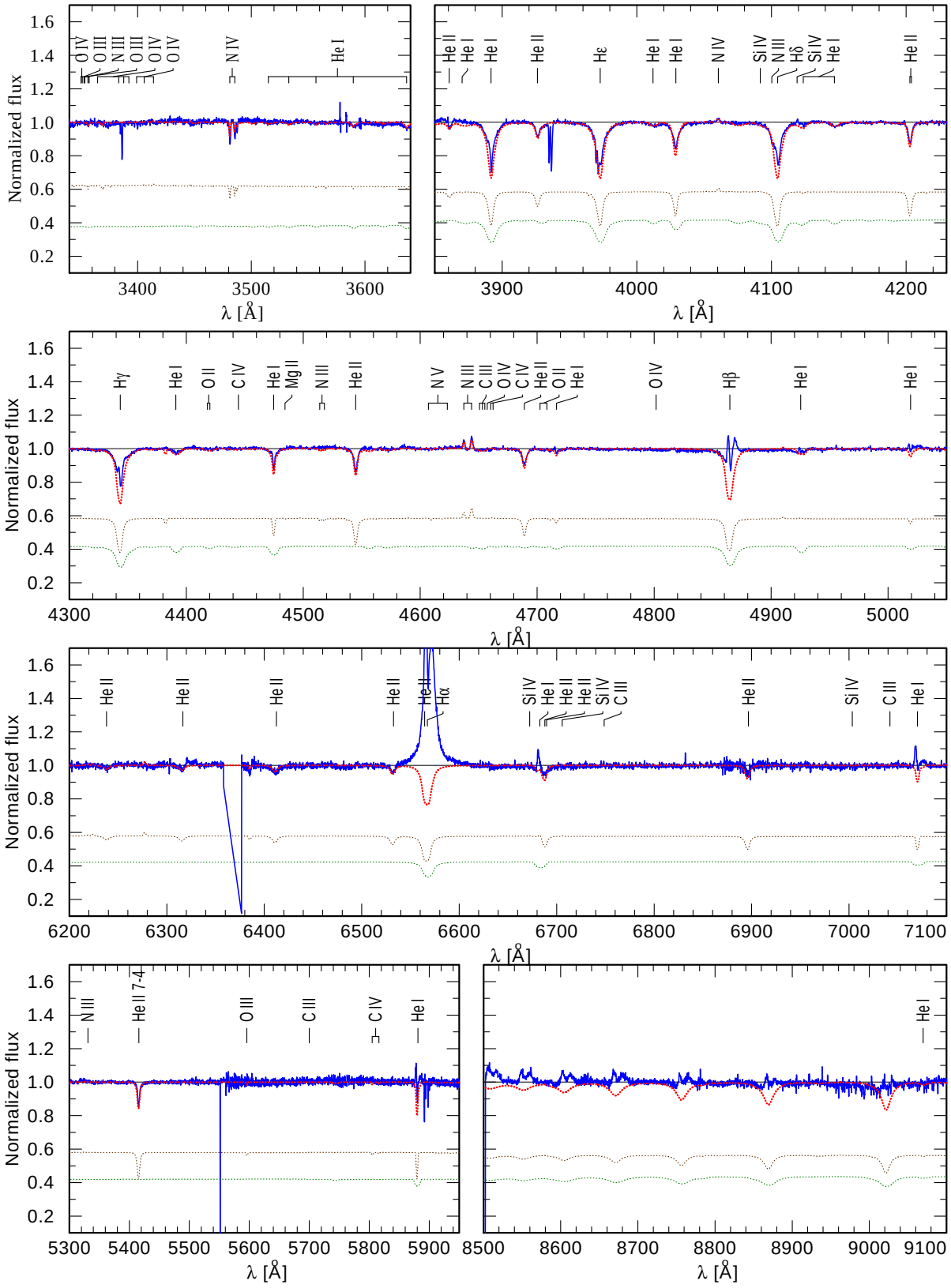

Fig. E.5.1. Observed spectra of 2dFS 2553 (blue) compared to the model spectra. The composite model (dashed red) is the weighted sum of the stripped star primary (dotted brown) and rapidly rotating Be star secondary (dashed green) model spectra

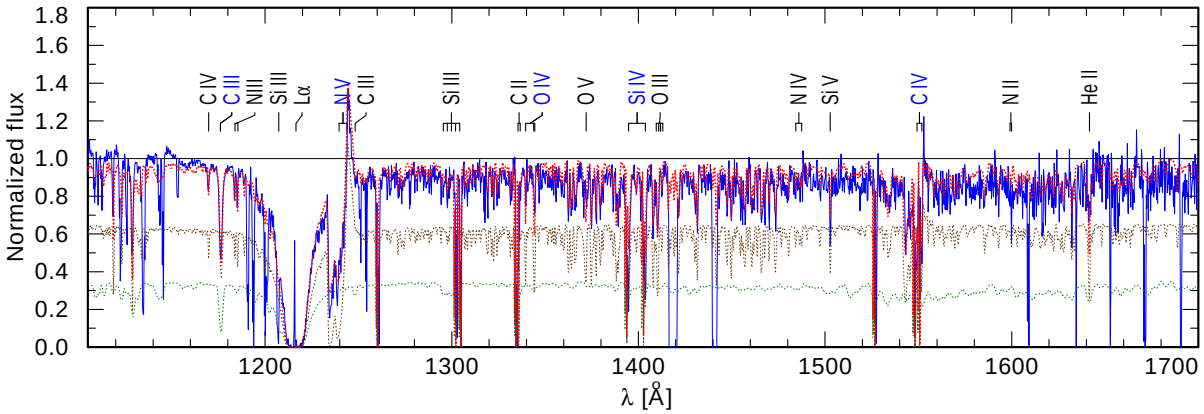

Fig. E.5.2. Observed HST UV spectra of 2dFS 2553 (blue) compared to the model spectra. The composite model (dashed red) is the weighted sum of the stripped star primary (dotted brown) and rapidly rotating Be star secondary (dashed green) model spectra

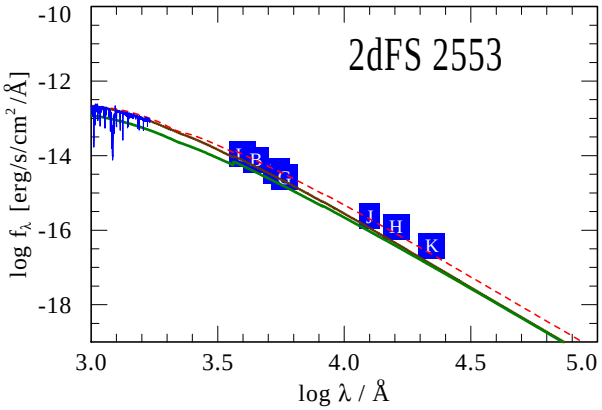

Fig. E.5.3. Observed flux calibrated UV spectra and photometry of 2dFS 2553 (blue) compared to the model SED. The composite model (dashed red) is the weighted sum of the stripped star primary (brown) and rapidly rotating B star secondary (green) model

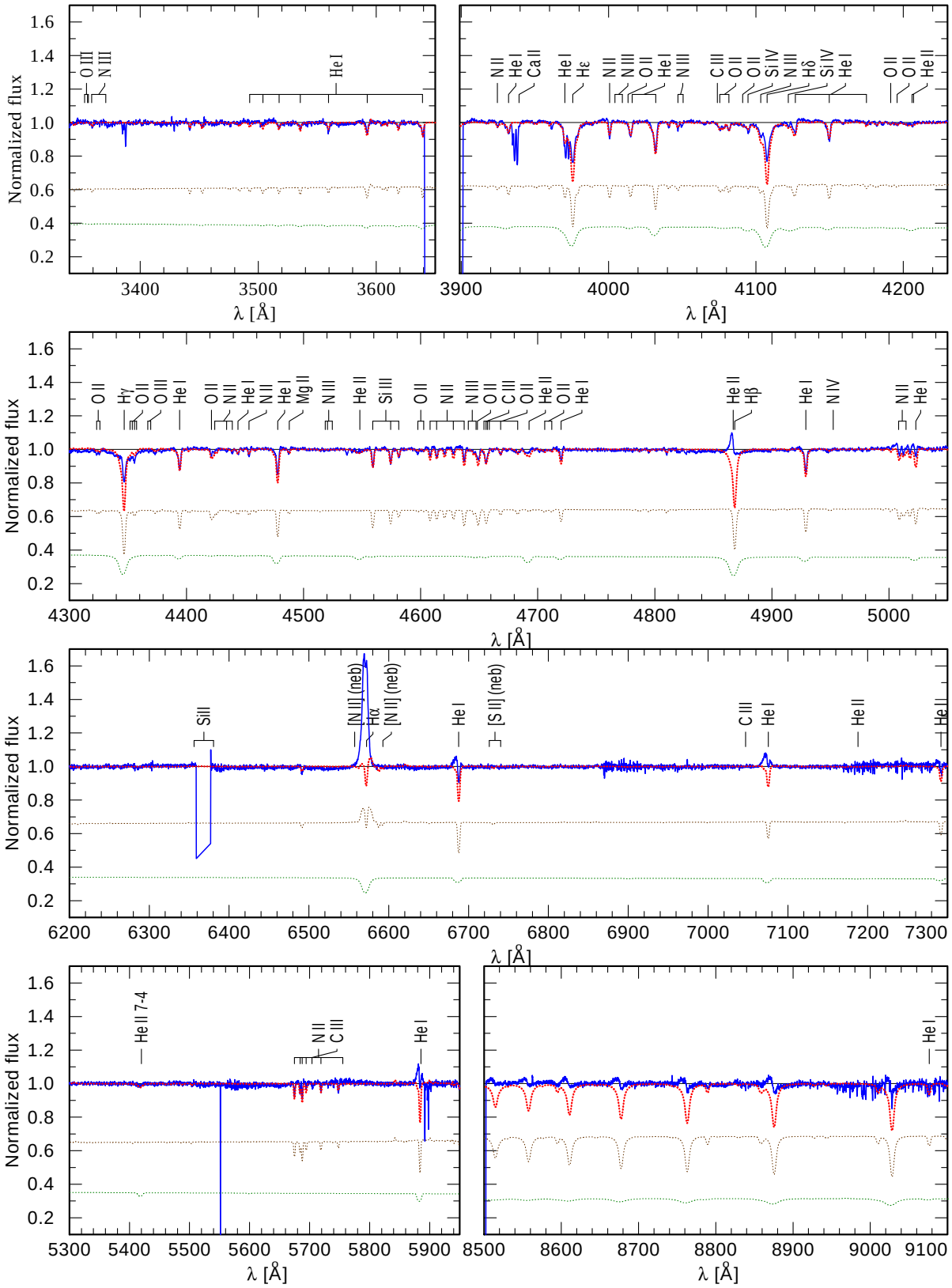

Fig. E.5.4. Observed spectra of Sk -71 35 (blue) compared to the model spectra. The composite model (dashed red) is the weighted sum of the stripped star primary (dotted brown) and rapidly rotating Oe star secondary (dashed green) model spectra

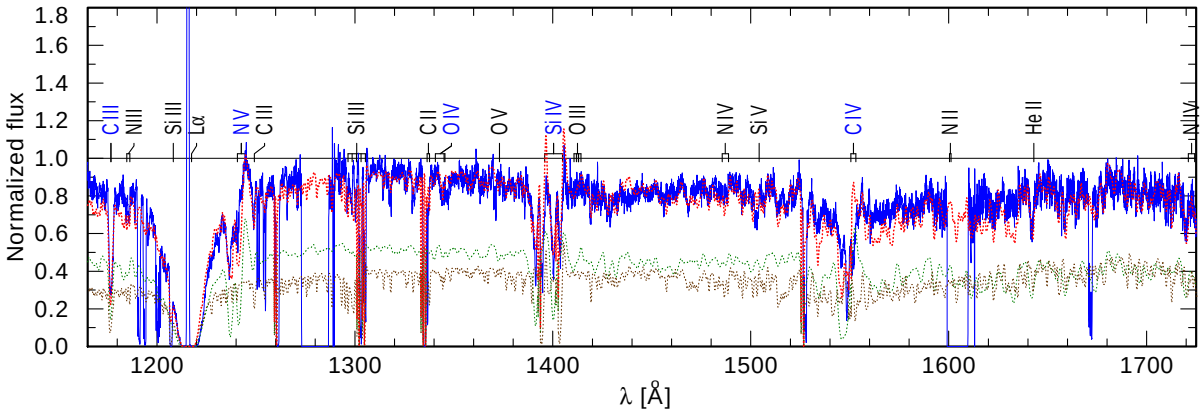

Fig. E.5.5. Observed HST UV spectra of Sk -71 35 (blue) compared to the model spectra. The composite model (dashed red) is the weighted sum of the stripped star primary (dotted brown) and rapidly rotating Oe star secondary (dashed green) model spectra

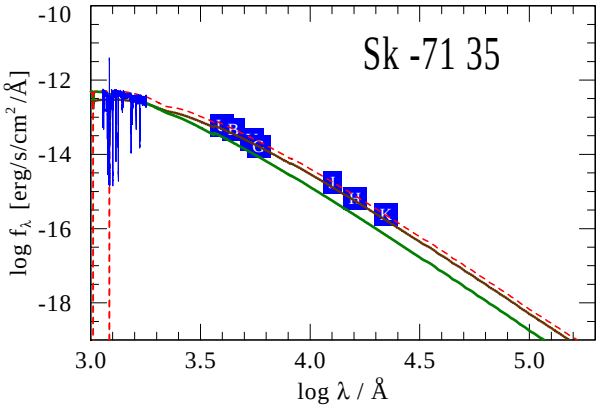

Fig. E.5.6. Observed flux calibrated UV spectra and photometry of Sk -71° 35 (blue) compared to the model SED. The composite model (dashed red) is the weighted sum of the stripped star (brown) and rapidly rotating Be star (green) models.